TECHNISCHE
UNIVERSITÄT
WIEN
Vienna University of Technology

DISSERTATION

Numerical analysis of many-body effects in cuprate and nickelate superconductors

ausgeführt zum Zwecke der Erlangung des akademischen Grades des

Doktors der technischen Wissenschaften (Dr. techn.)

am Institut für Festkörperphysik der

Technischen Universität Wien

unter Anleitung von

Prof. Dr. Liang Si
Univ.-Prof. Dr. Karsten Held

durch

Dipl.-Ing. Paul Worm

[redacted]
Matrikelnummer [redacted]

Wien, February, 2023

Die approbierte gedruckte Originalversion dieser Dissertation ist an der TU Wien Bibliothek verfügbar.
The approved original version of this doctoral thesis is available in print at TU Wien Bibliothek.

Die approbierte gedruckte Originalversion dieser Dissertation ist an der TU Wien Bibliothek verfügbar.
The approved original version of this doctoral thesis is available in print at TU Wien Bibliothek.

Eidesstattliche Erklärung

Ich erkläre an Eides statt, dass die vorliegende Arbeit nach den anerkannten Grundsätzen für wissenschaftliche Abhandlungen von mir selbstständig erstellt wurde. Alle verwendeten Hilfsmittel, insbesondere die zugrunde gelegte Literatur, sind in dieser Arbeit genannt und aufgelistet. Die aus den Quellen wörtlich entnommenen Stellen, sind als solche kenntlich gemacht.

Das Thema dieser Arbeit wurde von mir bisher weder im In- noch Ausland einer Beurteilerin/einem Beurteiler zur Begutachtung in irgendeiner Form als Prüfungsarbeit vorgelegt.

Datum, Ort | Unterschrift

Affidavit

I declare in lieu of oath, that I wrote this thesis and performed the associated research myself, using only literature cited in this volume. If text passages from sources are used literally, they are marked as such.

I confirm that this work is original and has not been submitted elsewhere for any examination, nor is it currently under consideration for a thesis elsewhere.

Date, Place | Signature

Die approbierte gedruckte Originalversion dieser Dissertation ist an der TU Wien Bibliothek verfügbar.
The approved original version of this doctoral thesis is available in print at TU Wien Bibliothek.
TU Bibliothek Your knowledge hub WIEN

Die approbierte gedruckte Originalversion dieser Dissertation ist an der TU Wien Bibliothek verfügbar.
The approved original version of this doctoral thesis is available in print at TU Wien Bibliothek.

Abstract

High-temperature unconventional superconductivity is arguably one of the most studied but least understood phenomena in solid-state physics. Indeed the discovery of the first high-temperature superconductor, a copper oxide compound (cuprate), already dates back more than 35 years. Yet, there is no consensus concerning the mechanism behind superconductivity in those materials. Recently, also nickel oxide superconductors (nickelates), which are isostructural to cuprates, were discovered. This thesis focuses on applying advanced numerical tools to study these two families of superconductors.

One aspect responsible for the complexity of cuprates and nickelates is the strong Coulomb interaction between the $3d$ electrons. As a result, they become strongly correlated, and simple mean-field theories no longer capture the relevant physics. Most methods that can treat strong correlations non-perturbatively are, however, restricted to a few orbitals and/or sites. One way to address these methodological shortcomings is a two-step procedure: first, obtain an approximate solution of the exact many-body Hamiltonian and subsequently use it to construct an approximate Hamiltonian which can be solved (more) exactly.

Within this thesis, we adopt this approach and start by briefly reviewing density-functional theory and how to construct effective low-energy Hamiltonians. Following this, the many-body Green's function formalism, which forms the basis for the methods used to study the previously obtained effective models, is introduced. Our method of choice is the dynamical vertex approximation, a Feynman diagrammatic extension of the dynamical mean-field theory.

The remainder of this thesis deals with the physics of cuprates and nickelates, with a particular focus on their respective models. Cuprates are first introduced, and a parameter region where the density of states displays a depression at the Fermi energy, commonly known as "pseudogap", is studied. Based on calculations of the Hubbard model, we unveil how the imaginary part of the spin-fermion vertex can lead to the formation of the pseudogap. Furthermore, we show that the pseudogap can be understood as a momentum-selective insulator, where the Fermi surface at the antinode becomes gapped. At the same time, coherent states remain at the node.

The next sections focus on the "new kids on the block" of high-temperature superconductors: nickelates. Currently, there is no consensus regarding the minimal model for superconductivity in nickelates within the community. Hence, the first section reviews the electronic structure and establishes our view on the minimal model: a single-band Hubbard model. Subsequently, this model is tested by comparing the calculated superconducting transition temperature and magnetic response to experimental measurements. Additionally, we extend our framework to finite-layer nickelates and identify "superconductivity without rare-earth pockets".

The last part of this thesis focuses on hydrogen defects in nickelate superconductors. Intercalating hydrogen during the synthesis process of infinite-layer nickelates is energetically favorable. Hence, it is crucial to determine possible ways of detecting its presence in samples and understand how it influences their physics.

Die approbierte gedruckte Originalversion dieser Dissertation ist an der TU Wien Bibliothek verfügbar.
The approved original version of this doctoral thesis is available in print at TU Wien Bibliothek.
TU Bibliothek Your knowledge hub WIEN

Die approbierte gedruckte Originalversion dieser Dissertation ist an der TU Wien Bibliothek verfügbar.
The approved original version of this doctoral thesis is available in print at TU Wien Bibliothek.

Deutsche Kurzfassung

Die Entdeckung von Hochtemperatursupraleitung in Kupferoxidverbindungen (Cupraten) liegt bereits mehr als 35 Jahre zurück. Dennoch gibt es noch keine mikroskopische Theorie, welche die Sprungtemperatur quantitativ beschreiben kann und selbst der Mechanismus der Supraleitung dieser Materialien ist kontrovers. Hinzu kommt, dass kürzlich Nickeloxid-Supraleiter (Nickelate), welche isostrukturell zu Cupraten sind, entdeckt wurden. Diese Arbeit widmet sich der numerischen Berechnung von elektronischen Eigenschaften dieser beiden Familien von Supraleitern.

Ein Grund für die Komplexität von Cupraten und Nickelaten ist die starke Coulombwechselwirkung zwischen den $3d$ Elektronen. Diese Elektronen sind daher stark korreliert, weshalb deren Physik nicht mehr mittels einfacher Molekularfeldtheorien beschrieben werden kann. Methoden, welche starke Korrelationen behandeln können, sind derzeit allerdings aufgrund ihrer Komplexität auf nur wenige Orbitale und/oder Gitterplätze beschränkt. Eine Möglichkeit dennoch stark korrelierte Materialien zu beschreiben ist mit einem zweistufigen Ansatz: im ersten Schritt wird der exakte Hamiltonian näherungsweise gelöst, im zweiten Schritt daraus ein angenäherter Hamiltonian konstruiert, welcher dann exakt(er) gelöst werden kann.

Diese Arbeit beginnt mit einer kurzen Einführung in die Dichtefunktionaltheorie und die Wannierisierung, um effektive Modelle zu erstellen. Anschließend wird der Formalismus der Greenschen Funktionen der Quantenvielteilchentheorie behandelt. Dieser bildet die Grundlage für die Theorien, welche verwenden werden, um die Modellsysteme zu lösen. Dies ist in dieser Arbeit insbesondere die dynamische Molekularfeldtheorie und die dynamische Vertexapproximation.

Der Hauptteil dieser Arbeit befasst sich mit der Physik von Cupraten und Nickelaten. Zuerst wird ein Parameterbereich von Cupraten, in dem die Zustandsdichte eine Senke bei der Fermienergie aufweist, was allgemein als “Pseudogap” bekannt ist, untersucht. Als Modell für Cuprate verwenden wir ein Einband-Hubbardmodell und finden, dass der Imaginärteil von Spinfluktuationen eine entscheidende Rolle spielen kann. Weiters zeigen wir, dass der Pseudogap ein impulsselektiver Isolator ist. Hierbei bildet sich eine Bandlücke in der Nähe der Antinode, während die Node metallisch bleibt.

Auch für Nickelate gibt es noch keinen Konsens bezüglich des Mechanismus für Supraleitung. Wir starten daher mit einem Überblick über die elektronische Struktur und stellen unsere Sichtweise vor: ein Einband-Hubbardmodell. Um unser Modell zu testen, vergleichen wir die Sprungtemperatur für Supraleitung und die Magnonendispersion mit experimentellen Messungen. Anschließend wenden wir uns Nickelaten mit mehr als einer NiO_2-Schicht in der Einheitszelle zu und finden Supraleitung ohne Bänder von Seltenen Erden an der Fermienergie.

Der letzte Abschnitt dieser Arbeit behandelt Wasserstoffdefekte in Nickelaten. Diese können während der Synthese entstehen und die Eigenschaften der Proben dramatisch verändern. Wasserstoff ist aber in herkömmlichen experimentellen Methoden nur schwer detektierbar. Aus diesem Grund wird nach Signaturen von Wasserstoffdefekten, welche experimentell zur Detektion derselben genutzt werden können, gesucht.

Die approbierte gedruckte Originalversion dieser Dissertation ist an der TU Wien Bibliothek verfügbar.
The approved original version of this doctoral thesis is available in print at TU Wien Bibliothek.
TU Bibliothek Your knowledge hub WIEN

Die approbierte gedruckte Originalversion dieser Dissertation ist an der TU Wien Bibliothek verfügbar.
The approved original version of this doctoral thesis is available in print at TU Wien Bibliothek.

List of Publications

Below we provide a list of published articles. Those marked by ♦ contributed the core part to this thesis, while papers marked by ▲ could − for lack of space − be discussed only briefly. Papers marked by • are on a different topic and are not discussed in this thesis.

Peer-reviewed journal publications:

- ♦ **Explaining the pseudogap through damping and antidamping on the Fermi surface by imaginary spin scattering**, *Friedrich Krien, Paul Worm, Patrick Chalupa-Gantner, Alessandro Toschi, Karsten Held*; Commun Phys **5**, 336 (2022)
- ♦ **Correlations tune the electronic structure of pentalayer nickelates into the superconducting regime**, *Paul Worm, Liang Si, Motoharu Kitatani, Ryotaro Arita, Jan M. Tomczak, Karsten Held*; Phys. Rev. M **6**, L091801 (2022)
- ♦ **Hidden, one-dimensional, strongly nested, and almost half-filled Fermi surface in Ba2CuO$_{3+y}$ superconductors**, *Paul Worm, Motoharu Kitatani, Jan M. Tomczak, Liang Si, Karsten Held*; Phys. Rev. B **105**, 085110 (2022)
- ♦ **Phase diagram of nickelate superconductors calculated by dynamical vertex approximation**, *Karsten Held, Liang Si, Paul Worm, Oleg Janson, Ryotaro Arita, Zhicheng Zhong, Jan M. Tomczak and Motoharu Kitatani*; Front. Phys. **9**, 810394 (2022)
- ♦ **Fingerprints of Topotactic Hydrogen in Nickelate Superconductors**, *Liang Si, Paul Worm, Karsten Held*; Crystals **12**(5), 656 (2022)
- • **Photoexcitations in the Hubbard model: Generalized Loschmidt amplitude analysis of impact ionization in small clusters**, *Clemens Watzenböck, Markus Wallerberger, Laurenz Ruzicka, Paul Worm, Karsten Held, Anna Kauch*; Phys. Rev. B **106**, 085135 (2022)
- • **Broadening and sharpening of the Drude peak through antiferromagnetic fluctuations**, *Paul Worm, Clemens Watzenböck Matthias Pickem, Anna Kauch, Karsten Held*; Phys. Rev. B **104**, 115153 (2021)
- • **Enhancement of impact ionization in Hubbard clusters by disorder and next-nearest-neighbor hopping**, *Anna Kauch, Paul Worm, Paul Prauhart, Michael Innerberger, Clemens Watzenböck, Karsten Held*; Phys. Rev. B **102**, 245125 (2020)
- • **Electron-light interaction in nonequilibrium: exact diagonalization for time-dependent Hubbard Hamiltonians**, *Michael Innerberger, Paul Worm, Paul Prauhart, Anna Kauch*; Eur. Phys. J. Plus **135** (2020)

Die approbierte gedruckte Originalversion dieser Dissertation ist an der TU Wien Bibliothek verfügbar.
The approved original version of this doctoral thesis is available in print at TU Wien Bibliothek.
TU Bibliothek Your knowledge hub WIEN

Preprints:

- ▲ **Formation of hydrogen chains in ABO_2 nickelate superconductors**, *Liang Si, Paul Worm, Karsten Held*; arXiv:2208.11085 (2022)
- ▲ **Optimizing superconductivity: from cuprates via nickelates to palladates**, *Motoharu Kitatani, Liang Si, Paul Worm, Jan M. Tomczak, Ryotaro Arita, Karsten Held*; arXiv:2207.14038 (2022)
- **Merging numerical renormalization group and intermediate representation to compactify two- and three-point correlators**, *Sebastian Huber, Markus Wallerberger, Paul Worm, Karsten Held*; arXiv:2207.01681 (2022)

Die approbierte gedruckte Originalversion dieser Dissertation ist an der TU Wien Bibliothek verfügbar.
The approved original version of this doctoral thesis is available in print at TU Wien Bibliothek.
TU Bibliothek Your knowledge hub WIEN

Contents

Die approbierte gedruckte Originalversion dieser Dissertation ist an der TU Wien Bibliothek verfügbar.
The approved original version of this doctoral thesis is available in print at TU Wien Bibliothek.

Die approbierte gedruckte Originalversion dieser Dissertation ist an der TU Wien Bibliothek verfügbar.
The approved original version of this doctoral thesis is available in print at TU Wien Bibliothek.
TU Bibliothek Your knowledge hub WIEN

Die approbierte gedruckte Originalversion dieser Dissertation ist an der TU Wien Bibliothek verfügbar.
The approved original version of this doctoral thesis is available in print at TU Wien Bibliothek.
TU Bibliothek Your knowledge hub WIEN

Die approbierte gedruckte Originalversion dieser Dissertation ist an der TU Wien Bibliothek verfügbar.
The approved original version of this doctoral thesis is available in print at TU Wien Bibliothek.

List of abbreviations

Abbreviation	Explanation
AFM	Antiferromagnetic
AIM	Anderson impurity model
ARPES	Angular-resolved photoemission spectroscopy
AZB	Antiferromagnetic zone boundary
BCS	Bardeen-Cooper-Schrieffer
BEPS	Boson-exchange parquet solver
BSE	Bethe-Salpeter equation
BZ	Brillouin zone
1BZ	First Brillouin zone
CDMFT	Cluster DMFT
cRPA	Constrained random phase approximation
CT-QMC	Continuous-time quantum Monte Carlo
CT-HYB	CT-QMC in hybridization expansion
DCA	Dynamical cluster approximation
DE	Dyson equation
DFT	Density-functional theory
DMFT	Dynamical mean-field theory
DOS	Density of states
DΓA	Dynamical vertex approximation
EOM	Equation of motion
E_F	Fermi energy
E_{XC}	Exchange-correlation functional
FL	Fermi liquid
FLT	Fermi liquid theory
FS	Fermi surface
GF	Green's function
GGA	Generalized gradient approximation
GS	Ground state
HM	Hubbard model
HTC	High-temperature superconductivity
HTS	High-temperature superconductors

Die approbierte gedruckte Originalversion dieser Dissertation ist an der TU Wien Bibliothek verfügbar.
The approved original version of this doctoral thesis is available in print at TU Wien Bibliothek.
TU Bibliothek Your knowledge hub WIEN

Abbreviation	Explanation
KS	Kohn-Sham
LC	Luttinger count
LT	Luttinger's theorem
LDA	Local density approximation
MaxEnt	Maximum entropy method
MIT	Metal-insulator transition
MWT	Mermin-Wagner theorem
PBE	Perdew-Burke-Ernzerhof (functional)
PE	Photoemission
PG	Pseudogap
QMC	Quantum Monte Carlo
QPD	Quasiparticle dispersion
RIXS	Resonant inelastic X-ray scattering
SDE	Schwinger-Dyson equation of motion
STM	Scanning tunneling microscopy
STEM	Scanning transmission electron microscopy
STS	Scanning tunneling spectroscopy
T_c	Critical temperature for superconductivity
$T_{\text{Néel}}$	Néel temperature
VHS	Van Hove singularity
XC	Exchange-correlation
XRD	X-ray powder diffraction
2D	Two-dimensional
1PIR	One-particle irreducible
2PR	Two-particle reducible

Die approbierte gedruckte Originalversion dieser Dissertation ist an der TU Wien Bibliothek verfügbar.
The approved original version of this doctoral thesis is available in print at TU Wien Bibliothek.

Chapter 1

Introduction and Outline

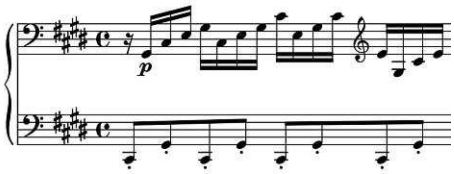

— L. van Beethoven
Moonlight Sonata 3rd movement

1.1 Introduction

It seems that you, dear reader, hold this thesis and contemplate whether or not to read further. Let us capture your interest and introduce you to the topic of this thesis, why you should care, and what there is to learn by reading this thesis.

What are superconductors? — A superconductor is a material that, below a certain temperature T_c, becomes (i) a perfect conductor, i.e. zero resistivity, and (ii) a perfect diamagnet, i.e. all magnetic flux is expelled. First discovered in mercury by K. Onnes [1] in 1911, superconductivity has since become a prominent field of study in condensed matter physics. The first microscopic description was formulated in 1957 by J. Bardeen, L. Cooper and J. R. Schriefer [2]. In simple terms, electrons close to the Fermi energy will pair to form a bound state, called "Cooper pair", if an effective attractive interaction between them is present and the temperature is sufficiently low. These Cooper pairs behave like bosons that condense at low temperatures and form a superconducting state. In "conventional superconductors", like mercury or lead, electron-phonon coupling leads to an effective attractive interaction. However, not all superconductors are captured by this framework.

What are cuprates and why are they different? — Copper-oxide superconductors, here just cuprates for short, are a family of layered quasi-two-dimensional superconductors[1]. They consist of CuO_2 planes, where superconductivity occurs [4], spaced by insulating layers that act as charge reservoirs. A simple representative is La_2CuO_4, which becomes superconducting upon doping, for example, by substituting some of the trivalent La^{3+} with divalent Sr^{2+} [5]. What makes cuprates so interesting is that they can exceed superconducting transition temperatures of 100 K at ambient pressure [6], far above what was deemed possible in phonon-mediated superconductivity [7, 8]. Indeed, standard phonon BCS theory is not able to explain the observed T_c in cuprates [9, 10]. Modifications or new theories altogether are needed, but despite several decades of research since the original discovery in 1986 by G. Bednorz and K. Müller [11], no

[1] See Ref. [3] for a comprehensive review.

Die approbierte gedruckte Originalversion dieser Dissertation ist an der TU Wien Bibliothek verfügbar.
The approved original version of this doctoral thesis is available in print at TU Wien Bibliothek.

consensus regarding the microscopic origin of superconductivity in cuprates has yet been reached in the scientific community. Some theories, including the one used in this thesis [12], are based on the electronic system alone and the "pairing glue" is a result of the strong mutual interaction between the electrons.

However, d-wave superconductivity is not the only feature that is exotic and interesting about cuprates. In the regime of low chemical doping, typically up to 15–20 % hole doping, cuprates remain metallic but show a depression of the density of states at the Fermi energy [13]. Momentum resolved, the Fermi surface shows disconnected segments coined "Fermi arcs" [14–16]. Their microscopic origin and whether or not the arcs are "real" is debated within the community [3]. Within this thesis, we analyze approximate numeric solutions of the Hubbard model for parameters where a pseudogap appears and discuss its origin.

And how do nickelates fit into the picture? — Nickel-oxide superconductors, nickelates for short, are a family of superconductors structurally akin to cuprates [17]. $LaNiO_2$, as a simple representative [18], is built from alternating NiO_2 and La square-planar layers and hosts a nominal Ni-$3d^9$ configuration, same as cuprates [19]. Yet, whether or not they are truly a "cuprate analog" is an ongoing debate in the community, not least because their electronic structure shows significant differences when compared to cuprates [20, 21]. Furthermore, they are experimentally extremely difficult to synthesize [22] and so far, superconductivity has only been observed in thin-film samples grown on a substrate (usually $SrTiO_3$) [23]. Within this thesis, we argue for a description based on a single-band Hubbard model plus decoupled electron pockets, which act as charge reservoirs. Subsequently, we compare observables like the transition temperature T_c and the paramagnon dispersion to experiments.

What is many body in this context? — Both nickelates and cuprates have partially filled $3d$ shells with low spatial extend and electrons in orbitals of those $3d$ shells feel the strong mutual Coulomb interaction of the others. As a result, the movements of those electrons are not independent. We say they are "correlated" and a many-body description is needed. One of the arguably most famous examples of many-body effects in condensed matter physics is the Mott metal-insulator transition [24]. Suppose the (local) interaction between electrons, i.e. the energy cost of doubly occupying a site, becomes very large. Then electrons will localize, and the system will undergo a phase transition from a metal to an insulator without spontaneously breaking any symmetry. Cuprates are one example of such a system. Furthermore, the quasi-two-dimensionality of nickelates and cuprates enhances non-local fluctuations[2], which might be at the origin of the pseudogap or superconductivity.

This thesis deals with systems where such many-body effects are relevant or even dominant. While a simple "brute force" solution of mutually interacting electrons quickly becomes unfeasible, the last decades of research on this topic provide us with powerful methods that nevertheless capture key physics in those materials.

What numerics do we need? — Our aim is to understand materials form "first principles" and on a (semi) quantitative basis. That is, given the unit cell of a crystal,

[2]For a comparison between two-dimensional and three-dimensional systems see, e.g., Ref. [25].

Die approbierte gedruckte Originalversion dieser Dissertation ist an der TU Wien Bibliothek verfügbar.
The approved original version of this doctoral thesis is available in print at TU Wien Bibliothek.
TU Bibliothek Your knowledge hub WIEN

we want to predict its electronic temperature-doping phase diagram. Specifically, we would like to be able to estimate the superconducting transition temperature and use those results to guide the future efforts of our experimental colleagues. This is, no doubt, a difficult task and by no means do we claim to have reached this goal. Nevertheless, the development of numeric tools like density-functional theory plus dynamical mean-field theory (DFT+DMFT) [26–28] provides an excellent framework. Building upon these calculations, we build an effective low-energy model, which only incorporates the degrees of freedom around the Fermi energy. While, in general, still too complicated to be solved analytically, we focus on approximate numerical solutions, including non-local fluctuations. Our primary tool is the dynamical vertex approximation (DΓA), which is based on the many-body Green's function formalism.

Why should we care about such materials in the first place? — Aside from satisfying our curious and intellectual minds, it is not at all difficult to come up with applications for materials with zero resistivity[3]. However, the highest T_c at ambient pressure is still well below 200 K and the constant need for cooling reduces the technological applicability of superconductors. A predictive theory for unconventional superconductors would be of much use in the quest to find a superconducting compound at ambient pressure and room temperature.

What is the main content and contribution of this thesis? — This thesis is organized in three parts. The first section is a pedagogical introduction to DFT, Wannier functions, and the many-body Green's function formalism[4]. Along the way, we showcase the presented concepts at hand by applying them to a representative of cuprates and nickelates, respectively.

The remaining two parts cover the original research of the author. The first of those concerns cuprates with a particular focus on the pseudogap. Starting from the single-band Hubbard model, we discuss the origin of the pseudogap, its real-frequency structure, and how to understand Fermi arcs.

The last part deals with nickelates. We introduce the reader to their electronic structure and what we view to be essential for superconductivity. Furthermore, we discuss the magnetic response of nickelates, how to model a finite-layer nickelate, what is the influence of hydrogen defects on the electronic system, and ways to detect them.

1.2 Outline

In the following, the content of this thesis is outlined in detail.

Chapter 2 starts from the "ground truth" in solid-state theory: the full many-electron Schrödinger equation. Since solving this equation using exact numerical methods scales exponentially with system size, we introduce density-functional theory (DFT)

[3] Superconducting coils as electromagnets are one prominent example of current uses.
[4] One should note that there are other frameworks, like GW + DMFT [29–31], which will not be discussed here.

Die approbierte gedruckte Originalversion dieser Dissertation ist an der TU Wien Bibliothek verfügbar.
The approved original version of this doctoral thesis is available in print at TU Wien Bibliothek.
TU Bibliothek Your knowledge hub WIEN

as our theory of choice for ab-initio calculations. Following this, we demonstrate how to construct effective low-energy Hamiltonians from the DFT bands using maximally localized Wannier functions.

Chapter 3 introduces the Green's function formalism for the many-body electron problem. We start by defining the one-particle propagator, discuss symmetries to reduce computational complexity, and introduce the concept of a self-energy. Following this, we extend the discussion to the two-particle Green's function. Particular focus is given to the vertex function, which contains all Feynman diagrams connecting two incoming and two outgoing electrons. Once the vertex function and its properties are understood, we connect it with the self-energy using the Schwinger-Dyson equation of motion. The end of the section is devoted to the idea and core approximations of DMFT and DΓA.

Chapter 4 applies the previously developed tools to high-temperature cuprate superconductors. Specifically, we discuss the microscopic origin of the pseudogap from a Hubbard model perspective. First, a previously unknown mechanism, based on imaginary spin scattering, contributing to the opening of the pseudogap, is discussed. Subsequently, numerical results of the Hubbard model, where this mechanism is relevant, are presented. Next, we compare calculated Fermi surface spectra, using a simple model based on this mechanism, with different angular-resolved photoemission (ARPES) experiments on cuprates in Section 4.2.1. The end of the chapter, Section 4.3, presents an analysis of the real-frequency structure of the pseudogap for solutions obtained from DΓA. Based on these calculations, we discuss the possibility of violating Luttinger's theorem and elaborate on a previous study concerning an "s-wave" like structure of the pseudogap.

Chapter 5 deals with the electronic structure and origin of superconductivity in nickelate superconductors. Similarities and differences between nickelates and cuprates are discussed and a possibly minimal model for superconductivity is developed in Section 5.1. Subsequently, we extend these ideas to finite-layer nickelates in Section 5.2 and show that an effective single-band-per-NiO_2-layer description is reasonable and yields a transition temperature comparable to the experimentally measured one. Our theoretical description of nickelates yields a d-wave pairing symmetry, where the pairing interaction has a large contribution from spin fluctuations. Recent resonant inelastic X-ray scattering (RIXS) measurements on nickelates [32] opens the possibility of directly comparing the theoretical spin fluctuations, which enter the pairing interaction in our calculations, to those measured. This is the topic of Section 5.3. The final on nickelates, Section 5.5, deals with the influence of intercalated hydrogen on the electronic structure and we identify phonon modes as a "fingerprint" of hydrogen which can experimentally be used to identify its presence.

Die approbierte gedruckte Originalversion dieser Dissertation ist an der TU Wien Bibliothek verfügbar.
The approved original version of this doctoral thesis is available in print at TU Wien Bibliothek.
TU Bibliothek Your knowledge hub WIEN

Chapter 2

From solids to models

The Guide is definitive. Reality is frequently inaccurate.
— D. Adams

2.1 The solid-state theory of everything

Nowadays, many people seek, as one of the great goals of modern physics, to find the "theory of everything". A theory from which everything else follows. While there might still be a long way to go until we can formulate such a thing, the "theory of everything: solid-state edition" has been around for almost a century. After Erwin Schrödinger published his seminal paper [33] in 1926, everything was known to write down the Hamiltonian ($\mathcal{H}$) that describes the behavior of a (non-relativistic) solid constructed from N_{ion} atomic cores and N_{el} electrons:

$$\mathcal{H} = \underbrace{-\sum_{i}^{N_{\text{ion}}} \frac{\hbar^2 \nabla^2_{\mathbf{R}_i}}{2M_l}}_{\mathcal{H}_{\text{kin,ion}}} \underbrace{-\sum_{l}^{N_{\text{el}}} \frac{\hbar^2 \nabla^2_{\mathbf{r}_i}}{2m}}_{\mathcal{H}_{\text{kin,el}}} + \underbrace{\sum_{l,k,l>k}^{N_{\text{ion}}} \frac{Z_l Z_k e^2}{|\mathbf{R}_l - \mathbf{R}_k|}}_{\mathcal{H}_{\text{int,ion}}} + \underbrace{\sum_{i,j,j>i}^{N_{\text{el}}} \frac{e^2}{|\mathbf{r}_i - \mathbf{r}_j|}}_{\mathcal{H}_{\text{int,el}}} \underbrace{-\sum_{i}^{N_{\text{el}}} \sum_{l}^{N_{\text{ion}}} \frac{Z_l e^2}{|\mathbf{r}_i - \mathbf{R}_l|}}_{\mathcal{H}_{\text{int,el-ion}}}, \tag{2.1}$$

where $\mathbf{r}_i$ ($\mathbf{R}_l$) are the positions of the electrons (ions), m (M_l) the respective masses and Z_l the atomic number of the cores from which the crystal is constructed. The Hamiltonian itself is easily understood: the first two terms describe the kinetic energy of the ions (electrons), while the third and fourth describes the mutual Coulomb interaction of all ions (electrons). Finally, the last term in Eq. 2.1 captures the coupling between the ions and the electrons. Now the only thing left to do is solve the Schrödinger equation

$$\mathcal{H}\psi(\{\mathbf{r}_i\}, \{\mathbf{R}_l\}) = E\psi(\{\mathbf{r}_i\}, \{\mathbf{R}_l\}), \tag{2.2}$$

to obtain the corresponding energy E and wave function ψ, from which further information about the system can be obtained. Naturally, one might ask the question: "So why not just solve Eq. 2.1 and be done with it?", to which we would reply: "Be my guest and try". As it turns out, this "solid-state theory of everything" is, for most systems of interest, equally "useless" as it is elegant. The wave function depends on the coordinates of all electrons and ions within the solid we wish to describe, a number typically of the order of Avogadro's number ($\sim 6 \cdot 10^{23}$). Consequently, the general wave function of such systems is neither obtainable nor practicable and storable could we calculate it. Thus, it becomes evident that the difficulty in solid-state theory is not to find the underlying fundamental Hamiltonian but instead to construct an approximation that contains all the physics necessary while still being tractable. Already Paul Dirac had this insight in 1929 when he famously wrote[34]:

Die approbierte gedruckte Originalversion dieser Dissertation ist an der TU Wien Bibliothek verfügbar.
The approved original version of this doctoral thesis is available in print at TU Wien Bibliothek.

"The underlying physical laws necessary for the mathematical theory of a large part of physics and the whole of chemistry are thus completely known, and the difficulty is only that the exact application of these laws leads to equations much too complicated to be soluble. It, therefore, becomes desirable that approximate practical methods of applying quantum mechanics should be developed, which can lead to an explanation of the main features of complex atomic systems without too much computation."

While the meaning of "without too much computation" has certainly changed with the advent of modern computers, the essence of Dirac's statement remains the same. Following this paradigm, we will devote the next sections to introduce frameworks with which Eq. 2.1 can be solved approximately.

2.1.1 Approximate Hamiltonians or approximate methods?

Approximations for Eq. 2.1 can generally be classified as either (i) solving the exact Hamiltonian with approximate methods or (ii) solving an approximate Hamiltonian with (more) exact methods. Density-functional theory (DFT) [35] and somewhat more recently *GW* [29] are the arguably most notable members of the former. Contrary to those, the latter approaches first build a so-called model Hamiltonian that only incorporates a specific subset of degrees of freedom, e.g. the valence shell. Subsequently, this model Hamiltonian is solved within more accurate, but also more expensive, frameworks. Examples of those are quantum Monte Carlo, see e.g. [36], the dynamical mean-field theory (DMFT) [37], or the dynamical vertex approximation (DΓA) [38]. Within this thesis we primarily use a combined approach: first, a band-structure is computed with DFT, which lets us determine the orbitals relevant for low-temperature and/or low-energy physics, i.e. the ones close to the Fermi surface. Subsequently, we use those orbitals to construct an effective low-energy model Hamiltonian, which we can then treat with suitable methods like DMFT or DΓA.

2.1.2 Born-Oppenheimer approximation

In section 2.1 Eq. 2.1 we considered the ions and electrons on equal footing. However, already in 1927 M. Born and R. Oppenheimer [39] recognized that the timescales of these two systems are vastly different due to their different masses. Indeed, a proton is roughly ~ 1800 times heavier than an electron. Solids, however, often contain heavy cores like gold, which are five orders of magnitude heavier than an individual electron. As time scales for relaxation processes scale inversely with mass, electrons typically relax so fast that one can treat them to always be in equilibrium as the atoms of the lattice move. In turn, this means one can, to a (very) good approximation, solve the electronic problem for a frozen set of ionic coordinates. There are phenomena where the coupling of lattice vibrations (phonons) with electrons cannot be ignored, e.g. conventional phonon-mediated superconductivity [40]. Nevertheless, those cases can, most of the time, be treated in perturbation theory by starting from a solution obtained with the Born-Oppenheimer approximation. If not stated otherwise, we will always employ

Die approbierte gedruckte Originalversion dieser Dissertation ist an der TU Wien Bibliothek verfügbar.
The approved original version of this doctoral thesis is available in print at TU Wien Bibliothek.
TU Bibliothek Your knowledge hub WIEN

the Born-Oppenheimer approximation in this thesis and mostly concern ourselves with the electronic system.

2.2 Density-functional theory (DFT)

In this section, we will introduce DFT, which is the starting point of all material calculations presented in this thesis. We refer the reader to Ref. [41–43] for a more detailed outline of the theory.

2.2.1 Hohenberg-Kohn theorems

DFT is arguably one of the most used and most successful theories of condensed matter physics. The underlying principle dates back to P. Hohenberg and W. Kohn [35] who formulated what are now known as the Hohenberg-Kohn theorems. Let us recall that the energy of a quantum system E is given by the expectation value of the Hamiltonian,

$$E[\psi] = \frac{\langle\psi|\mathcal{H}|\psi\rangle}{\langle\psi|\psi\rangle}, \tag{2.3}$$

and is thus a functional of the wave function ψ. We define the ground state of a system to be the state with the lowest energy[1]:

$$E_0 = \min_{\psi} E[\psi]. \tag{2.4}$$

Within the Born-Oppenheimer approximation, the Hamiltonian for the electronic system is given by,

$$\mathcal{H} = \underbrace{-\sum_{l}^{N_{\text{el}}} \frac{\hbar^2\nabla^2_{\mathbf{r}_i}}{2m}}_{\mathcal{H}_{\text{kin,el}}} + \underbrace{\sum_{i,j,j>i}^{N_{\text{el}}} \frac{e^2}{|\mathbf{r}_i - \mathbf{r}_j|}}_{\mathcal{H}_{\text{int,el}}} + \underbrace{\sum_{i}^{N_{\text{el}}} V_{\text{ext}}(\mathbf{r}_i)}_{\mathcal{H}_{\text{ext}}}, \tag{2.5}$$

where V_{ext} describes any external potential, e.g. from ions of the lattice. Hohenberg and Kohn realized that given a non-degenerate ground state charge density,

$$n_0(\mathbf{r}) = N \prod_{i=2}^{N} \int d^3 r_i \psi_0^*(\{\mathbf{r}_i\})\psi_0(\{\mathbf{r}_i\}), \tag{2.6}$$

there exists only one unique external potential V_{ext} for which $n_0(\mathbf{r})$ is realized. Hence, we can also formulate the ground state energy as a functional of the electron density $E[\psi] \to E[n]$. The second Hohenberg-Kohn theorem tells us that the variational principle (Eq. 2.3) still applies for $E[n]$.

Essentially, we have now replaced the dependence of the ground state energy on the wave function $\psi(\{\mathbf{r}_i\})$, depending on $3N$ variables, with the density $n(\mathbf{r})$ only depending on 3 variables. However, as an old saying puts it: "there is no free lunch". While

[1] This is well defined since the Hamiltonian is bounded from below if the ground state is non-degenerate. Let us note that the Hohenberg-Kohn theorems can (non-trivially) be extended to systems with degenerate ground states [44]. For a review see Ref. [45].

Die approbierte gedruckte Originalversion dieser Dissertation ist an der TU Wien Bibliothek verfügbar.
The approved original version of this doctoral thesis is available in print at TU Wien Bibliothek.
TU Bibliothek Your knowledge hub WIEN

the complexity is reduced tremendously on paper, in practice the exact energy functional $E[n]$ is not known. In principle one could compute it from the wave function ψ, however obtaining ψ is precisely what we are trying to avoid. Instead, several different approximations for the exchange-correlation part of the energy functional[2] have been developed. Instead, several different approximations for (the exchange-correlation part of) this energy functional have been developed.

Let us now discuss the energy functional in more detail. To do so it is preferable to rewrite the Hamiltonian of Eq. 2.5 in second quantization,

$$\mathcal{H} = \int d^3r \;\; \hat{\psi}^\dagger(\mathbf{r})\Big[\frac{-\hbar^2\nabla^2}{2m} + V_{\text{ion}}(\mathbf{r})\Big]\hat{\psi}(\mathbf{r}) + \frac{1}{2}\int d^3r \int d^3r' \;\; \hat{\psi}^\dagger(\mathbf{r})\hat{\psi}^\dagger(\mathbf{r}') \underbrace{\frac{e^2}{|\mathbf{r}-\mathbf{r}'|}}_{V_{\text{ee}}(\mathbf{r}-\mathbf{r}')} \hat{\psi}(\mathbf{r}')\hat{\psi}(\mathbf{r}), \tag{2.7}$$

where $\hat{\psi}^\dagger(\mathbf{r})$ ($\hat{\psi}(\mathbf{r})$) are field operators that create (annihilate) an electron at position $\mathbf{r}$. $V_{\text{ion}}(\mathbf{r})$ is the potential created by the lattice ions and $V_{\text{ee}}(\mathbf{r}-\mathbf{r}')$ the Coulomb interaction between the electrons. Albeit it is (currently) not known how to express all terms of Eq. 2.7 in terms of the density only, the ionic potential

$$E_{\text{ion}}[n] = \int d^3r V_{\text{ion}} n(\mathbf{r}) \tag{2.8}$$

and the density-density part of the Coulomb interaction, usually called Hartree term,

$$E_{\text{Hartree}}[n] = \frac{1}{2}\int d^3r \int d^3r' V_{\text{ee}}(\mathbf{r}-\mathbf{r}')n(\mathbf{r}')n(\mathbf{r}) \tag{2.9}$$

can be expressed in the electronic density easily and exactly. For all other contributions no exact functional exists and approximations become necessary. In the following, we will discuss the most frequently used framework to include the major part of the kinetic energy: Kohn-Sham DFT [46].

2.2.2 Kohn-Sham DFT

How to express the kinetic energy as a functional of the density for a general electronic system is, at least so far, not known. In the case of non-interacting electrons, however, the wave function is given by a single Slater determinant,

$$\psi(\{\mathbf{r}_i\}) = \begin{vmatrix} \phi_1(\mathbf{r}_1) & \phi_2(\mathbf{r}_1) & \dots & \phi_N(\mathbf{r}_1) \\ \phi_1(\mathbf{r}_2) & \phi_2(\mathbf{r}_2) & \dots & \phi_N(\mathbf{r}_2) \\ \vdots & \vdots & \ddots & \vdots \\ \phi_1(\mathbf{r}_N) & \phi_2(\mathbf{r}_N) & \dots & \phi_N(\mathbf{r}_N) \end{vmatrix}, \tag{2.10}$$

where ϕ_i are single-particle wave functions. For this simple case, the kinetic energy of the many-electron system decomposes into a sum of single-particle contribution,

$$T_{\text{KS}}[\psi] = \sum_i^N \int d^3r \;\; \phi_i^*(\mathbf{r})\left(\frac{-\hbar^2\nabla^2}{2m}\right)\phi_i(\mathbf{r}), \tag{2.11}$$

[2] See next section.

Die approbierte gedruckte Originalversion dieser Dissertation ist an der TU Wien Bibliothek verfügbar.
The approved original version of this doctoral thesis is available in print at TU Wien Bibliothek.
TU Bibliothek Your knowledge hub WIEN

which can be related to the density by applying the Hohenberg-Kohn theorems to the non-interacting Hamiltonian [41]. Furthermore, the total density is simply the sum of the probability amplitudes $n(\mathbf{r}) = \sum_i^N |\psi_i(\mathbf{r})|^2$. Hence, we can write the energy functional for the Kohn-Sham (KS) system as

$$E_{\mathrm{KS}}[n] = T_{\mathrm{KS}}[n] + E_{\mathrm{Hartree}}[n] + E_{\mathrm{ion}}[n] + E_{\mathrm{XC}}[n], \tag{2.12}$$

where we put all remaining parts into the so-called exchange-correlation functional $E_{\mathrm{XC}}[n] = E[n] - E_{\mathrm{ion}}[n] - E_{\mathrm{Hartree}}[n] - T_{\mathrm{KS}}[n]$. Crucially, if we were to know the exact expression of E_{XC} then the KS energy functional would coincide with the original interacting one. Thus minimizing the Kohn-Sham functional leads to the same ground state energy and density[3]. This can be understood as follows: there exists a non-interacting (KS) system in an (auxiliary) external field, which has the same ground state electronic density as the interacting one. In practice, however, the exact exchange-correlation functional is not known and has to be approximated. Consequently, also the solution to the KS system becomes an approximation of the true solution.

2.2.3 Local-density approximation

In theory, there is no difference between theory and practice.
But, in practice, there is.
— JAN L. A. VAN DE SNEPSCHEUT

As already mentioned above the exact form of E_{XC} is not known. Nevertheless, various flavors of approximations have emerged over the years. We will only briefly discuss one of the most simple, yet successful ones. Let us take a closer look at E_{XC}

$$E_{\mathrm{XC}}[n] = \underbrace{T[n] - T_{\mathrm{KS}}[n]}_{\delta T[n]} + \underbrace{E_{\mathrm{ee}}[n] - E_{\mathrm{Hartree}}[n]}_{\delta E_{\mathrm{ee}}[n]}, \tag{2.13}$$

where the first part is a correction to the KS kinetic energy, which can be assumed to be negligible, provided the electron density varies sufficiently slowly. What remains is thus a correction to the electron-electron interaction. One of the first successful approximations for this term is the so-called *local-density approximation* (LDA). Here, E_{XC} is assumed to depend only on the local electron density

$$E_{\mathrm{XC}}^{\mathrm{LDA}}[n] = \int d^3r\, n(\mathbf{r}) \epsilon_{\mathrm{XC}}(n(\mathbf{r})), \tag{2.14}$$

where $\epsilon_{\mathrm{XC}}(n(\mathbf{r}))$ is the exchange energy per particle obtained from the homogeneous electron gas, which is defined by $V_{\mathrm{ion}}(\mathbf{r}) = \text{constant}$, with density $n(\mathbf{r})$. Crucially, $E_{\mathrm{XC}}^{\mathrm{LDA}}[n]$ is independent of the material considered and can thus be pre-computed, e.g. by using quantum Monte-Carlo simulations [48].

This local approximation is, of course, rather crude and a natural extension would be to also include information about the gradient in the energy density, i.e. $\epsilon_{\mathrm{XC}}(n(\mathbf{r}), \nabla n(\mathbf{r}))$.

[3] This is, however, *not* true for the wave function and all dynamic quantities such as the band structure or the band gap[47].

Die approbierte gedruckte Originalversion dieser Dissertation ist an der TU Wien Bibliothek verfügbar.
The approved original version of this doctoral thesis is available in print at TU Wien Bibliothek.
TU Bibliothek Your knowledge hub WIEN

Such approaches are commonly called *generalized gradient approximation* (GGA), or *meta-GGA* if higher order derivatives are also considered. DFT results discussed in later chapters have mostly been obtained using the GGA-PBE functional [49], which is one of the popular GGA functionals nowadays.

Box 1: Crystal structure of $CaCuO_2$ and $LaNiO_2$

We will guide the reader through the method sections with the aid of two showcase materials. Specifically, we use $CaCuO_2$ as a simple candidate for cuprates and $LaNiO_2$ as a representative for nickelates. Using those two compounds, we will illustrate the methods of each section and develop an understanding of the materials along the way. These boxes here merely serve as a guide for the reader. More comprehensive studies and comparisons between those two compounds have already been carried out, see for example [21, 50, 51].

Before we discuss the DFT-calculated band structure in the next Box 2, let us first review the crystal structure. Both $CaCuO_2$ and $LaNiO_2$ crystallize in a tetragonal ($P4/mmm$) structure under ambient conditions [52]. In the following, in-plane always refers to the square-planar CuO_2 (NiO_2) sheets which span the $a-b$ lattice plane as seen in Fig. 2.1. These quasi-2D planes are one of the hallmarks of both cuprates and nickelate superconductors, as superconductivity is confined within them [53]. Lattice parameters were taken from literature, with in-plane lattice parameter $a = b = 3.86$ (3.88) and out-of-plane $c = 3.2$ (3.35) for $CaCuO_2$ [51] ($LaNiO_2$ [50]).

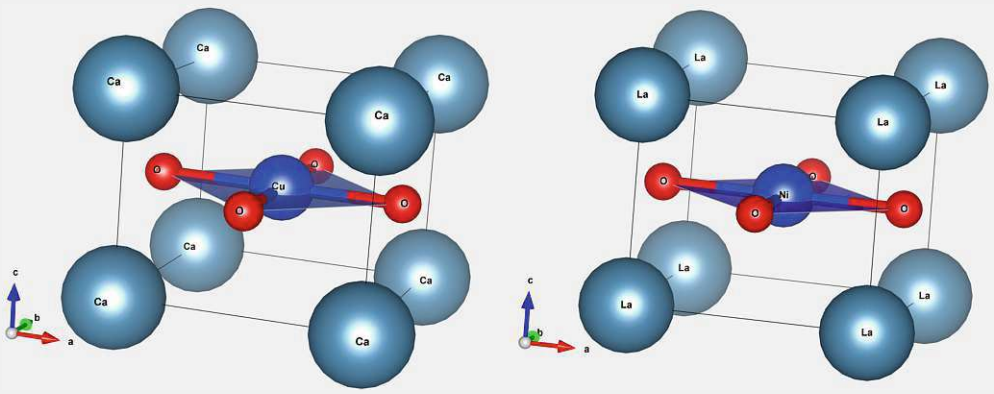

Figure 2.1: Crystal structure of $CaCuO_2$ (left) and $LaNiO_2$ (right). The same color was chosen for Cu/Ni and Ca/La to emphasize their similarity.

Die approbierte gedruckte Originalversion dieser Dissertation ist an der TU Wien Bibliothek verfügbar.
The approved original version of this doctoral thesis is available in print at TU Wien Bibliothek.
TU Bibliothek Your knowledge hub WIEN

Box 2: DFT band structure of $CaCuO_2$ and $LaNiO_2$

Despite the identical crystal structure, as displayed in the previous Box 1, and the same nominal valence, i.e. Cu(Ni)-$3d^9$, differences can be observed for the corresponding band structures as seen in Fig. 2.2. While $CaCuO_2$ displays a single orbital crossing the Fermi surface, there are three in $LaNiO_2$. We will discuss these differences and their implications for superconductivity more deeply in Section 5.1. The band structure was obtained using the WIEN2K code [54, 55] to solve the Kohn-Sham DFT equations. We chose GGA-PBE as exchange-correlation functional [49] and plot the Kohn-Sham eigenenergies along a high-symmetry path in the Brillouin zone[a]. The coordinates of the momenta chosen for the k-path are $\Gamma = (0,0,0)$, $X = (\pi,0,0)$, $M = (\pi,\pi,0)$, $Z = (0,0,\pi)$, $R = (\pi,0,\pi)$ and $A = (\pi,\pi,\pi)$. Let us note that DFT predicts both materials to be metals due to their half-filled shells. However, $CaCuO_2$ is in fact an insulator [57, 58]. Experimental results on $LaNiO_2$ are not yet conclusive. Samples on $LaNiO_2$ showed superconductivity at $\sim 1\,K$ [18], though measurements of the closely related compound $NdNiO_2$ point towards a weakly insulating regime [59], which becomes metallic once the system is doped, e.g. by replacing trivalent La with bivalent Sr as in $La_{1-x}Sr_xNiO_2$ or $Nd_{1-x}Sr_xNiO_2$.

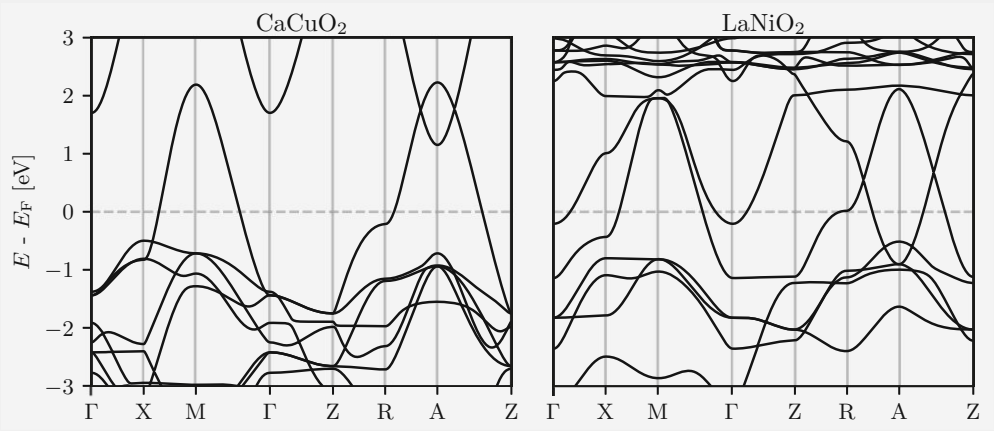

Figure 2.2: DFT-PBE band structure along a high-symmetry path of $CaCuO_2$ (left) and $LaNiO_2$ (right).

[a] One should note that Kohn-Sham orbitals are *per se* only auxiliary and the interpretation of Kohn-Sham eigenenergies as excitation spectra is "difficult" to say the least [56]. That being said, empirically Kohn-Sham band structures often yield a reasonable or even good approximation.

Die approbierte gedruckte Originalversion dieser Dissertation ist an der TU Wien Bibliothek verfügbar.
The approved original version of this doctoral thesis is available in print at TU Wien Bibliothek.

2.3 Model Hamiltonians

All models are wrong, some are useful.
— G. Box

The previous chapter covered the question of how to obtain an approximate solution to Eq. 2.1 from first principles. However, for materials where the orbitals are more localized, like in d-shell or f-shell compounds, corrections to DFT become large and can no longer be ignored[4]. One example where standard DFT breaks down is La_2CuO_4: it is predicted to be a metal by DFT [63] but displays insulating behavior in experiment [5]. Standard DFT-PBE is, quite generally, not suited to describe the electronic properties of Mott- or charge-transfer insulators, where one (or more) of the bands open a Mott gap due to a strong on-site Coulomb repulsion [24]. Here Mott insulator implies that the gap is between bands from the same shell (e.g. $3d$ in $LaNiO_2H$ [64]), whereas in charge-transfer insulators it is between different shells (e.g. Cu-$3d$ and O-$2p$ in cuprates [65]). Let us note that one can include a (static) Coulomb interaction within DFT (called DFT+U). This DFT+U approach, however, always splits the bands for which the interaction is considered [26].

A method that can describe both the metallic and the insulating regime is the dynamical mean-field theory [37], whose technical details are discussed in more detail in section 3.7. As a downside, DMFT comes with a significantly higher computational cost and therefore usually cannot treat the full Hamiltonian (Eq. 2.7), hence the construction of an effective low-energy one is required. Furthermore, in DMFT interactions are usually assumed to be local[5], and thus all correlated orbitals[6] in the effective Hamiltonian should be as localized as possible.

To obtain an effective Hamiltonian, a DFT solution is typically used as starting point. In the following, we will briefly outline how this is done in practice. Again we refer the reader to Ref. [26, 67] for a more in-depth discussion.

However, before one can even try to build an effective model, one needs to know which bands, or degrees of freedom in general, need to be included. Below we plot again the DFT-PBE band structure for $CaCuO_2$ and $LaNiO_2$, but also indicate the corresponding band-character in color[7] and next to it the corresponding density of states (DOS). Based on this we discuss possible sets of bands that can be used for an effective Hamiltonian.

[4] As a side-note: this is not the only case where standard LDA/GGA DFT is insufficient. For example, more advanced functionals perform better when calculating band gaps of semiconductors, see e.g. Ref. [60–62].
[5] All contributions of non-local density-density interactions are reduced to Hartree-Fock in DMFT [66].
[6] I.e. orbitals where we take the (local) Coulomb interaction into account.
[7] Plotting tools were inspired by w2kplot [68].

Die approbierte gedruckte Originalversion dieser Dissertation ist an der TU Wien Bibliothek verfügbar.
The approved original version of this doctoral thesis is available in print at TU Wien Bibliothek.
TU Bibliothek Your knowledge hub WIEN

Box 3: $CaCuO_2$ band character

Below in Fig. 2.3 we plot the orbital character of the DFT-PBE band structure in $CaCuO_2$.

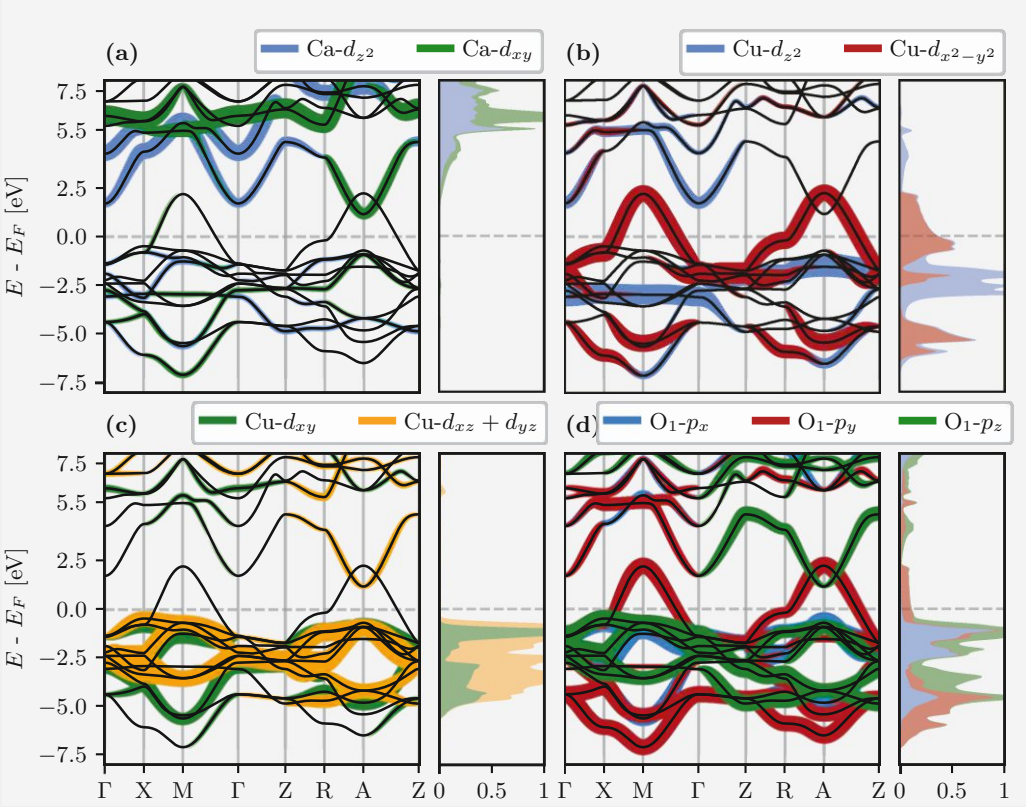

Figure 2.3: Band character plot of $CaCuO_2$. (a) Ca, (b) Cu-e_g, (c) Cu-t_{2g}, (d) O_1-p. The small panel always shows the cumulative ("stacked") density of states (DOS). Note that we only plot the DOS for *one* of the two oxygen atoms.

Let us note several key observations: (I) the Ca-derived states are located above E_F and show essentially no weight at energies below E_F. (II) The orbital that crosses E_F is mostly comprised of Cu-$d_{x^2-y^2}$ and O_1-p_y (lobes pointing towards Cu) character[a]. (III) Cu-t_{2g} and Cu-e_g hybridize with O-p, but do not share a significant contribution to the band that crosses E_F. Let us present three of the possible effective models in increasing complexity[b]:

(i) Cu-$d_{x^2-y^2}$: only incorporate the orbital with the dominant contribution to the band that crosses E_F. (1 orbital)

(ii) Cu-$d_{x^2-y^2}$ + O_1-p_y + O_2-p_x: include all orbitals that have a significant contribution to the band that crosses E_F. (3 orbitals)

(iii) Cu-d + O-p: include the full Cu d-shell and the Oxygen p-shell. (11 orbitals)

The most simple approach would be to consider only the dominant orbital contribution to the band crossing E_F (i). Whether such a one-band model is truly sufficient

Die approbierte gedruckte Originalversion dieser Dissertation ist an der TU Wien Bibliothek verfügbar.
The approved original version of this doctoral thesis is available in print at TU Wien Bibliothek.
TU Bibliothek Your knowledge hub WIEN

to capture the key physics of cuprates, or whether the oxygen degrees of freedom have to be included explicitly, as in (ii), has been a long debate in the community. Recent theoretical [65] and experimental [70] work points more towards the latter. While, ultimately, including even more orbitals in the effective Hamiltonian (iii) would be desirable, many existing methods that also include electronic interactions in a non-perturbative way and are able to capture d-wave superconductivity are, however, limited to a few or even one orbital, see e.g. [12, 71, 72].

[a] The oxygen atoms are equivalent apart from a rotation of $\pi/2$, hence O_1-p_y is equivalent to O_2-p_x.
[b] There are other models, e.g. including the Cu 4s [69], which we do not discuss here.

Die approbierte gedruckte Originalversion dieser Dissertation ist an der TU Wien Bibliothek verfügbar.
The approved original version of this doctoral thesis is available in print at TU Wien Bibliothek.

Box 4: $LaNiO_2$ band character

In $LaNiO_2$, contrary to $CaCuO_2$, the band around the Fermi surface is almost entirely composed of Ni-$d_{x^2-y^2}$ character, thus precluding the need to take oxygen degrees of freedom into account explicitly. However, again there is no "free lunch" and two La-Ni hybrid bands crossing E_F appear. One band, comprised mainly of La-d_{z^2} and Ni-d_{z^2} character, forms a pocket around the Γ-momentum, while the second is a La-d_{xy} and Ni-d_{xz+yz} hybrid, which forms the A-pocket. Whether or not those pockets are relevant for superconductivity has been extensively discussed in the literature and our current view will be discussed in Section 5.1.

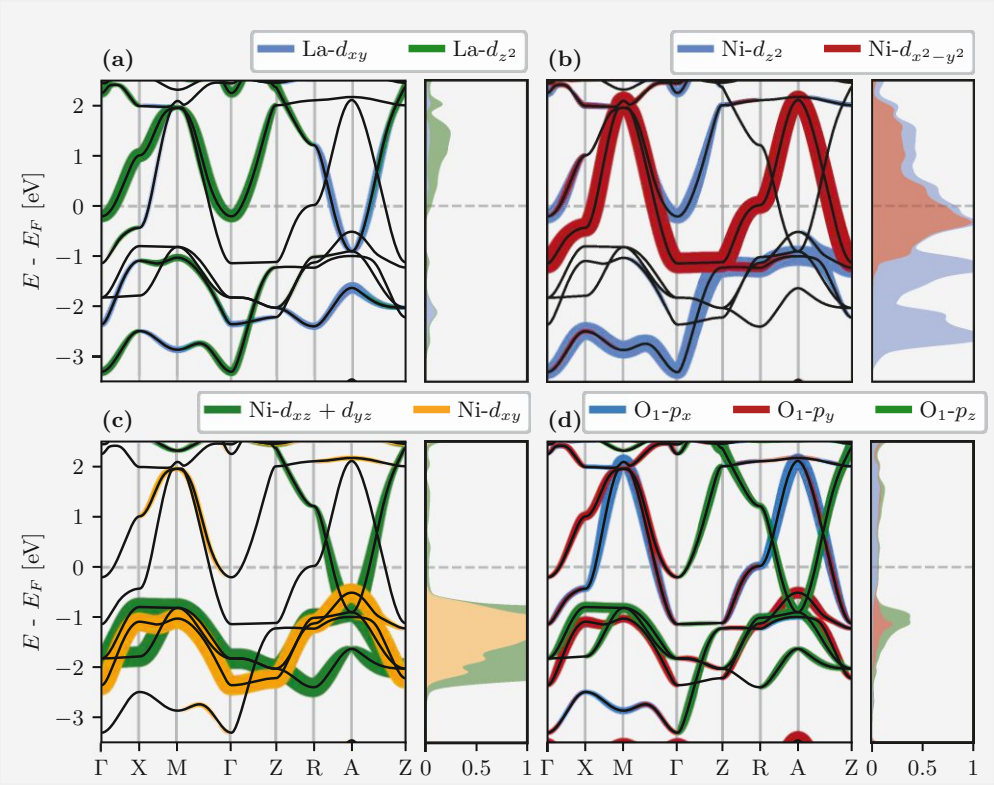

Figure 2.4: Band character plot of $LaNiO_2$. (a) La, (b) Ni-e_g, (c) Ni-t_{2g}, (d) O_1-p. The small panel always shows the cumulative ("stacked") density of states (DOS). Note that we only plot the DOS for *one* of the two oxygen atoms.

2.3.1 Wannier functions

In Box 3 (Box 4) we display the band-character of $CaCuO_2$ ($LaNiO_2$), which can be used to determine the relevant orbitals for the effective (tight-binding) Hamiltonian. What remains to be discussed is how to construct corresponding effective Hamiltonians from them. Specifically, we would like to construct localized orbitals to best justify the approximation of a local Coulomb interaction, which we will use later in DMFT.

The eigenstates of Schrodinger's equation in a periodic potential, i.e. a lattice, are Bloch

Die approbierte gedruckte Originalversion dieser Dissertation ist an der TU Wien Bibliothek verfügbar.
The approved original version of this doctoral thesis is available in print at TU Wien Bibliothek.
TU Bibliothek Your knowledge hub WIEN

functions [73]

$$\psi_{n\mathbf{k}}(\mathbf{r}) = e^{i\mathbf{k}\mathbf{r}} u_n(\mathbf{r}), \tag{2.15}$$

where $u_n(\mathbf{r}+\mathbf{R}) = u_n(\mathbf{r})$ has the periodicity of the lattice and n is the band index. Here $\mathbf{R} = c_1 \cdot \mathbf{a}_1 + c_2 \cdot \mathbf{a}_2 + c_3 \cdot \mathbf{a}_3$, with $c_i \in \mathbf{N}$, is a vector of the Bravais lattice described by the three primitive translations $\mathbf{a}_i$. Due to their periodicity, Bloch functions are naturally extended in real space. To obtain a local set of functions one performs a Fourier transform

$$w_{n\mathbf{R}}(\mathbf{r}) = \frac{1}{\sqrt{N}} \sum_{\mathbf{k}}^{\mathrm{BZ}} e^{-i\mathbf{k}\mathbf{R}} \psi_{n\mathbf{k}}(\mathbf{r}), \tag{2.16}$$

where $w_{n\mathbf{R}}(\mathbf{r})$ is a Wannier function [74], which is centered around the lattice site R. Wannier functions contain the same information as the Bloch wave functions and thus form an equivalent basis, even though they are not eigenfunctions of the Hamiltonian[8]. Eq. 2.16 is, however, not the end of the story, as there exists a gauge freedom in the Bloch functions. Indeed any set of Bloch functions obtained from the transformation

$$\psi_{n_1\mathbf{k}}(\mathbf{r}) = \sum_{n_2} U^{\mathbf{k}}_{n_1 n_2} \psi_{n_2\mathbf{k}}(\mathbf{r}), \tag{2.17}$$

where $U^{\mathbf{k}}_{n_1 n_2}$ is a unitary matrix that mixes the orbitals (n_1 and n_2) at each $\mathbf{k}$ point, is a valid set of eigenfunctions of the Hamiltonian [75]. While physical observables are gauge invariant, Wannier functions and, more importantly, their spread in real space are not. Since there is no preferred gauge for the Bloch functions, Wannier functions are highly non-unique and so are the parameters of Hamiltonians constructed from them. Needless to say, this poses a serious issue concerning the reproducibility and robustness of results. One of the choices that uniquely define the gauge and thus cure this problem was put forth by N. Marzari and D. Vanderbilt in 1997 [76]. The idea is to generate "maximally localized Wannier functions" and is a widely used approach today.

Maximally localized Wannier functions — The idea of *maximally localized Wannier functions* is to choose a gauge $U^{\mathbf{k}}_{n_1 n_2}$ of the Bloch functions, such that the sum of quadratic spreads of the Wannier functions is minimized [67, 75]. To measure the spread, we define the localization functional Ω,

$$\Omega = \sum_n \left[\langle \mathbf{r}^2 \rangle_n - \langle \mathbf{r} \rangle_n^2\right] = \sum_n \left[\langle \mathbf{0}n|\mathbf{r}^2|\mathbf{0}n\rangle_n - \langle \mathbf{0}n|\mathbf{r}|\mathbf{0}n\rangle_n^2\right], \tag{2.18}$$

which is to be minimized and where $|\mathbf{R}n\rangle$ is a Wannier ket with $w_{n\mathbf{R}}(\mathbf{r}) = \langle \mathbf{r}|\mathbf{R}n\rangle$. Thus, Eq. 2.16 becomes

[8] Except for a few special cases like isolated atoms.

Die approbierte gedruckte Originalversion dieser Dissertation ist an der TU Wien Bibliothek verfügbar.
The approved original version of this doctoral thesis is available in print at TU Wien Bibliothek.

$$w_{n_1\mathbf{R}}(\mathbf{r}) = \frac{1}{\sqrt{N}} \sum_{\mathbf{k}}^{\mathrm{BZ}} e^{-i\mathbf{k}\mathbf{R}} \sum_{n_2} \underbrace{\widetilde{U}^{\mathbf{k}}_{n_1 n_2} \psi_{n_2\mathbf{k}}(\mathbf{r})}_{\widetilde{\psi}_{n_2\mathbf{k}}(\mathbf{r})}, \tag{2.19}$$

where $\widetilde{U}^{\mathbf{k}}_{n_1 n_2}$ is chosen such that the corresponding Wannier functions are the minimizer of Eq. 2.18.

Hamiltonian in the basis of Wannier functions — Let us again take a close look at the Hamiltonian of the electronic system and rewrite Eq. 2.7 here for brevity:

$$\mathcal{H} = \int d^3r \;\; \hat{\psi}^\dagger(\mathbf{r}) \Big[\frac{-\hbar^2\nabla^2}{2m} + V_{\mathrm{ion}}(\mathbf{r}) \Big] \hat{\psi}(\mathbf{r}) + \frac{1}{2} \int d^3r \int d^3r' \;\; \hat{\psi}^\dagger(\mathbf{r}) \hat{\psi}^\dagger(\mathbf{r}') \underbrace{\frac{e^2}{|\mathbf{r}-\mathbf{r}'|}}_{V_{\mathrm{ee}}(\mathbf{r}-\mathbf{r}')} \hat{\psi}(\mathbf{r}') \hat{\psi}(\mathbf{r}). \tag{2.20}$$

One can also expand the field operators $\hat{\psi}^{(\dagger)}(\mathbf{r})$ in any given basis α

$$\begin{aligned} \hat{\psi}^\dagger(\mathbf{r}) &= \sum\!\!\!\!\!\!\int d\alpha \;\; \phi^*_\alpha(\mathbf{r}) \;\; \hat{c}^\dagger_\alpha \\ \hat{\psi}(\mathbf{r}) &= \sum\!\!\!\!\!\!\int d\alpha \;\; \phi_\alpha(\mathbf{r}) \;\; \hat{c}_\alpha, \end{aligned} \tag{2.21}$$

where $\{\phi_\alpha(\mathbf{r})\}$ is a set of basis functions and $\hat{c}^\dagger_\alpha$ ($\hat{c}_\alpha$) create (annihilate) an electron in the state α. $\sum\!\!\!\!\!\!\int d\alpha$ denotes the summation (integration) over all basis functions, depending on whether the basis is discrete (continuous). Let us now pick Wannier functions as the corresponding basis

$$\begin{aligned} \hat{\psi}^\dagger(\mathbf{r}) &= \frac{1}{\sqrt{N}} \sum_{\mathbf{R}} \sum_{n\sigma} \;\; w^*_{n\mathbf{R}\sigma}(\mathbf{r}) \;\; \hat{c}^\dagger_{n\mathbf{R}\sigma} \\ \hat{\psi}(\mathbf{r}) &= \frac{1}{\sqrt{N}} \sum_{\mathbf{R}} \sum_{n\sigma} \;\; w_{n\mathbf{R}\sigma}(\mathbf{r}) \;\; \hat{c}_{n\mathbf{R}\sigma}, \end{aligned} \tag{2.22}$$

where $\hat{c}^\dagger_{n\mathbf{R}\sigma}$ ($\hat{c}_{n\mathbf{R}\sigma}$) are creation (annihilation) operators for Wannier orbitals with orbital index n at lattice site $\mathbf{R}$ and spin σ. To avoid writing $\{n\mathbf{R}\sigma\}$ we will use a compound index $\mathfrak{1} \equiv \{n_1\mathbf{R}_1\sigma_1\}$. Using Eq. 2.22 we can represent the Hamiltonian of Eq. 2.20 in the basis of Wannier functions as

$$\mathcal{H} = \underbrace{-\sum_{\mathfrak{12}} t_{\mathfrak{12}} \hat{c}^\dagger_{\mathfrak{1}} \hat{c}_{\mathfrak{2}}}_{\mathcal{H}_{\mathrm{kin}} \equiv \mathcal{H}_0} + \underbrace{\frac{1}{2} \sum_{\mathfrak{1234}} U_{\mathfrak{1234}} \hat{c}^\dagger_{\mathfrak{1}} \hat{c}^\dagger_{\mathfrak{3}} \hat{c}_{\mathfrak{4}} \hat{c}_{\mathfrak{2}}}_{\mathcal{H}_{\mathrm{int}} \equiv \mathcal{H}_{\mathrm{I}}}, \tag{2.23}$$

where $t_{\mathfrak{12}}$ is coined the "hopping matrix", as it describes the transition (or transfer) of an electron from site $\mathbf{R}_2$ to $\mathbf{R}_1$ (possibly changing spin and orbital in the process), while

Die approbierte gedruckte Originalversion dieser Dissertation ist an der TU Wien Bibliothek verfügbar.
The approved original version of this doctoral thesis is available in print at TU Wien Bibliothek.
TU Bibliothek Your knowledge hub WIEN

U_{1234} is called the "interaction matrix", as it directly stems from the mutual Coulomb interaction between the electrons. These matrices can directly be evaluated from the Wannier functions

$$\begin{aligned} t_{12} &= \int d^3r \;\; w_1^*(\mathbf{r})\Big[\frac{-\hbar^2\nabla^2}{2m} + V_{\text{ion}}(\mathbf{r})\Big] w_2(\mathbf{r}) \\ U_{1234} &= \int d^3r \int d^3r' \;\; w_1^*(\mathbf{r}) w_3^*(\mathbf{r}') \frac{e^2}{|r-r'|} w_4(\mathbf{r}') w_2(\mathbf{r}). \end{aligned} \tag{2.24}$$

While we have already restricted ourselves only to a selected subspace of orbitals (e.g. the $3d$ shell), Eq. 2.23 is still far too complicated to be solved exactly in the most general case. In the following, we will discuss how its complexity can be further reduced, partly by using further assumptions and partly by using symmetries of the Hamiltonian, which are reflected in the number of independent elements of t_{12} and U_{1234}. One should note that Eq. 2.24 overestimates the Coulomb interaction because screening effects from electrons outside the subspace are not taken into account. We will discuss this in more detail in Section 2.3.3.

2.3.2 Wannier Hamiltonian

We refer to the Wannier Hamiltonian as the one-particle (kinetic) part of Eq. 2.23 ($\mathcal{H}_0$),

$$\mathcal{H}_0 = -\sum_{12} t_{12} \hat{c}_1^\dagger \hat{c}_2. \tag{2.25}$$

While this part is rarely the bottleneck for calculations, let us nevertheless examine t_{12} more closely. Specifically, the magnitude of t_{12} depends on the (integrated) overlap of two Wannier functions located at lattice sites $\mathbf{R}_1$ and $\mathbf{R}_2$. Since (maximally localized) Wannier functions are by construction localized around a given lattice site, the hopping elements will decay fast with distance. While only nearest-neighbor hopping is usually not enough to faithfully reproduce the band dispersion, taking just a few more hopping terms are typically sufficient.

Let us illustrate this with our showcase materials, by Wannier projecting only on the Cu(Ni) $3d_{x^2-y^2}$ orbitals.

Box 5: Single orbital Wannier projection

Using the output from the WIEN2K [55] calculation (Box 3 and Box 4) we obtain a maximally localized Wannier function for the single band that crosses the Fermi surface using the `wien2wannier` interface [77]. The corresponding Wannier band is displayed in Fig. 2.5. We also display the result using only the nearest neighbor hopping (t), including also next-nearest hopping (t') and including next-next-nearest hopping (t'') in the Cu(Ni)O_2 planes. We fix the filling to that of the full Wannier projection, which is 1 for $CaCuO_2$ and 0.9 for $LaNiO_2$. The reduced filling in $LaNiO_2$ is a direct consequence of the self-doping due to the Γ and A

Die approbierte gedruckte Originalversion dieser Dissertation ist an der TU Wien Bibliothek verfügbar.
The approved original version of this doctoral thesis is available in print at TU Wien Bibliothek.
TU Bibliothek Your knowledge hub WIEN

pockets.
As we can see already the first three terms in the hopping matrix ($t - t' - t''$) yield a very good approximation to the full Wannier fit, while the same cannot be said about taking only t or $t - t'$.

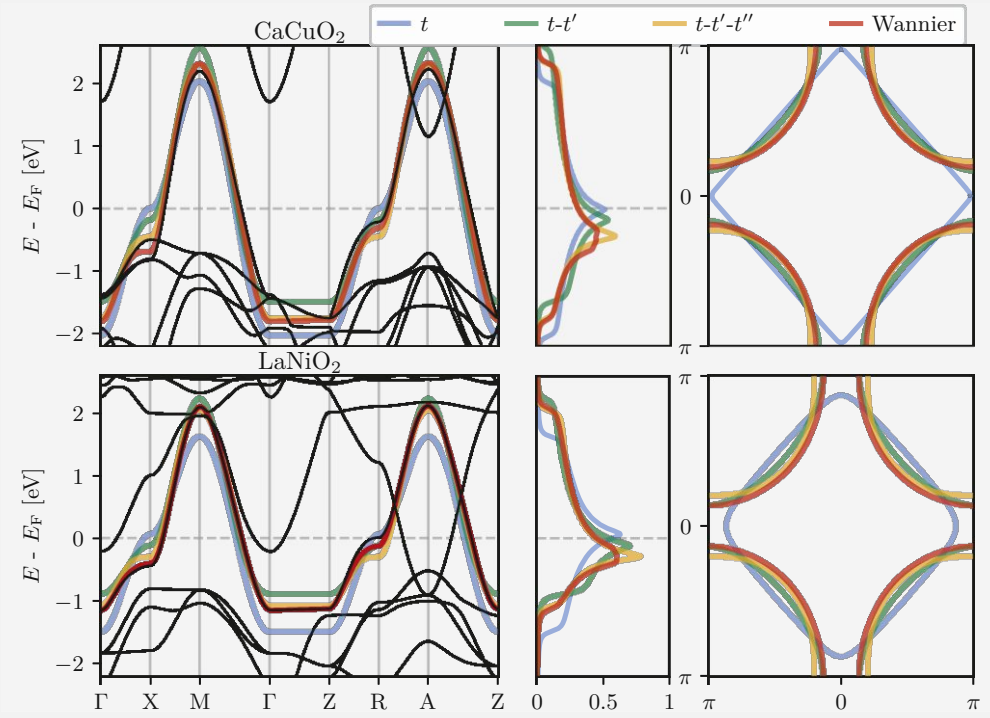

Figure 2.5: We display a single orbital Wannier projection for $CaCuO_2$ (top) and $LaNiO_2$ (bottom), as well as truncated versions of it. Blue: taking only the nearest neighbor hopping (t) in the CuO_2 planes. Green: also include the next-nearest hopping (t'). Orange: also include the next-next-nearest hopping (t''). Red: include the full real space Wannier Hamiltonian. Left: DFT-PBE band structure (black) and the corresponding one-band approximations. Middle: corresponding DOS per spin. Right: Fermi surface at $k_z = 0$.

Material	spread [Å^2]	t [eV]	t' [eV]	t'' [eV]	t_z [eV]	t'/t	t''/t [t]
$CaCuO_2$	2.365	-0.508	0.091	-0.063	-0.032	-0.18	0.13
$LaNiO_2$	2.599	-0.389	0.098	-0.047	-0.036	-0.25	0.12

Table 2.1: Hopping parameters for the single-band $d_{x^2-y^2}$ projection of $CaCuO_2$ and $LaNiO_2$.

2.3.3 Kanamori Hamiltonian

While the hopping matrix t_{12} can be computed directly from the Wannier functions using Eq. 2.24, the same does not apply to U_{1234}. Computing it directly from the Wannier functions as in Eq. 2.24 overestimates the Coulomb interaction since screening from electrons not in the projected subspace is ignored. One way to (somewhat) remedy the

Die approbierte gedruckte Originalversion dieser Dissertation ist an der TU Wien Bibliothek verfügbar.
The approved original version of this doctoral thesis is available in print at TU Wien Bibliothek.

problem is the constrained random phase approximation (cRPA) [78–80]. While interaction values from cRPA are more realistic, the screening process introduces a frequency dependence, which many methods, employed for the effective low-energy Hamiltonian, cannot treat and is thus often ignored. As compensation for this static approximation, an enhanced interaction value $U > U_{\mathrm{cRPA}}(\omega = 0)$ is employed in this thesis. How to properly determine the degree of enhancement is still ongoing research and we refer the reader to Ref. [81] for an in-depth discussion.

While cRPA can be used to compute the elements of the interaction matrix U_{1234}, we have not yet discussed how to reduce the complexity of U_{1234}. In the previous section, we argued that, as a consequence of Wannier functions being localized in space, hopping elements $t_{\mathbf{R}1\mathbf{R}2}$, which depend on the overlap between two orbitals, should decay quickly with $|\mathbf{R}1 - \mathbf{R}2|$. Indeed, in Box 5 we observed that using only the first three terms of t_{12} is sufficient. Elements of U_{1234} decay even faster as they involve an integral over four orbitals instead of just two.

Let us now examine the following assumptions:

(i) the Coulomb interaction of electrons located on different sites is small compared to the on-site Coulomb interaction, i.e. $U_{\mathbf{R}_1\mathbf{R}_1\mathbf{R}_1\mathbf{R}_1} >> U_{\mathbf{R}_2\mathbf{R}_1\mathbf{R}_1\mathbf{R}_2}$.

(ii) the Wannier functions of the sub-manifold preserve orbital symmetry

(iii) the Wannier functions preserve spin SU(2) symmetry

Assumption (i) is justified as long as the Wannier functions are well localized around their corresponding lattice site, which is typically the case for d of f shells. Assumption (ii) is fulfilled for degenerate sub-manifolds like the $3d$ t_{2g} or e_g shell. However, in practice even if the orbital symmetry is lifted, e.g. by a Jahn-Teller distortion, the corresponding interaction elements will usually not differ much. Furthermore, (ii) implies $U' = U - 2J$ of Eq. 2.26 for cubic symmetry. And finally, (iii) is satisfied for the paramagnetic phase and if spin-orbit coupling is neglected [82].

Under those assumptions U_{1234} has only three independent elements [82, 83], usually denoted by U (intra-orbital interaction), U' (inter-orbital interaction) and J (Hund's exchange),

$$\begin{aligned} U = U_{n_1n_1n_1n_1} &= \int d^3r \int d^3r' \;\; |w_{n_1}(\mathbf{r})|^2 \;\; V_c(\mathbf{r}-\mathbf{r}') \;\; |w_{n_1}(\mathbf{r}')|^2, \\ U' = U_{n_1n_1n_2n_2} &= \int d^3r \int d^3r' \;\; |w_{n_1}(\mathbf{r})|^2 \;\; V_c(\mathbf{r}-\mathbf{r}') \;\; |w_{n_2}(\mathbf{r}')|^2, \\ J = U_{n_1n_2n_2n_1} &= \int d^3r \int d^3r' \;\; w^*_{n_1}(\mathbf{r}) w^*_{n_2}(\mathbf{r}') \;\; V_c(\mathbf{r}-\mathbf{r}') \;\; w_{n_1}(\mathbf{r}') w_{n_2}(\mathbf{r}). \end{aligned} \tag{2.26}$$

$V_c(\mathbf{r}-\mathbf{r}')$ denotes here the *screened* Coulomb interaction[9]. Using this so-called Kanamori parametrization of the interaction matrix, we can write the Hamiltonian as

[9]For details on how to define $V_c(\mathbf{r}-\mathbf{r}')$ in cRPA we refer the reader to Ref. [79, 84].

Die approbierte gedruckte Originalversion dieser Dissertation ist an der TU Wien Bibliothek verfügbar.
The approved original version of this doctoral thesis is available in print at TU Wien Bibliothek.
TU Bibliothek Your knowledge hub WIEN

$$\begin{aligned}\mathcal{H}_{\text{int}}^{\text{Kanamori}} = U\sum_{n}\hat{n}_{n\uparrow}\hat{n}_{n\downarrow} + U'\sum_{n_1\neq n_2}\hat{n}_{n_1\uparrow}\hat{n}_{n_2\downarrow} + (U'-J)\frac{1}{2}\sum_{n_1\neq n_2,\sigma}\hat{n}_{n_1\sigma}\hat{n}_{n_2\sigma} \\ - J\sum_{n_1\neq n_2}\hat{c}^{\dagger}_{n_1\uparrow}\hat{c}_{n_1\downarrow}\hat{c}^{\dagger}_{n_2\downarrow}\hat{c}_{n_2\uparrow} + J\sum_{n_1\neq n_2}\hat{c}^{\dagger}_{n_1\uparrow}\hat{c}^{\dagger}_{n_1\downarrow}\hat{c}_{n_2\downarrow}\hat{c}_{n_2\uparrow}.\end{aligned} \tag{2.27}$$

Before we discuss how to solve Eq. 2.27 combined with a corresponding kinetic part (Eq. 2.25) let us briefly introduce the one-band version of it.

2.3.4 Hubbard Hamiltonian

The optimist thinks this is the best of all possible worlds, and the pessimist knows it is.
— J. Robert Oppenheimer

Previously, we discussed interactions in a general multi-orbital system. In the case of a single band, interactions that incorporate different orbitals like U' and J naturally no longer exist. Keeping the approximation of a purely local interaction U we can write down the Hamiltonian of the *Hubbard model*:

$$\mathcal{H}_{\text{Hubbard}} = -\sum_{i\neq j,\sigma} t_{ij}\hat{c}^{\dagger}_{i\sigma}\hat{c}_{j\sigma} + U\sum_{i}\hat{n}_{i\uparrow}\hat{n}_{i\downarrow} + \mu\hat{n}, \tag{2.28}$$

where we now use i, j as a shorthand for $\mathbf{R}_i, \mathbf{R}_j$ and assume a spin independent hopping matrix t_{ij}. $\mu = t_{ii}$ denotes the chemical potential and $\hat{n} = \sum_{i\sigma}\hat{n}_{i\sigma}$ is the average occupation. While Eq. 2.28 is a substantial simplification to the full electronic Hamiltonian of a crystal in Eq. 2.20, an analytic, or even numerically exact method to solve it does not exist for the general case[10].

After discussing the procedure and methods for extracting an effective low-energy Hamiltonian from DFT calculation, let us now turn to the methods used in this thesis to solve these model Hamiltonians in the next chapter.

[10] One should note, however, that recent advances have extended the parameter range, where exact numerical methods can be converged, see e.g. [85].

Die approbierte gedruckte Originalversion dieser Dissertation ist an der TU Wien Bibliothek verfügbar.
The approved original version of this doctoral thesis is available in print at TU Wien Bibliothek.
TU Bibliothek Your knowledge hub WIEN

Die approbierte gedruckte Originalversion dieser Dissertation ist an der TU Wien Bibliothek verfügbar.
The approved original version of this doctoral thesis is available in print at TU Wien Bibliothek.

Chapter 3

Methods for many-body quantum field theory

It is a mistake to think you can solve any major problems just with potatoes.
— D. Adams

In this chapter, we introduce the formalism of many-body correlation functions, which forms the basis for the dynamical mean-field theory (DMFT) and the dynamical vertex approximation (DΓA), which are the main methods we will use in subsequent chapters to study strongly correlated electron systems. We start by introducing the one-particle propagator $G^{(1)}$ in Section 3.1 and subsequently discuss symmetries and the lowest order diagrams. Section 3.2 contains a similar discussion, but for the two-particle Green's function $G^{(2)}$. Subsequently, we discuss the related vertex function in Section 3.3 and introduce the concept of two-particle irreducibility and the parquet decomposition of the vertex function. Generalized susceptibilities are briefly introduced in Section 3.4, while Section 3.5 discusses the Bethe-Salpeter equations, which allow for the construction of the full vertex from its irreducible components. The equation of motion for the self-energy, which connects two- and one-particle quantities, is introduced in Section 3.6. After this part, the stage is set to briefly introduce and discuss DMFT in Section 3.7. Approximations made in DΓA and a derivation of the resulting equations for the (approximated) vertex and the self-energy are detailed in Section 3.8. Finally, we briefly outline the linearized Eliashberg equations used to obtain superconducting eigenvalues in Section 3.9.

In the following, we deal with n-point correlation functions, which depend, in all generality, on n frequency (ν)/time (τ), momentum ($\mathbf{k}$)/coordinate ($\mathbf{R}$), orbital (n) and spin (σ) indices. To increase brevity, we follow Ref. [86] and often group all indices which are not explicitly written into a compound index. We will refer to this compound index as "flavor" and simply denote it by a number (e.g. $\mathfrak{1} \equiv \{\tau_1, \mathbf{R}_1, \sigma_1, n_1\}$). If an equation only contains the compound index $\mathfrak{1}$, it is formally equivalent in real and Fourier space. As sum over these compound indices means to sum over all indices they contain and the normalization of the sum is already implicitly included. Specifically, starting from Section 3.1.1, every frequency summation carries a $\frac{1}{\beta}$ and every momentum summation a $\frac{1}{N_\mathbf{k}}$.

3.1 One-particle Green's function

Propagators, also often called Green's functions (GF), will be at the heart of all many-body theories discussed in this thesis. Not only are they especially handy, but they are also connected to experimental observables, most notably the (local) density of states, which we will discuss in more detail later. Since we are dealing with finite temperatures, it is practical to use the so-called Matsubara formalism [87]. Here, instead of working

Die approbierte gedruckte Originalversion dieser Dissertation ist an der TU Wien Bibliothek verfügbar.
The approved original version of this doctoral thesis is available in print at TU Wien Bibliothek.
TU Bibliothek Your knowledge hub WIEN

with real time, we perform a Wick rotation [88] to imaginary time $t \to -i\tau$[1]. The two-point correlator, or one-particle Green's function, ($G^{(1)}$) at finite temperatures and in imaginary time can be defined as

$$G^{(1)}_{\sigma_1\sigma_2,n_1n_2}(\tau_1,\mathbf{R}_1;\tau_2,\mathbf{R}_2) \coloneqq -\langle \mathcal{T}[\hat{c}_{\{\sigma_1,n_1\}}(\tau_1,\mathbf{R}_1)\hat{c}^\dagger_{\{\sigma_2,n_2\}}(\tau_2,\mathbf{R}_2)]\rangle, \tag{3.1}$$

where $\hat{c}^\dagger_{\{\sigma,n\}}(\tau,\mathbf{R})$ ($\hat{c}_{\{\sigma,n\}}(\tau,\mathbf{R})$) are second quantization operators which create (annihilate) a Fermion with spin σ and band index n at a lattice site $\mathbf{R}$ and (imaginary) time τ. Further $\mathcal{T}[\cdot]$ is the (imaginary) time ordering operator, which has the property

$$\mathcal{T}[\hat{c}^{(\dagger)}_1(\tau_1)\hat{c}^{(\dagger)}_2(\tau_2)] = \hat{c}^{(\dagger)}_1(\tau_1)\hat{c}^{(\dagger)}_2(\tau_2)\Theta(\tau_1-\tau_2) - \hat{c}^{(\dagger)}_2(\tau_2)\hat{c}^{(\dagger)}_1(\tau_1)\Theta(\tau_2-\tau_1). \tag{3.2}$$

Finally, $\langle\cdot\rangle = \mathrm{Tr}\{e^{-\beta\hat{\mathcal{H}}}\cdot\}$ denotes the thermal expectation value, where $\beta = \frac{1}{k_BT}$ is the inverse temperature and $\hat{\mathcal{H}}$ the Hamiltonian of the system. With Eq. 3.1 one can also understand why $G^{(1)}$ is called a *propagator*: if $\tau_1 > \tau_2$ it creates an electron of flavor 2, e.g. with a certain band/spin index, at time τ_2; lets it propagate in the system and then annihilates an electron of flavor 1 at time τ_1. In the case that $\tau_1 < \tau_2$, a hole, instead of an electron, is created. The Green's function measures the probability amplitude of this process and can graphically also be represented in terms of a Feynman diagram:

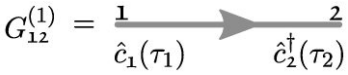

Figure 3.1: Feynman diagrammatic depiction of the one-particle Green's function. We choose to draw the arrow from τ_1 to τ_2 such that each G_{12} runs from 1 to 2. One should note that time and also the electron propagate from 2 to 1.

As a result of working with lattice systems, which are periodic by definition, it is often preferable to work in reciprocal rather than in real space. Let us now introduce the lattice translation operator $\hat{T}(\mathbf{R})$, which we define by its action on creation/annihilation operators $\hat{c}^{(\dagger)}_{\{\sigma,n\}}(\tau,\mathbf{R}) = \hat{T}^{-1}(\mathbf{R})\ \hat{c}^{(\dagger)}_{\{\sigma,n\}}(\tau,0)\ \hat{T}(\mathbf{R})$. If the Hamiltonian is invariant under translations by a lattice vector R, i.e. $[\hat{\mathcal{H}},\hat{T}(\mathbf{R})] = 0$, one can use the cyclic properties of the trace to show that the Green's function satisfies [89]

$$G^{(1)}_{\sigma_1\sigma_2,n_1n_2}(\tau_1,\mathbf{R}_1;\tau_2,\mathbf{R}_2) = G^{(1)}_{\sigma_1\sigma_2,n_1n_2}(\tau_1,\mathbf{R}_1-\mathbf{R}_2;\tau_2,0) \equiv G^{(1)}_{\sigma_1\sigma_2,n_1n_2}(\tau_1,\mathbf{R};\tau_2), \tag{3.3}$$

which will come in handy when we perform the Fourier transform (FT) of $G^{(1)}$. Let us write down how the FT of creation and annihilation operators is defined,

[1] This way the Boltzmann factor $e^{-\beta\mathcal{H}}$, appearing in thermal expectation values, can be interpreted as an additional (imaginary) time evolution.

Die approbierte gedruckte Originalversion dieser Dissertation ist an der TU Wien Bibliothek verfügbar.
The approved original version of this doctoral thesis is available in print at TU Wien Bibliothek.
TU Bibliothek Your knowledge hub WIEN

$$\hat{c}^\dagger(\mathbf{k}) = \frac{1}{\sqrt{N}} \sum_{\mathbf{R}} e^{-i\mathbf{R}\cdot\mathbf{k}} \hat{c}^\dagger(\mathbf{R}) \qquad \hat{c}^\dagger(\mathbf{R}) = \frac{1}{\sqrt{V_{\mathrm{BZ}}}} \int_{\mathrm{BZ}} d\mathbf{k} e^{i\mathbf{R}\cdot\mathbf{k}} \hat{c}^\dagger(\mathbf{k}) \tag{3.4}$$

$$\hat{c}\ (\mathbf{k}) = \frac{1}{\sqrt{N}} \sum_{\mathbf{R}} e^{i\mathbf{R}\cdot\mathbf{k}} \hat{c}\ (\mathbf{R}) \qquad \hat{c}\ (\mathbf{R}) = \frac{1}{\sqrt{V_{\mathrm{BZ}}}} \int_{\mathrm{BZ}} d\mathbf{k} e^{-i\mathbf{R}\cdot\mathbf{k}} \hat{c}\ (\mathbf{k}), \tag{3.5}$$

where V_{BZ} is the volume of the first Brillouin zone (BZ) and $\sum_{\mathbf{R}}$ runs over all lattice sites N. Replacing the operators in Eq. 3.1 by their corresponding Fourier transformed ones defines the FT of $G^{(1)}$,

$$\begin{aligned} G^{(1)}_{\sigma_1\sigma_2,n_1n_2}(\tau_1,\mathbf{k}_1;\tau_2,\mathbf{k}_2) &= \frac{1}{N}\sum_{\mathbf{R}_1}\sum_{\mathbf{R}_2} e^{i\mathbf{R}_1\mathbf{k}_1} e^{-i\mathbf{R}_2\mathbf{k}_2} G^{(1)}_{\sigma_1\sigma_2,n_1n_2}(\tau_1,\mathbf{R}_1;\tau_2,\mathbf{R}_2) \\ &= \sum_{\overline{\mathbf{R}}=R_1-R_2} \frac{1}{N}\sum_{\mathbf{R}_2} e^{i\overline{\mathbf{R}}\mathbf{k}_1} e^{-i\mathbf{R}_2(\mathbf{k}_2-\mathbf{k}_1)} G^{(1)}_{\sigma_1\sigma_2,n_1n_2}(\tau_1,\overline{\mathbf{R}};\tau_2) \\ &= \delta(\mathbf{k}_1-\mathbf{k}_2) \sum_{\overline{\mathbf{R}}=R_1-R_2} e^{i\overline{\mathbf{R}}\mathbf{k}_1} G^{(1)}_{\sigma_1\sigma_2,n_1n_2}(\tau_1,\overline{\mathbf{R}};\tau_2) \\ &\equiv G^{(1)}_{\sigma_1\sigma_2,n_1n_2}(\tau_1,\mathbf{k}=\mathbf{k}_1;\tau_2), \end{aligned} \tag{3.6}$$

where we used lattice translation symmetry (Eq. 3.3) to reduce the number of independent momentum arguments.

Let us now also consider the Fourier transform to frequency space and define the time-translation operator $\hat{U}(\tau) = e^{-\tau\mathcal{H}}$ with $\hat{c}^{(\dagger)}_{\{\sigma,n\}}(\tau,\mathbf{k}) = e^{\tau\hat{\mathcal{H}}}\ \hat{c}^{(\dagger)}_{\{\sigma,n\}}(0,\mathbf{k})\ e^{-\tau\hat{\mathcal{H}}}$. As long as the Hamiltonian is independent of time, which will be the case throughout this thesis, it commutes with $\hat{U}(\tau)$, i.e. $[\mathcal{H}(\tau_1),\hat{U}(\tau)] = 0$. We proceed along the same lines as before, assume $[\mathcal{H}(\tau_1),\hat{U}(\tau)] = 0$ and use it in combination with the cyclic properties of the trace to show that

$$G^{(1)}_{\sigma_1\sigma_2,n_1n_2}(\tau_1,\mathbf{k};\tau_2) = G^{(1)}_{\sigma_1\sigma_2,n_1n_2}(\tau_1-\tau_2,\mathbf{k};0) \equiv G^{(1)}_{\sigma_1\sigma_2,n_1n_2}(\tau,\mathbf{k}). \tag{3.7}$$

For imaginary time the Green's function is additionally anti-periodic with a period of β, since $e^{-\beta\hat{\mathcal{H}}}$ can be interpreted as propagation with imaginary time $\tau = \beta$

$$\begin{aligned} \langle \hat{c}_1^{(\dagger)}(\tau)\hat{c}_2^{(\dagger)}\rangle &= \mathrm{Tr}\{e^{-\beta\hat{\mathcal{H}}}e^{\tau\hat{\mathcal{H}}}\hat{c}_1^{(\dagger)}e^{-\tau\hat{\mathcal{H}}}\hat{c}_2^{(\dagger)}\} = \mathrm{Tr}\{e^{-\tau\hat{\mathcal{H}}}\hat{c}_2^{(\dagger)}e^{-\beta\hat{\mathcal{H}}}e^{\tau\hat{\mathcal{H}}}\hat{c}_1^{(\dagger)}\} \\ &= \mathrm{Tr}\{e^{-\beta\hat{\mathcal{H}}}e^{(\beta-\tau)\hat{\mathcal{H}}}\hat{c}_2^{(\dagger)}e^{-(\beta-\tau)\hat{\mathcal{H}}}\hat{c}_1^{(\dagger)}\} = \langle \hat{c}_2^{(\dagger)}(\beta-\tau)\hat{c}_1^{(\dagger)}\rangle \end{aligned} \tag{3.8}$$

and

$$\langle \hat{c}_2^{(\dagger)}\hat{c}_1^{(\dagger)}(\tau)\rangle = \langle \hat{c}_1^{(\dagger)}\hat{c}_2^{(\dagger)}(\beta+\tau)\rangle. \tag{3.9}$$

Die approbierte gedruckte Originalversion dieser Dissertation ist an der TU Wien Bibliothek verfügbar.
The approved original version of this doctoral thesis is available in print at TU Wien Bibliothek.
TU Bibliothek Your knowledge hub WIEN

Using the previous results one directly sees that,

$$\begin{aligned} G^{(1)}_{\sigma_1\sigma_2,n_1n_2}(\tau,\mathbf{k}) &= -G^{(1)}_{\sigma_1\sigma_2,n_1n_2}(\beta-\tau,\mathbf{k}) \quad \text{if } \tau>0 \text{ and} \\ G^{(1)}_{\sigma_1\sigma_2,n_1n_2}(\tau,\mathbf{k}) &= -G^{(1)}_{\sigma_1\sigma_2,n_1n_2}(\beta+\tau,\mathbf{k}) \quad \text{if } \tau<0\ , \end{aligned} \tag{3.10}$$

where the minus sign stems from the time ordering. Consequently, using Eq. 3.10 we can restrict all times to the interval $0<\tau<\beta$. Furthermore, the anti-periodicity in imaginary time leads to the Fourier transform to be defined over a set of discrete imaginary frequencies, which are given by $i\nu_n = \frac{(2n+1)\pi}{\beta}$. Let us note at this point that bosonic functions are instead periodic in τ with period β and the corresponding frequencies are given by $i\omega_n = \frac{(2n)\pi}{\beta}$.[2] Creation and annihilation operators transform given by,

$$\hat{c}^\dagger(i\nu_n) = \int_0^\beta d\tau e^{-i\nu_n\tau}\hat{c}^\dagger(\tau) \qquad \hat{c}^\dagger(\tau) = \frac{1}{\beta}\sum_{n=-\infty}^{\infty} e^{i\nu_n\tau}\hat{c}^\dagger(i\nu_n) \tag{3.11}$$

$$\hat{c}\ (i\nu_n) = \int_0^\beta d\tau e^{i\nu_n\tau}\hat{c}\ (\tau) \qquad \hat{c}\ (\tau) = \frac{1}{\beta}\sum_{n=-\infty}^{\infty} e^{-i\nu_n\tau}\hat{c}\ (i\nu_n), \tag{3.12}$$

which can now be used to compute the Fourier transform from imaginary time to Matsubara frequency,

$$\begin{aligned} G^{(1)}_{\sigma_1\sigma_2,n_1n_2}(\nu_1,\mathbf{k};\nu_2) &= \int_0^\beta d\tau_1 \int_0^\beta d\tau_2 e^{i\nu_1\tau_1}e^{-i\nu_2\tau_2}G^{(1)}_{\sigma_1\sigma_2,n_1n_2}(\tau_1,\mathbf{k};\tau_2) \\ &= \int_0^\beta d(\overline{\tau}=\tau_1-\tau_2)\int_0^\beta d\tau_2 e^{i\nu_1\overline{\tau}}e^{-i(\nu_2-\nu_1)\tau_2}G^{(1)}_{\sigma_1\sigma_2,n_1n_2}(\overline{\tau},\mathbf{k};0) \\ &= \beta\delta(\nu_1-\nu_2)\int_0^\beta d\overline{\tau}e^{i\nu_1\overline{\tau}}G^{(1)}_{\sigma_1\sigma_2,n_1n_2}(\overline{\tau},\mathbf{k};0) \\ &\equiv G^{(1)}_{\sigma_1\sigma_2,n_1n_2}(\nu=\nu_1,\mathbf{k}). \end{aligned} \tag{3.13}$$

As a result of energy and momentum conservation $G^{(1)}$ only depends on one frequency and momentum. In the case of SU(2) symmetry and we are within the paramagnetic phase, the one-particle Green's functions also does not depend on spin, i.e. $G^{(1)}_{\sigma_i\sigma_j} = \delta_{ij}G^{(1)}$ [89].

3.1.1 S-matrix expansion

The computational cost of evaluating the Green's function in Eq. 3.1, directly scales, in general, exponentially with the system size for interacting lattice models. Consequently,

[2] As a general note we will always donate fermionic Matsubara frequencies with ν and bosonic ones with ω.

Die approbierte gedruckte Originalversion dieser Dissertation ist an der TU Wien Bibliothek verfügbar.
The approved original version of this doctoral thesis is available in print at TU Wien Bibliothek.

it is often preferred to start from a known limit and perform an expansion around it. In the following, we will start from the non-interacting ($U = 0$) limit, which is diagonal in momentum space, and formulate a perturbation series in the interaction parameter U. To do so, let us recall Eq. 2.23, which is the basis for all model Hamiltonians considered in this thesis:

$$\mathcal{H} = \underbrace{-\sum_{12} t_{12}\hat{c}_1^\dagger \hat{c}_2}_{\mathcal{H}_0} + \underbrace{\frac{1}{2}\sum_{1234} U_{1234}\hat{c}_1^\dagger \hat{c}_3^\dagger \hat{c}_4 \hat{c}_2}_{\mathcal{H}_I}. \tag{3.14}$$

Before we proceed, let us draw the Feynman diagram for the interaction term $U_{1234}\hat{c}_1^\dagger \hat{c}_3^\dagger \hat{c}_4 \hat{c}_2$,

$U_{1234}\ \hat{c}_1^\dagger \hat{c}_3^\dagger \hat{c}_4 \hat{c}_2\ =$

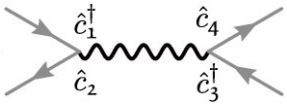

Figure 3.2: Feynman diagram for the interaction vertex. External legs are drawn in gray.

The Green's function is trivial to compute in the non-interacting limit, i.e. $U_{1234} = 0$. For systems with translational symmetry[3] and without interaction Eq. 3.14 is diagonal in momentum space and can be written as

$$\mathcal{H}(U = 0) = \sum_{\mathbf{k};12} \epsilon_{12}(\mathbf{k})\hat{c}_{\mathbf{k};1}^\dagger \hat{c}_{\mathbf{k};2}, \tag{3.15}$$

where $\epsilon_{12}(\mathbf{k}) = -\sum_{\mathbf{R};12} t_{12}(\mathbf{R})e^{i\mathbf{R}\mathbf{k}}$ is the momentum dispersion of the (Wannier) band. For this simple case the (non-interacting) Green's function $G_0^{(1)}$ is given by

$$G_{0;12}^{(1)}(\nu, \mathbf{k}) = \left[(i\nu_n + \mu)\delta_{12} - \epsilon_{12}(\mathbf{k})\right]^{-1}, \tag{3.16}$$

which reduces to

$$G_0^{(1)}(\nu, \mathbf{k}) = \frac{1}{i\nu_n - \epsilon(\mathbf{k}) + \mu} \tag{3.17}$$

in the single-band spin-symmetric case.

To perform an expansion around this non-interacting limit, it is most beneficial to switch into the interaction picture, where the time-evolution of an operator $\hat{A}$ is performed only with respect to the non-interacting Hamiltonian,

$$\hat{A}_I(\tau) = e^{\mathcal{H}_0\tau}\hat{A}e^{-\mathcal{H}_0\tau}. \tag{3.18}$$

[3] In that case $t_{\mathbf{R}_1\mathbf{R}_2}$ only depends on $|\mathbf{R}_1 - \mathbf{R}_2|$.

Die approbierte gedruckte Originalversion dieser Dissertation ist an der TU Wien Bibliothek verfügbar.
The approved original version of this doctoral thesis is available in print at TU Wien Bibliothek.
TU Bibliothek Your knowledge hub WIEN

An expression for the time-evolution operator in the interaction picture $S(\tau)$ can be obtained by requiring the equivalence of the expectation value $\langle \hat{A} \rangle$ in all (Heisenberg, Schrodinger and interaction) pictures. $S(\tau)$, the S-matrix, takes the following form:

$$S(\tau) = e^{\mathcal{H}_0 \tau} e^{-\mathcal{H}\tau}. \tag{3.19}$$

Using the equation of motion for $S(\tau)$,

$$\frac{\partial S(\tau)}{\partial \tau} = \underbrace{e^{\mathcal{H}_0 \tau}(\mathcal{H}_0 - \mathcal{H})}_{-\mathcal{H}_I(\tau) e^{\mathcal{H}_0 \tau}} e^{-\mathcal{H}\tau} = -\mathcal{H}_I(\tau) S(\tau), \tag{3.20}$$

we find:

$$S(\tau) = \mathcal{T} e^{-\int_0^\tau \mathcal{H}_I(\tau_1) d\tau_1} = 1 - \int_0^\tau d\tau_1 \mathcal{H}_I(\tau_1) + \int_0^\tau d\tau_1 \int_0^{\tau_1} d\tau_2 \mathcal{H}_I(\tau_1)\mathcal{H}_I(\tau_2) + ... \tag{3.21}$$

Expressing the one-particle Green's function $G^{(1)}$ in the interaction picture yields,

$$G^{(1)}_{12}(\tau) = -\frac{Tr\left[e^{-\mathcal{H}_0 \beta} \mathcal{T} \hat{c}_1(\tau) \hat{c}_2^\dagger(0) S(\beta)\right]}{Tr\left[e^{-\mathcal{H}_0 \beta} S(\beta)\right]}. \tag{3.22}$$

In the following discussion, time-evolution operators, as in Eq. 3.22, are in the interaction picture. Using Eq. 3.21 and Eq. 3.22 we arrive at an expansion of the Green's function in terms of the interacting Hamiltonian,

$$G^{(1)}_{12}(\tau) = -\frac{1}{\langle S(\beta) \rangle_0} \cdot \sum_{n=0}^{\infty} \frac{(-1)^n}{n!} \int_0^\beta d\tau_1 ... \int_0^\beta d\tau_n \langle \mathcal{T} \hat{c}_1(\tau) \hat{c}_2^\dagger \mathcal{H}_I(\tau_1) ... \mathcal{H}_I(\tau_n) \rangle_0, \tag{3.23}$$

where $\langle \cdot \rangle_0$ is the thermal expectation value with respect to $\mathcal{H}_0$. The zeroth-order of Eq. 3.23 is simply the non-interacting Green's function, hence let us consider the first-order term,

$$G^{(1)}_{(1);12}(\tau) = \frac{1}{2} \sum_{5678} \int_0^\beta d\tau_1 \langle \mathcal{T} \hat{c}_1(\tau) \hat{c}_2^\dagger U_{5678} \hat{c}_5^\dagger(\tau_1) \hat{c}_7^\dagger(\tau_1) \hat{c}_8(\tau_1) \hat{c}_6(\tau_1) \rangle_0^{\text{conn}}. \tag{3.24}$$

Eq. 3.23 no longer contains $\frac{1}{\langle S(\beta) \rangle_0}$, since all disconnected diagrams exactly cancel the partition sum in the denominator, which is known as the "linked cluster theorem" [90]. To emphasize that only connected diagrams should be counted we use "conn" as a superscript. To proceed, we use what is called "Wick's theorem" [91], which states that the *non*-interacting expectation value of n creation and annihilation operators is

Die approbierte gedruckte Originalversion dieser Dissertation ist an der TU Wien Bibliothek verfügbar.
The approved original version of this doctoral thesis is available in print at TU Wien Bibliothek.
TU Bibliothek Your knowledge hub WIEN

equivalent to all possible contractions of pairs. As all expectation values of two creation(annihilation) operators are zero, we are left with two inequivalent contractions[4],

$$G^{(1)}_{(1);12}(\tau) = \sum_{5678} \int_0^\beta d\tau_1 U_{5678} \Big[- \langle \mathcal{T}\hat{c}_1(\tau)\hat{c}^\dagger_5(\tau_1)\rangle_0 \, \langle \mathcal{T}\hat{c}_8(\tau_1)\hat{c}^\dagger_7(\tau_1)\rangle_0 \, \langle \mathcal{T}\hat{c}_6(\tau)\hat{c}^\dagger_2\rangle_0 + \langle \mathcal{T}\hat{c}_1(\tau)\hat{c}^\dagger_5(\tau_1)\rangle_0 \, \langle \mathcal{T}\hat{c}_6(\tau_1)\hat{c}^\dagger_7(\tau_1)\rangle_0 \, \langle \mathcal{T}\hat{c}_8(\tau)\hat{c}^\dagger_2\rangle_0 \Big], \tag{3.25}$$

where the remaining expectation values are nothing more than (minus) the non-interacting Green's function. Expressed in Feynman diagrams this becomes,

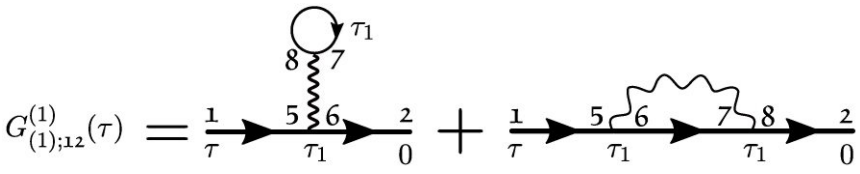

Figure 3.3: first-order diagrams for the interaction expansion of $G^{(1)}$. The part between the "outer" Green's functions are the Hartree and Fock contributions of the self-energy, which we will revisit in Section 3.1.2. The opposite minus sign from Eq. 3.25 is accounted for by the Fermionic loop rule: $(-1)^n$ where n is the number of closed loops.

3.1.2 Self-energy

In the previous paragraph we discussed the S-matrix expansion of the Green's function in the presence of interactions. Formally, one can reformulate Eq. 3.23 as,

$$G^{(1)}_{12} = G^{(1)}_{0;12} + \sum_{34} G^{(1)}_{0;13} \Sigma_{34} G^{(1)}_{42}, \tag{3.26}$$

which is called the Dyson equation [93]. Here we introduced the self-energy Σ_{34}, which diagrammatically contains (i) all one-particle irreducible (1PIR) diagrams build from $G^{(1)}_0$, or equivalently (ii) all *skeleton* diagrams build from $G^{(1)}$. A diagram is 1PIR if it cannot be separated in two disconnected parts by cutting only a single Green's function line. Skeleton means the same, but also for cutting two lines[5]. To obtain the self-energy from the Green's function one has to invert Eq. 3.26,

$$\Sigma_{12} = \left[G^{(1)}_{0;12}\right]^{-1} - \left[G^{(1)}_{12}\right]^{-1}. \tag{3.27}$$

Solving Eq. 3.27 in frequency and momentum space yields the Green's function

[4] See [92] for more details on the Wick contractions.

[5] This is similar to the two-particle irreducibility we will introduce in Section 3.3, but for two-point, instead of four-point, functions.

Die approbierte gedruckte Originalversion dieser Dissertation ist an der TU Wien Bibliothek verfügbar.
The approved original version of this doctoral thesis is available in print at TU Wien Bibliothek.
TU Bibliothek Your knowledge hub WIEN

$$G^{(1)}_{\mathfrak{12}}(\nu,\mathbf{k}) = \left[(i\nu_n+\mu)\delta_{\mathfrak{12}} - \epsilon_{\mathfrak{12}}(\mathbf{k}) - \Sigma_{\mathfrak{12}}(\nu,\mathbf{k})\right]^{-1}, \tag{3.28}$$

which again reduces to

$$G^{(1)}(\nu,\mathbf{k}) = \frac{1}{i\nu_n - \epsilon(\mathbf{k}) + \mu - \Sigma(\nu,\mathbf{k})}. \tag{3.29}$$

for the case of spin-independent single-band systems.

In essence we shifted the problem of computing $G^{(1)}(\nu,\mathbf{k})$ to computing $\Sigma(\nu,\mathbf{k})$. At first glance, it is not obvious that this is an improvement. However, empirically making (good) approximations for the self-energy is usually easier and many such methods have been developed over the years. Two of them, the dynamical mean-field theory (DMFT) and the dynamical vertex approximation (DΓA), are discussed in detail in Section 3.7 and Section 3.8, respectively.

3.1.3 Spectral function

One important aspect of the Green's function is its direct connection to the (**k**-resolved) spectral function $A(\mathbf{k},\omega)$, which is accessible in photo-emission experiments[6]. The connection is given by

$$A(\omega,\mathbf{k}) = -\frac{1}{\pi}\,\mathrm{Im}\,G^{(1)}(\omega,\mathbf{k}), \tag{3.30}$$

where ω is a *real* frequency, which can be obtained from the Matsubara one using analytic continuation $\nu \to \omega + i0^+$.

3.2 Two-particle Green's function

The two-particle Green's function ($G^{(2)}$)[7], often also referred to as four-point correlator, is defined as

$$G^{(2)}_{\mathfrak{1234}}(\tau_1,\tau_2,\tau_3,\tau_4) \coloneqq \langle \mathcal{T}[\hat{c}_{\mathfrak{1}}(\tau_1)\hat{c}^\dagger_{\mathfrak{2}}(\tau_2)\hat{c}_{\mathfrak{3}}(\tau_3)\hat{c}^\dagger_{\mathfrak{4}}(\tau_4)]\rangle, \tag{3.31}$$

where we use the compound index $\mathfrak{1} = \{R_1,\, \sigma_1,\, n_1\}$. The transformation to Fourier space is similar to the one-particle case and we will write it explicitly only for the frequency arguments,

[6] The spectral function is identical to the density of states in the non-interacting case.
[7] When no confusion with $G^{(1)}$ is possible, we will sometimes drop the superscript (2).

Die approbierte gedruckte Originalversion dieser Dissertation ist an der TU Wien Bibliothek verfügbar.
The approved original version of this doctoral thesis is available in print at TU Wien Bibliothek.
TU Bibliothek Your knowledge hub WIEN

$$G^{(2)}_{1234}(\nu_1,\nu_2,\nu_3,\nu_4) = \int_0^\beta\int_0^\beta\int_0^\beta\int_0^\beta d\tau_1 d\tau_2 d\tau_3 d\tau_4 G^{(2)}_{1234}(\tau_1,\tau_2,\tau_3,\tau_4) e^{\mathrm{i}(\nu_1\tau_1-\nu_2\tau_2+\nu_3\tau_3-\nu_4\tau_4)}$$
$$= \int_0^\beta\int_0^\beta\int_0^\beta d\tilde{\tau}_1 d\tilde{\tau}_2 d\tilde{\tau}_3 G^{(2)}_{1234}(\tilde{\tau}_1,\tilde{\tau}_2,\tilde{\tau}_3,0) e^{\mathrm{i}\nu_1\tilde{\tau}_1} e^{-\mathrm{i}\nu_2\tilde{\tau}_2} e^{\mathrm{i}\nu_3\tilde{\tau}_3} \underbrace{\int_0^\beta d\tau_4 e^{\mathrm{i}(\nu_1-\nu_2+\nu_3-\nu_4)\tau_4}}_{\beta\delta(\nu_1-\nu_2+\nu_3-\nu_4)}, \tag{3.32}$$

where in the second equality of Eq. 3.32 we assumed time-translation invariance and shifted each time-argument by τ_4 ($\tilde{\tau}_i = \tau_i - \tau_4$). Energy conservation is again manifested directly by canceling one frequency argument. Three frequency arguments remain and there are three equivalent choices of independent frequencies ν, ν', ω, where ν, ν' are fermionic and ω is bosonic (cf. Fig. 3.4)[8]:

ph-notation:	$\overline{\text{ph}}$-notation:	pp-notation:
$\nu_1 = \nu$	$\nu_1 = \nu$	$\nu_1 = \nu$
$\nu_2 = \nu - \omega$	$\nu_2 = \nu'$	$\nu_2 = \omega - \nu'$
$\nu_3 = \nu' - \omega$	$\nu_3 = \nu' - \omega$	$\nu_3 = \omega - \nu$
$\nu_4 = \nu'$	$\nu_4 = \nu - \omega$	$\nu_4 = \nu'$

Within this thesis, we mark the frequency notation by a superscript and imply ph otherwise. Identically as for frequencies, momentum conservation reduces the number of momentum indices to three. In the following, we use a four-vector notation $k = \{\nu, \mathbf{k}\}$ and $q = \{\omega, \mathbf{k}\}$ to collect frequency and momentum into a single index.

[8] The notation used here differs from [89] (due to different labeling of the legs) but is consistent with [94].

Die approbierte gedruckte Originalversion dieser Dissertation ist an der TU Wien Bibliothek verfügbar.
The approved original version of this doctoral thesis is available in print at TU Wien Bibliothek.
TU Bibliothek Your knowledge hub WIEN

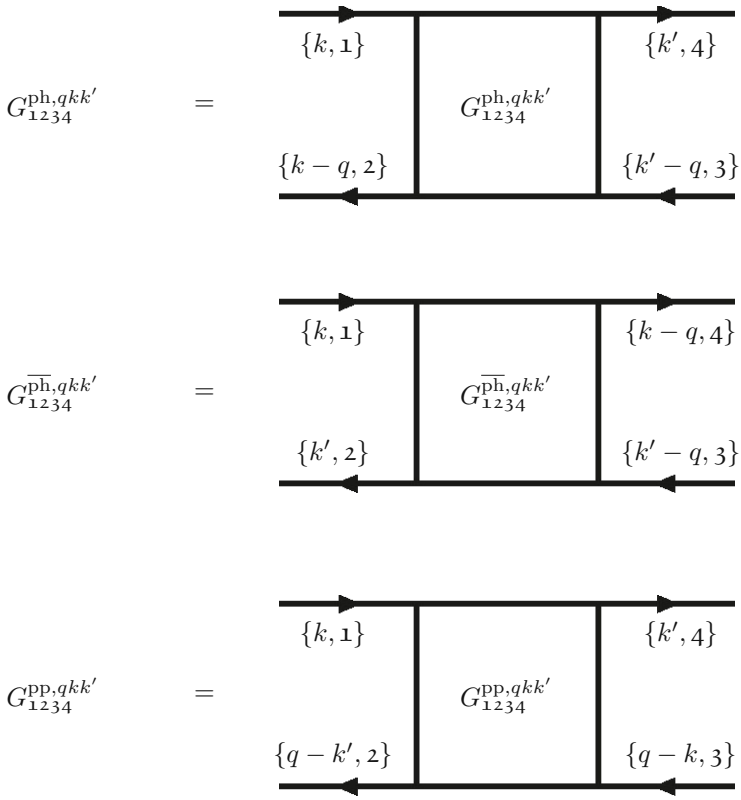

Figure 3.4: Feynman diagrammatic representation of the two-particle Green's function in the different momentum/frequency notations. Top: particle-hole (ph) notation. Middle: particle-hole transversal notation ($\overline{\text{ph}}$). Bottom: particle-particle notation (pp).

The physical content of $G^{(2)}$ does, of course, not depend on the chosen frequency notation. Nevertheless, as we will see later in Section 3.5, different notations are more convenient for different circumstances. Hence, let us explicitly write down the momentum shifts which relate the ph notation to the other two:

$$\begin{aligned} G^{\mathrm{ph},qkk'}_{1234} &= G^{\mathrm{pp},(k+k'-q)kk'}_{1234}, \\ G^{\mathrm{pp},qkk'}_{1234} &= G^{\mathrm{ph},(k+k'-q)kk'}_{1234}, \end{aligned} \qquad (3.33)$$

$$\begin{aligned} G^{\mathrm{ph},qkk'}_{1234} &= G^{\overline{\mathrm{ph}},(k-k')k(k-q)}_{1234}, \\ G^{\overline{\mathrm{ph}},qkk'}_{1234} &= G^{\mathrm{ph},(k-k')k(k-q)}_{1234}. \end{aligned}$$

3.2.1 SU(2) symmetry

Following the discussion of momentum and energy conservation, we will now address spin conservation, which is usually the case if spin-orbit coupling is not considered. In

Die approbierte gedruckte Originalversion dieser Dissertation ist an der TU Wien Bibliothek verfügbar.
The approved original version of this doctoral thesis is available in print at TU Wien Bibliothek.
TU Bibliothek Your knowledge hub WIEN

this case the total incoming and outgoing spin $\sigma \in \{\pm 1/2\}$ must coincide and only six spin combinations remain non-zero [94],

$$\sigma_1 = \sigma_2 = \sigma_3 = \sigma_4, \qquad (\sigma_1 = \sigma_2) \neq (\sigma_3 = \sigma_4), \qquad (\sigma_1 = \sigma_4) \neq (\sigma_2 = \sigma_3).$$

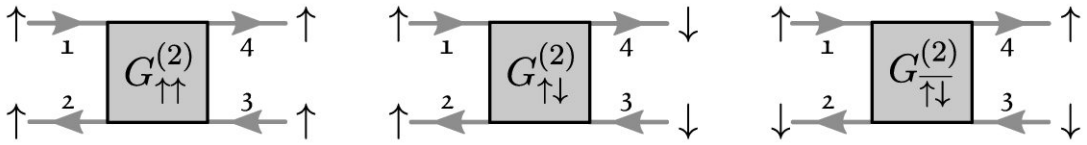

Figure 3.5: Non-zero spin combinations in the case of spin-conservation. The remaining three are obtained by replacing $\uparrow$ with $\downarrow$ and vice versa.

Within this thesis, we will only deal with spin-conserving Hamiltonians and it is thus convenient to use a more compact notation:

$$G_{\sigma\sigma'} \equiv G_{\sigma\sigma\sigma'\sigma'},$$
$$G_{\overline{\sigma\sigma'}} \equiv G_{\sigma\sigma'\sigma'\sigma},$$

where we group the spin to the left/right for $G_{\sigma\sigma'}$ and the ones on the top/bottom for $G_{\overline{\sigma\sigma'}}$. If we are additionally in the paramagnetic state, SU(2) symmetry applies for the spins-indices, and as a result, only two of the six combinations ($G_{\sigma\sigma'}$ and $G_{\sigma\sigma}$) remain independent [94]:

$$\begin{aligned} G_{\sigma\sigma'} &= G_{(-\sigma)(-\sigma')} = G_{\sigma'\sigma}, \\ G_{\sigma\sigma} &= G_{\sigma(-\sigma)} + G_{\overline{\sigma(-\sigma)}}. \end{aligned} \tag{3.34}$$

For the remaining independent spin combinations, two sets of linear combinations are particularly useful: (i) the density (d) and magnetic (m) channel and (ii) the singlet (s) and triplet (t) channel.[9]

$$\begin{aligned} G_{\mathrm{d}} &= G_{\uparrow\uparrow} + G_{\uparrow\downarrow}, \\ G_{\mathrm{m}} &= G_{\uparrow\uparrow} - G_{\uparrow\downarrow} = G_{\overline{\uparrow\downarrow}}, \\ \\ G_{\mathrm{s}} &= G_{\uparrow\downarrow} - G_{\overline{\uparrow\downarrow}}, \\ G_{\mathrm{t}} &= G_{\uparrow\downarrow} + G_{\overline{\uparrow\downarrow}}. \end{aligned} \tag{3.35}$$

3.2.2 Crossing symmetry

One additional symmetry relation is discussed in this thesis: the "crossing symmetry". As the name suggests, it corresponds to exchanging two incoming, or two outgoing lines and

[9] Their usefulness will become clear in Section 3.5. In the spin SU(2) symmetric case, the Bethe-Salpeter equation is diagonal in the density/magnetic spin combinations for the ph/$\overline{\text{ph}}$-channels, while the pp-channel is diagonal in the singlet/triplet combinations.

Die approbierte gedruckte Originalversion dieser Dissertation ist an der TU Wien Bibliothek verfügbar.
The approved original version of this doctoral thesis is available in print at TU Wien Bibliothek.
TU Bibliothek Your knowledge hub WIEN

is a direct manifestation of the Pauli principle. Indeed, the two-particle Green's function is antisymmetric with respect to exchanging two creation/annihilation operators $G^{(2)}_{1234} = -G^{(2)}_{3214}$. If one of the reduced frequency notations $\{\mathrm{ph}, \overline{\mathrm{ph}}, \mathrm{pp}\}$ is used exchanging two legs will also introduce a frequency/momentum shift. In ph-notation[10] and if spin is conserved[11] this is given by [95]:

$$\underbrace{G^{\mathrm{ph},qkk'}_{\sigma\sigma',1234}}_{①} = -\underbrace{G^{\mathrm{ph},(k'-k)(k'-q)k'}_{\overline{\sigma'\sigma},3214}}_{②} = \underbrace{G^{\mathrm{ph},(-q)(k'-q)(k-q)}_{\sigma'\sigma,3412}}_{③} = -\underbrace{G^{\mathrm{ph},(k-k')k(k-q)}_{\overline{\sigma\sigma'},1432}}_{④}. \tag{3.36}$$

The crossing symmetry and specifically the ensuing momentum shifts are most intuitive when viewed in Feynman diagrammatic form, which we display below in Fig. 3.6.

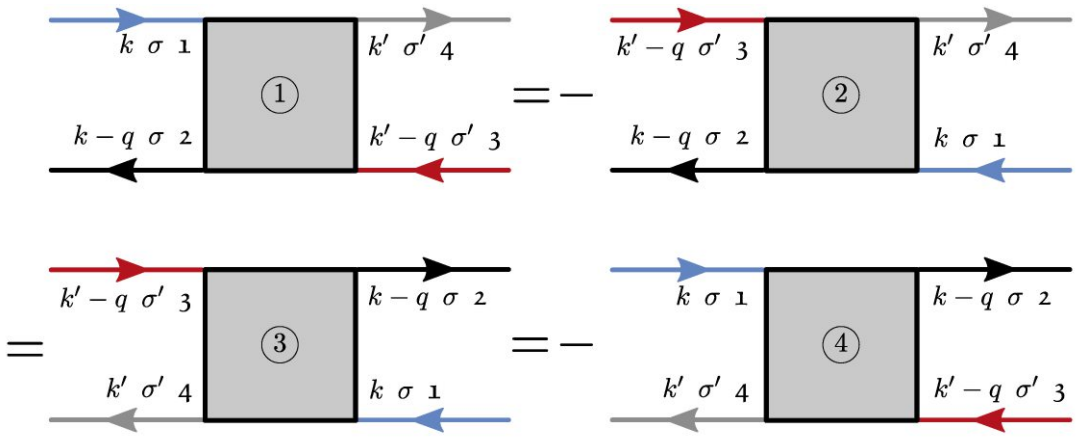

Figure 3.6: Feynman diagrammatic representation of the crossing symmetry for the two-particle Green's function in ph notation. Incoming and outgoing lines are color-coded to identify swapped lines easily. The encircled numbers match those of Eq. 3.36.

3.3 Vertex function

Let us, like in the one-particle case, take a look at the non-interacting limit ($U = 0$). Here, we can use Wick's theorem [96] to decompose the expectation value of Eq. 3.31 into two possible contractions of each one creation and one annihilation operator, which are simply two non-interacting (bare) one-particle Green's functions.

$$G^{(2),U=0}_{1234} = \langle \mathcal{T}[\hat{c}_1\hat{c}_2^\dagger]\rangle\langle \mathcal{T}[\hat{c}_3\hat{c}_4^\dagger]\rangle - \langle \mathcal{T}[\hat{c}_1\hat{c}_4^\dagger]\rangle\langle \mathcal{T}[\hat{c}_3\hat{c}_2^\dagger]\rangle = G^{(1)}_{0,12}G^{(1)}_{0,34} - G^{(1)}_{0,14}G^{(1)}_{0,32}. \tag{3.37}$$

The two terms in Eq. 3.37 describe the propagation of two non-interacting electrons.

[10] The principle is identical in any notation and thus only explicitly written for the ph one.
[11] In case that spin is not conserved the spin index is simply to be put into the compound one.

Die approbierte gedruckte Originalversion dieser Dissertation ist an der TU Wien Bibliothek verfügbar.
The approved original version of this doctoral thesis is available in print at TU Wien Bibliothek.
TU Bibliothek Your knowledge hub WIEN

To get a better understanding of what is happening once we turn on the interaction, it is instructive to explicitly compute the first-order diagrams in the interaction U_{1234}. To do so, we turn back to the two-particle Green's function in Eq. 3.31 and make use of the interaction picture[12],

$$G^{(2)}_{1234}(\tau_1,\tau_2,\tau_3,\tau_4) = \frac{Tr\left[e^{-\mathcal{H}_0\beta}\mathcal{T}\hat{c}_1(\tau_1)\hat{c}_2^\dagger(\tau_2)\hat{c}_3(\tau_3)\hat{c}_4^\dagger(\tau_4)S(\beta)\right]}{Tr\left[e^{-\mathcal{H}_0\beta}S(\beta)\right]}, \tag{3.38}$$

where the time evolution of all operators is expressed in the interaction picture. The zeroth-order diagrams in Eq. 3.38 have already been discussed in the non-interacting limit above. Thus, following the same steps as for the one-particle case in Section 3.1.1, we take a closer look at the first-order term in the S-matrix expansion,

$$G^{(2)}_{(1);1234} = -\frac{1}{2}\sum_{5678}\langle\mathcal{T}\hat{c}_1\hat{c}_2^\dagger\hat{c}_3\hat{c}_4^\dagger U_{5678}\hat{c}_5^\dagger\hat{c}_7^\dagger\hat{c}_8\hat{c}_6\rangle_0^{\text{conn}}, \tag{3.39}$$

where we dropped the (imaginary) time arguments and integrals for clarity. Eq. 3.39 contains three types of diagrams: (i) disconnected diagrams, (ii) renormalizations of the bare one-particle propagators, and (iii) fully connected diagrams. The "linked cluster theorem" [90] states that all diagrams corresponding to (i) are canceled by the partition sum in the denominator. Furthermore, all diagrams corresponding to (ii) can be included by drawing all diagrams using interacting instead of bare Green's functions. Hence, we only deal with (iii) here. All topologically distinct first-order diagrams belonging to (iii) are written down in Eq. 3.40 and are displayed in Feynman diagrams together with the zeroth-order in Fig. 3.7.

$$\begin{aligned} G^{(2)}_{(1);1234} = -\sum_{5678} U_{5678}\Big[&+\langle\mathcal{T}\hat{c}_1\hat{c}_5^\dagger\rangle_0\,\langle\mathcal{T}\hat{c}_6\hat{c}_2^\dagger\rangle_0\,\langle\mathcal{T}\hat{c}_3\hat{c}_7^\dagger\rangle_0\,\langle\mathcal{T}\hat{c}_8\hat{c}_4^\dagger\rangle_0 \\ &-\langle\mathcal{T}\hat{c}_1\hat{c}_5^\dagger\rangle_0\,\langle\mathcal{T}\hat{c}_8\hat{c}_2^\dagger\rangle_0\,\langle\mathcal{T}\hat{c}_3\hat{c}_7^\dagger\rangle_0\,\langle\mathcal{T}\hat{c}_6\hat{c}_4^\dagger\rangle_0\Big]. \end{aligned} \tag{3.40}$$

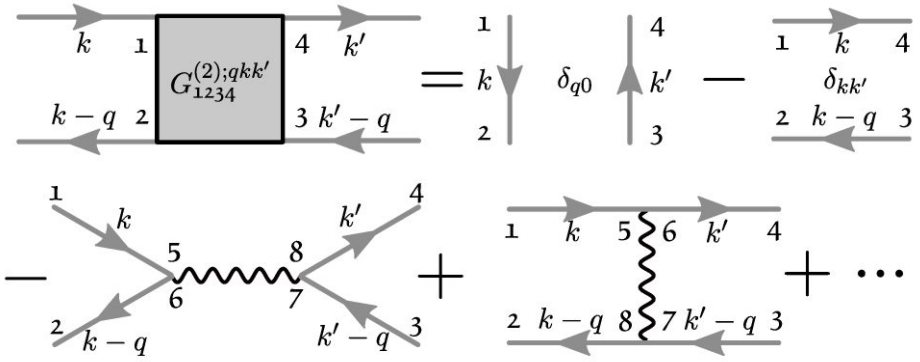

Figure 3.7: Zeroth- and first-order diagrams contributing to $G^{(2)}$.

[12] See Section 3.1.1 for further information regarding the interaction picture and the S-matrix.

Die approbierte gedruckte Originalversion dieser Dissertation ist an der TU Wien Bibliothek verfügbar.
The approved original version of this doctoral thesis is available in print at TU Wien Bibliothek.
TU Bibliothek Your knowledge hub WIEN

One can combine all connected diagrams into a single scattering object: the so-called vertex function F,

$$G^{(2)}_{1234} = G^{(1)}_{12}G^{(1)}_{34} - G^{(1)}_{14}G^{(1)}_{32} - \frac{1}{\beta}\sum_{5678} G^{(1)}_{15}G^{(1)}_{62}F_{5678}G^{(1)}_{37}G^{(1)}_{84}, \tag{3.41}$$

which we also draw as Feynman diagram in Fig. 3.8. Let us note that the sign of the vertex function can be chosen arbitrarily and was fixed here such that for a single-band Hubbard model the following relations hold:

$$\lim_{U\to 0^+} F_d = \lim_{U\to 0^+} F_{\uparrow\downarrow} = \lim_{U\to 0^+} +U, \qquad \lim_{U\to 0^+} F_m = \lim_{U\to 0^+} -F_{\overline{\uparrow\downarrow}} = \lim_{U\to 0^+} -U. \tag{3.42}$$

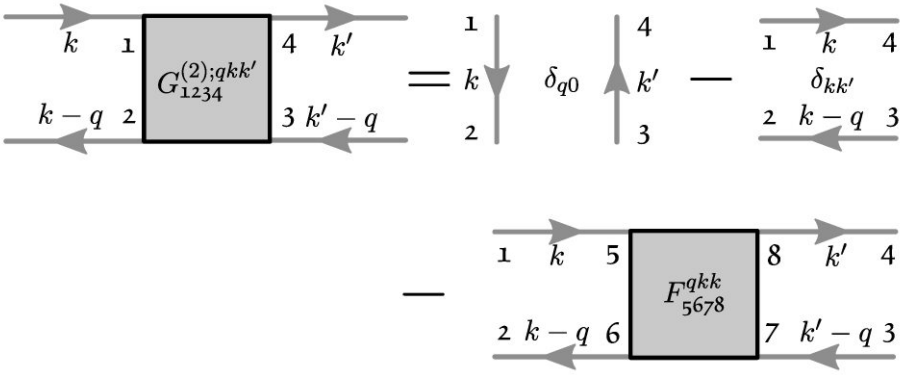

Figure 3.8: Decomposition of the two-particle Green's function $G^{(2)}$ into disconnected and connected parts in the ph notation.

By its previous definition, the vertex function contains all diagrams connecting two incoming and two outgoing lines. It is important to note that all diagrams contained in F can be classified uniquely based on two-particle reducibility (2PR). In essence, if cutting two fermionic lines separates a diagram into two disconnected pieces, the diagram is called 2PR. The classification according to 2PR yields four distinct groups of diagrams, coined parquet decomposition (Eq. 3.43) [97–99], which is illustrated in Fig. 3.43. Depending on which incoming and outgoing lines are contained in the sub-diagrams, it is denoted as ph- (12 and 34), $\overline{\text{ph}}$- (14 and 23) or pp- (13 and 24) reducible. Reducible diagrams are collected in Φ_{ph}, $\Phi_{\overline{\text{ph}}}$ and Φ_{pp}, respectively, while all remaining diagrams are called fully two-particle irreducible and grouped together in Λ. Importantly, any diagram belongs to one and only one channel, allowing us to write

$$F_{1234} = \Lambda_{1234} + \Phi_{\text{ph},1234} + \Phi_{\overline{\text{ph}},1234} + \Phi_{\text{pp},1234}. \tag{3.43}$$

Let us note here that the frequency convention and the channel reducibility are intimately linked together. Indeed, the Bethe-Salpeter equation, discussed later in Section 3.5, is diagonal in the bosonic (transfer) index q only if the frequency convention is the same

Die approbierte gedruckte Originalversion dieser Dissertation ist an der TU Wien Bibliothek verfügbar.
The approved original version of this doctoral thesis is available in print at TU Wien Bibliothek.

as the channel. Nevertheless, it should be noted that these concepts, although named the same, are *per se* detached. The former describes the used frequency convention and the latter the type of two-particle reducibility. Thus a ph reducible diagram can both be represented in ph or in any other (pp or $\overline{\text{ph}}$) frequency notation. To avoid confusion we will use the convention that superscript refers to the frequency notation, while subscript to the channel reducibility[13]. If no superscript is present ph frequency notation is implied (e.g $\Gamma^{qkk'}_{\text{pp}}$ is implied to be in ph frequency notation).

Since we have defined Φ_r with $r \in \{\text{ph}, \overline{\text{ph}}, \text{pp}\}$ as the set of reducible diagrams it is natural to also define the set of all irreducible diagrams Γ_r,

$$\Gamma_r = F - \Phi_r, \tag{3.44}$$

which is simply all diagrams minus the reducible ones. For a detailed discussion of the different vertex components and their frequency structure, we recommend Ref. [98] and Ref. [100], which are excellent reads.

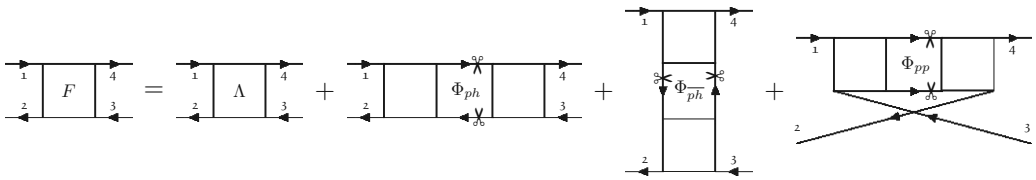

Figure 3.9: Parquet decomposition of the vertex function. Scissors indicate the lines that can be cut to separate the diagram. Adapted from [101] to match the conventions used here.

3.3.1 Crossing symmetry for the parquet components

The crossing symmetry of the full two-particle Green's function (Eq. 3.36) directly transfers to the vertex function F. However, for the components of the parquet decomposition (Eq. 3.43) the ph and $\overline{\text{ph}}$ channels trade places under crossing [98, 99][14],

$$\begin{aligned}
\Lambda^{qkk'}_{\sigma\sigma',1234} &= -\Lambda^{(k-k')k(k-q)}_{\overline{\sigma\sigma'},1432}, \\
\Phi^{qkk'}_{\text{pp},\sigma\sigma',1234} &= -\Phi^{(k-k')k(k-q)}_{\text{pp},\overline{\sigma\sigma'},1432}, \\
\Phi^{qkk'}_{\overline{\text{ph}},\sigma\sigma',1234} &= -\Phi^{(k-k')k(k-q)}_{\text{ph},\overline{\sigma\sigma'},1432} = -\Phi^{\overline{\text{ph}},qkk'}_{\text{ph},\overline{\sigma\sigma'},1432}, \\
\Phi^{qkk'}_{\text{ph},\sigma\sigma',1234} &= -\Phi^{(k-k')k(k-q)}_{\overline{\text{ph}},\overline{\sigma\sigma'},1432} = -\Phi^{\overline{\text{ph}},qkk'}_{\overline{\text{ph}},\overline{\sigma\sigma'},1432}.
\end{aligned} \tag{3.45}$$

[13] Hence $\Phi^{\text{pp}}_{\text{ph}}$ are all ph-reducible diagrams in pp frequency notation, while $\Phi^{\text{ph}}_{\text{pp}}$ are all pp-reducible diagrams in ph frequency notation. If no superscript is present ph frequency notation is implied.

[14] One can think about this as flipping the diagram along the anti-diagonal in Fig.3.9.

Die approbierte gedruckte Originalversion dieser Dissertation ist an der TU Wien Bibliothek verfügbar.
The approved original version of this doctoral thesis is available in print at TU Wien Bibliothek.

3.4 Susceptibility

In many experiments, the response of the system (material) to an external perturbation, e.g. an electric or magnetic field, is probed. Thereby one measures how the expectation value of an operator $\langle \hat{A} \rangle$ changes when an external field h is applied. Up to linear order and assuming time translational invariance for h this reads [102, 103],

$$\langle \hat{A}(\tau) \rangle_h = \langle \hat{A}(\tau) \rangle_{h=0} + \int_0^\beta d\tau' \ \chi(\tau - \tau') h(\tau') + \mathcal{O}(h^2). \tag{3.46}$$

$\chi(\tau - \tau')$ is usually called (physical) susceptibility and, crucially, does not depend on the applied field h. It can be obtained directly by taking a functional derivative of $\langle \hat{A} \rangle$ with respect to the field h [103],

$$\chi(\tau - \tau') = \frac{\delta}{\delta h} \langle \hat{A} \rangle \Big|_{h=0}. \tag{3.47}$$

Of particular interest for us are the magnetic and density susceptibilities [103],

$$\chi_m(\tau) = \frac{1}{2} \frac{\delta \langle \hat{\sigma}_i \rangle}{\delta h_i(\tau)}, \tag{3.48}$$

$$\chi_d(\tau) = -\frac{1}{2} \frac{\delta \langle \hat{n} \rangle}{\delta \mu(\tau)}. \tag{3.49}$$

Here χ_m is the response of the electron spins $\hat{\sigma}_i$ to an external magnetic field h_i with $i \in \{x, y, z\}$, while χ_d describes the change of occupation $\hat{n}$ with respect to the chemical potential μ. As we will see below, these physical susceptibilities can also be obtained from the two-particle Green's function. We will, however, not present a derivation or discussion of this connection and refer the reader to Ref. [102, 103] instead.

Let us now define the generalized susceptibility χ_{1234} as,

$$\begin{aligned} \chi^{qkk'}_{1234} &= \beta \left[G^{(2);qkk'}_{1234} - \delta_{0q} G^{(1);k}_{12} G^{(1);k'}_{34} \right] \\ &= \underbrace{-\beta \delta_{kk'} G^{(1);k}_{14} G^{(1);k-q}_{32}}_{\chi^{qkk'}_{0;1234}} - \sum_{5678} \underbrace{G^{(1);k}_{15} G^{(1);k-q}_{62}}_{-\frac{1}{\beta}\chi^{qkk}_{0;1265}} F^{\mathrm{ph};qkk'}_{5678} \underbrace{G^{(1);k'-q}_{37} G^{(1);k'}_{84}}_{-\frac{1}{\beta}\chi^{qk'k'}_{0;8734}}, \end{aligned} \tag{3.50}$$

where $\chi^{qkk'}_{0;1234}$ is called the generalized bubble. From Eq. 3.50 a physical susceptibility χ^q_{12} can be obtained by summing over kk' and 23 (also called contracting the legs in Feynman diagram jargon),

$$\chi^q_{14} = \sum_{\substack{kk' \\ 23}} \chi^{\mathrm{ph};qkk'}_{1234}. \tag{3.51}$$

Die approbierte gedruckte Originalversion dieser Dissertation ist an der TU Wien Bibliothek verfügbar.
The approved original version of this doctoral thesis is available in print at TU Wien Bibliothek.
TU Bibliothek Your knowledge hub WIEN

It can be shown [102, 103] that taking the magnetic and density spin combinations (Eq. 3.35) in Eq. 3.51 corresponds to (the Fourier transform of) χ_m and χ_d as defined in Eq. 3.49, respectively.

$$\chi_m^q = \chi_{\uparrow\uparrow}^q - \chi_{\uparrow\downarrow}^q, \tag{3.52}$$

$$\chi_d^q = \chi_{\uparrow\uparrow}^q + \chi_{\uparrow\downarrow}^q. \tag{3.53}$$

The bubble contribution to the susceptibility $\chi_{0;12}^q$ is obtained by contracting the generalized bubble,

$$\chi_{0;14}^q = \sum_{\substack{kk' \\ 23}} \chi_{0;1234}^{\mathrm{ph};qkk'}, \tag{3.54}$$

where $\chi_{0;1234}^{\mathrm{ph};qkk'}$ is defined in the underbraces of Eq. 3.50.

To gain a better understanding of the susceptibility, we discuss below in Box 6 χ_{d} and χ_{m} for the 2D square lattice Hubbard model. To keep the connection to cuprates and nickelates, we chose the set of tight-binding parameters corresponding to $LaNiO_2$ discussed in Box 4. For the Hubbard interaction we use the same value as in [50].

Die approbierte gedruckte Originalversion dieser Dissertation ist an der TU Wien Bibliothek verfügbar.
The approved original version of this doctoral thesis is available in print at TU Wien Bibliothek.

Box 6: Susceptibility

Below we plot the λ-corrected susceptibility obtained from the Bethe-Salpeter ladder in the ph channel[a] at zero frequency for Wannier parameters of the $LaNiO_2$ single-band projection[b]. The top row shows the λ-corrected magnetic susceptibility, while the bottom shows the density one. The main panel always shows a cut along a high-symmetry path (see inset of panel (a) for information about the special momenta), while the inset shows a colormap of the full BZ. Calculations were performed at $T = 1/25\,t^{-1}$ (226 K) using an on-site Coulomb interaction of $U = 8t$ (3.11 eV)[c].

Let us observe two key features: (i) the magnetic response is larger than the density response for both fillings displayed, which is especially noticeable for $n = 0.95$. This is no surprise, as antiferromagnetic fluctuations are largest precisely at half-filling. Furthermore, for the close to optimally doped case ($n = 0.85$) the maximum of the susceptibility moves away from the antiferromagnetic ordering vector $Q = (\pi, \pi)$. This incommensurability of the magnetic susceptibility has already been observed for cuprates in neutron scattering experiments [104, 105].

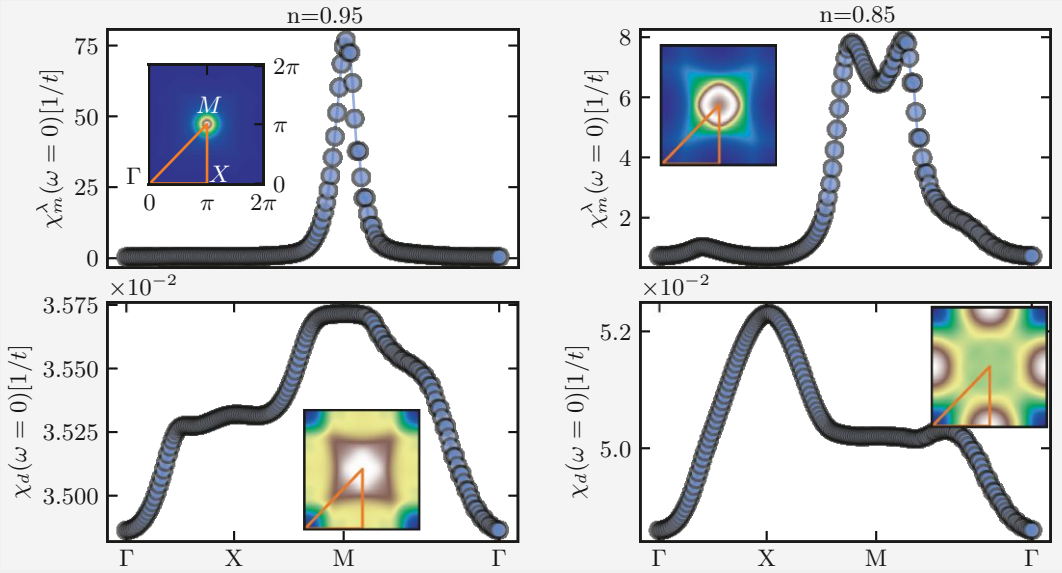

Figure 3.10: Zero-frequency part of the DMFT lattice susceptibility for the $LaNiO_2$ single-band Wannier model and two different fillings. Green's function and irreducible vertex are from DMFT. Top: λ-corrected magnetic susceptibility. Bottom: density susceptibility. Inset shows the full BZ at zero frequency. Orange line shows the path for the large panels. Calculations were performed at $T = 1/25\,t$ (226 K) using an on-site Coulomb interaction of $U = 8t$ (3.11 eV).

[a] See Section 3.5 and Section 3.8 for more details on the Bethe-Salpeter equation and the λ-correction, respectively.

[b] Let us note that results for the cuprate one-band model only differ on a quantitative level, but the discussion would remain essentially the same.

[c] Since we are now more in the model Hamiltonian territory we use the nearest-neighbor hopping t as unit of energy.

Die approbierte gedruckte Originalversion dieser Dissertation ist an der TU Wien Bibliothek verfügbar.
The approved original version of this doctoral thesis is available in print at TU Wien Bibliothek.
TU Bibliothek Your knowledge hub WIEN

3.5 Bethe-Salpeter equation

After our small excursion to introduce (generalized) susceptibilities, we turn our attention back to the vertex function and its components. Specifically, using Eq. 3.44 one can also write the vertex as $F = \Gamma_r + \Phi_r$, i.e. as the sum of all reducible and all irreducible diagrams in a given channel. However, as illustrated in Fig. 3.9, a reducible diagram is nothing but two (possibly irreducible) blocks connected by fermionic lines ($G^{(1)}$). Thus starting from the set of all irreducible diagrams Γ_r, one can generate all reducible ones recursively by building "ladders" with Γ_r and $G^{(1)}G^{(1)}$ as alternating building blocks. E.g. for the ph channel [89, 99],

$$\begin{aligned}\Phi_{\mathrm{ph};1234} = &\sum_{5678} \Gamma_{\mathrm{ph};1256} G^{(1)}_{67} G^{(1)}_{85} \Gamma_{\mathrm{ph};7834} \\ &+ \sum_{\substack{5678 \\ \mathfrak{abcd}}} \Gamma_{\mathrm{ph};1256} G^{(1)}_{67} G^{(1)}_{85} \Gamma_{\mathrm{ph};78\mathfrak{ab}} G^{(1)}_{\mathfrak{bc}} G^{(1)}_{\mathfrak{da}} \Gamma_{\mathrm{ph};\mathfrak{cd}34} \\ &+ \ldots.\end{aligned} \tag{3.55}$$

By using Eq. 3.55 the vertex function F can be expressed only in terms of Γ_r and $G^{(1)}$, which is called the Bethe-Salpeter equation (BSE)[106]:

$$\begin{aligned} F_{1234} &= \Gamma_{\mathrm{ph};1234} + \sum_{5678} \Gamma_{\mathrm{ph};1256} G^{(1)}_{67} G^{(1)}_{85} F_{7834}, \\ F_{1234} &= \Gamma_{\overline{\mathrm{ph}};1234} - \sum_{5678} \Gamma_{\overline{\mathrm{ph}};1654} G^{(1)}_{67} G^{(1)}_{85} F_{7238}, \\ F_{1234} &= \Gamma_{\mathrm{pp};1234} + \frac{1}{2} \sum_{5678} \Gamma_{\mathrm{pp};1836} G^{(1)}_{67} G^{(1)}_{85} F_{7254}, \end{aligned} \tag{3.56}$$

where the minus in the second line is necessary to obey the crossing relation and the $\frac{1}{2}$ for the pp channel is a result of indistinguishable particles [90]. Eq. 3.56 can also be rewritten in terms of the susceptibility χ by substituting F with Eq. 3.50,

$$\begin{aligned} \chi_{1234} &= \chi_{0;1234} - \frac{1}{\beta^2} \sum_{5678} \chi_{0;1265} \Gamma_{\mathrm{ph};5678} \ \chi_{8734}, \\ \chi_{1234} &= \chi_{0;1234} - \frac{1}{2\beta^2} \sum_{5678} \chi_{0;1735} \Gamma_{\mathrm{pp};5678} \ \Big[\chi_{8264} + \chi_{0;8264}\Big], \end{aligned} \tag{3.57}$$

where the $\overline{\mathrm{ph}}$ channel is formally equivalent to the ph one. Eq. 3.57 also acquired an additional prefactor $\frac{1}{\beta^2}$. One $\frac{1}{\beta}$ stems from using χ_0 instead of $G^{(1)}G^{(1)}$ and the second from the conversion of $F \to \chi$ (Eq. 3.50). The additional χ_0 in the pp channel corrects the $\frac{1}{2}$ for the first-order diagram in Γ_{pp}, where all lines are distinguishable.

Die approbierte gedruckte Originalversion dieser Dissertation ist an der TU Wien Bibliothek verfügbar.
The approved original version of this doctoral thesis is available in print at TU Wien Bibliothek.
TU Bibliothek Your knowledge hub WIEN

While Eq. 3.56 is elegant and general, its complexity can be reduced if symmetries are obeyed. Let us assume energy and momentum conservation as well as SU(2) symmetry for the spins[15]. These simplifications bring us back to the previous Section 3.2.1 about spin SU(2) symmetry, where we introduced the density (d) and magnetic (m) spin combinations. Indeed these spin combinations decouple the BSE in the ph and $\overline{\text{ph}}$ channel[16] [98],

$$\begin{aligned} F^{\text{ph};qkk'}_{\text{d/m};n_1n_2n_3n_4} &= \Gamma^{\text{ph};qkk'}_{\text{ph;d/m};n_1n_2n_3n_4} + \sum_{\substack{k_1 \\ n_5n_6n_7n_8}} \Gamma^{\text{ph};qkk_1}_{\text{ph;d/m},n_1n_2n_5n_6} G^{(1),k_1}_{n_6n_7} G^{(1),k_1-q}_{n_8n_5} F^{\text{ph};qk_1k'}_{\text{d/m},n_7n_8n_3n_4} \\ &= \Gamma^{\text{ph};qkk'}_{\text{ph;d/m};n_1n_2n_3n_4} - \frac{1}{\beta} \sum_{\substack{k_1k_2 \\ n_5n_6n_7n_8}} \Gamma^{\text{ph};qkk_1}_{\text{ph;d/m},n_1n_2n_5n_6} \chi^{qk_1k_2}_{0,n_6n_5n_8n_7} F^{\text{ph};qk_2k'}_{\text{d/m},n_7n_8n_3n_4}. \end{aligned} \tag{3.58}$$

Quite generally, choosing the momentum/frequency notation $n \in \{\text{ph}, \overline{\text{ph}}, \text{pp}\}$ as the channel reducibility $r \in \{\text{ph}, \overline{\text{ph}}, \text{pp}\}$ will diagonalize the BSE for the corresponding bosonic four-index q. Fig. 3.11 shows the Feynman diagrammatic representation of the BSE in all three channels using ph notation.

Analogously to the ph and $\overline{\text{ph}}$ channel, the BSE decouples in the pp channel for the s/t spin combinations. It is worth writing them down explicitly, as the s-channel acquires an additional minus sign,

$$\begin{aligned} F^{\text{pp};qkk'}_{\uparrow\downarrow;1234} &= \Gamma^{\text{pp};qkk'}_{\text{pp};\uparrow\downarrow;1234} + \frac{1}{2} \sum_{\sigma;5678} \Gamma^{\text{pp};qkk_1}_{\text{pp};\substack{1836 \\ \uparrow\sigma\downarrow\bar{\sigma}}} G^{(1);k_1}_{67} G^{(1);q-k_1}_{85} F^{\text{pp};qk_1k'}_{\substack{7254 \\ \bar{\sigma}\uparrow\sigma\downarrow}}, \\ F^{\text{pp};qkk'}_{\overline{\uparrow\downarrow};1234} &= \Gamma^{\text{pp};qkk'}_{\text{pp};\overline{\uparrow\downarrow};1234} + \frac{1}{2} \sum_{\sigma;5678} \Gamma^{\text{pp};qkk_1}_{\text{pp};\substack{1836 \\ \uparrow\sigma\downarrow\bar{\sigma}}} G^{(1);k_1}_{67} G^{(1);q-k_1}_{85} F^{\text{pp};qk_1k'}_{\substack{7254 \\ \bar{\sigma}\downarrow\sigma\uparrow}}. \end{aligned} \tag{3.59}$$

Building the singlet $\text{s} = \uparrow\downarrow - \overline{\uparrow\downarrow}$ and triplet $\text{t} = \uparrow\downarrow + \overline{\uparrow\downarrow}$ combinations from Eq. 3.59 one obtains [98],

$$\begin{aligned} F^{\text{pp};qkk'}_{\text{s};1234} &= \Gamma^{\text{pp};qkk'}_{\text{pp;s};1234} - \frac{1}{2} \sum_{5678} \Gamma^{\text{pp};qkk_1}_{\text{pp;s};1836} G^{(1);k_1}_{67} G^{(1);q-k_1}_{85} F^{\text{pp};qk_1k'}_{\text{s};7254}, \\ F^{\text{pp};qkk'}_{\text{t};1234} &= \Gamma^{\text{pp};qkk'}_{\text{pp;s};1234} + \frac{1}{2} \sum_{5678} \Gamma^{\text{pp};qkk_1}_{\text{pp;t};1836} G^{(1);k_1}_{67} G^{(1);q-k_1}_{85} F^{\text{pp};qk_1k'}_{\text{t};7254}. \end{aligned} \tag{3.60}$$

Below we briefly remark on how Eq. 3.58 can be inverted and solved to yield the vertex function F if the irreducible vertex Γ is known. For numerical implementations, it is

[15] Within this thesis, we will exclusively consider systems where these simplifications are justified.

[16] Only the ph channel is shown. The BSE in the $\overline{\text{ph}}$ can directly be obtained from Eq. 3.58 by replacing all ph with $\overline{\text{ph}}$.

Die approbierte gedruckte Originalversion dieser Dissertation ist an der TU Wien Bibliothek verfügbar.
The approved original version of this doctoral thesis is available in print at TU Wien Bibliothek.
TU Bibliothek Your knowledge hub WIEN

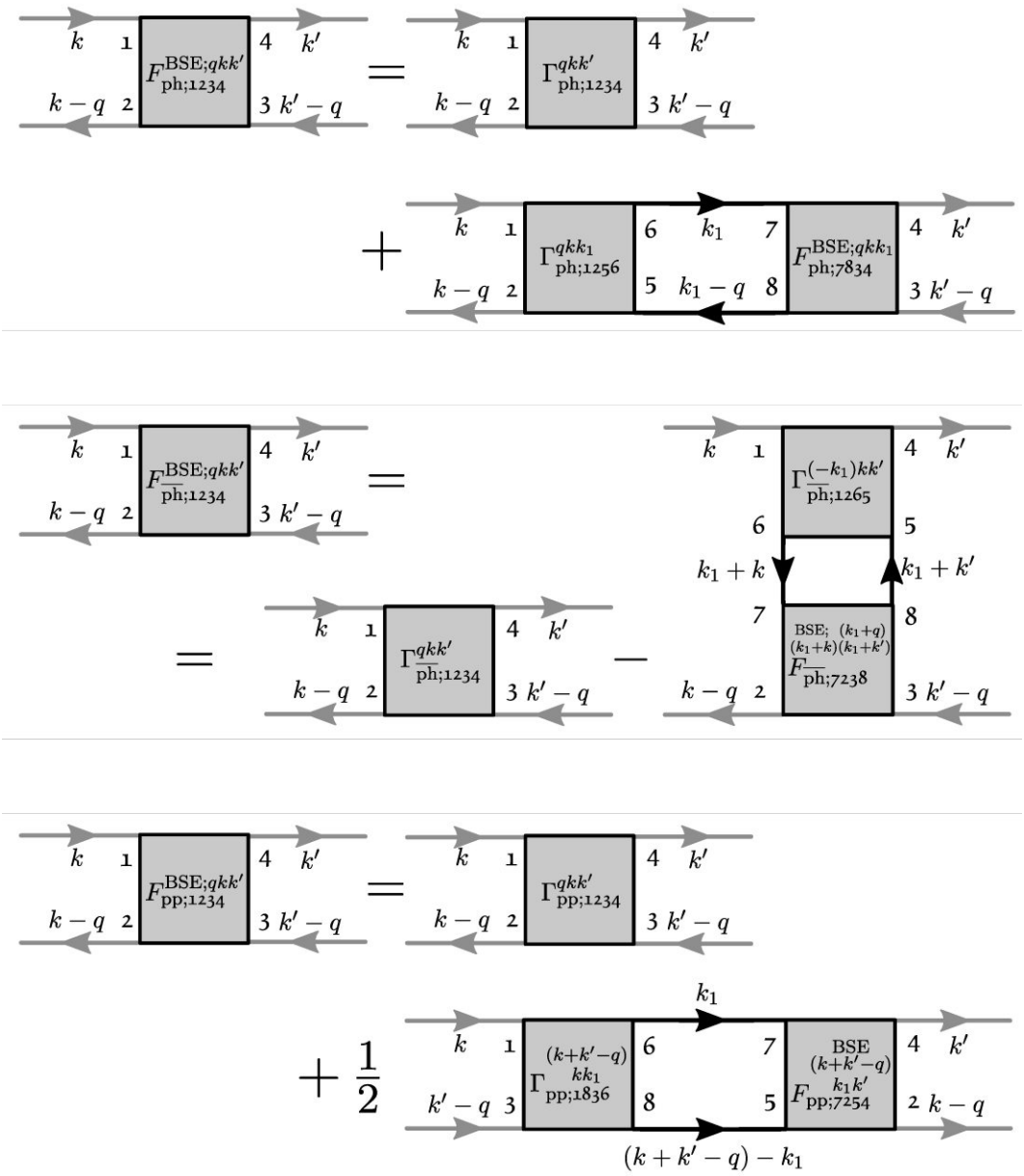

Figure 3.11: Feynman diagrammatic depiction of the Bethe-Salpeter equation. We include both a generalized leg index as well as the three independent momenta in ph frequency notation. Note that the two lower external legs are swapped for the pp channel and thus, the lower arrows are revered.

Die approbierte gedruckte Originalversion dieser Dissertation ist an der TU Wien Bibliothek verfügbar.
The approved original version of this doctoral thesis is available in print at TU Wien Bibliothek.

especially useful to treat four-point functions (M) as 2D matrices for each element of the bosonic four-vector q, by grouping the remaining indices $\mathrm{c} = \{k, n_1, n_2\}$ in the following way [94]

$$\boldsymbol{M}^{q}_{\mathrm{c}_1\mathrm{c}_2} \equiv M^{qkk'}_{n_1 n_2 n_3 n_4}. \tag{3.61}$$

Here doubly occurring indices are to be treated as (appropriately normed[17]) matrix-matrix multiplications in the spirit of the Einstein summation convention. Thus inverting Eq. 3.58 yields for F,

$$\boldsymbol{F}^{\mathrm{ph};q}_{\mathrm{d/m};\mathrm{c}_1\mathrm{c}_2} = \left[\mathbb{1}_{\mathrm{c}_1\mathrm{c}_2} + \frac{1}{\beta}\boldsymbol{\Gamma}^{\mathrm{ph};q}_{\mathrm{ph;d/m};\mathrm{c}_1\mathrm{c}_3}\boldsymbol{\chi}^{q}_{0;\mathrm{c}_3\mathrm{c}_2}\right]^{-1}, \tag{3.62}$$

where the inversion is with respect to $\mathrm{c}_1\mathrm{c}_2$.

3.6 Equation of motion for the self-energy

One important equation still left to be discussed is the equation of motion for the self-energy, also called Schwinger-Dyson equation (SDE). The SDE is a key element of almost all diagrammatic approaches, as it connects the vertex F to the self-energy [95]. It reads for multi-orbital Hubbard-like Hamiltonians [94]

$$\Sigma^{k}_{12} = \underbrace{\sum_{k';43} U_{1234} n^{k'}_{43} - \sum_{q;43} U_{1432} n^{k-q}_{43}}_{\Sigma^{\mathrm{HF};k}_{12}} - \sum_{qk';345678} U_{3278} F^{qkk'}_{1456} G^{(1);k-q}_{43} \underbrace{G^{(1);k'-q}_{85} G^{(1);k'}_{67}}_{-\frac{1}{\beta}\chi^{qk'k'}_{0;6587}}, \tag{3.63}$$

where $\Sigma^{\mathrm{HF};k}_{14}$ is the Hartree-Fock contribution, visualized in Fig. 3.12 (including external legs).

[17] This means every frequency summation carries a $\frac{1}{\beta}$ and every momentum summation a $\frac{1}{N_{\mathbf{k}}}$.

Die approbierte gedruckte Originalversion dieser Dissertation ist an der TU Wien Bibliothek verfügbar.
The approved original version of this doctoral thesis is available in print at TU Wien Bibliothek.
TU Bibliothek Your knowledge hub WIEN

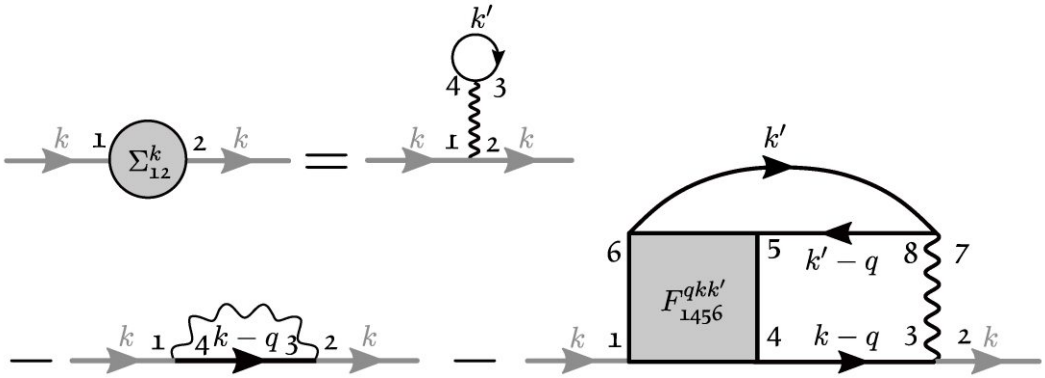

Figure 3.12: Feynman diagrammatic depiction of the Schwinger-Dyson equation. The first contribution is the Hartree term and the second the Fock term. The last term connects the vertex F to the self-energy. External legs are colored gray.

Hedin form of the equation of motion — Some approximations, like the dynamical vertex approximation (DΓA), prefer the SDE in terms of physical susceptibilities instead of vertices[18]. As a first step we rewrite Eq. 3.50 in terms of the vertex function F,

$$F^{qkk'}_{1234} = \beta^2 \left[\left[\chi^{qkk'}_{0;1234} \right]^{-1} - \sum_{kk';5678} \left[\chi^{qkk}_{0;1265} \right]^{-1} \chi^{qkk'}_{5678} \left[\chi^{qk'k'}_{0;8734} \right]^{-1} \right]. \tag{3.64}$$

In the following, we make use of a particularly useful property of Dyson- and BSE-like equations. Consider the following Dyson equation (Eq. 3.26),

$$G_2 = G_0 + G_0(\Sigma_1 + \Sigma_2)G_2, \tag{3.65}$$

where G_0 is the non-interacting Green's function and G_2 the interacting one. Here we separated the self-energy into two parts $\Sigma = \Sigma_1 + \Sigma_2$. Instead of solving Eq. 3.65 directly, one could also solve it in a two-step procedure by defining an "intermediate" Green's function G_1 [107],

$$\begin{aligned} G_1 &= G_0 + G_0\Sigma_1 G_1, \\ G_2 &= G_1 + G_1\Sigma_2 G_2. \end{aligned} \tag{3.66}$$

Although the equivalence of Eq. 3.65 and Eq. 3.66 may be surprising, or at least not obvious at first glance, it can easily be proven by inverting the first line of Eq. 3.66 and use the result to replace G_1 in the second line. The same principle also applies to the BSE and it is used here to separate the lowest order diagrams ($\Gamma_{(0)}$) contributing to Γ from the rest ($\delta\Gamma$). In Section 3.3, the lowest order diagrams contributing to $G^{(2)}$ were computed. Amputating the legs in Eq. 3.40, see also Fig. 3.7, yields the lowest order contribution to the vertex F, which is two-particle irreducible and hence also contained in Γ_r[19]:

[18] The DΓA makes use of renormalized physical susceptibilities (see λ-correction in Section 3.8).

[19] Since the lowest order contribution is essentially only the bare interaction U it is irreducible in all three channels $r \in \{\mathrm{ph}, \overline{\mathrm{ph}}, \mathrm{pp}\}$.

Die approbierte gedruckte Originalversion dieser Dissertation ist an der TU Wien Bibliothek verfügbar.
The approved original version of this doctoral thesis is available in print at TU Wien Bibliothek.
TU Bibliothek Your knowledge hub WIEN

$$\Gamma_{r,5678} = \underbrace{\left[U_{5678} - U_{5876}\right]}_{\Gamma_{(0)}} + \delta\Gamma_{r,5678}. \tag{3.67}$$

Diagrammatically, $\Gamma_{(0)}$ is displayed as a dot, see Fig. 3.13[20].

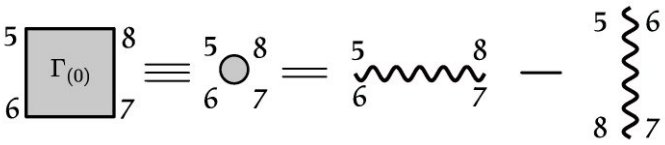

Figure 3.13: Feynman diagrammatic depiction of the lowest order contribution to the irreducible vertex Γ.

We now use Eq. 3.67 to split Eq. 3.57 similar to Eq. 3.66[21] [94, 108],

$$\chi^{*;qkk'}_{\mathrm{r};1234} = \left[\left[\chi^{qkk'}_{0;1234}\right]^{-1} + \frac{1}{\beta^2}\left[\Gamma^{qkk'}_{\mathrm{r};1234} - (U_{1234} - U_{1432})\right]\right]^{-1}, \tag{3.68}$$

$$\chi^{qkk'}_{1234} = \chi^{*;qkk'}_{\mathrm{ph};1234} - \sum_{k_1k_2;5678} \chi^{*;qkk_1}_{\mathrm{ph};1265}\left[U^{k_1k_2}_{5678} - U^{k_1k_2}_{5876}\right]\chi^{qk_2k'}_{8734}, \tag{3.69}$$

where Eq. 3.68 is the (inverted) first step and Eq. 3.69 the second. Previously (Eq. 3.57), we formulated the BSE as a "ladder" in χ_0 and Γ_r, where Γ_r was the two-particle irreducible part[22]. Eq. 3.69, instead, can be seen as a ladder with $\Gamma_{(0)}$ and χ^* as building blocks (see Fig. 3.14).

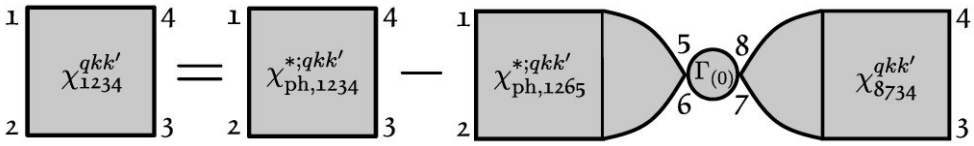

Figure 3.14: Feynman diagrammatic depiction of Eq. 3.69.

χ^* is the corresponding irreducible part, but with respect to $\Gamma_{(0)}$ (interaction line) and not χ_0 (two Green's function lines), as was the case for two-particle reducibility. This is commonly referred to as interaction-, or U-reducibility[23]. Combining Eq. 3.63, Eq. 3.64 and Eq.3.69 yields [110]:

[20] The different sign between the lowest order diagrams in $G^{(2)}$ and in F/Γ originates from the minus sign in the definition of F (see Eq. 3.41).
[21] We only show the ph channel, but the $\overline{\text{ph}}$ channel follows analogously.
[22] For a detailed discussion about two-particle reducibility we refer the reader to the discussion of Eq. 3.43.
[23] Similarily to the parquet decomposition (Eq. 3.43) a decomposition of the vertex function in terms of $\Gamma_{(0)}$ "lines" can be formulated [109].

Die approbierte gedruckte Originalversion dieser Dissertation ist an der TU Wien Bibliothek verfügbar.
The approved original version of this doctoral thesis is available in print at TU Wien Bibliothek.
TU Bibliothek Your knowledge hub WIEN

$$
\begin{aligned}
\Sigma^{F;k}_{12} &= \beta \sum_{qk';3478} U_{3278}\left[\delta_{17}\delta_{48}\delta_{kk'} - \sum_{56}\left[\chi^{qkk}_{0;1456}\right]^{-1}\chi^{qkk'}_{6587}\right] G^{(1);k-q}_{43} \\
&= \beta \sum_{q;3478} U_{3278}\Bigg[\frac{1}{\beta}\delta_{17}\delta_{48} - \underbrace{\sum_{k';56}\left[\chi^{qkk}_{0;1456}\right]^{-1}\chi^{*;qkk'}_{\mathrm{ph};6587}}_{\frac{1}{\beta}\gamma^{qk}_{1287}} \\
&+ \sum_{\mathfrak{abcd}}\left[U_{\mathfrak{abcd}} - U_{\mathfrak{adcb}}\right]\underbrace{\sum_{k_1;56}\left[\chi^{qkk}_{0;1456}\right]^{-1}\chi^{*;qkk_1}_{\mathrm{ph};65\mathfrak{ba}}}_{\frac{1}{\beta}\gamma^{qk}_{14\mathfrak{ba}}}\underbrace{\sum_{k_2k'}\chi^{qk_2k'}_{\mathfrak{dc}87}}_{\chi^{q}_{\mathfrak{dc}87}}\Bigg] G^{(1);k-q}_{43} \\
&= \sum_{q;3478} U_{3278}\left[\delta_{17}\delta_{48} - \gamma^{qk}_{1487} + \sum_{\mathfrak{abcd}}\left[U_{\mathfrak{abcd}} - U_{\mathfrak{adcb}}\right]\gamma^{qk}_{14\mathfrak{ba}}\chi^{q}_{\mathfrak{dc}87}\right] G^{(1);k-q}_{43}.
\end{aligned}
\tag{3.70}
$$

Here $\chi^{q}_{\mathfrak{cd}78}$ is a physical susceptibility where all orbital and spin indices have been retained. $\gamma^{qk}_{12\mathfrak{ba}}$ is the Fermi Bose vertex, which we define as[24],

$$
\gamma^{qk}_{1234} = \beta \sum_{k_1;56}\left[\chi^{qkk}_{0;1256}\right]^{-1}\chi^{*;qkk_1}_{6534}. \tag{3.71}
$$

Below we also show the Feynman diagrammatic version of Eq. 3.70. Let us note that Eq. 3.70 and Fig. 3.15 only display the vertex contribution to the self-energy and do *not* include the Hartree-Fock contribution[25].

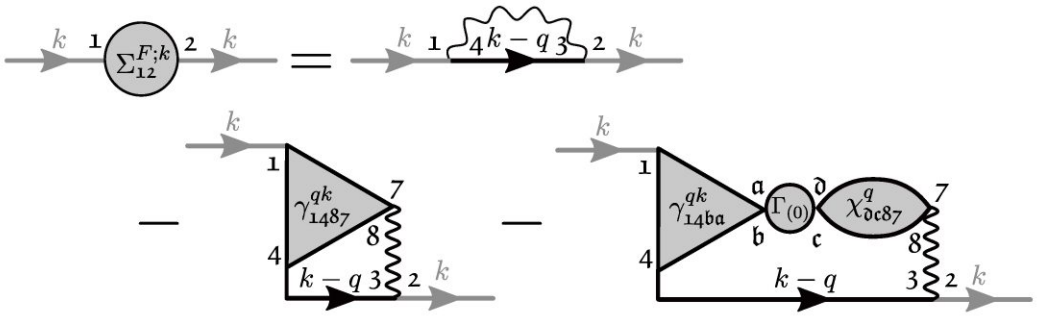

Figure 3.15: Feynman diagrammatic depiction of the vertex part from the Schwinger-Dyson equation in terms of Fermi bose vertices γ and physical susceptibilities χ.

One-band spin SU(2)-symmetric case — In the previous section, we presented the general multi-orbital case for the Schinger-Dyson equation. However, in this thesis, we

[24] Eq. 3.70 is formally identical to Eq. 3.63, however, in the DΓA routine all susceptibilities can now be replaced with the corresponding λ-corrected ones.

[25] The first diagram in Fig. 3.15, which is the Fock diagram including an additional a minus sign, is merely a double-counting correction.

Die approbierte gedruckte Originalversion dieser Dissertation ist an der TU Wien Bibliothek verfügbar.
The approved original version of this doctoral thesis is available in print at TU Wien Bibliothek.
TU Bibliothek Your knowledge hub WIEN

mostly deal with the paramagnetic single-band Hubbard model (Eq. 2.28) and provide the corresponding simplified SDE below. Not only can we drop all orbital indices, but the interaction also contains only two non-zero ($U_{\downarrow\downarrow\uparrow\uparrow} = U_{\uparrow\uparrow\downarrow\downarrow} \equiv U_{\uparrow\downarrow} \equiv U$) spin combinations. As a result the SDE simplifies to,

$$\begin{aligned}
\Sigma^k &= \frac{Un}{2} - U \sum_{qk'} F^{qkk'}_{\uparrow\downarrow} G^{(1);k-q} G^{(1);k'-q} G^{(1);k'}, \\
\Sigma^k &= \frac{Un}{2} - U \sum_{q} \left[(1 - U\chi^q_{\uparrow\downarrow})\, \gamma^{qk}_{\uparrow\downarrow} - U\chi^q_{\downarrow\downarrow} \gamma^{qk}_{\uparrow\uparrow} \right] G^{(1);k-q}, \\
&= \frac{Un}{2} - \frac{U}{2} \sum_{q} \left[(1 - U\chi^q_{\mathrm{d}})\, \gamma^{qk}_{\mathrm{d}} - (1 + U\chi^q_{\mathrm{m}}) \gamma^{qk}_{\mathrm{m}} \right] G^{(1);k-q},
\end{aligned} \tag{3.72}$$

where we dropped the spin indices for the one-particle Green's function and self-energy since $G^{(1)} \equiv G^{(1)}_{\uparrow} = G^{(1)}_{\downarrow}$ and $\Sigma \equiv \Sigma_{\uparrow} = \Sigma_{\downarrow}$.

3.7 Dynamical mean-field theory

We have now discussed the tools necessary to introduce dynamical mean-field theory (DMFT). After W. Metzner and D. Vollhardt showed in 1989 the locality of the self-energy in infinite dimension [111], A. Georges and G. Kotliar noticed the connection between the Hubbard model in infinite dimensions and the Anderson impurity model [112] and formulated the self-consistency conditions first in 1992. Since then, DMFT has developed to be a widely used tool for studying correlated electron systems [113] and, as already mentioned in previous sections, DMFT performs best for materials with localized d/f shells. Below we discuss the core approximations in DMFT and when they are most justified[26].

Core approximation of DMFT — In the following we consider Hamiltonians of the form

$$\mathcal{H} = \mathcal{H}_0 + \mathcal{H}_{\mathrm{I}}, \tag{3.73}$$

where the kinetic part $\mathcal{H}_0$ is defined as in Eq. 2.25 and the interaction part is of Kanamori form (Eq. 2.27). We can now formally write down the one-particle Green's function similar to Eq. 3.29,

$$G^{(1);k}_{12} = \left[(i\nu_n + \mu)\ \mathbb{1}_{12} - \epsilon^{\mathbf{k}}_{12} - \Sigma^k_{12} \right]^{-1}, \tag{3.74}$$

[26] For further reading, we recommend the review by A. Georges et al. [37], the Jülich summer school book series, e.g. [114] and a review by K. Held [26].

Die approbierte gedruckte Originalversion dieser Dissertation ist an der TU Wien Bibliothek verfügbar.
The approved original version of this doctoral thesis is available in print at TU Wien Bibliothek.
TU Bibliothek Your knowledge hub WIEN

where the inversion is with respect to the (spin-orbit) indices 1 and 2. DMFT assumes that the self-energy is purely local[27],

$$\Sigma^{\mathrm{DMFT};\nu}_{ij;12} = \mathbb{1}_{ij}\Sigma^{\nu}_{12}, \tag{3.75}$$

$$\Sigma^{\mathrm{DMFT};k}_{12} = \mathrm{J}_{\mathbf{k}}\Sigma^{\nu}_{12}, \tag{3.76}$$

where i, j denote two different lattice sites, $\mathbb{1}$ is the identity matrix and J a "matrix of ones", i.e. a matrix with one in all its entries. As a side remark, a self-energy that is purely local in real space will naturally be flat in momentum space.

When is the self-energy (mostly) local? — It turns out that in the limit of infinite lattice connectivity, or infinite dimensions, the approximation of a local self-energy becomes exact. This was first noticed by W. Metzner and D. Vollhardt [111] and subsequently generalized by E. Müller-Hartmann [66]. Here we will only give a brief outline of the reasoning and refer the interested reader to Refs. [26, 37, 114] for an in-depth discussion.

Let us consider the formal "limit of infinite dimensions" $\lim_{\mathrm{d}\to\infty} = \lim_{Z_{||\mathbf{R}_i-\mathbf{R}_j||}\to\infty}$, where $Z_{||\mathbf{R}_i-\mathbf{R}_j||}$ is the number of lattice sites at a distance $||\mathbf{R}_i - \mathbf{R}_j||$[28]. Whereas the potential energy $E_{pot} = \langle\mathcal{H}_{\mathrm{I}}\rangle$, being a local quantity, does not depend on the connectivity of the system, the kinetic energy,

$$E_{kin} = \langle\mathcal{H}_0\rangle = -2\sum_{i\neq j} t_{ij} \underbrace{\langle\hat{c}_i^\dagger\hat{c}_j\rangle}_{G^{(1)}_{ji}(\tau=0^-)} = -2\sum_{R=||\mathbf{R}_i-\mathbf{R}_j||} Z_R t_R G^{(1)}_R(\tau=0^-), \tag{3.77}$$

scales as Z_R for each hopping t_R. Since Z_R diverges as the lattice connectivity tends to infinity, t_R and $G^{(1)}_R$ have to be rescaled accordingly to keep the kinetic energy finite. By taking a look at the Fourier transform of the Green's function in Eq. 3.74 we see that it is directly connected to the hopping amplitudes and thus scales in the same way [26]. From this the only possible scaling of t_{ij} follows[29]

$$t^*_{ij} = \frac{t_{ij}}{\sqrt{Z_{||\mathbf{R}_i-\mathbf{R}_j||}}}. \tag{3.78}$$

Now let us use this scaling to determine which contributions to the self-energy remain finite in the limit of infinite dimensions. Any two interaction vertices in a self-energy diagram are connected by at least three independent paths [115]. If it would only be one it would violate 1PIR; and if it were only two the diagram would not be skeleton

[27] I.e. that all diagrams contributing to the self-energy start at a lattice site i and end on the same site i.

[28] The norm is to be understood in terms of counting the number of hoppings required to reach $\mathbf{R}_j$ from $\mathbf{R}_i$. This reduces to the Manhattan norm for the hypercubic lattice.

[29] There is no justification why hopping amplitudes should behave this way as the dimensionality of the physical system increases. Instead, the reasoning is that this scaling does not result in a non-trivial Hamiltonian with only $\mathcal{H}_0$ or only $\mathcal{H}_{\mathrm{I}}$ surviving.

Die approbierte gedruckte Originalversion dieser Dissertation ist an der TU Wien Bibliothek verfügbar.
The approved original version of this doctoral thesis is available in print at TU Wien Bibliothek.
TU Bibliothek Your knowledge hub WIEN

as cutting the corresponding lines would separate it. As a result the path between interaction vertices at two different sites i, j scales at best with $\mathcal{O}(Z_{||\mathbf{R}_i-\mathbf{R}_j||}^{-\frac{3}{2}})$, while the sum over the different equivalent neighbors scales as $\mathcal{O}(Z_{||\mathbf{R}_i-\mathbf{R}_j||})$. Consequently, all self-energy diagrams which are not purely local are suppressed by $\mathcal{O}(Z_{||\mathbf{R}_i-\mathbf{R}_j||}^{-\frac{1}{2}})$. Thus the DMFT approximation of a local self-energy becomes *exact* in infinite dimensions.

While the crystals we work with on a daily basis are not exactly infinite dimensional, one finds empirically that assuming a local self-energy is a good approximation already in three dimensions, see, for example, a DMFT study on Sr_2RuO_4 [116].

Impurity mapping and self-consistency — Approximating the self-energy to be local greatly simplifies the complexity, but nevertheless, one still needs a way to compute all local diagrams. While this cannot be done analytically in general, A. Georges and G. Kotliar [112] noticed that the diagrams contained in the local self-energy are the same as those for an impurity model with the same local interaction. For the Hubbard/Kanamori Hamiltonian this is the Anderson impurity model (AIM),

$$\mathcal{H}_{\text{AIM}} = \sum_{\mathbf{k};12} \epsilon_{\mathbf{k};12}\hat{c}^\dagger_{\mathbf{k};1}\hat{c}_{\mathbf{k};2} + \sum_{12} \epsilon_{d;12}\hat{d}^\dagger_1\hat{d}_2 + \frac{1}{2}\sum_{1234} U_{1234}\hat{d}^\dagger_1\hat{d}^\dagger_3\hat{d}_4\hat{d}_2 + \sum_{\mathbf{k};12}\left[V_{\mathbf{k};12}\hat{d}^\dagger_1\hat{c}_{\mathbf{k};2} + h.c.\right], \tag{3.79}$$

where $\hat{d}^\dagger(\hat{d}\ )$ creates (annihilates) an electron on the impurity, while $\hat{c}^\dagger(\hat{c}\ )$ describe non-interacting bath electrons, which can hop on or off the impurity with amplitude $V_{\mathbf{k};12}$. To map the Hubbard model on the AIM, DMFT has three equations that describe a self-consistency cycle [26, 95]:

$$\begin{aligned}
G^{(1);\nu}_{12} &= \langle \mathcal{T}\hat{d}_1\hat{d}^\dagger_2\rangle, && \text{(i)}\\
G^{(1);\nu}_{12} &= \left[\left[\mathcal{G}^\nu_{12}\right]^{-1} - \Sigma^\nu_{12}\right]^{-1}, && \text{(ii)}\\
G^{(1);\nu}_{12} &= \int d\mathbf{k}\left[i\nu_n - \epsilon_{\mathbf{k}} + \mu - \Sigma^\nu_{12}\right]^{-1} = \int d\epsilon\rho(\epsilon)\left[i\nu_n - \epsilon + \mu - \Sigma^\nu_{12}\right]^{-1}, && \text{(iii)}
\end{aligned} \tag{3.80}$$

where $\rho(\epsilon)$ is the non-interacting density of states and $\mathcal{G}^\nu_{12}$ is the local non-interacting propagator of the impurity, also often called the *dynamical Weiss field* in analogy to static mean-field theory. Let us note that $G^{(1);\nu}_{12}$ refers to the local impurity GF in the first two equations and to the local lattice propagator in the third. Convergence is reached once they are the same and one usually solves Eq. 3.80 numerically by iteration. The numerically expensive part of the DMFT cycle is computing the Green's function of the AIM ($G^{(1);\nu}_{12} = \langle \mathcal{T}\hat{d}_1\hat{d}^\dagger_2\rangle$). For this task several numerical solvers like exact diagonalization, see e.g. [117, 118], numerical renormalization group, see e.g. [119], or quantum Monte Carlo methods, see e.g. [120], have been developed. Within this thesis we will almost exclusively use continuous-time quantum Monte Carlo in the hybridization expansion [121] (CT-HYB).

Die approbierte gedruckte Originalversion dieser Dissertation ist an der TU Wien Bibliothek verfügbar.
The approved original version of this doctoral thesis is available in print at TU Wien Bibliothek.
TU Bibliothek Your knowledge hub WIEN

Box 7: $LaNiO_2$ DMFT spectral function

To better understand how the band dispersion discussed in Box 5 changes if local interactions are taken into account on the level of DMFT, we plot results in Fig. 3.16 below. Specifically, we use the $t - t' - t''$ approximation of the hopping matrix for $LaNiO_2$ and supplement the tight-binding Hamiltonian with an on-site Hubbard interaction of 3.11 eV[a].

In the left panel one can see the k-resolved spectral function, which was obtained by analytically continuing the DMFT result using the maximum-entropy method (MaxEnt) [122]. We use a high-symmetry path where the special points are $\Gamma = (0, 0, 0)$, $X = (\pi, 0, 0)$ and $M = (\pi, \pi, 0)$. In comparison to the Wannier band (white line) one can observe three key features: (i) Hubbard bands appear (best visible at ~ 3 eV around M and $\sim -2\,$eV around Γ), which are a hallmark signature of correlated metals, and (ii) temperature and scattering effects result in a broadening of features that correspond to finite lifetimes of the states, (iii) the bandwidth of the quasiparticle band around the Fermi energy is renormalized compared to the original non-interacting one. This corresponds to a reduced bandwidth and to a renormalization of the effective mass $m^*/m = 3.53$[b]. This mass renormalization is, in Fermi liquid theory, also connected to the quasiparticle weight $Z = m/m^*$, which can directly be computed from the (local) self-energy,

$$Z = \left[1 - \frac{\partial \operatorname{Re}\Sigma(\omega)}{\partial\omega}\Big|_{\omega\to 0}\right]^{-1}. \tag{3.81}$$

The middle panel shows the k-integrated spectral function compared to the one obtained from the Wannier band (gray). Per se one would expect that analytically continuing the self-energy, solving the Dyson equation (Eq. 3.27) and then integrating over the Brillouin zone is identical to simply continuing the local Green's function. However, using numeric analytic continuation, this is usually not the case, as can be seen from the difference between the blue (direct continuation) and red (first procedure) in Fig. 3.16. As a consequence, one should always be cautious when using quantities obtained by analytical continuation and perform checks concerning the stability of relevant features.

Die approbierte gedruckte Originalversion dieser Dissertation ist an der TU Wien Bibliothek verfügbar.
The approved original version of this doctoral thesis is available in print at TU Wien Bibliothek.

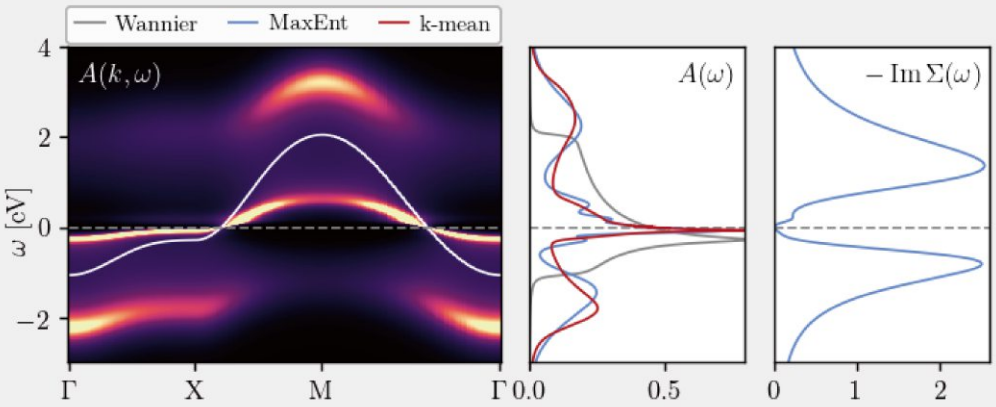

Figure 3.16: DMFT spectral function for the one-band Wannier projection of $LaNiO_2$. Left: k-resolved spectral function (colormap) and Wannier band (white line). Middle: k-integrated spectral function for the Wannier band (gray), directly continued with MaxEnt (blue) and k-integrated from $A(\omega, k)$ (red). Right: Imaginary part of the self-energy. The calculation was performed at 90 K and the band-filling was set to $n = 0.95$, which roughly corresponds to $LaNiO_2$ [50].

[a] This corresponds to $U = 8t$ in units of the hopping t, which we use to stay consistent with previous studies [20, 50].
[b] See also Fig. A.6 in the appendix for information an the effective mass of finite-layer nickelates.

Die approbierte gedruckte Originalversion dieser Dissertation ist an der TU Wien Bibliothek verfügbar.
The approved original version of this doctoral thesis is available in print at TU Wien Bibliothek.

3.8 Dynamical vertex approximation

There is no magic. There is only the grind.
— D. WONG

In the previous section, we discussed DMFT as a way to sum up all local diagrams contributing to the self-energy. DMFT captures several phenomena beyond standard PBE-DFT, the arguably most famous example being the Mott metal-insulator transition. Nevertheless, once non-local correlations become dominant, also DMFT can no longer capture all relevant physics. Cuprates and nickelates both fall into this category since spatial correlations are enhanced for quasi-2D systems, see e.g. [25, 123]. These non-local correlations give rise to exotic phenomena like the pseudogap, or d-wave superconductivity and methods beyond DMFT are required to capture them adequately.

Attempts of extending DMFT to also include non-local correlations can, for the most part, be grouped into two routes [95]: One route contains so-called *cluster methods*, where instead of considering a single impurity, a small cluster of interacting sites is embedded in a bath. Depending on whether this cluster is constructed in real space or momentum space, one speaks of cluster DMFT (CDMFT) or dynamical cluster approximation (DCA), respectively. These cluster extensions have successfully been applied to the Hubbard model for a variety of parameters, see e.g. [124, 125], and excel at capturing short-range fluctuations. This thesis will, however, use another approach usually referred to as *diagrammatic extensions of DMFT*.

As the name already suggests, approximations at the level of Feynman diagrams will be at the heart of those theories. Also, several flavors exist for those and we refer the reader to [95] and [126] for an in-depth discussion and comparison. The primary focus of this thesis is on the dynamical vertex approximation (DΓA)[38] or, more precisely, the λ-corrected ladder approximation of it [123]. Other flavors are not discussed and we refer the reader to Ref. [127] for its parquet implementation, to Ref. [128] for a self-consistent version of it, to Ref. [129] for a new λ-correction scheme and to Ref. [130] for an extension to SU(2)-symmetry broken phases. For a pedagogical introduction, see Ref. [131].

Let us also note that extensions of DMFT are not the only diagrammatic route to treat non-local correlations in the Hubbard model. Alternative approaches include, but are not limited to, diagrammatic Monte Carlo methods, see e.g. [85], functional renormalization group, see e.g. [132], or the two-particle self-consistent approach [133].

The dynamical vertex approximation uses a converged DMFT solution as a starting point; thus, all fully local diagrams contributing to the self-energy are included. Non-local diagrams for the self-energy are generated by solving the SDE (Eq. 3.72) with an approximated vertex. We discuss the approximations made in DΓA and the ensuing equations in detail below[30]. For the following, we assume that a converged DMFT solution already exists for the Hamiltonian of interest. The needed input for the DΓA is the lattice DMFT Green's function $G_{12}^{\mathrm{DMFT};k}$ and the ph-irreducible vertex of the

[30] The derivation presented here follows a slightly different approach to the problem than usual. Alternative derivations can be found, e.g. in Ref. [94] and Ref. [38]

Die approbierte gedruckte Originalversion dieser Dissertation ist an der TU Wien Bibliothek verfügbar.
The approved original version of this doctoral thesis is available in print at TU Wien Bibliothek.
TU Bibliothek Your knowledge hub WIEN

corresponding auxiliary AIM $\Gamma^{\omega\nu\nu'}_{\text{ph}}$.

Core approximation of ladder DΓA — Let us start from the parquet decomposition of the vertex (Eq. 3.43) and use Eq. 3.44[31] to rewrite it

$$F = \underbrace{F_{\text{ph}} - \Gamma_{\text{ph}}}_{\Phi_{\text{ph}}} + \underbrace{F_{\overline{\text{ph}}} - \Gamma_{\overline{\text{ph}}}}_{\Phi_{\overline{\text{ph}}}} + \Phi_{\text{pp}} + \Lambda, \tag{3.82}$$

where (for now) $F = F_{\text{ph}} = F_{\overline{\text{ph}}}$. Later we will replace F_{ph} and $F_{\overline{\text{ph}}}$ with "ladders" in the ph and $\overline{\text{ph}}$ channel, respectively. In DΓA, it is assumed that the following quantities are local and identical to the corresponding ones of DMFT[32]

$$\begin{aligned}
\Gamma^{\text{DΓA};qkk'}_{\text{ph}} &= \mathrm{J}_{\mathbf{kk}'}\Gamma^{\text{DMFT};\omega\nu\nu'}_{\text{ph}} \equiv \Gamma^{\omega\nu\nu'}_{\text{ph}}, \\
\Gamma^{\text{DΓA};qkk'}_{\overline{\text{ph}}} &= \mathrm{J}_{\mathbf{kk}'}\Gamma^{\text{DMFT};\omega\nu\nu'}_{\overline{\text{ph}}} \equiv \Gamma^{\omega\nu\nu'}_{\overline{\text{ph}}}, \\
\Phi^{\text{DΓA};qkk'}_{\text{pp}} &= \mathrm{J}_{\mathbf{kk}'}\Phi^{\text{DMFT};\omega\nu\nu'}_{\text{pp}} \equiv \Phi^{\omega\nu\nu'}_{\text{pp}}, \\
\Lambda^{\text{DΓA};qkk'} &= \mathrm{J}_{\mathbf{kk}'}\Lambda^{\text{DMFT};\omega\nu\nu'} \equiv \Lambda^{\omega\nu\nu'},
\end{aligned} \tag{3.83}$$

where J is a matrix with ones in all its entries. Here and in subsequent sections, we mark local quantities by simply dropping the momentum index[33]. The next step in DΓA is to solve the BSE (Eq. 3.58) with these *local* irreducible vertices and DMFT propagators. We call the resulting vertices F^{ladder} and will subsequently replace F_{ph} and $F_{\overline{\text{ph}}}$ in Eq. 3.82 with their respective "ladders" as defined in Eq. 3.84.

$$F^{q\nu\nu'}_{\text{ph};\substack{\text{d/m}\\1234}} \approx F^{\text{ladder};q\nu\nu'}_{\text{ph};\substack{\text{d/m}\\1234}} = \Gamma^{\omega\nu\nu'}_{\text{ph};\substack{\text{d/m}\\1234}} - \frac{1}{\beta}\sum_{\nu_1;5678}\Gamma^{\omega\nu\nu_1}_{\text{ph};\substack{\text{d/m}\\1256}}\chi^{q\nu_1\nu_1}_{0;6587}F^{\text{ladder};q\nu_1\nu'}_{\text{ph};\substack{\text{d/m}\\7874}}, \tag{3.84}$$

where $\chi^{q\nu\nu'}_{0;n_6n_5n_8n_7} = \sum_{\mathbf{kk}'}\chi^{qkk'}_{0;n_6n_5n_8n_7}$. Eq. 3.84 has two distinct properties when compared to the exact BSE: (i) $F^{\text{ladder}}_{\text{ph}}$ only explicitly depends on a single (the bosonic transfer) momentum and (ii) $F^{\text{ladder}}_{\text{ph}}$ no longer satisfies the crossing symmetry, which is a direct consequence of its single momentum dependence in Eq. 3.84. However, one may analogously define $F^{\text{ladder}}_{\overline{\text{ph}}}$, which now satisfies the following relation[34],

$$F^{\text{ladder};q\nu\nu'}_{\overline{\text{ph}};\sigma\sigma';1234} = -F^{\text{ladder};(k-k')\nu(\nu-\omega)}_{\text{ph};\overline{\sigma\sigma'};1432}. \tag{3.85}$$

Eq. 3.84 and 3.85 can be used to rewrite the DΓA vertex from Eq. 3.82, which we call $F^{\text{DΓA}}$ to distinguish it from the exact F.

[31] For the following, we always work in ph frequency/momentum notation if not stated otherwise

[32] To be more precise, for one-particle quantities we mean the DMFT lattice Green's function, while for "DMFT" two-particle quantities we refer to the corresponding AIM.

[33] $F^{q\nu\nu'}$ for example, depends only on the bosonic momentum $\mathbf{q}$, while being constant in $\mathbf{kk}'$.

[34] One should note that this relation is only valid as long as the corresponding local irreducible vertices satisfy the crossing relation.

Die approbierte gedruckte Originalversion dieser Dissertation ist an der TU Wien Bibliothek verfügbar.
The approved original version of this doctoral thesis is available in print at TU Wien Bibliothek.
TU Bibliothek Your knowledge hub WIEN

$$
\begin{aligned}
F^{\mathrm{D\Gamma A};qkk'}_{\sigma\sigma';1234} &= F^{\mathrm{ladder};q\nu\nu'}_{\mathrm{ph};\sigma\sigma';1234} - \underbrace{F^{\mathrm{DMFT};\omega\nu\nu'}_{\sigma\sigma';1234} + \Phi^{\mathrm{DMFT};\omega\nu\nu'}_{\mathrm{ph};\sigma\sigma';1234}}_{\Gamma^{\mathrm{DMFT};\omega\nu\nu'}_{\mathrm{ph};\sigma\sigma';1234}} - \\
&+ \underbrace{F^{\mathrm{ladder};q\nu\nu'}_{\overline{\mathrm{ph}};\sigma\sigma';1234}}_{-F^{\mathrm{ladder};(k-k')\nu(\nu-\omega)}_{\mathrm{ph};\overline{\sigma\sigma'};1432}} - \underbrace{F^{\mathrm{DMFT};\omega\nu\nu'}_{\sigma\sigma';1234} + \Phi^{\mathrm{DMFT};\omega\nu\nu'}_{\overline{\mathrm{ph}};\sigma\sigma';1234}}_{\Gamma^{\mathrm{DMFT};\omega\nu\nu'}_{\overline{\mathrm{ph}};\sigma\sigma';1234}} + \Phi^{\mathrm{DMFT};\omega\nu\nu'}_{\mathrm{pp};\sigma\sigma';1234} + \Lambda^{\mathrm{DMFT};\omega\nu\nu'}_{\sigma\sigma';1234} \\
&= F^{\mathrm{ladder};q\nu\nu'}_{\mathrm{ph};\sigma\sigma';1234} - F^{\mathrm{ladder};(k-k')\nu(\nu-\omega)}_{\mathrm{ph};\overline{\sigma\sigma'};1432} - F^{\mathrm{DMFT};\omega\nu\nu'}_{\sigma\sigma';1234},
\end{aligned}
\tag{3.86}
$$

where we used the local parquet equation (Eq. 3.43) in the last equality. The DΓA vertex is thus a sum of two BSE ladders minus the local DMFT vertex, which can be understood as a double counting correction.

DΓA equation of motion — The primary idea of the DΓA is to obtain a non-local self-energy, which is done by solving the SDE in Eq. 3.63 using the DΓA vertex from Eq. 3.86,

$$
\begin{aligned}
\Sigma^{F;k}_{12} &= \\
&= -\sum_{qk';345678} U_{3278}\left[F^{\mathrm{ladder};q\nu\nu'}_{\mathrm{ph};1456} - F^{\mathrm{ladder};k-k'\nu\nu-\omega}_{\mathrm{ph};1654} - F^{\mathrm{DMFT};\omega\nu\nu'}_{1456}\right] G^{(1);k-q}_{43} G^{(1);k'-q}_{85} G^{(1);k'}_{67}, \\
&= -\sum_{qk';345678} \left[U_{3278}\left[F^{\mathrm{ladder};q\nu\nu'}_{\mathrm{ph};1456} - F^{\mathrm{DMFT};\omega\nu\nu'}_{1456}\right] - U_{3872} F^{\mathrm{ladder};q\nu\nu'}_{\mathrm{ph};1456}\right] G^{(1);k-q}_{43} G^{(1);k'-q}_{85} G^{(1);k'}_{67},
\end{aligned}
\tag{3.87}
$$

where we used the subsequent substitutions $q \to k - \overline{k}$, $k' \to k - q$, $\overline{k} \to k'$, $4 \leftrightarrow 6$ and $3 \leftrightarrow 7$ to rewrite the summand containing $F^{\mathrm{ladder};k-k'\nu\nu-\omega}_{\mathrm{ph};1654}$. For the single-band SU(2) spin symmetric case Eq. 3.87 simplifies to,

$$
\begin{aligned}
\Sigma^{F;k} &= -U\sum_{qk'}\left[F^{\mathrm{ladder};q\nu\nu'}_{\mathrm{ph};\uparrow\downarrow} - F^{\mathrm{ladder};q\nu\nu'}_{\mathrm{ph};\overline{\uparrow\downarrow}} - F^{\mathrm{DMFT};\omega\nu\nu'}_{\mathrm{ph};\uparrow\downarrow}\right] G^{(1);k-q} G^{(1);k'-q} G^{(1);k'}. \\
\Sigma^{F;k} &= +U\sum_{q}\Big[\underbrace{-(1+U\chi^{q}_{\uparrow\downarrow})\,\gamma^{q\nu}_{\uparrow\downarrow} - U\chi^{q}_{\downarrow\downarrow}\gamma^{q\nu}_{\uparrow\uparrow}}_{\text{from } F^{\mathrm{ladder};q\nu\nu'}_{\mathrm{ph};\uparrow\downarrow}} \underbrace{-1 + (1+U\chi^{\omega}_{\overline{\uparrow\downarrow}})\,\gamma^{q\nu}_{\overline{\uparrow\downarrow}}}_{\text{from } F^{\mathrm{ladder};q\nu\nu'}_{\mathrm{ph};\overline{\uparrow\downarrow}}}\Big] G^{(1);k-q} - \Sigma^{F;k}_{\mathrm{dc}} \\
&= -\frac{U}{2}\sum_{q}\left[2 + (1-U\chi^{q}_{\mathrm{d}})\,\gamma^{q\nu}_{\mathrm{d}} - 3(1+U\chi^{q}_{\mathrm{m}})\,\gamma^{q\nu}_{\mathrm{m}}\right] G^{(1);k-q} - \Sigma^{F;k}_{\mathrm{dc}}
\end{aligned}
\tag{3.88}
$$

where $\Sigma^{F;\nu}_{\mathrm{dc}}$ is the double counting correction defined as

Die approbierte gedruckte Originalversion dieser Dissertation ist an der TU Wien Bibliothek verfügbar.
The approved original version of this doctoral thesis is available in print at TU Wien Bibliothek.
TU Bibliothek Your knowledge hub WIEN

$$\Sigma_{\mathrm{dc}}^{F;k} = U \sum_{qk'} F_{\mathrm{ph};\uparrow\downarrow}^{\mathrm{DMFT};\omega\nu\nu'} G^{(1);k-q} G^{(1);k'-q} G^{(1);k'}. \tag{3.89}$$

Note that the Hartree-Fock contribution to the self-energy is not included in Eq. 3.88. In Eq. 3.88 $\chi_{\mathrm{d/m}}^{q}$ is replaced by the λ-corrected susceptibility $\chi_{\mathrm{d/m}}^{\lambda,q}$ if a λ-correction scheme is used (see discussion in the next subsections).

Asymptotic behavior of the DΓA self-energy — Let us analyze the asymptotic form of the DΓA self-energy with the help of the equations derived previously. *Only* the $\frac{1}{i\nu}$ contribution from the vertex part to the self-energy Σ^F is discussed. The static part for the single-band Hubbard model is simply the Hartree term $\frac{Un}{2}$.

To better understand the $\nu \to \infty$ limit of Eq. 3.88, let us write Σ^F as a sum of three terms,

$$\Sigma^{F;k} = \Sigma_{\mathrm{ph}}^{F;k} + \Sigma_{\overline{\mathrm{ph}}}^{F;k} - \Sigma_{\mathrm{dc}}^{F;k}, \tag{3.90}$$

where,

$$\Sigma_{\mathrm{ph}}^{F;k} = -\frac{U}{2} \sum_{q} \left[(1 - U\chi_{\mathrm{d}}^{q})\, \gamma_{\mathrm{d}}^{q\nu} - (1 + U\chi_{\mathrm{m}}^{q})\, \gamma_{\mathrm{m}}^{q\nu} \right] G^{(1);k-q}, \tag{3.91}$$

$$\Sigma_{\overline{\mathrm{ph}}}^{F;k} = -\frac{U}{2} \sum_{q} \left[2 - 2(1 + U\chi_{\mathrm{m}}^{q})\, \gamma_{\mathrm{m}}^{q\nu} \right] G^{(1);k-q}, \tag{3.92}$$

and $\Sigma_{\mathrm{dc}}^{F;k}$ was already defined in Eq. 3.89. We start by analyzing the $\nu \to \infty$ limit for Eq. 3.91 [89]:

$$\begin{aligned} \lim_{\nu\to\infty} \Sigma_{\mathrm{ph}}^{F;k} &= -\lim_{\nu\to\infty} \frac{U}{2} \sum_{q} \left[(1 - U\chi_{\mathrm{d}}^{q})\, \gamma_{\mathrm{d}}^{qk} - (1 + U\chi_{\mathrm{m}}^{q}) \gamma_{\mathrm{m}}^{qk} \right] G^{(1);k-q} \\ &= \frac{1}{i\nu_n} \frac{U^2}{2} \sum_{q} \left[\chi_{\mathrm{d}}^{q} + \chi_{\mathrm{m}}^{q} \right] + \mathcal{O}\left[\frac{1}{(i\nu)^2} \right] = \frac{1}{i\nu_n} U^2 \sum_{q} \chi_{\uparrow\uparrow}^{q} + \mathcal{O}\left[\frac{1}{(i\nu)^2} \right]. \end{aligned} \tag{3.93}$$

The q sum over the susceptibility $\chi_{\uparrow\uparrow}^{q}$ can be evaluated analytically for the AIM and the Hubbard model [89, 134],

$$\sum_{qkk'} \frac{1}{2} \left[\chi_{\mathrm{d}}^{qkk'} + \chi_{\mathrm{m}}^{qkk'} \right] = \sum_{qkk'} \chi_{\uparrow\uparrow}^{qkk'} = \langle \hat{n}_\uparrow \hat{n}_\uparrow \rangle - \langle \hat{n}_\uparrow \rangle \langle \hat{n}_\uparrow \rangle = \frac{n}{2} \left(1 - \frac{n}{2} \right). \tag{3.94}$$

Eq. 3.94, which also directly reflects the Pauli principle ($\langle \hat{n}_\uparrow \hat{n}_\uparrow \rangle = \langle \hat{n}_\uparrow \rangle$), is satisfied for any *exact* solution, but not necessarily in an approximation such as DΓA. One way to restore the Pauli principle in DΓA is a λ-correction, discussed in the next subsection below.

Die approbierte gedruckte Originalversion dieser Dissertation ist an der TU Wien Bibliothek verfügbar.
The approved original version of this doctoral thesis is available in print at TU Wien Bibliothek.
TU Bibliothek Your knowledge hub WIEN

Let us note that $\Sigma_{\mathrm{ph}}^{F;k}$ and $\Sigma_{\overline{\mathrm{ph}}}^{F;k}$ coincide in any exact theory[35]. To prove this statement, let us consider the SDE (Eq. 3.87) and use the crossing symmetry of the vertex function

$$\begin{aligned}\Sigma_{12}^{F} &= -\sum_{345678} U_{3278} F_{1456} G_{43}^{(1)} G_{85}^{(1)} G_{67}^{(1)} \quad \text{(i)} \\ &= +\sum_{345678} U_{3278} F_{1654} G_{43}^{(1)} G_{85}^{(1)} G_{67}^{(1)} \quad \text{(ii)}.\end{aligned} \tag{3.95}$$

Assuming SU(2) symmetry for the spins and considering the single-band case with a Hubbard interaction $U \equiv U_{\uparrow\downarrow}$ Eq. 3.95 reduces to

$$\begin{aligned}\Sigma_{\uparrow\uparrow}^{F;k} &= -U \sum_{qk'} F_{\uparrow\uparrow\downarrow\downarrow}^{qkk'} G_{\uparrow\uparrow}^{(1);k-q} G_{\downarrow\downarrow}^{(1);k'-q} G_{\downarrow\downarrow}^{(1);k'} \quad \text{(i)} \\ &= +U \sum_{qk'} F_{\uparrow\downarrow\downarrow\uparrow}^{qkk'} G_{\uparrow\uparrow}^{(1);k'} G_{\downarrow\downarrow}^{(1);k'-q} G_{\downarrow\downarrow}^{(1);k-q} \quad \text{(ii)}.\end{aligned} \tag{3.96}$$

where we used the subsequent substitutions $q \to k - \overline{k}$, $k' \to k - q$ and $\overline{k} \to k'$ for (ii). Furthermore, $G_{\uparrow\uparrow} = G_{\downarrow\downarrow} \equiv G$ and transformation to the corresponding Hedin form yields $\Sigma_{\mathrm{ph}}^{F;k}$ (Eq. 3.91) and $\Sigma_{\overline{\mathrm{ph}}}^{F;k}$ (Eq. 3.92) from for (i) and (ii), respectively. By subtracting (i) from (ii) we can thus show that

$$0 = -U \sum_{qk'} F_{\uparrow\uparrow}^{qkk'} G^{(1);k-q} G^{(1);k'-q} G^{(1);k'}. \tag{3.97}$$

One should note that Eq. 3.97 is, in general, only satisfied for the *exact* solution, but similarly to Eq. 3.94 not necessarily for the ladder vertices constructed in DΓA. One possibility to restore Eq. 3.97 is again a (slightly different) λ-correction, which we discuss below.

Last but not least, the asymptotic behavior of $\Sigma_{\mathrm{dc}}^{F;k}$ corresponds to that of the DMFT self-energy since $G^k = G^\nu = \frac{1}{i\nu} + \mathcal{O}\left[\frac{1}{(i\nu)^2}\right]$, as $\nu \to \infty$ and Eq. 3.89 becomes purely local and therefore,

$$\lim_{\nu\to\infty} \Sigma_{\mathrm{dc}}^{F;k} = \lim_{\nu\to\infty} \Sigma_{\mathrm{DMFT}}^{F;k} = \frac{1}{i\nu_n} U^2 \frac{n}{2}\left(1 - \frac{n}{2}\right) + \mathcal{O}\left[\frac{1}{(i\nu)^2}\right], \tag{3.98}$$

which corresponds to the exact $\frac{1}{i\nu}$ asymptotic of the self-energy [89, 134, 135].

[35] DΓA is exact for impurity models where $G^{(1)}$ and Γ are local. In that case, DΓA returns essentially the self-energy which was used as input to construct $G^{(1)}$. While this is not particularly useful for practical applications, it can be helpful when benchmarking codes or checking equations.

Die approbierte gedruckte Originalversion dieser Dissertation ist an der TU Wien Bibliothek verfügbar.
The approved original version of this doctoral thesis is available in print at TU Wien Bibliothek.
TU Bibliothek Your knowledge hub WIEN

Mean-field phase transitions and λ-correction — In the previous sections, we introduced the core approximation of DΓA, derived the corresponding vertices, and discussed the asymptotic behavior. The vertex defined in Eq. 3.86, however, does not respect the Pauli principle and also does not reproduce the correct asymptotic form of the self-energy. Moreover, it does not respect the Mermin-Wagner theorem (MWT) [136], which states that phase transitions that break continuous symmetries at a finite temperature are forbidden in two dimensions.

There are, however, two approaches to cure these issues within ladder DΓA[36]: (i) so-called λ-correction schemes [123] where one (or more) renormalization parameter λ for the susceptibilities is (are) introduced and subsequently fixed by enforcing sum rules [89, 134], or (ii) using a self-consistency cycle [128]. In the following, we will focus on the λ-correction, which seems preferable for one-band systems [126, 128], but as a downside, has no straightforward extension to multi-orbital systems.

In the single-orbital Hubbard model, the MWT can be respected by introducing parameters $\lambda_{\mathrm{d/m}}$ to regularize the physical susceptibility[37],

$$\chi_{\mathrm{d/m}}^{\lambda_{\mathrm{d/m}};q} = \frac{1}{\frac{1}{\chi_{\mathrm{d/m}}^{q}} + \lambda_{\mathrm{d/m}}}, \tag{3.99}$$

where $\chi_{\mathrm{d/m}}^{q}$ is the susceptibility computed from the BSE as in Eq. 3.56, but using a local Γ and DMFT propagators. As one can easily see from Eq. 3.99 as long as

$$\min_{q}\left(\frac{1}{\chi_{\mathrm{d/m}}^{q}}\right) + \lambda_{\mathrm{d/m}} > 0, \tag{3.100}$$

$\chi_{\mathrm{d/m}}^{\lambda;q}$ remains finite with supremum $1/\lambda_{\mathrm{d/m}}$ and there is no long-range order. The question remains, how to fix $\lambda_{\mathrm{d/m}}$. While simply setting $\lambda_{\mathrm{d/m}} = \min_q\left(\frac{1}{\chi_{\mathrm{d/m}}^{q}}\right) + \epsilon$, with $\epsilon > 0$, will satisfy MWT in two dimensions, it will also artificially suppress the Néel order in three dimensions. An alternative is to formulate exact relations or sum rules and use them to adjust all λ parameters. Before discussing sum rules in more detail, let us briefly remark on the physical interpretation of $\lambda_{\mathrm{d/m}}$.

$\lambda_{\mathrm{d/m}}$ can be understood as adding an effective mass to the boson, i.e. to the spin or charge fluctuations [89], or equivalently as a reduction of the correlation length ξ. For spin fluctuations, for example, it is common to use an Ornstein-Zernicke approximation of the susceptibility χ_{OZ} [101, 126, 139]

$$\chi_{\mathrm{OZ}}^{\mathbf{q}} = \frac{A}{(\mathbf{q}-\mathbf{Q}) + \xi^{-2}}, \tag{3.101}$$

[36] One could, of course, also use the related parquet-DΓA instead. The high numerical cost, however, restricts it to a low momentum resolution and thus regimes where correlation lengths are small [137, 138].

[37] From the DMFT solution, we can infer which susceptibility is diverging. For the single-band Hubbard model at all parameters considered in this thesis, this is the magnetic susceptibility corresponding to an (possibly incommensurate) antiferromagnetic order.

Die approbierte gedruckte Originalversion dieser Dissertation ist an der TU Wien Bibliothek verfügbar.
The approved original version of this doctoral thesis is available in print at TU Wien Bibliothek.
TU Bibliothek Your knowledge hub WIEN

where A is a prefactor that determines the magnitude and $Q = (\pi, \pi)$ is the vector of antiferromagnetic fluctuations. A λ-correction of Eq. 3.101 keeps the same functional form, but with a renormalized correlation length $\widetilde{\xi}^{-2} = \xi^{-2} + A\lambda$.

Let us now discuss sum rules which can be used to fix $\lambda_{\mathrm{d/m}}$. One of them is Eq. 3.94, which corresponds to enforcing $\langle \hat{n}_\uparrow \hat{n}_\uparrow \rangle = \langle \hat{n}_\uparrow \rangle$, as discussed in the previous subsection. When using Eq. 3.94 in numerical calculations, one would like to avoid box-size effects due to a finite number of Matsubara frequencies. To do so, we use that the local susceptibilities from DMFT (AIM) already satisfy Eq. 3.94 and hence adjust $\lambda_{\mathrm{d/m}}$ such that [89, 134]:

$$\sum_{qkk'} \frac{1}{2}\left[\chi_{\mathrm{d}}^{\lambda_{\mathrm{d}};qkk'} + \chi_{\mathrm{m}}^{\lambda_{\mathrm{m}};qkk'}\right] = \sum_{\omega\nu\nu'} \frac{1}{2}\left[\chi_{\mathrm{d}}^{\mathrm{DMFT};\omega\nu\nu'} + \chi_{\mathrm{m}}^{\mathrm{DMFT};\omega\nu\nu'}\right] = \frac{n}{2}\left(1 - \frac{n}{2}\right). \tag{3.102}$$

Eq. 3.102 is, however, not enough to ensure the correct asymptotic behavior of the self-energy. This can be understood by considering the three parts of the DΓA self-energy in Eq. 3.90 again. Eq. 3.102 guaranties that $\lim_{\nu\to\infty} \Sigma_{\mathrm{ph}}^{F;k} = \frac{1}{i\nu_n} U^2 \sum_q \chi_{\uparrow\uparrow}^q + \mathcal{O}\left[\frac{1}{(i\nu)^2}\right] = \lim_{\nu\to\infty} \Sigma_{\mathrm{dc}}^{F;k}$. Consequently, the asymptotic contributions of $\Sigma_{\mathrm{ph}}^{F;k}$ and $-\Sigma_{\mathrm{dc}}^{F;k}$ cancel, thus leaving only the contribution from $\Sigma_{\overline{\mathrm{ph}}}^{F;k}$.

As mentioned above $\Sigma_{\overline{\mathrm{ph}}}^{F;k}$ is identical to $\Sigma_{\mathrm{ph}}^{F;k}$ in any *exact* solution, but not necessarily in DΓA since Eq. 3.97 may be violated. One way to assure that $\Sigma_{\overline{\mathrm{ph}}}^{F;k}$ shows the correct asymptotic behavior is by adjusting λ_{m} such that

$$\sum_q \chi_{\mathrm{m}}^{\lambda_{\mathrm{m}};q} = \sum_\omega \chi_{\mathrm{m}}^{\mathrm{DMFT};\omega}. \tag{3.103}$$

When combining Eq. 3.102 with Eq. 3.103 we see that the sum over $\chi_{\mathrm{m}}^{\lambda_{\mathrm{m}};q}$ and $\chi_{\mathrm{d}}^{\lambda_{\mathrm{d}};q}$ can separately be adjusted to the DMFT susceptibilities, i.e.

$$\begin{aligned} \sum_q \chi_{\mathrm{m}}^{\lambda_{\mathrm{m}};q} &= \sum_\omega \chi_{\mathrm{m}}^{\mathrm{DMFT};\omega}, \\ \sum_q \chi_{\mathrm{d}}^{\lambda_{\mathrm{d}};q} &= \sum_\omega \chi_{\mathrm{d}}^{\mathrm{DMFT};\omega}. \end{aligned} \tag{3.104}$$

Using Eq. 3.104 ensures that the correct asymptotic of the self-energy is restored and that the Pauli principle ($\langle \hat{n}_\uparrow \hat{n}_\uparrow \rangle = \langle \hat{n}_\uparrow \rangle$) is satisfied. However, Eq. 3.104 also fixes the double-occupation to that of DMFT[38]. Hence, if large corrections to the DMFT double-occupation are expected, a different lambda-correction scheme might be preferable, e.g.

[38] Eq. 3.104 guarantees that the sum over $\chi_{\uparrow\downarrow}$ is the same as in DMFT, which is connected to the double occupation via $\sum_q \chi_{\uparrow\downarrow} = \langle \hat{n}_\uparrow \hat{n}_\downarrow \rangle - \langle \hat{n}_\uparrow \rangle \langle \hat{n}_\downarrow \rangle$.

Die approbierte gedruckte Originalversion dieser Dissertation ist an der TU Wien Bibliothek verfügbar.
The approved original version of this doctoral thesis is available in print at TU Wien Bibliothek.
TU Bibliothek Your knowledge hub WIEN

that of Ref. [129][39].

For the single-band case, only Eq. 3.102 and a single parameter (λ_m) are required to suppress the (mean-field) antiferromagnetic order in DMFT and satisfy MWT [135], while still retaining a finite $T_\mathrm{Néel}^{\mathrm{D\Gamma A}}$ in three dimensions [140][40].

One should note that λ_m alone is not enough to guarantee that both the sum rule for $\chi_{\uparrow\uparrow}$ (Eq. 3.94) and the correct asymptotic of the self-energy (Eq. 3.93) are satisfied. However, in practice adjusting only λ_m (Eq. 3.94) or both λ_m and λ_d (Eq. 3.94 + Eq. 3.93) yields similar results [126], at least for the systems studied so far where charge fluctuations play a secondary role.

To understand how the DMFT solution from Box 7 changes if non-local correlations are taken into account we show and discuss DΓA results for a similar set of parameters below. For the results presented, we only adjust λ_m.

Box 8: DΓA spectrum

Below we show the spectral function of a single-band Hubbard model as calculated with DΓA using the lambda correction in the magnetic channel λ_m. Here we use the same tight-binding parameters that will also be used in the next chapter concerning the pseudogap and cuprates. Those tight-binding parameters are $t = 0.5\,\mathrm{eV}$, $t' = -0.2\,t$, $t'' = 0.1\,t$ and $U = 8t$ was used for the Hubbard interaction.
Fig. 3.17 shows the k-resolved spectral function along a high-symmetry path in the Brillouin zone. Special momentum points are $\Gamma = (0,0,0)$, $\mathrm{X} = (\pi,0,0)$ and $\mathrm{M} = (\pi,\pi,0)$. At first glance, it looks quite similar to the DMFT spectrum in Fig. 3.16[a]. Closer inspection around the Fermi surface (see Fig. 3.18), however, reveals the presence of a gap around the X point and a suppression of the spectral weight at the Fermi surface. This k-dependent gap is coined pseudogap, whose origin here is due to a k-dependent self-energy as shown in Fig. 3.18(c).
We will discuss the pseudogap and possible underlying mechanisms in the Hubbard model more detailed in Section 4.2.

[39] The scheme of Ref. [129] guarantees the consistency of the potential energy between the one-particle and two-particle level. As a trade-off, the self-energy does not display the correct asymptotic behavior.
[40] $T_\mathrm{Néel}^{\mathrm{D\Gamma A}}$ is defined as the temperature where Eq. 3.102 Eq. 3.100 cannot be satisfied simultaneously.

Die approbierte gedruckte Originalversion dieser Dissertation ist an der TU Wien Bibliothek verfügbar.
The approved original version of this doctoral thesis is available in print at TU Wien Bibliothek.
TU Bibliothek Your knowledge hub WIEN

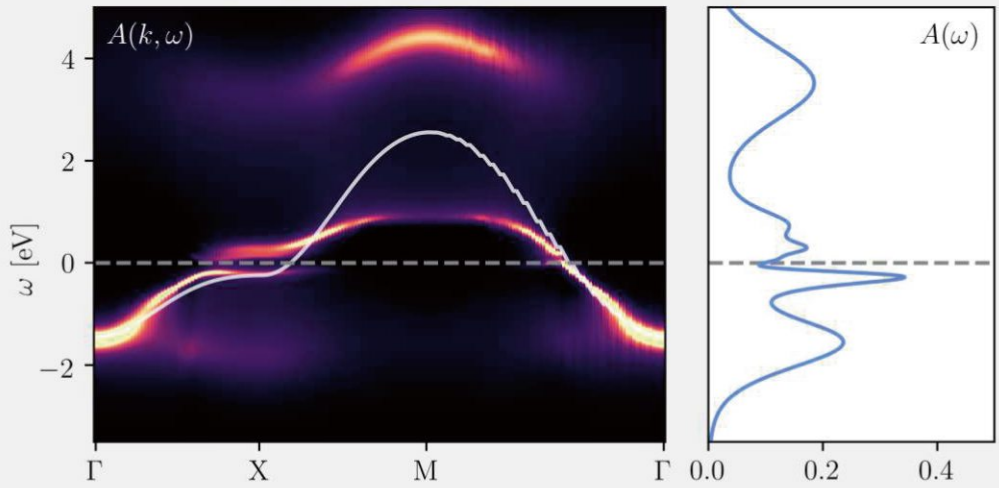

Figure 3.17: DΓA spectral function for tight-binding parameters relevant to cuprates. Left: k-resolved spectral function (colormap) and Wannier band (white line). Right: k-integrated spectral function. Calculations were performed at 290 K and the band-filling was set to $n = 0.90$. Tight-binding parameters are $t = 0.5$ eV, $t' = -0.2t$, $t'' = 0.1t$ and $U = 8t$ was used for the Hubbard interaction.

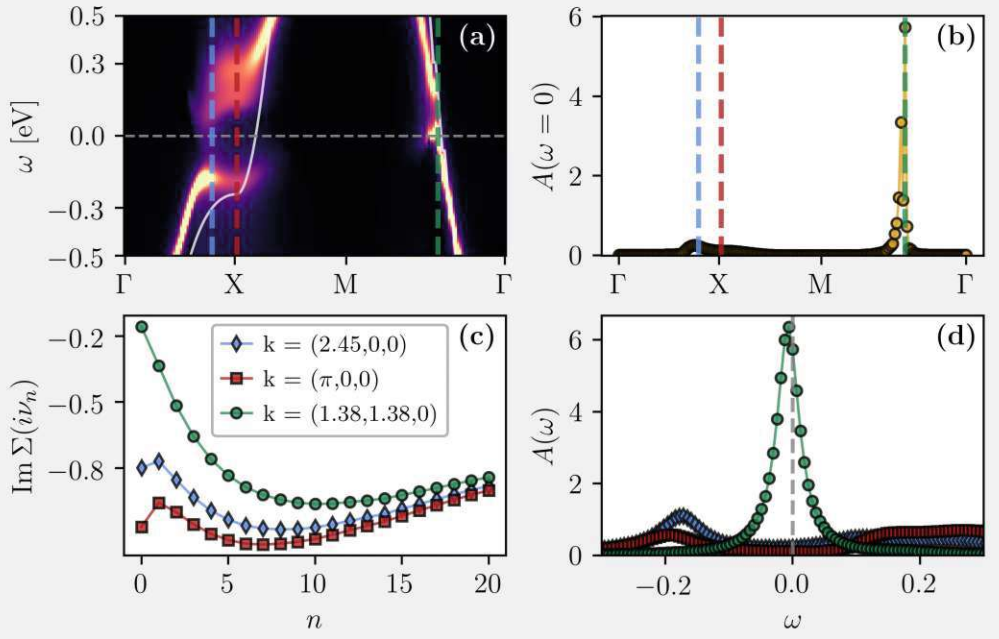

Figure 3.18: **(a)**: zoom-in around the Fermi surface of the k-resolved spectral function (colormap) and Wannier band (white line). **(b)**: spectral function at the Fermi energy ($\omega = 0$). **(c)**: imaginary part of the Matsubara self-energy and **(d)** spectral function $A(\omega, k_i)$ at three distinct k_i points, marked by the dashed lines in (a) and (b). Parameters are the same as in Fig. 3.17.

[a] While the results here are at slightly different parameters, the DMFT spectrum is quite similar for both parameter sets.

Die approbierte gedruckte Originalversion dieser Dissertation ist an der TU Wien Bibliothek verfügbar.
The approved original version of this doctoral thesis is available in print at TU Wien Bibliothek.

3.9 Linearized Eliashberg equation

By now we have developed and discussed all the tools necessary to obtain both the one-particle propagators and the scattering vertices for our effective model Hamiltonians. In order to study superconductivity in the normal state, we use what is called the *linearized Eliashberg equation* [12]. Let us assume SU(2) spin-symmetry and start by considering the BSE-like equation for the susceptibility in the singlet and triplet channel,

$$\chi^{\mathrm{s/t}}_{1234} = \chi^{\mathrm{s/t}}_{0;1234} - \frac{1}{2}\sum_{5678} \chi^{\mathrm{s/t}}_{0;1735}\Gamma^{\mathrm{s/t}}_{\mathrm{pp};5678}\left[\chi^{\mathrm{s/t}}_{8264} + \chi^{\mathrm{s/t}}_{0;8264}\right], \tag{3.105}$$

where the bubble in the singlet/triplet channel is defined as: $\chi^{\mathrm{s/t}}_0 = \chi_{0;\uparrow\downarrow} \mp \chi_{0;\overline{\uparrow\downarrow}} = \mp\chi_{0;\overline{\uparrow\downarrow}} \equiv \mp\chi_0$. A transition to a singlet/triplet superconducting state occurs when the respective susceptibility in Eq. 3.105 diverges, which corresponds to the largest eigenvalue of $-\frac{1}{2}\chi^{\mathrm{s/t}}_0\Gamma^{\mathrm{s/t}}_{\mathrm{pp}}$ becoming unity. We call this eigenvalue problem the linearized Eliashberg equation and it reads as follows,

$$\lambda_{\mathrm{s/t}}\Delta^{\mathrm{s/t}}_{12} = \pm\frac{1}{2}\sum_{3456}\Gamma^{\mathrm{s/t}}_{\mathrm{pp};1324}G^{(1)}_{45}G^{(1)}_{36}\Delta^{\mathrm{s/t}}_{56}, \tag{3.106}$$

where λ is the eigenvalue. The eigenfunction Δ is usually called gap function, as it corresponds to the symmetry of the superconducting gap. Loosely speaking we can view the Green's function appearing in Eq. 3.106 as the Fermions which will form the Cooper pairs and Γ_{pp} as the pairing interaction. Eq. 3.106 is also expressed in Feynman diagrams in pp notation and for $q = 0$ in Fig. 3.19. Finite q correspond to pair-density waves [141], which will not be discussed here.

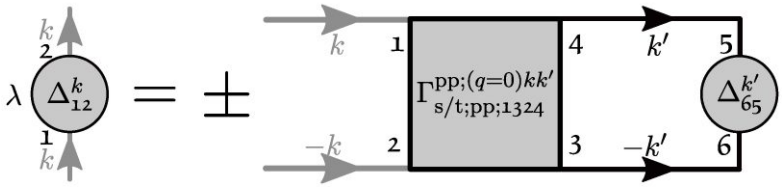

Figure 3.19: Feynman diagrammatic depiction of Eq. 3.106 in the pp notation and with $q = 0$.

λ-DΓA and Eliashberg — The pairing vertex Γ_{pp} can directly be extracted from the full vertex function via the relation in Eq. 3.44. While this is, in principle, straight forward if the vertex is known, complications arise in the λ-corrected DΓA routine. Namely, λ-DΓA uses the SDE in terms of λ-corrected susceptibilities $\chi^{\mathrm{phys}}_{\mathrm{d/m}}$[41], which are defined in the d/m channel and not the s/t channel. As a consequence, we need (i) $F_{\mathrm{d/m}}$ in terms of $\chi^{\mathrm{phys}}_{\mathrm{d/m}}$ and (ii) $F_{\mathrm{s/t}}$ in terms of $F_{\mathrm{d/m}}$. The latter is rather straightforward and written down below in Eq. 3.107.

[41] If no momentum/frequency arguments are present, we use the superscript "phys" to distinguish physical susceptibilities from generalized ones.

Die approbierte gedruckte Originalversion dieser Dissertation ist an der TU Wien Bibliothek verfügbar.
The approved original version of this doctoral thesis is available in print at TU Wien Bibliothek.
TU Bibliothek Your knowledge hub WIEN

$$\begin{aligned} F_\mathrm{s} &= \frac{1}{2}F_\mathrm{d} - \frac{3}{2}F_\mathrm{m}, \\ F_\mathrm{t} &= \frac{1}{2}F_\mathrm{d} + \frac{1}{2}F_\mathrm{m}. \end{aligned} \tag{3.107}$$

Expressing the vertex function in terms of the λ-corrected susceptibilities is more cumbersome and the derivation for the single band case has been carried out in the supplementary information of [12]. Here, we merely reproduce the result for completeness:

$$F_\mathrm{d/m}^{q\nu\nu'} = \left[\chi_0^{q\nu\nu}\right]^{-1}\left[\delta_{\nu\nu'} - \chi_\mathrm{d/m}^{*;\nu\nu'}\left[\chi_0^{q\nu'\nu'}\right]^{-1}\right] + U_\mathrm{d/m}(1 - U_\mathrm{d/m}\chi_\mathrm{d/m}^q)\gamma_\mathrm{d/m}^{q\nu}\gamma_\mathrm{d/m}^{q\nu'}, \tag{3.108}$$

where $U_\mathrm{d} = +U$ and $U_\mathrm{m} = -U$.

Die approbierte gedruckte Originalversion dieser Dissertation ist an der TU Wien Bibliothek verfügbar.
The approved original version of this doctoral thesis is available in print at TU Wien Bibliothek.
TU Bibliothek Your knowledge hub WIEN

Die approbierte gedruckte Originalversion dieser Dissertation ist an der TU Wien Bibliothek verfügbar.
The approved original version of this doctoral thesis is available in print at TU Wien Bibliothek.

Chapter 4

Cuprates

The most exciting phrase to hear in science, the one that heralds new discoveries, is not 'Eureka!' but 'That's funny...'

— I. Asimov

In this chapter, the properties of copper-oxide superconductors (cuprates) are investigated. After a short introduction to the history of cuprates, we review their phase diagram in Section 4.1. Following this, we focus on the pseudogap (PG), characterized by a loss of spectral weight at the Fermi energy and the display of disconnected "Fermi arcs". Section 4.2 extends the work of Ref. [139], where we discuss the PG in the context of the Hubbard model. Specifically, we investigate the influence of a complex-valued spin-fermion vertex on the self-energy and discuss how this will favor the formation of the PG. In Section 4.2, we use the dynamical vertex approximation (DΓA) to perform a temperature-doping scan of the PG region in the single-band Hubbard model. A violation of Luttinger's theorem is found, which we connect to the momentum-selective insulating behavior in the PG. Furthermore, we observe that the PG never closes in momentum space at sufficiently low temperatures. Nevertheless, the nodal gap is above the Fermi energy (similar to Ref. [142]). Thus, the metallic behavior and Fermi arcs are retained. The last Section 4.4 presents a DFT+DMFT study (Ref. [143]) on a more peculiar cuprate: Ba_2CuO_4. Experiments find superconductivity in this compound at unusually large doping, which we connect to the formation of a layered structure. Charge transfer between the layers recovers a doping of the Cu-O layers similar to those of other cuprates.

History of cuprates — Cuprate superconductors are arguably the most intensely studied class of high-temperature superconductors and their transition temperatures can exceed $100\,K$ [144]. The discovery of their superconducting properties dates back to 1986 when G. Bednorz and K. Müller [11] discovered the first unconventional high-temperature superconductor $Ba_xLa_{5-x}Cu_5O_{5(3-y)}$. Prior to that discovery, the common consensus was that superconductors are described by BCS theory [2] with phonons acting as "pairing glue". A slightly inaccurate, though illustrative, picture is that of two electrons moving through the positively charged lattice. The first electron slightly deforms the lattice due to its negative charge, thus creating a positive trail, which, in turn, attracts the second electron. As a consequence, the electrons feel an effective attractive interaction and form cooper pairs if the temperature is low enough. However, due to limitations of the electron-phonon coupling strength, transition temperatures $T_c > 30\,\mathrm{K}$ were believed to be impossible[1] [7, 8]. Precisely this supposed upper limit of the critical temperature is why the discovery of the cuprates, clearly exceeding said limit, marked a new era for superconductivity and the Nobel prize in physics was awarded to G. Bednorz

[1] One should add that for this limit ambient pressure was considered. Recently superconductivity at temperatures $T > 200\,\mathrm{K}$ was reported in hydride compounds [145], albeit under extraordinary pressure of ∼200 GPa.

Die approbierte gedruckte Originalversion dieser Dissertation ist an der TU Wien Bibliothek verfügbar.
The approved original version of this doctoral thesis is available in print at TU Wien Bibliothek.
TU Bibliothek Your knowledge hub WIEN

and K. Müller only one year after their seminal discovery.

Since then the quest for understanding superconductivity in cuprates has been one of the defining challenges in solid-state physics over the last decades. Despite a tremendous effort, both experimentally, as well as theoretically, no generally accepted consensus regarding several key questions, including the nature of the "pairing glue", has been reached. Due to the difficulty of understanding the superconducting state itself, one paradigm has been that understanding the dominant types of fluctuations in the normal state (i.e. the state above the superconducting transition temperature) will lead to the answer of how superconductivity emerges from it. However, it turned out that this "normal" state was anything but normal, displaying a rich variety of competing and possibly intertwined orders [3].

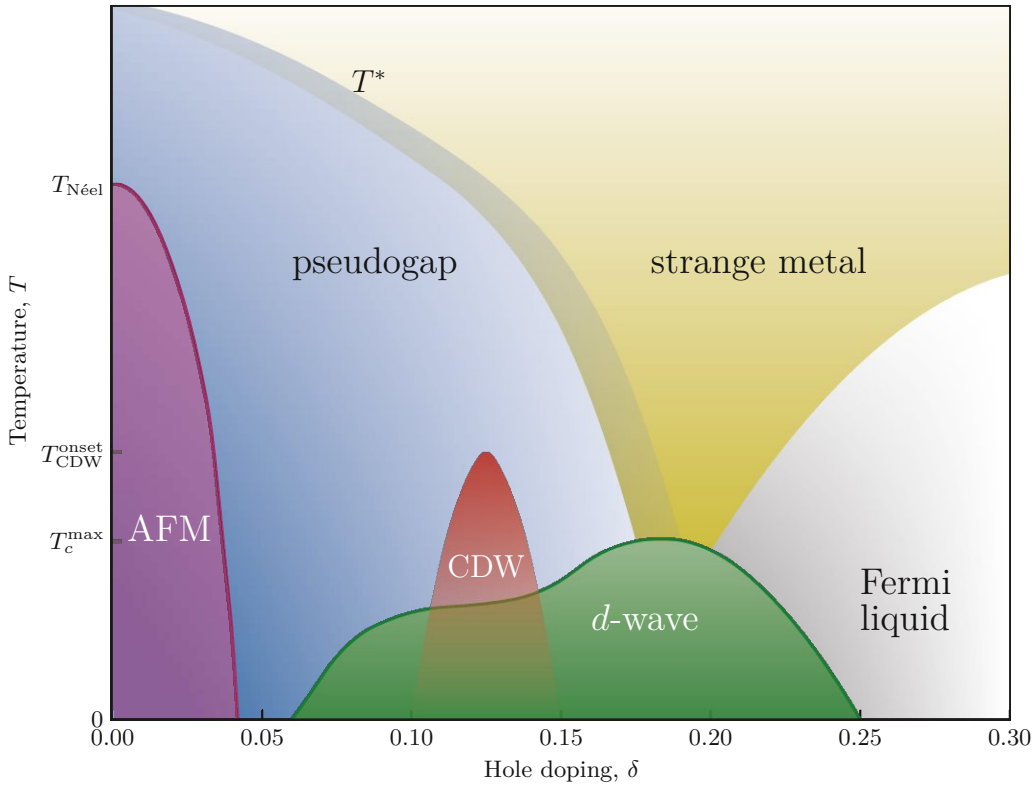

Figure 4.1: Schematic temperature versus hole-doping phase diagram of generic features in cuprate superconductors. At high temperatures, a doping-dependent transition from AFM (purple) into the PG (blue) and finally the strange-metal regime (yellow) can be seen. At lower temperatures, charge-density-wave (CDW) fluctuations (red) and d-wave superconductivity (green) emerge. For large doping, Fermi-liquid properties are recovered. T_c^{max} marks the highest critical temperature, $T_{\text{CDW}}^{\text{onset}}$ the onset temperature for CDW fluctuations, $T_{\text{Néel}}$ the Néel temperature and T^* the temperature where signatures of the pseudogap appear. Corresponding values for $YBa_2Cu_3O_y$ are according to Fig. 3 of Ref. [146]: $T_c^{\text{max}} \simeq 100\,\text{K}$, $T_{\text{Néel}} \simeq 400\,\text{K}$, $T_{\text{CDW}}^{\text{onset}} \simeq 150\,\text{K}$ and $T^*(\delta = 0.1) \simeq 250\,\text{K}$. The precise values are compound dependent and we merely present them to give context.

Die approbierte gedruckte Originalversion dieser Dissertation ist an der TU Wien Bibliothek verfügbar.
The approved original version of this doctoral thesis is available in print at TU Wien Bibliothek.
TU Bibliothek Your knowledge hub WIEN

4.1 Phase diagram of cuprates

In the following, we provide a short summary of, in our view, important aspects of the phase diagram in cuprates, which we also display in Fig. 4.1. For a more in-depth discussion, we refer the reader to Ref. [3], which is also the basis of the experimental part discussed here. For a recent discussion of the Hubbard model that also includes parameters relevant to cuprates, we refer the reader to Ref. [147].

Parent compound — Let us consider $La_{2-x}Sr_xCuO_4$ as a simple example for cuprates. The parent compound, i.e. $x = 0$, hosts a Cu-$3d^9$ configuration with one electron in the e_g shell, which goes into the $3d_{x^2-y^2}$ orbital due to a tetragonal elongation of the oxygen octahedra surrounding the Cu atom [3]. One would thus naively expect cuprates to be metals, however, they are insulating in practice [148, 149]. The Coulomb interaction of the more localized Cu $3d$ shell is quite large[2], thus resulting in the opening of a Mott gap in the Cu-$3d_{x^2-y^2}$ orbital, which would be the one crossing the Fermi surface in non-spin-polarized DFT calculations, see for example Box 3 on the related cuprate $CaCuO_2$. Contrary to Mott insulators, where no states appear in the Mott gap, in cuprates states, derived from the O-p shell, lie within the Mott gap of the Cu-$3d_{x^2-y^2}$ orbital [65, 151]. Consequently, the spectral gap (of about 2 eV [3]) is between the upper Hubbard band of the Cu-$3d_{x^2-y^2}$ and the O-p_x and O-p_y states. Thus excitations above the gap involve electron transfer between the O and Cu sites, giving rise to the name "charge-transfer insulator". It should also be noted that this insulating state appears without any broken symmetry and is not related to the Néel order, which only appears at lower temperatures [152, 153]. This antiferromagnetic order (AFM) can easily be understood in the context of a single-band Hubbard model (Eq. 2.28) derived from the Cu-$3d_{x^2-y^2}$ orbital. At large interaction strength, the double occupation of a single site is suppressed as it "costs" an energy of U. Sites of opposite spin allow for virtual hopping processes, which are forbidden for same-spin electrons due to the Pauli principle. At sufficiently low temperatures the energy gain from this process dominates the entropy difference between the paramagnetic and the antiferromagnetic status, thus setting the Néel temperature $T_{\text{Néel}}$. This Néel order has already been confirmed theoretically in the Hubbard model by unbiased Monte-Carlo approaches, see e.g. [154]. Hence both the charge-transfer insulator and the antiferromagnetic state are well understood in the parent compound. The same cannot be said, however, once the system becomes doped.

Underdoped cuprates — Hole-doping is often achieved by changing the chemical composition of the insulating layers between the CuO_2 planes, e.g. substituting some of the trivalent La^{3+} with divalent Sr^{2+} in $La_{2-x}Sr_xCuO_4$[3]. To compensate for the lost valency, electrons will be removed from the CuO_2 planes, effectively creating a Cu-$3d^{9-\delta}$ configuration, where δ is the concentration of extra holes in the CuO_2 sheets. At higher temperatures and once the system is sufficiently doped, both antiferromagnetic and charge-transfer gap will close and a metallic behavior is recovered [3, 155]. However, the state which emerges from AFM is not a simple metal, but a rather peculiar state coined "pseudogap" (PG)[156]. While signatures of the PG are seen in many probes

[2] Constrained random phase approximation (cRPA) calculations yield $U \simeq 2.5 - 3.6$ eV [150].
[3] See Ref. [5] for the superconducting dome of $La_{2-x}Sr_xCuO_4$.

Die approbierte gedruckte Originalversion dieser Dissertation ist an der TU Wien Bibliothek verfügbar.
The approved original version of this doctoral thesis is available in print at TU Wien Bibliothek.
TU Bibliothek Your knowledge hub WIEN

like transport, both in plane, see e.g. [157], and out of plane, see e.g. [158], nuclear magnetic resonance (NMR), see e.g. [159], and others, its hallmark feature is arguable the appearance of Fermi arcs as observed in angular-resolved photoemission spectroscopy (ARPES) experiments, see e.g. [14–16]. While many explanations of the PG have been put forth, no consensus has yet been reached in the community. We will discuss the PG and how it appears in the single band Hubbard model in Section 4.2.

When looking at lower temperatures instead, one can observe what cuprates are so famous for: unconventional d-wave superconductivity [160]. Similar to the PG, the microscopic mechanism is controversial and no generally accepted theory exists. Calculations based on the Hubbard model suggest AFM spin-fluctuations [12, 161–165], but also loop-currents [166], resonating valence bonds [167], a possible connection to the vicinity of a quantum critical point [166, 168, 169] and many other mechanisms have been suggested as possible origins of superconductivity. Moreover, recent calculations based on three-band Emery-type models [65] underline the importance of the O-p bands and the charge-transfer gap.

While this work focuses on the PG and d-wave superconductivity, also charge order has been observed in underdoped cuprates [170, 171]. This order appears typically close to 1/8 doping and is often accompanied by a "dip" in, or flattening of, the superconducting dome, see Fig. 4.1. It can also be induced by applying a magnetic field [172] and is generally understood to be competing with superconductivity [173].

Optimally doped and overdoped cuprates — Superconductivity extends up to roughly 25% doping [5, 157, 174–176], with details of course depending on the compound. At large dopings, a metallic state with Fermi liquid properties and a single continuous Fermi surface sheet emerges, see e.g. [177]. Above the superconducting dome, the pseudogap will transition into what is called the *strange metal* regime, see e.g. [178], and is characterized by a resistivity scaling linearly with temperature. Naively one would expect a T^2 scaling from Fermi liquid theory (FLT) due to the T^2 scaling of the scattering rate in FLT. As for the PG and superconductivity, the microscopic origin is highly debated and controversial. Proposals to explain this phenomenon include, among others, Planckian limits for the scattering rate [179], or argue that Fermi liquid scaling is obeyed, but rather charge carriers are lost [180].

As briefly discussed above, the cuprate phase diagram hosts a plethora of interesting phenomena, most of which remain controversial on a microscopic level. Below we will discuss the pseudogap in the context of the single-band Hubbard model. Superconductivity will later be studied for nickelates, a related class of materials, in chapter 5.

Die approbierte gedruckte Originalversion dieser Dissertation ist an der TU Wien Bibliothek verfügbar.
The approved original version of this doctoral thesis is available in print at TU Wien Bibliothek.
TU Bibliothek Your knowledge hub WIEN

4.2 Pseudogap

*Parts of the following section, marked by a vertical bar, have already been published in Commun Phys **5**, 336 (2022). Some parts include minor changes from the original manuscript to improve the brevity. To keep a consistent notation within this thesis we replaced the symbol for the spin-fermion vertex (Γ in the original paper) with γ, as Γ is in this thesis reserved for the two-particle irreducible vertices.*

Among the unsolved "mysteries" in the cuprates is the so-called pseudogap (PG), which is characterized by a loss of spectral weight on the Fermi surface and famously displays disconnected Fermi arcs in angular resolved photoemission spectroscopy (ARPES) [14]. However, the pseudogap is also visible in transport measurements where a kink in the resistivity is observed upon crossing a characteristic temperature scale T^* [157] and was even originally observed in nuclear magnetic resonance experiments as a kink in the Knight shift [159]. Despite the numerous experimental techniques that observe characteristic features upon entering the pseudogap region, its nature, origin and whether or not it corresponds to a broken symmetry is still debated. In cuprates, the pseudogap exists near (at least) three distinct phases [3] (i) antiferromagnetism towards lower dopings (ii) superconductivity at somewhat higher dopings and low temperatures and (iii) charge-density-wave order in the vicinity of 1/8 doping. Following this proximity to an ordered phase the PG has been interpreted as the precursor of any of these phases [181]. To understand the origin of the pseudogap from a microscopic perspective, we study the arguably simplest model for strongly correlated electrons on a (square) lattice: the Hubbard model 2.28. [4] The discussion below contains three key elements. First, we will discuss a simple semi-analytical ansatz for the contribution of spin-fluctuation to the self-energy. Following this, we will show that, within this ansatz, assuming the spin-fermion coupling vertex γ to be real-valued does not lead to the creation of Fermi arcs at short correlation lengths. However, once an imaginary part is introduced, Fermi arcs as measured in ARPES can be observed. And finally, we will present numerical results of the Hubbard model, where we find a pseudogap originating from spin fluctuations as discussed. Therewith, we not only show numerically that spin-fluctuations are responsible for the pseudogap formation in the hole-doped Hubbard model at the parameters considered, but also identify the imaginary part of γ as the crucial ingredient to the spin-fluctuation model.

The discussion below starts from the Schwinger-Dyson equation in its Hedin form for in the SU(2) spin-symmetric and single-band case (Eq. 3.72), which we rewrite here for convenience[5]

$$\Sigma^k = \frac{Un}{2} - \frac{U}{2}\sum_q \left[(1 - U\chi_{\mathrm{d}}^q)\,\gamma_{\mathrm{d}}^{qk} - (1 + U\chi_{\mathrm{m}}^q)\gamma_{\mathrm{m}}^{qk}\right] G^{(1);k-q}. \tag{4.1}$$

[4] It should be noted that the applicability of a one-band Hubbard model for cuprates is also debated in the community. Here we do not discuss the minimal model of cuprates but describe how the pseudogap forms in a Hubbard model with parameters relevant for cuprates.

[5] We refer the reader to Section 3.6 for an in-depth discussion.

Die approbierte gedruckte Originalversion dieser Dissertation ist an der TU Wien Bibliothek verfügbar.
The approved original version of this doctoral thesis is available in print at TU Wien Bibliothek.

Spin-fermion self-energy — To illustrate the mechanism in the spirit of fluctuation diagnostics [182, 183], we consider the following ansatz for the contribution of spin fluctuations with an energy ω and momentum $\mathbf{q}$ to the self-energy, $\Sigma_{\rm sp}(k,q) \propto -G_{k+q}W_q\gamma_{kq}$. Here, $k=(\mathbf{k},\nu), q=(\mathbf{q},\omega)$ are momentum-energy four-vectors, $W_q = -U - \frac{1}{2}U\chi_q U$ denotes the (real-valued) screened interaction, χ_q the spin susceptibility, ν (ω) denote fermionic (bosonic) Matsubara frequencies. To obtain the full self-energy $\Sigma_{\rm sp}(k)$ due to spin fluctuations one still has to sum over momenta $\mathbf{q}$ and frequencies ω. In addition, the full self-energy contains also a momentum-independent contribution $\Sigma^{\rm loc}(\nu)$ due to strong local correlations, i.e., $\Sigma(k) = \Sigma^{\rm loc}(\nu) + \Sigma_{\rm sp}(k)$. In the following we consider only the dominant static $q_0 = (\mathbf{q}, \omega = 0)$ contribution to the imaginary part of the self-energy,

$$\Sigma''_{\rm sp}(k,q_0) \propto -[G''_{k+q_0}\gamma'_{kq_0} + G'_{k+q_0}\gamma''_{kq_0}]W_{q_0}. \tag{4.2}$$

As we will discover later it is crucial that γ has a real (γ') and an imaginary part (γ''). Previously, in what we call "weak coupling approaches", γ was either set to be 1, or has negligible imaginary part. Let us assume a simple semi-analytical model for Eq. 4.2 to obtain an intuition regarding the effect of spin-fluctuations on the self-energy.

Semi-analytical model self-energy — To describe this interplay in a minimal model we define the ansatz (spin-fluctuations in the static, $\omega = 0$ limit)

$$\Sigma_{\rm sp}(\mathbf{k}, i\eta) \propto \gamma_c \frac{T}{N}\sum_{\mathbf{q}} \frac{G^0(\mathbf{k}+\mathbf{q}, i\eta)}{(\mathbf{Q}-\mathbf{q})^2 + \xi^{-2}}, \tag{4.3}$$

where G^0 is the noninteracting Green's function shown in Fig. 4.5. For simplicity, we use here $\eta = \pi T$, which does not affect results qualitatively. Further, $\gamma_c = e^{i\kappa}$ is a complex number with phase $0 \geq \kappa \geq -\pi/2$ and of unit length, $T/t = 1/5$, and N the number of lattice sites. We restrict the discussion to $\omega = 0$ as before, and assume the Ornstein-Zernike form for χ_q peaked around $\mathbf{Q} = (\pi, \pi)$ with correlation length ξ. For simplicity we consider only $\gamma_c \equiv \gamma_c(i\eta)$. Here, we rotate $\gamma_c = e^{i\kappa}$ in the complex plane by an angle κ away from $\gamma_c = 1$ ($\kappa = 0$) which corresponds to weak coupling [184].

Next, we show how the Fermi surface looks if the weak coupling approach for the ansatz of the self-energy is chosen. Here weak coupling corresponds to $\gamma = 1$ and a large correlation length $\xi = 100$. Let us at this point note that by assuming $\omega = 0$ we are not considering effects of the van Hove singularity (VHS), if it is below or above the Fermi surface. Since the VHS is located near the antinode, it has been surmised to be responsible, or at least connected to the pseudogap formation, see e.g. [185]. While our model ansatz does not rule out the influence of the VHS, it provides an alternative mechanism. The (relative) importance of those two, or any other possible mechanisms, has to be checked with (numerical) calculations of the Hubbard model. In Fig. 4.8, we present numerical results on the Hubbard model, using the boson-exchange parquet solver (BEPS)[6] and we find that the mechanism described here cannot be neglected. One can clearly see in Fig. 4.2(e) that pseudogap-like behaviour, here defined by a vanishing

[6] We will not cover the theoretical background of BEPS in this thesis and refer the reader to Ref.[186] instead.

Die approbierte gedruckte Originalversion dieser Dissertation ist an der TU Wien Bibliothek verfügbar.
The approved original version of this doctoral thesis is available in print at TU Wien Bibliothek.
TU Bibliothek Your knowledge hub WIEN

spectral weight at locations where $\mathrm{Re}(1/G) = 0$, only appears at hot spots, i.e. points where the (imaginary part of the) self-energy (b) intersects the non-interacting Fermi surface (a)[7]. In (e), only the imaginary part of the self-energy, i.e. the scattering rate of the model self-energy in Eq. 4.3, was used to calculate the spectral function $A_{\mathrm{Im}\,\Sigma}$. While $\mathrm{Im}\,\Sigma$ introduces a finite lifetime, visible at the hot spots when comparing the upper left quadrant of (a) to that of (e), $\mathrm{Re}\,\Sigma$ renormalizes the band dispersion. Its effect is depicted in (g) and results in an additional warping of the Fermi surface. This seems to be overestimated in this simple approach, but a flattening of the Fermi surface[8] due to $\mathrm{Re}\,\Sigma$ has been observed in advanced numerical techniques [184, 187].

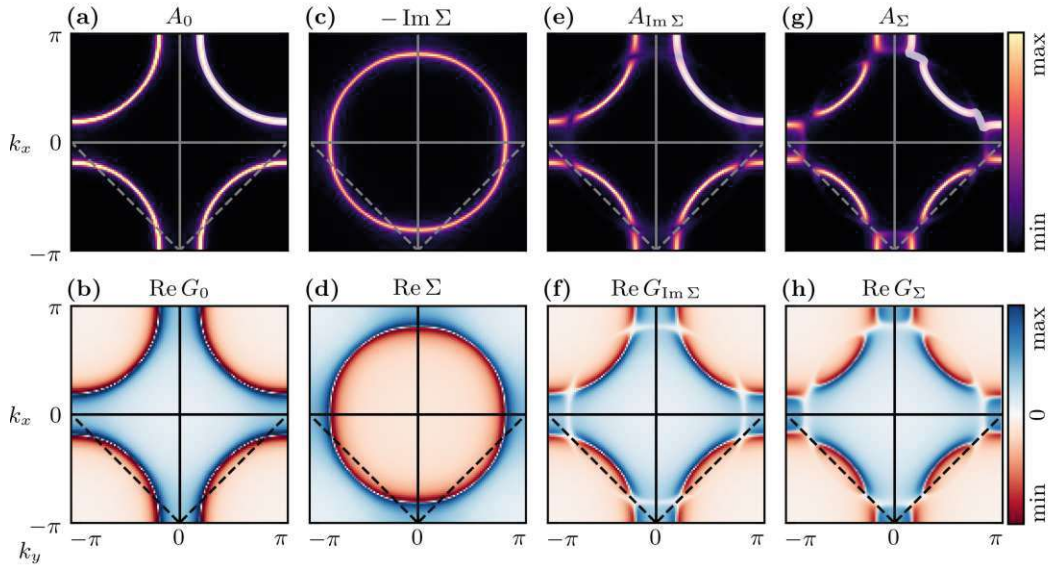

Figure 4.2: "Weak-coupling" pseudogap for Eq. 4.2. Top shows the spectral function (imaginary part) and bottom the real part. **(a,b)** Fermi surface of the non-interacting Green's function. **(c,d)** Spin-model self-energy. **(e,f)** Fermi surface when only $\mathrm{Im}\,\Sigma$ is taken into account. **(g,h)** Fermi surface using the full self-energy. White line marks where $\mathrm{Re}(1/G) = 0$. Dashed lines mark the antiferromagnetic zone boundary (AZB) in the lower half. Colorbar normalisation is the same for all A and $\mathrm{Re}\,G$, but different for the self-energy. As tight-binding parameters we use $t = 1$; $t' = -0.2\,t$; $t'' = 0.1\,t$ and fix the filling to $n = 0.95$, which corresponds to the underdoped region. The spin-fermion vertex is set to one $\gamma = 1$ and we pick a large correlation length by choosing $\xi = 100$.

As demonstrated above the conventional, weak-coupling picture opens a spectral gap near hot spots [133, 184, 188], which is observed in electron-doped cuprates [189, 190].

For hole-doped cuprates this is not the case, instead, the gap opens near the antinodes [191], and a reconstruction of the FS [184, 192–194] is evidenced by quantum oscillations [195]. Other features not explained by weak-coupling spin fluctuations are

[7] For the $x - y$ symmetric square lattice Hubbard model and commensurate ($Q = (\pi, \pi, 0)$) spin-fluctuations this also corresponds to the intersection of the antiferromagnetic zone boundary with the spectral function.

[8] Which essentially corresponds to a renormalization of t' and t''.

Die approbierte gedruckte Originalversion dieser Dissertation ist an der TU Wien Bibliothek verfügbar.
The approved original version of this doctoral thesis is available in print at TU Wien Bibliothek.
TU Bibliothek Your knowledge hub WIEN

the good Fermi liquid properties of underdoped cuprates [180] and indications of broken time-reversal symmetry [196–198]. Alternative origins of the pseudogap [3, 199–203] are hence under consideration.

However, as already alluded to in the beginning of the section, we will now show how a simple adjustment to the "weak-coupling" spin-fluctuation mechanism completely changes the picture. Specifically, we will now consider a finite imaginary part of the spin-fermion vertex γ''.

Imaginary part of the spin-fermion vertex — Let us start by considering the conditions for a sizeable γ'' in the simpler case of the Anderson impurity model (AIM). We denote its local spin-fermion vertex as $\gamma_{\mathrm{loc}}(\nu,\omega)$. The leading vertex correction due to local spin exchange has the imaginary part [204, 205],

$$\gamma''_{\mathrm{loc}}(\nu,\omega=0) \approx -\frac{TU^2}{2}\chi^{\mathrm{sp}}_{\omega=0}g'(\nu)g''(\nu), \tag{4.4}$$

where χ^{sp} is the spin susceptibility, T the temperature, g' and g'' denote real and imaginary part of the impurity Green's function. Eq. 4.4 can be considered as a local one-loop correction to the spin-fermion vertex. Let us emphasize that this expression only illustrates how the imaginary part of the vertex arises. The dual fermion numerical results presented later do not rely on this approximation, nor on the restriction to the zeroth bosonic frequency.

Sufficient for a large $\gamma''_{\mathrm{loc}}(\imath\eta,\omega=0)$ [with small positive η] are the following conditions: (i) strong particle-hole asymmetry (g' vanishes at symmetry), (ii) large enough spectral weight $-g''(\imath\eta)/\pi$, (iii) large $\chi^{\mathrm{sp}}_{\omega=0}$ (preformed local moment). All of these conditions are satisfied by the DMFT solution of the Hubbard model in the relevant parameter regime for hole-doped cuprates. In general the vertex γ in the Hubbard model depends on momenta, however, as our numerical calculations below show, the here outlined conditions remain relevant for a large γ''.

Die approbierte gedruckte Originalversion dieser Dissertation ist an der TU Wien Bibliothek verfügbar.
The approved original version of this doctoral thesis is available in print at TU Wien Bibliothek.

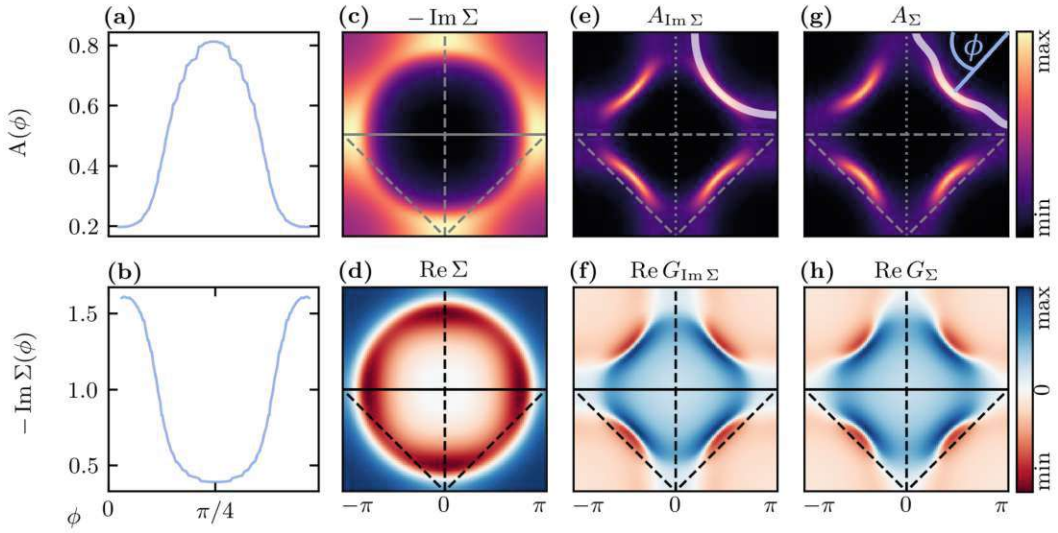

Figure 4.3: "Strong-coupling" pseudogap Eq. 4.2. **(a)/(b)** Spectral function and $-\operatorname{Im}\Sigma$ along the the white line in (g), which is defined by $\operatorname{Re}(1/G) = 0$. For the remaining panels the top shows the spectral function (imaginary part) and bottom the real part. **(c,d)** Spin-model self-energy. **(e,f)** Fermi surface when only $\operatorname{Im}\Sigma$ is taken into account. **(g,h)** Fermi surface using the full self-energy. Colorbar normalisation is the same for all A and $\operatorname{Re} G$, but different for the self-energy. Dashed lines mark the antiferromagnetic zone boundary (AZB) in the lower half. As tight-binding parameters we use $t = 1$; $t' = -0.2\,t$; $t'' = 0.1\,t$ and fix the filling to $n = 0.95$, which corresponds to the underdoped region and is identical to the ones used in Fig. 4.2. The spin-fermion vertex is set to $\gamma = e^{-\pi/4i} = 1 - i$ and we pick a short correlation length by choosing $\xi = 3$.

In Fig. 4.3 we show the "strong-coupling" result of the spin-model self-energy in Eq. 4.3. By strong-coupling we mean here that the spin-fermion vertex acquires a large imaginary part. Furthermore, both experiments on cuprates [206] and our numerical results presented later find that the antiferromagnetic correlation length is only of a few lattice sites. In accordance with these observations we pick for the following discussion $\gamma = 1 - i$ ($\kappa = \pi/4$) and a correlation length of $\xi = 3$[9]. Even though we use the same tight-binding parameters as in Fig. 4.2, we can clearly observe qualitative differences introduced by γ''. Namely, we find that the spectral weight is concentrated primarily inside the antiferromagnetic zone boundary (AZB), while on the outside the spectral weight is suppressed, thus showing Fermi arcs. To depict this more clearly, we also plot the spectral function A and $-\operatorname{Im}\Sigma$ parameterized along the line defined by $\operatorname{Re}(1/G) = 0$ in (a) and (b), respectively. $\operatorname{Re}(1/G) = 0$ is also displayed as a white line in (g). As we can see from (b), the scattering rate is largest at the Brillouin-zone boundary and not at the hot spots, as was the case for the "weak-coupling" solution.

One should note that hot-spot scattering still exists. Nevertheless, the mechanism for the pseudogap due to γ'' is superimposed with the conventional one based on γ' and the outcome depends qualitatively on the ratio γ''/γ'.

[9] A large imaginary part of γ and short correlations lengths occur for solutions of the Hubbard model at higher interaction values U, while small a imaginary part and long correlation lengths appear at low U. Hence the names strong- and weak-coupling.

Die approbierte gedruckte Originalversion dieser Dissertation ist an der TU Wien Bibliothek verfügbar.
The approved original version of this doctoral thesis is available in print at TU Wien Bibliothek.
TU Bibliothek Your knowledge hub WIEN

Let us now analyze how the self-energy changes as a function κ, the complex phase of γ.

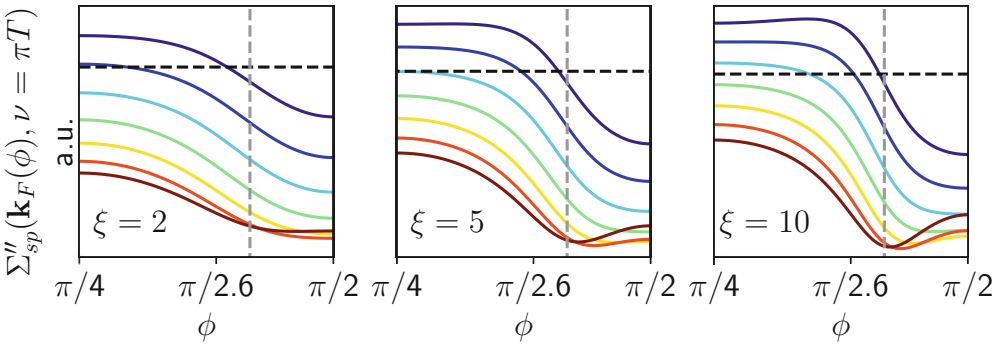

Figure 4.4: Model self-energy Eq. 4.3 on the FS parameterized by the angle ϕ from $\pi/4$ (nodal direction) to $\pi/2$ (antinodal direction) for various $\gamma_c = e^{\imath\kappa}$. The complex phase is turned from $\kappa = 0$ (brown) to $\kappa = -\frac{\pi}{2}$ (dark blue) in steps of $\frac{\pi}{12}$. Panels correspond to the different correlation lengths ξ as indicated. Vertical lines show the hot spot.

Fig. 4.4 shows $\Sigma''_{\text{sp}}(\mathbf{k}_F(\phi), \imath\eta)$ along the FS parameterized by $\phi = \arctan(k_y/k_x)$ from the nodal direction to the antinodal direction, with increasing correlation length. Brown lines show the result for $\kappa = 0$ ($\gamma_c = 1$), which is always negative and for large enough ξ develops a minimum near the hot spot ($\phi_{\text{HS}} \approx 1.31$), as expected. Dark blue lines show the result for $\kappa = -\frac{\pi}{2}$ ($\gamma_c = -\imath$) where real and imaginary part of the weak-coupling self-energy are essentially interchanged. Evidently, for suitable ξ and κ the minimum of Σ''_{sp} lies at $\phi = \frac{\pi}{2}$, i.e., a gap first opens in the antinodal direction instead of the hot spot. At the same time a finite $\gamma''_c = \sin(\kappa) < 0$ can lead to positive values of Σ''_{sp} for angles $\phi < \phi_{\text{HS}}$: clearly, for large γ''_c the ansatz (Eq. 4.3) is meaningful only as a *correction* to a negative $\Sigma^{\text{loc}}(\nu)$, representing local correlations. That is, non-local spin fluctuations *enhance* the lifetime of Fermi arcs. In the supplemental material of Ref. [139] Eq. 4.3 is compared to our numerical results.

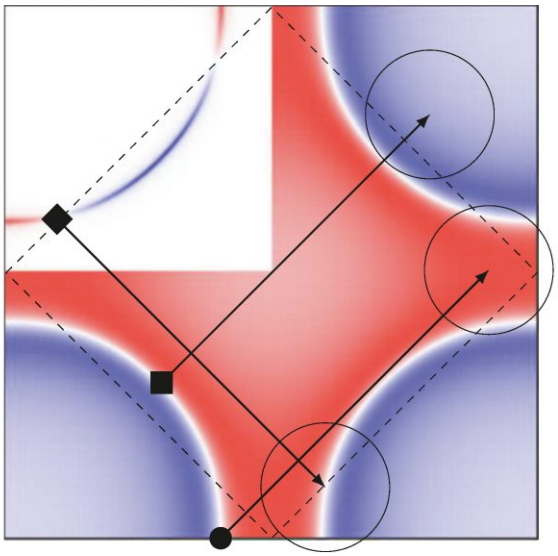

Figure 4.5: Top left quadrant: damping (red) and antidamping (blue) on the FS. Right and bottom quadrants: real part of the noninteracting Green's function. Blue (red) color indicates particle-like (hole-like) states above (below) the Fermi level. Filled symbols: antinode (circle), node (square), hot spot (diamond). Arrows represent the antiferromagnetic wave vector $\mathbf{Q}$. Open circles $\sim 1/\xi$ comprise available target states; red (blue) states are occupied (unoccupied) and promote damping (antidamping). Dashed lines show the AZB [207].

Die approbierte gedruckte Originalversion dieser Dissertation ist an der TU Wien Bibliothek verfügbar.
The approved original version of this doctoral thesis is available in print at TU Wien Bibliothek.
TU Bibliothek Your knowledge hub WIEN

Physical picture—— Here we unravel the physical origin of the discrepancy between the conventional picture of spin fluctuations on the one hand, and both experiments on hole-doped cuprates and numerical investigations of the single-band Hubbard model on the other. In particular, we unveil the strong-coupling spin-fluctuation mechanism responsible for the pseudogap sketched in the top left quadrant of Fig. 4.5: spin fluctuations diminish lifetimes of quasiparticles near the antinodes (red), while they even enhance lifetimes near the nodes (blue). The antiferromagnetic zone boundary (AZB, dashed) marks the crossover between these opposite behaviors. Remarkably, the strong-coupling mechanism has no effect near hot spots. Here only the conventional weak-coupling mechanism for spin scattering [133, 184, 188, 208–210] is active. Its effect is however too small to open a gap due to a short antiferromagnetic correlation length of less than 1 or 2 lattice spacings.

Compared to conventional weak-coupling theory, the effective interaction between spin fluctuations and fermions——the spin-fermion vertex, γ——plays a radically different role. At weak coupling γ is real-valued, which promotes scattering between states 'on shell', i.e., close to the Fermi surface. This constraint is ideally fulfilled for hot spots (e.g., filled diamond in Fig. 4.5), which are connected to other hot spots through the antiferromagnetic wave vector, here $\mathbf{Q} = (\pm\pi, \pm\pi)$ [arrows]. As spin fluctuations extend over a correlation length ξ, the transferred momentum can deviate from $\mathbf{Q}$ in a circle $\sim 1/\xi$.

As displayed in Fig. 4.2 for large ξ this weak-coupling mechanism opens a gap beginning with the hot spots, in evident disagreement with experiments on hole-doped cuprates.

In the past, it was reported [211–213] that for strong coupling, and if particle-hole symmetry is broken [214], γ acquires a large imaginary part. However, neither Refs. [211, 212] nor, to our knowledge, any previous work noted the crucial link between this quantity and the pseudogap at strong coupling. Here, based on calculations for the Hubbard model with high spatial resolution, combined with analytic considerations, we identify the imaginary part of γ as the key to the pseudogap dichotomy.

Remarkably, this quantity effectively lifts the nesting condition for spin scattering, allowing fermions to be scattered into off-shell states. Fig. 4.5 shows that antinodal and nodal (filled square) fermions can be scattered into high-energy states far from the Fermi surface. However, the overall feedback on the self-energy depends on the occupancy of the target states: antinodal (nodal) fermions are predominantly scattered into hole-like (particle-like) states, marked with red (blue) color in Fig. 4.5.

As we showed in Fig. 4.4 this increases (diminishes) the scattering rate at the origin. We refer to this dichotomy as damping (red) and antidamping (blue). Near hot spots these effects cancel and hence only the weak-coupling mechanism, represented by the real part of γ, is active in their vicinity.

Effect on lifetime —— We analyze Eq. 4.2 and put the qualitative considerations regarding Fig. 4.5 on mathematical grounds. The real part of the vertex, γ', universally enhances the magnitude of the imaginary part of the self energy (the scattering

Die approbierte gedruckte Originalversion dieser Dissertation ist an der TU Wien Bibliothek verfügbar.
The approved original version of this doctoral thesis is available in print at TU Wien Bibliothek.
TU Bibliothek Your knowledge hub WIEN

rate) [126, 133, 135, 184, 209]: the corresponding term in Eq. 4.2 is always negative: $-G''\gamma' W < 0$, since $G'' < 0$, $\gamma' \sim 1 > 0$, and $W < 0$.

On the contrary, the sign of $-G'\gamma'' W$ in Eq. 4.2 depends on the target state with momentum $\mathbf{k}+\mathbf{q}$. We find in our calculations that $\gamma''(\mathbf{k}, \nu, \mathbf{q}, \omega = 0)$ is an odd function of ν and in the parameter regime for hole-doped cuprates $\gamma'' < 0$ for Matsubara frequency $\nu > 0$. However, the sign of the real part of the Green's function differs: $G'(\mathbf{k}+\mathbf{q}, i\eta) = [\mu - \varepsilon_{\mathbf{k}+\mathbf{q}} - \Sigma'(\mathbf{k}+\mathbf{q}, i\eta)]/[(\mu - \varepsilon_{\mathbf{k}+\mathbf{q}} - \Sigma'(\mathbf{k}+\mathbf{q}, i\eta))^2 + \Sigma''(\mathbf{k}+\mathbf{q}, i\eta)^2] < 0$ (> 0) for particle-like (hole-like) target states shown in blue (red) color in Fig. 4.5. We set $\nu > 0$, hence

$$-G'_{k+q_0}\gamma''_{kq_0}W_{q_0} \begin{cases} < 0 & \text{if } \mathbf{k}+\mathbf{q} \text{ is hole-like,} \\ > 0 & \text{if } \mathbf{k}+\mathbf{q} \text{ is particle-like.} \end{cases} \tag{4.5}$$

The former enhances the electronic scattering at the Fermi level (damping), the latter *diminishes* it (antidamping). This dichotomy resembles a chemical bonding, where the hybridization with a virtual state at higher (lower) energy reduces (enhances) the energy of the initial state [215]. The difference is that, due to the complex vertex, this now becomes a dichotomy for the state's lifetime (not its energy).

Results and discussion above focused on the semi-analytical model for a spin-fluctuation self-energy in Eq. 4.3. However, we have yet to show whether such spin-fluctuations are truly relevant for the opening of the pseudogap in the Hubbard model. To answer this question we present unbiased numerical results below and use fluctuation diagnostic tools to pin down what is the driving force.

Method and Model — Diagrammatic extensions [216] of dynamical mean-field theory (DMFT) [37] have proven useful to study spin fluctuations in strongly correlated systems. To reduce bias [205] we employ BEPS [186], corresponding to the parquet approximation [99] for dual fermions [217, 218]. Through the boson-exchange formalism [109, 219] we establish a relationship to the spin-fermion model. We apply this machinery to the hole-doped Hubbard model, $H = -\sum_{\langle ij\rangle\sigma} t_{ij} c^\dagger_{i\sigma} c_{j\sigma} + U \sum_i n_{i\uparrow} n_{i\downarrow}$. Here, $c^\dagger_{i\sigma}$ ($c_{i\sigma}$) create (annihilate) an electron with spin σ at site i; $n_\sigma = c^\dagger_\sigma c_\sigma$. The nearest $t = 1$, next-nearest $t' = -0.2t$, and next-next-nearest $t'' = 0.1t$ neighbor hopping parameters, and interaction $U = 8t$ correspond to $Bi_2Sr_{2-x}La_xCuO_6$ [220].

Numerical Results — We apply the parquet solver for dual fermions presented in Ref. [186] and evaluate the self-energy Σ_k and the (dual) spin-fermion vertex γ_{kq}. The dual formulation implies some more specific features addressed in the supplemental material of Ref. [139], but the physical interpretation of γ is consistent with the discussion above. We fix the lattice size to $N = 16 \times 16$, the temperature is $T = 0.15t$. Below we refer to node, antinode, and hot spot as 'ARC', 'PG', and 'HS', respectively.

Fig. 4.6 (a,b) shows the Green's function in the pseudogap phase at doping $\delta = 0.01$. The structure of G' is consistent with Fig. 4.5. As expected, G'' is suppressed near the antinodes. Panel (c) shows Σ'', which is insulating-like at PG; at ARC and HS

Die approbierte gedruckte Originalversion dieser Dissertation ist an der TU Wien Bibliothek verfügbar.
The approved original version of this doctoral thesis is available in print at TU Wien Bibliothek.
TU Bibliothek Your knowledge hub WIEN

it is metallic. Notice that Σ'' at PG is enhanced even compared to its value at $(\pi, 0)$ (dashed red, [205]). In the dual formalism the lattice self-energy is given as, $\Sigma_k = \Sigma_\nu^{\mathrm{DMFT}} + \tilde{\Sigma}_k/(1 + g_\nu \tilde{\Sigma}_k)$, where $\tilde{\Sigma}$ is the dual self-energy, g is the Green's function of the AIM corresponding to DMFT. At ARC Σ_k'' is smaller, in absolute value, compared to DMFT. We show that this is the result of nonlocal spin fluctuations.

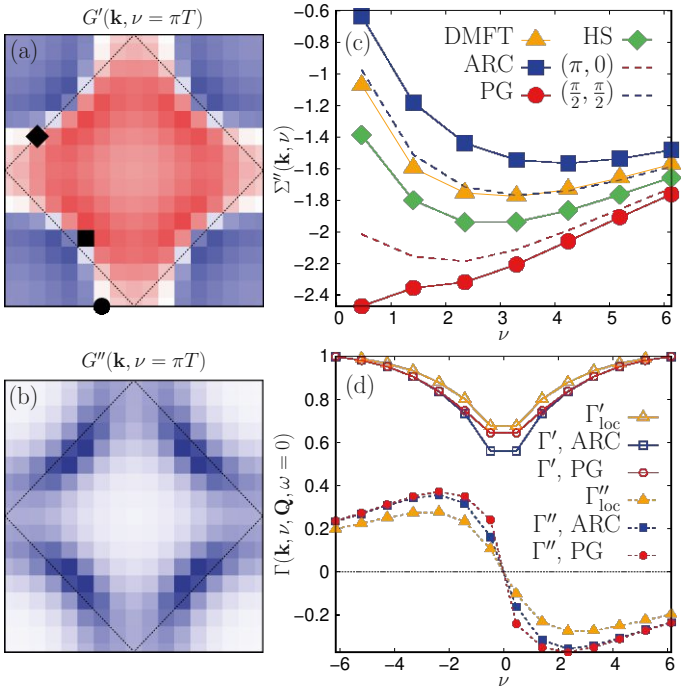

Figure 4.6: (a) Real and (b) imaginary part of the Matsubara Green's function for doping $\delta = 0.01$ (here, and in all figures, $U = 8t$, $t' = -0.2t$, $t'' = 0.1t$). The correlation length is $\xi \approx 1.6$. Black symbols mark Fermi arc (ARC), pseudogap (PG), and hot spot (HS) momentum on the FS. (c) Self-energy and (d) spin-fermion vertex ($\mathbf{q} = \mathbf{Q}, \omega = 0$) at these and further momenta as a function of ν. Triangles show local DMFT quantities. Note that here Γ corresponds to γ in the text.

Fig. 4.6 (d) shows the vertex that couples spin fluctuations with momentum $\mathbf{Q}$ to fermions at ARC and PG. Note that the imaginary part γ'' is of similar magnitude as the real part γ'. Triangles show the local vertex $\Gamma_{\mathrm{loc}}(\nu, \omega = 0)$ of the AIM. Its imaginary part is sizable but nonlocal corrections further enhance it. Fig. 4.7 shows γ for $\nu = \pi T$ as a function of $\mathbf{q}$ for various dopings. The real part is overall reduced by vertex corrections ($\gamma' < 1$) and it is suppressed in particular near $\mathbf{Q}$. This is a precursor to the decoupling of Goldstone excitations from fermions in the antiferromagnet, known as Adler principle [211, 212, 221–224]; in the extreme case $\xi \to \infty$ it requires that the vertex vanishes at the ordering vector [222]. For larger dopings the suppression moves to incommensurate momenta [205]. At PG, the Adler principle does not apply for small doping because of the gap.

Die approbierte gedruckte Originalversion dieser Dissertation ist an der TU Wien Bibliothek verfügbar.
The approved original version of this doctoral thesis is available in print at TU Wien Bibliothek.

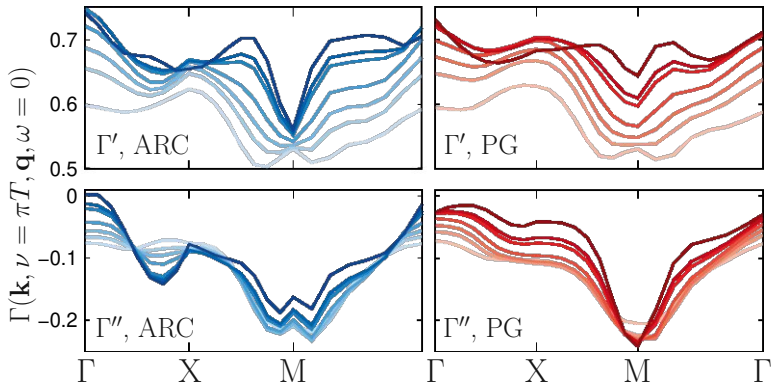

Figure 4.7: Real and imaginary part of the spin-fermion vertex for ARC and PG as a function of $\mathbf{q}$. Shadings from dark to light: $\delta = 0.01, 0.05, 0.07, 0.12, 0.16, 0.2, 0.27$.

Figs. 4.6 and 4.7 show that γ'' is large and, hence, the scattering mechanism sketched in Fig. 4.5 needs to be taken into consideration. To reveal its quantitative effect we analyze the contribution $\tilde{\Sigma}_{\mathrm{sp}}(k, q)$ of nonlocal spin fluctuations to the dual self-energy, it has a form similar to Eq. 4.2 [205]. First, we integrate $\tilde{\Sigma}''_{\mathrm{sp}}(\mathbf{k}, \nu = \pi T, \mathbf{q}, \omega = 0)$ with respect to $\mathbf{q}$ over a circle with radius r_q, centered at $\mathbf{Q}$. This corresponds to circles as in Fig. 4.5, beginning with $\mathbf{Q}$ and ending with the entire Brillouin zone [225]. The result is shown as full lines in Fig. 4.8. A patch of momenta $\mathbf{q} \approx \mathbf{Q}$ contributes to the integral, whose final result is negative for PG and HS, but positive for ARC.

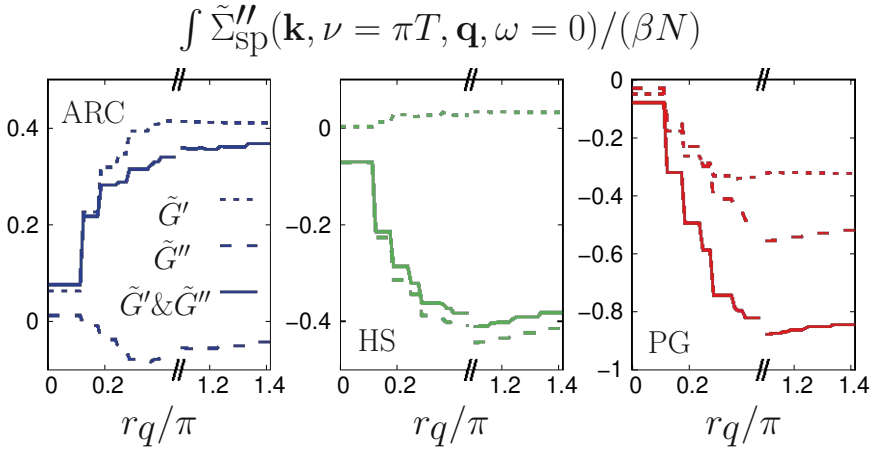

Figure 4.8: Integrated fluctuation diagnostic for $\delta = 0.01$ as a function of the integration radius (cf. circles in Fig. 4.5, see text). Dotted and dashed lines show the separate contributions of real and imaginary part of $\tilde{G}$, respectively.

This dichotomy can be traced back to γ''. To show this, we split the fluctuation diagnostic into contributions from the real and imaginary part, $\tilde{G}'$ and $\tilde{G}''$, of the dual Green's function. We remind that for $\gamma'' = 0$ the real part $\tilde{G}'$ contributes nothing to the integral for $\tilde{\Sigma}''_{\mathrm{sp}}$ [cf. Eq. 4.2]. Dashed lines in Fig. 4.8 show the contribution of $\tilde{G}''$,

Die approbierte gedruckte Originalversion dieser Dissertation ist an der TU Wien Bibliothek verfügbar.
The approved original version of this doctoral thesis is available in print at TU Wien Bibliothek.

which is negative, and absolutely smaller at ARC than at HS and PG. This corresponds to the conventional mechanism which opens a gap near hot spots for $\xi \to \infty$ [133, 184, 188]. Dotted lines in Fig. 4.8 show the contribution of $\tilde{G}'$, which is positive at ARC, negative at PG, and vanishingly small at HS, corresponding to the mechanism sketched in Fig. 4.5. The pseudogap opens at PG as the *combined* effect of both mechanisms. Their contributions are comparable at PG, but it is $\tilde{G}'$ (γ'') which differentiates the PG from the HS (opens the gap at PG first). With only $\tilde{G}''$ (γ') PG and HS would have similar lifetimes. As already seen in the semi-analytical model, due to γ'' non-local spin fluctuations even protect (cool) the ARC ($\tilde{\Sigma}'' > 0$). We have thus shown that nonlocal spin fluctuations at strong coupling enhance (weaken) correlation effects outside (inside) the AZB.

Finally, we explicitly differentiate between scattering rate and quasiparticle weight by extrapolating the Matsubara self-energy with a fourth-order polynomial to the Fermi level. The left panel of Fig. 4.9 shows $-\Sigma''(\mathbf{k}, i\eta)$ as a function of doping. As expected, for small dopings the scattering rate is very large at PG, a gap opens and $Z_\mathbf{k}$, defined through the slope of Σ, loses its meaning as a quasiparticle weight [126]. At ARC the scattering rate is significantly suppressed compared to DMFT, while $Z_\mathbf{k}$ remains similar. Hence, the suppression of the self-energy inside the AZB corresponds primarily to a reduction of the scattering rate (enhancement of the lifetime). The protection of the ARC is so effective that down to $\delta = 0.01$ we do not observe the opening of a gap inside the AZB.

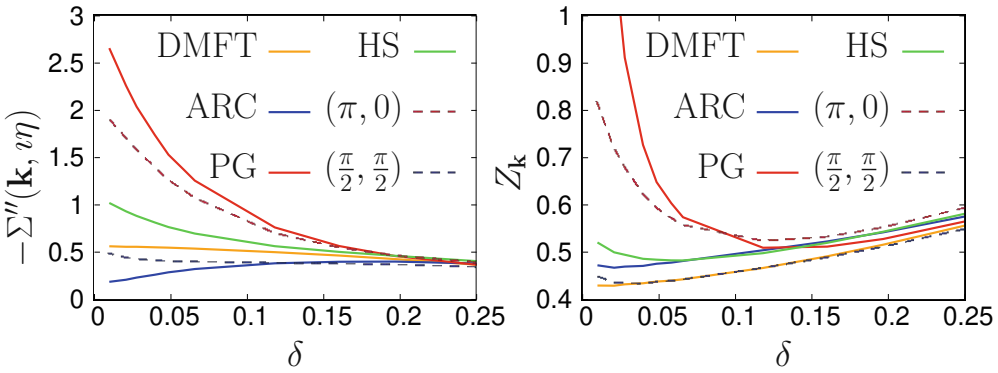

Figure 4.9: Scattering rate (left) and quasiparticle weight (right) vs. hole doping δ at indicated points in the Brillouin zone. Both quantities are obtained through polynomial extrapolation to the Fermi level, $\eta = 0^+$.

Discussion — We identified a mechanism for spin-fermion scattering that arises from a combination of strong correlations and particle-hole asymmetry. In the considered temperature and doping regime, it dampens quasiparticle excitations on those parts of the Fermi surface that lie outside of the antiferromagnetic zone boundary, whereas lifetimes on the inside are actually enhanced by spin fluctuations. This may explain why the Fermi arcs observed in underdoped cuprates are cut off at the antiferromagentic zone boundary [226] and exhibit remarkably good Fermi liquid properties [180]. This further

Die approbierte gedruckte Originalversion dieser Dissertation ist an der TU Wien Bibliothek verfügbar.
The approved original version of this doctoral thesis is available in print at TU Wien Bibliothek.

indicates that strong non-local correlations cannot simultaneously open an insulating gap on the entire Fermi surface.

This strong-coupling mechanism is also based on antiferromagentic spin fluctuations, but it opens the pseudogap already when the correlation length is still smaller than the thermal de Broglie wavelength (for $\delta = 0.01$ we estimate $\xi \approx 1.6$ [205], while $\xi_{\text{th}} \gtrsim 2.1$ [133]). Nevertheless, only classical spin fluctuations ($\omega = 0$) are relevant for the self-energy [227].

The presented explanation of the strong-coupling spin-fluctuation mechanism which controls the pseudogap allows us to resolve the contradiction between conventional spin-fluctuation theory and experiments/numerics. As a future perspective, it is tempting to also clarify its connection to unconventional superconductivity.

4.2.1 Fermi surface reconstruction without order

So far we have restricted the discussion to parameter regimes, where numerical results of the Hubbard model are available. Let us now change the parameters of the spin-model self-energy and venture into more uncharted and potentially dangerous territory. The numerical results presented above were at rather high temperatures $T = 0.15t \mathrel{\widehat{=}} 700-900\,K$, where correlation lengths are short. As the temperature is lowered, however, both the correlation length and the magnitude of the susceptibility will increase [126, 187]. Nevertheless, long-range magnetic order is forbidden in the 2D square lattice by the Mermin-Wagner theorem [136]. In Fig. 4.10 we show how Eq. 4.3 behaves as we enter this regime. The two panels on the left show results for $\kappa = -\pi/4$, i.e. a sizable γ'', while we set $\gamma'' = 0$ for the two panels on the right. The most interesting result is found in panels (c)/(d), where we observe a reconstruction of the Fermi surface into small hole-like pockets. Usually, such pockets are associated with the folding of the Brillouin zone due to symmetry breaking in the antiferromagnetic state [228]. However, here we are still within the paramagnetic phase and the Fermi surface reconstructs without any symmetry breaking or order, but simply because the self-energy becomes large. While this shows that spin fluctuations can, in principle, lead to hole pockets without AFM order, it is unclear at the moment whether this can also be observed in (exact) solutions of the Hubbard model. Parameter regimes where conditions favorable for such a behavior can be expected are in the 2D Hubbard model on a square lattice at low doping and (very) low temperatures. Here both the susceptibility and the correlation length grow rapidly with decreasing temperature [126, 187], but order is prohibited by the Mermin-Wagner theorem, which might thus lead to self-energies as discussed above.

Die approbierte gedruckte Originalversion dieser Dissertation ist an der TU Wien Bibliothek verfügbar.
The approved original version of this doctoral thesis is available in print at TU Wien Bibliothek.
TU Bibliothek Your knowledge hub WIEN

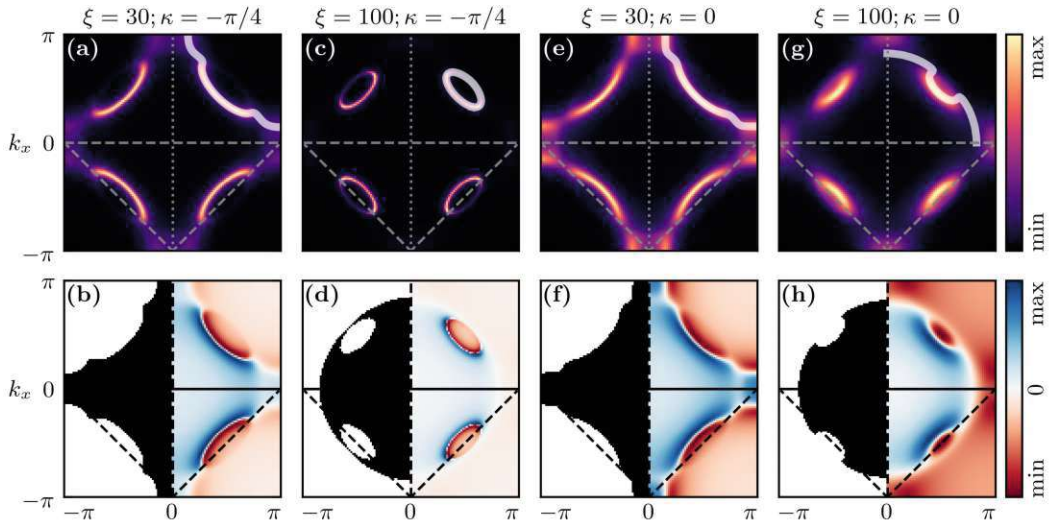

Figure 4.10: Long correlation and large susceptibility for Eq. 4.2. Top shows the spectral function (imaginary part) and bottom the real part of G. The white line on top of the spectral function marks where (numerically) $\mathrm{Re}\, 1/G = 0$.In (c) we only show the white line corresponding to the pocket for clarity. The left two panels show results for a sizable γ'', while $\gamma'' = 0$ for the two panels on the right. The black-white part in the lower panels shows where $\mathrm{Re}\, G$ is positive (black) and where it is negative (white). As tight-binding parameters we use $t = 1$; $t' = -0.2t$; $t'' = 0.1t$ and fix the filling to $n = 0.95$, which corresponds to the underdoped region. The correlation length and the complex phase of γ (κ) are listed in the subtitles. Note that in comparison to Fig. 4.2, here the scaling prefactor of the self-energy (which corresponds to the amplitude of the susceptibility) is larger by a factor of 10/3.

4.2.2 Connection to cuprates

After the discussion of how spin fluctuations give rise to the PG in the Hubbard model and how they differ qualitatively at "strong" and "weak" coupling, let us now shift our focus to cuprates. Specifically, we will discuss various ARPES experiments.

Hole doped cuprates: Fermi arcs and hole pockets — There has been a long-standing debate in the cuprate community, about whether or not Fermi arcs are actually one-half of hole pockets similar to those shown in Fig. 4.10 [229]. Recent ARPES experiments on $Ba_2Ca_4Cu_5O_{10}(F,O)_2$, a five-layer copper oxide compound, shed new light onto this topic [15]. Each of the three inequivalent layers in this compound has a different hole doping and shows different physics as a result. Most interestingly, the authors find both a Fermi arc as well as two hole pockets, which they attribute to the different layers. The inability to find the other side of one Fermi arc, while simultaneously seeing it for the two pockets, suggests that Fermi arcs are truly what they are called[10].

The Fermi arcs observed in [15] and similar ARPES measurements [14, 16] are qualitatively not too different from those shown in Fig. 4.6[11]. Hence it is reasonable to apply the model developed for understanding our numerical results in the section above also

[10] The pockets are reported to be of hole-like nature and thus do not correspond to the electron-like pockets found near the charge-density-wave state [230].
[11] See Fig. 4.16 for results using DΓA.

Die approbierte gedruckte Originalversion dieser Dissertation ist an der TU Wien Bibliothek verfügbar.
The approved original version of this doctoral thesis is available in print at TU Wien Bibliothek.
TU Bibliothek Your knowledge hub WIEN

for cuprates. Scattering of spin fluctuations with an imaginary coupling vertex will enhance the lifetime of quasiparticles along the nodes, while those at the antinodes are diminished. This is best illustrated in Fig. 4.5 above, where the color indicates the sign of the (non-interacting) Green's function.

The authors of [15] interpret the hole-pockets as proof of antiferromagnetic order and argue its coexistence with superconductivity in the same CuO_2 sheet. While it may be possible that such an exotic state of two simultaneously broken symmetries exists, our discussion above provides a possible explanation for hole pockets in the paramagnetic phase. To distinguish the two scenarios it would be desirable to confirm or disprove the antiferromagnetic order with an independent probe. Below in Fig. 4.11 we show that both the pockets as well as the arc can be well described with the spin-model self-energy in Eq. 4.3. One should, of course, be cautious about results containing fit parameters. As already John v. Neumann put it [231]:

With four parameters I can fit an elephant, and with five I can make him wiggle his trunk.

Let us thus remark on the chosen parameters and their physical plausibility. We choose a large correlation length for the pockets $\xi = 100$ and a small for the arc $\xi = 3$, which reflects the relative proximity to the AFM phase. Furthermore, we adjust the filling to that reported in experiment[12] ($n = \{0.92, 0.955, 0.98\}$), use the same tight-binding parameters for all layers ($t = 1$, $t' = -0.2t$ and $t'' = 0.1t$)[13] and set the isotropic background of $\mathrm{Im}\,\Sigma$ to -0.02[14]. This leaves us with two adjustable parameters, namely a complex multiplicative prefactor $a{\cdot}(1{+}ib)$[15], where a is the magnitude of the Ornstein-Zernicke form of the susceptibility $OZ(\mathbf{q}) = \frac{a}{(\mathbf{Q}-\mathbf{q})^2+\xi^{-2}}$ and b related to the imaginary part of γ. Overall the quality of the fit is not sensitive to any single parameter as long as we choose a finite and negative $b \mathrel{\widehat{=}} \gamma''$. Without it, no arcs inside the AZB form for small correlation lengths in our model and we would exclusively observe hot-spot physics instead.

[12] For the CuO_2 hosting the arc no filling is reported in [15]. By extending the Fermi arcs to form a continuous sheet we estimate the doping to be roughly 8%.

[13] The authors of [15] propose slightly different tight-binding parameters. However, since those are measured in experiment renormalization effects are already included, which is not the case for the non-interacting Green's function we use in Eq.4.3. Nevertheless, the qualitative structure and all conclusions would remain unchanged if we use the parameters from [15] instead.

[14] Previously this was set to $-\pi/beta$ to reflect the first Matsubara frequency, which mimics non-zero temperature.

[15] Here we use for convenience the representation $\gamma = (1 + ib)/(|1 + ib|)$ instead of $\gamma = e^{i\kappa}$.

Die approbierte gedruckte Originalversion dieser Dissertation ist an der TU Wien Bibliothek verfügbar.
The approved original version of this doctoral thesis is available in print at TU Wien Bibliothek.
TU Bibliothek Your knowledge hub WIEN

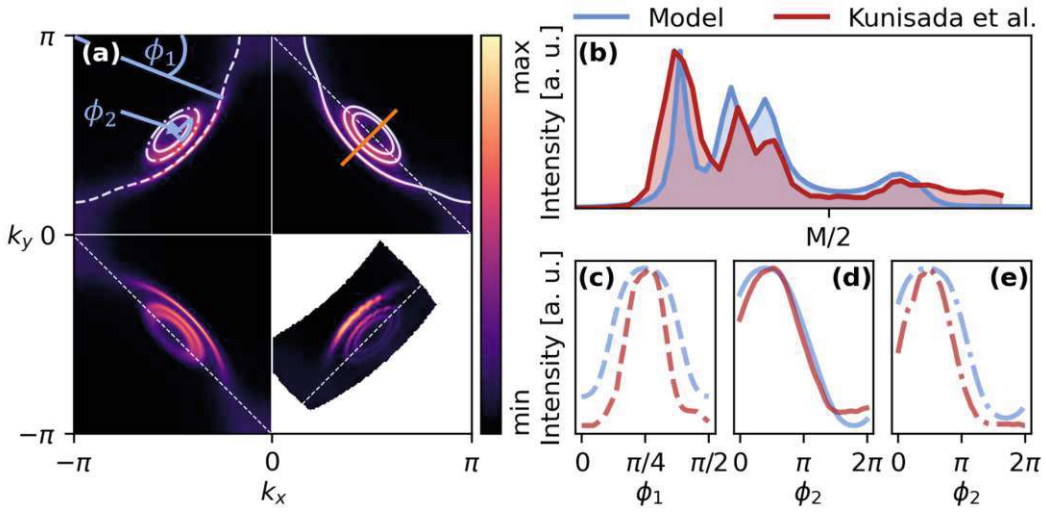

Figure 4.11: Comparison between the experimental ARPES data from [15] and a parameter adjusted spin-model Eq. 4.3. **(a)** Fermi surface where the lower right quadrant is the data taken from [15]. **(b)** Cut in the BZ as marked by the orange line in (a). **(c)(e)** Normalized intensity along the $\mathrm{Re}(1/G) = 0$ line (shown as white in (a)), parametrized by an angle ϕ_1 for the arc and ϕ_2 for the pockets (shown in (a)). Model is shown in blue and the experiment in red. (c) corresponds to the arc, while (d)-(e) are the two pockets. As parameters we choose a large correlation length for the pockets $\xi = 100$ and a small for the arc $\xi = 3$. Furthermore, we use tight-binding parameters as previously $t = 1$, $t' = -0.2t$ and $t'' = 0.1t$ for all three layers. We use and fit a complex-valued prefactor $a \cdot (1 + ib)$ to model the strength of the susceptibility and the imaginary part of γ. Values are $a = \{7, 10, 10\}$ and $b = \{-1.5, -0.35, -0.35\}$ for the three layers, respectively.

Electron doped cuprates — For electron-doped cuprates, the sign and thus also the effect of γ'' is reversed. That is scattering on the "arcs" is enhanced, while the antinodes are protected. As a result, also the pseudogap is "reversed" in the sense that long-lived quasiparticles now exist at the antinode, while the node is gapped. In Fig.4.12 we compare Eq. 4.3 with ARPES measurements for the electron doped cuprate $Nd_{2-x}Ce_xCuO_{4\pm d}$ from [232]. Like in the hole-doped case, we pick physically meaningful parameters and use the same tight-binding model. The doping is adjusted to the experimental values and we pick correlation lengths $=\{60, 30, 20\}$ for the dopings $\delta = \{0.04, 0.10, 0.15\}$, respectively, while we adjust the complex prefactor $a \cdot (1 + ib)$ such that a good fit is obtained. Values are $a = \{80, 20, 10\}$ and $b = \{0.6, 0.6, 0.0\}$ for the three dopings, respectively. Fig.4.12(a) displays the Fermi surface for the underdoped sample ($x = 0.04$), which displays electron-like pockets around the antinode [232], which are also captured in the spin-model as evidenced by the separated black regions in the lower left quadrant of (a). As doping is increased the pocket evolves into the electron-doped pseudogap (b), which shows disconnected arcs at the *antinode*. While this difference to hole-doped cuprates might seem strange on first glance, the change of sign of the imaginary part of γ'' provides a natural explanation. Let us note that the Coulomb interaction was reported to be weaker for electron-doped cuprates [233] and it is thus possible that the hot-spot scattering mechanism dominates and the results are already well described within weak-coupling theory [190]. In that case, a distortion of the Fermi surface, which is already close to the AZB might result in "hot lines" rather than hot spots. Thus distinguishing hot-spot physics from the effect of γ'' is

Die approbierte gedruckte Originalversion dieser Dissertation ist an der TU Wien Bibliothek verfügbar.
The approved original version of this doctoral thesis is available in print at TU Wien Bibliothek.

more difficult in electron-doped cuprates. To settle this question we propose to perform numerically unbiased calculations for the electron-doped Hubbard model, which allows for a distinction between hot-spot and γ'' physics. Nevertheless, spin fluctuations in this simple model contain the influence of the hot spot, as well as, of γ'', thus providing a unified framework for the pseudogap in cuprates including both the electron and the hole-doped case.

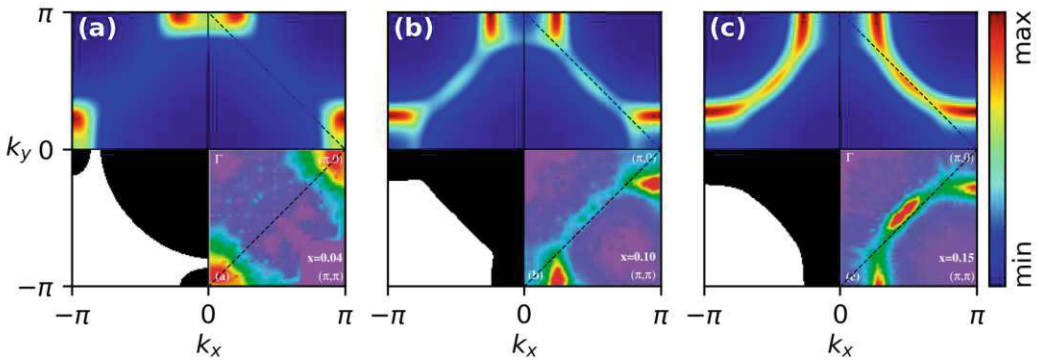

Figure 4.12: Comparison between the experimental ARPES data from [232] and a parameter adjusted spin-model (Eq. 4.3) at different dopings. **(a)** Fermi surface where the lower right quadrant is the data taken from [232] for electron doping $x = 0.04$. **(b)/(c)** same as (a), but for $x = 0.10/x = 0.15$. The lower left quadrant shows where $\mathrm{Re}\, G$ is positive (black) and negative (white). Spin-model parameters are discussed in the main text. We use tight-binding parameters as before: $t = 1$, $t' = -0.2t$ and $t'' = 0.1t$.

From arcs to pockets and back — To conclude the discussion about the Fermi surface structure within the spin-model approximation (Eq. 4.3) we show arcs and pockets for electron and hole doping in Fig. 4.13. The underlying non-interacting Green's function is that of Fig. 4.2(a) and the tight-binding parameters are the same as in the previous section. Each subplot in Fig. 4.13 shows the spectral function at the Fermi surface ($A(\omega = 0)$) in the right half of the Brillouin zone, while the left shows the real part of the Green's function. The lower left quadrant shows where $\mathrm{Re}\, G$ is positive (black) and where it is negative (white). We start in Fig. 4.13(a) on the electron-doped site ($n = 1.1$), where Fermi arcs at the antinode can be observed[16]. To mimic the effects of reducing the electron doping to 5% in Fig. 4.13(b) we increase both the correlation length from $\xi = 30$ in (a) to $\xi = 60$ in (b) and the amplitude from $a = 20$ (a) to $a = 80$ (b). These large spin fluctuations trigger a Fermi surface reconstruction around the antinodes into electron pockets[17]. We observe thus a transition from an antinodal arc to an antinodal electron-like pocket. Once we cross half-filling and move into the hole-doped side ($n = 0.95$) we find instead nodal hole-like pockets at large correlation length $\xi = 60$ and large amplitude $a = 40$, displayed in Fig. 4.13(c). These nodal hole pockets will transition into nodal Fermi arcs upon reducing the strength of the antiferromagnetic correlations, here mimicked by decreasing the correlation length to $\xi = 3$[18]. As discussed

[16] The other spin-model parameters are $\xi = 30$, $a = 20$ and $b = 0.6$. To minimize changing parameters we keep $b = \sigma \cdot 0.6$, where σ is $+1$ for the electron-doped case and -1 for the hole-doped case.
[17] See also the previous section for a discussion on ARPES results of electron-doped cuprates.
[18] We choose $a = 80$ for (d), which at first glance seems overly large. However, the magnitude of the

Die approbierte gedruckte Originalversion dieser Dissertation ist an der TU Wien Bibliothek verfügbar.
The approved original version of this doctoral thesis is available in print at TU Wien Bibliothek.
TU Bibliothek Your knowledge hub WIEN

in more detail in the previous sections above, all of these Fermi surface topologies have indeed been observed in ARPES experiments (see e.g. [189, 232] for electron doping and [15] for hole doping). While our simple model based on spin fluctuation with a complex coupling vertex provides a unified understanding of them, one should still point out questions that remain open. First and possibly foremost, our model is restricted to the Fermi surface. An extension to finite frequencies is needed in order to study the PG structure at finite frequencies, which requires a better understanding of the real-frequency structure of γ. Furthermore, confirming the appearance of electron and hole pockets in (numerical) calculations for the Hubbard model would be an important next step to check the validity of our considerations. And lastly, since the applicability of the Hubbard model for cuprates is still under debate, it would be interesting to extend the current discussion to the three-band Emery model.

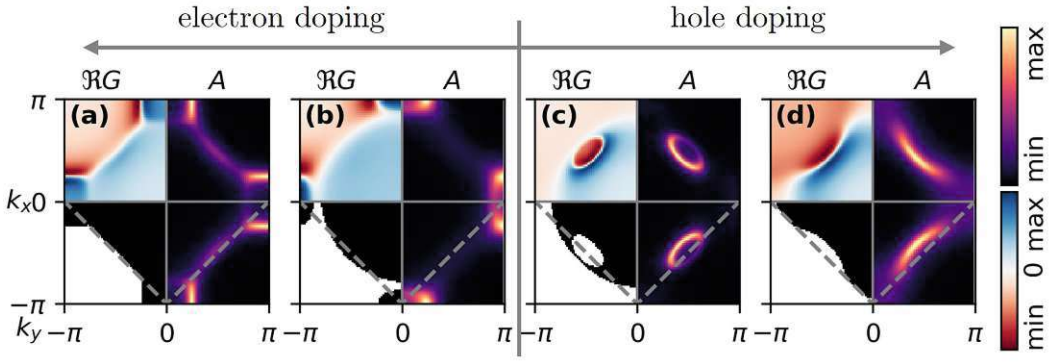

Figure 4.13: Different Fermi surfaces obtained within the spin-model in Eq. 4.3 for the square lattice Hubbard model. For a detailed discussion of the parameters see the main text. **(a)** 10% electron doped case with $\xi = 30$ and $a = 20$, which displays antinodal Fermi arcs. **(b)** 5% electron doped case with $\xi = 60$ and $a = 80$, which displays antinodal electron-like pockets. **(c)** 5% hole doping with $\xi = 60$ and $a = 40$, which displays nodal hole-like pockets. **(d)** 10% hole doping with $\xi = 3$ and $a = 80$, which displays nodal hole-like pockets. We keep $b = \sigma \cdot 0.6$, where σ is $+1$ for the electron-doped case and -1 for the hole-doped case. Tight-binding parameters are the same as in the previous section: $t = 1$, $t' = -0.2t$ and $t'' = 0.1t$.

4.3 Pseudogap within the dynamical vertex approximation

In the previous section, we discussed how spin-fluctuations described by a simple ansatz for the self-energy (Eq. 4.3) can create a pseudogap, characterized by a momentum-dependent spectral weight loss at the Fermi surface. These analytical considerations were based on numerical calculations of the Hubbard model using the boson-exchange parquet solver for dual fermions (BEPS) [186] in the strong-coupling regime, at relatively high temperature and low doping: a regime where we found only classical ($\omega = 0$) spin-fluctuations to be relevant and identified the imaginary part of the spin-fermion coupling vertex γ to be crucial for opening a pseudogap when correlation lengths are small.

As a next step, we would like to study signatures of the pseudogap across the whole

self-energy in Eq. 4.3 also depends on ξ. To compensate for this, seemingly large values for a have to be chosen at small correlation lengths.

Die approbierte gedruckte Originalversion dieser Dissertation ist an der TU Wien Bibliothek verfügbar.
The approved original version of this doctoral thesis is available in print at TU Wien Bibliothek.
TU Bibliothek Your knowledge hub WIEN

phase diagram for the single-band Hubbard model as well as to analyze the frequency dependence of the pseudogap. Since this involves lower temperatures, where a finer k-mesh and more Matsubara frequencies are required, we will use the dynamical vertex approximation (DΓA) [38][19]. Its main advantage compared to parquet approaches, see e.g. [89, 138, 186, 234], is its reduced numerical cost, which is primarily because of two reasons: firstly, the approximated vertex in DΓA only contains a single momentum index (Eq. 3.83), which drastically reduces the computational effort of solving the Bethe-Salpeter equation (BSE) (Eq. 3.84). Secondly, in λ-corrected DΓA there is no self-consistency, which means that the BSE and the Schwinger-Dyson equation (SDE) only needs to be solved a single time. Indeed, the numerical bottleneck of DΓA is usually sampling the two-particle Green's function of the Anderson impurity model (AIM), which becomes rather costly at low temperatures.[20] On the downside, however, mutual screening between the channels is not taken into account. Additionally, there is no feedback of the DΓA self-energy on the (magnetic) susceptibility χ_m, which enters the SDE. Nevertheless, a comparison to numerically exact quantum Monte Carlo solutions of the Hubbard model at half-filling and weak coupling showed good agreement [95, 126, 235]. While certainly not numerically exact, DΓA showed the same qualitative features and also compared reasonably well on a quantitative level even when correlation lengths are of the order $\xi \sim 10$. We are thus confident that DΓA is a suitable tool to study the pseudogap in the Hubbard model at strong interactions. Indeed, the pseudogap has already been studied in a similar parameter regime using DΓA, but in the context of infinite-layer nickelate superconductors [187]. For the following, we will always use the nearest-neighbor hopping $t = 1$ as unit of energy. Typical values for cuprates are $t \sim 0.45\,\mathrm{eV}$ [51, 148, 150, 236], while for nickelates $t \sim 0.4\,\mathrm{eV}$ [50, 51, 237].

4.3.1 Signatures of the pseudogap

As mentioned at the beginning of this chapter signatures of the pseudogap are visible in many different probes, ranging from spectroscopic experiments like ARPES [14–16, 181, 238–243] to transport measurements like in-plane resistivity, see e.g. [157]. Here we discuss how the pseudogap manifests for calculations of the Hubbard model.

Spectral function — When considering the real-frequency ($\mathbf{k}$-integrated) spectral function $A(\omega)$, which is accessible in photoemission (PE) or scanning tunneling spectroscopy (STS) experiments, the pseudogap is characterized by a depression of the spectral weight at the Fermi energy, which is however not a full gap [241]. To understand this better consider Fig. 4.14. Fig. 4.14(a) displays the (analytically continued) DMFT solution of the half-filled $t' = t'' = 0$ Hubbard model at $\beta = 25$. We show a solution for $U = 8$ (green) which is before the Mott metal-to-insulator transition and can be considered to be a strongly correlated metal. The metallic behavior is evidenced by the

[19] By DΓA we always mean the λ-corrected ladder DΓA introduced in Section 3.8.

[20] To give the reader some perspective, a single DΓA calculation for the 2D square lattice Hubbard model using a 140×140 k-mesh (~ 2500 points in the irreducible BZ) and 120/121 Matsubara frequencies for each fermionic/bosonic frequency takes only about 150 core hours on the Vienna scientific cluster 4 (VSC4). In contrast sampling the two-particle Green's function in the same frequency box takes about 5000 core hours at $\beta = 12.5\,1/t$ using `w2dynamics`.

Die approbierte gedruckte Originalversion dieser Dissertation ist an der TU Wien Bibliothek verfügbar.
The approved original version of this doctoral thesis is available in print at TU Wien Bibliothek.
TU Bibliothek Your knowledge hub WIEN

large quasi-particle peak at the Fermi energy, while the strong correlations manifest in the Hubbard side peaks at $\omega \simeq \pm U/2 \simeq \pm 4$. Contrary to the metal, the insulating solution for $U = 12$ (golden) has no spectral weight at the Fermi energy and thus also no free charge carriers that could contribute to the conductivity. The spectral function for the pseudogap, however, is somewhere in between as can be seen in Fig. 4.14(b)[21]. There is neither a well-defined quasiparticle peak visible at the Fermi energy, nor does the spectrum show a clear gap in the sense that the spectral weight vanishes at $\omega = 0$.

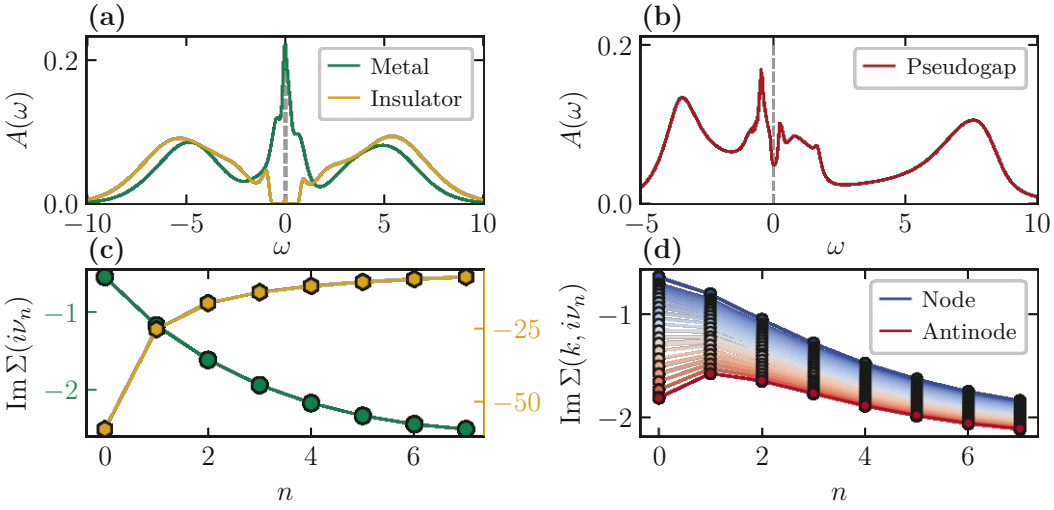

Figure 4.14: Real frequency spectral function $A(\omega)$ (top) and imaginary part of the self-energy on the Matsubara axis (bottom). Left shows the DMFT solution for the half-filled $t' = t'' = 0$ Hubbard model at $\beta = 25$ before the Mott transition at $U = 8$ (green) and after the Mott transition $U = 12$ (golden). Right shows the DΓA solution for the spectrum and self-energy in the pseudogap regime at $U = 8$, $n = 0.9$, $\beta = 27.5$ and $t' = -0.2$, $t'' = 0.1$. Here the nearest-neighbor hopping $t = 1$ sets the unit of energy. The self-energy for the pseudogap regime is plotted along the line defined by $\mathrm{Re}(1/G) = 0$ starting from the node $\mathbf{k} \sim (\pi/2, \pi/2)$ (blue) and ending at the antinode $\mathbf{k} \sim (\pi, 0)$ (red). See Fig. 4.16 below for more information on these k points.

Self-energy — To better understand the pseudogap feature in the spectrum let us take a look at the imaginary part of the self-energy on the Matsubara axis, displayed in Fig. 4.14(c,d). The self-energy of a Mott insulator (golden hexagons in Fig. 4.14(c)) has a pole at $i\nu_n \to 0$ which gaps the originally metallic non-interacting Green's function. Such a pole-like structure does not exist for the metallic case (green circles in Fig. 4.14(c)). The DΓA self-energy in the pseudogap regime is no-longer local, but develops a strong momentum anisotropy as can be seen in Fig. 4.14(d), see also e.g. [126, 128, 182]. While the self-energy close to the node at $\mathbf{k} \sim (\pi/2, \pi/2)$ (blue) remains metallic, a pole develops as we move towards the antinode $\mathbf{k} \sim (\pi, 0)$ (red). The pseudogap in the single-band Hubbard model can thus be understood as a momentum selective insulator, where well-defined quasiparticles live on the node, while the antinode is gapped. Such a momentum-selective insulator naturally explains the existence of Fermi arcs as observed in ARPES experiments, see e.g. [15, 16]. On the real-frequency

[21] For the pseudogap regime, we set $t = 1$ and use t as unit of energy. Other paramters are $n = 0.9$, $U = 8$, $\beta = 27.5$ and $t' = -0.2$, $t'' = 0.1$ and we show the DΓA solution.

Die approbierte gedruckte Originalversion dieser Dissertation ist an der TU Wien Bibliothek verfügbar.
The approved original version of this doctoral thesis is available in print at TU Wien Bibliothek.
TU Bibliothek Your knowledge hub WIEN

axis the self-energy develops an additional peak at, or close to, the Fermi energy, which suppresses the spectral weight and, once large enough, will completely gap the spectrum at those momenta.

This antinodal "kink" in the self-energy on the Matsubara axis has frequently been used as a proxy to determine whether or not the pseudogap is present [126, 128, 139, 244, 245]. However, especially at high temperatures where the first fermionic Matsubara frequency $i\nu_0 = \frac{\pi}{\beta}$ is relatively large one can observe a pseudogap without this "kink". Such a scenario is displayed in Fig. 4.15(b), where the self-energy was first analytically continued using the maximum entropy method, see also Fig. 4.15(a), and subsequently transformed back (line in Fig. 4.15(b)). Here the downturn on the imaginary axis only becomes apparent for imaginary frequencies smaller than the first Matsubara frequency and would thus be missed if only the Matsubara frequencies are considered. Furthermore, a polynomial fit using the first few Matsubara frequencies, which is often used to extrapolate to the Fermi level, is not applicable here. While there may be regimes where such an extrapolation is more reliable, for example at low temperatures where the first Matsubara frequency is smaller, we suggest that the validity of this procedure should always be confirmed.

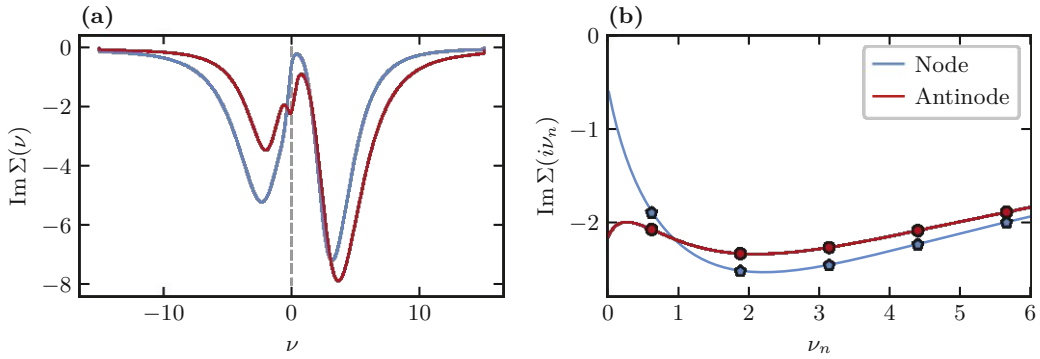

Figure 4.15: Self-energy on the real-frequency axis (left) and for Matsubara frequencies (right) at high temperatures corresponding to $\beta = 5$. We show the self-energy close to the node for $\mathbf{k} = (\pi/2, \pi/2)$ (blue) and close to the antinode for $\mathbf{k} = (\pi/2, 0)$ (red). Note that the "downturn" of the antinodal self-energy becomes visible only for imaginary frequencies smaller than the first Matsubara. Small imaginary frequencies (lines) were obtained by back-transforming the analytically continued self-energy shown (b). Parameters are: $U = 8$, $n = 0.9$ and $t' = -0.2$, $t'' = 0.1$.

4.3.2 Fermi arcs

The depression of the spectral weight at the Fermi surface can have many origins[22], but ARPES measurements on cuprate superconductors reveal an anisotropy of the momentum-resolved spectral function $A(\omega, k)$, as evidenced by the appearance of Fermi arcs, see e.g. [14–16] and previous Subsections 4.1-4.2.1. For cuprates, there is an ongoing debate whether or not Fermi arcs are real, or in fact the backside of a hole-pocket

[22] Consider for example an orbital selective Mott insulator, see e.g. Ref. [246, 247]. Each orbital is either metallic or insulating, but the combined spectral function will display a similar feature around the Fermi energy as in Fig. 4.14(b). In the case of cuprates, spin, superconducting and charge fluctuations are discussed as origin of the pseudogap. [181]

Die approbierte gedruckte Originalversion dieser Dissertation ist an der TU Wien Bibliothek verfügbar.
The approved original version of this doctoral thesis is available in print at TU Wien Bibliothek.
TU Bibliothek Your knowledge hub WIEN

as in Fig. 4.13(c). While we do not exclude the possibility of nodal hole-like pockets at (very) low temperatures[23], or at high magnetic fields, we do unambiguously observe Fermi arcs for the Hubbard model at high to intermediate dopings, an observation which is consistent with other numerical methods like BEPS [139] or diagrammatic Monte Carlo [248].

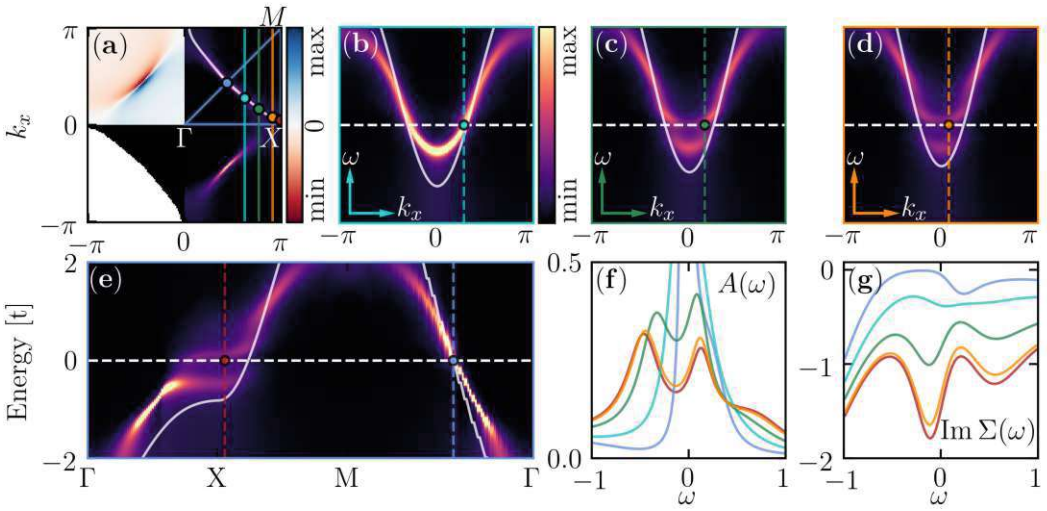

Figure 4.16: DΓA solution of the Hubbard model. **(a)** Spectral function (right half of the BZ) together with $\mathrm{Re}(1/G) = 0$ (white line). Momentum cuts for panels (b)-(e) are marked by colored lines (blue node to red antinode). $\mathrm{Re}(G)$ (upper left) and binary image of $\mathrm{Re}(1/G) = 0$ (lower left). Frequency is set to the Fermi energy $\omega = 0$. **(b)-(e)** energy-momentum cuts of $A(\omega, \mathbf{k})$ for the momenta indicated by the colored lines in (a). Vertical dashed colored line indicates at which momentum $\mathrm{Re}(1/G) = 0$. White lines show the non-interacting dispersion. **(f)** spectral function at the momentum location indicated by dots in (a) or respective lines in (b)-(e). **(g)** the same as (f), but for the imaginary part of the self-energy. Parameters are: $U = 8$, $n = 0.85$, $\beta = 12.5$ and $t' = -0.2$, $t'' = 0.1$.

To better understand the pseudogap and the Fermi arcs we plot several energy-momentum cuts in Fig. 4.16(b)-(e). Furthermore, we show the spectral function $A(\omega)$ (Fig. 4.16(f)) and the imaginary part of the self-energy $\mathrm{Im}\,\Sigma(\omega)$ (Fig. 4.16(g)) for all momenta indicated by colored dots in Fig. 4.16(a). These points are defined by the intersection of the momentum-cut (colored line) and the white line defined by $\mathrm{Re}(1/G) = 0$. For the energy-momentum cut close to the node in Fig. 4.16(b) we observe a simple parabolic dispersion, which is only renormalized compared to the tight-binding one as shown by the white line. The behavior close to the antinode is, however, drastically different as evidenced by the gap-opening in Fig. 4.16(d). Moving along the arc the nodal quasiparticle peak gradually evolves into a two-peak gap-like structure at the antinode, which is displayed in Fig. 4.16(f). This gapped antinode can be understood as two spectral peaks which are separated by a gap Δ. Since we are still at high temperature these peaks are rather broad, which is why the spectral weight does not go to zero at the Fermi energy. Since there is no kind of symmetry breaking in the system, all changes observed are directly related to the self-energy, which develops a peak for small frequencies as shown in Fig. 4.16(g) and already discussed previously.

[23] See Section 4.2.2.

Die approbierte gedruckte Originalversion dieser Dissertation ist an der TU Wien Bibliothek verfügbar.
The approved original version of this doctoral thesis is available in print at TU Wien Bibliothek.

Temperature evolution —— In Fig. 4.16 we discussed the real frequency structure of the pseudogap and the corresponding feature in the self-energy. Let us now discuss the temperature dependence of the Fermi arc in Fig. 4.17. We show again results for the Hubbard model using the DΓA for a filling of $n = 0.85$ and the same tight-binding parameters but for different inverse temperatures $\beta = \{2, 5, 12.5, 22.5\}$. The top row (a)-(d) shows the evolution of the spectrum at the Fermi energy ($A(\mathbf{k}, \omega = 0)$) in the right half of the Brillouin zone, while the left shows the real part of the Green's function (top) and a binary plot of $\mathrm{Re}(1/G)$ in the bottom. We mark points along the arc by colored dots and plot the frequency dependence at those momenta in Fig. 4.17(e)-(h). Red corresponds to the antinode, while blue marks the node. Furthermore, we show energy-momentum cuts moving along the arc from the antinode to the node in Fig. 4.17(i)-(l) and observe several key features. Firstly, let us remark that we see an opening of the pseudogap starting at the antinode and not the hot spots, which is consistent with [139] and ARPES experiments, e.g., [239].

As the temperature is decreased the length of the gapped part along the arc increases as evidenced by the difference between $\beta = 5$ and $\beta = 12.5$. If the temperature is lowered even further, however, even the node displays a gap-like structure, albeit above the Fermi energy and thus not visible in regular ARPES experiments. These features are, however, accessible to inverse ARPES, which measures unoccupied states and hence, performing such measurements would be of great interest. Such a structure of the pseudogap has already previously been observed in cellular DMFT [142] and was supported experimentally by measurements of Raman response in the same article. We will discuss the origin of this behavior in more detail further below. On the other hand, the spectrum at the Fermi energy for $\beta = 22.5$ in Fig. 4.17(d) suggests an electron-like Fermi surface and thus the occurrence of a Lifschitz transition between $\beta = 12.5$ and $\beta = 22.5$. However, the interpretation of electron- and hole-like Fermi surfaces, which we are used to from the non-interacting case, breaks down for the momentum selective insulating behavior in the pseudogap state.

Die approbierte gedruckte Originalversion dieser Dissertation ist an der TU Wien Bibliothek verfügbar.
The approved original version of this doctoral thesis is available in print at TU Wien Bibliothek.
TU Bibliothek Your knowledge hub WIEN

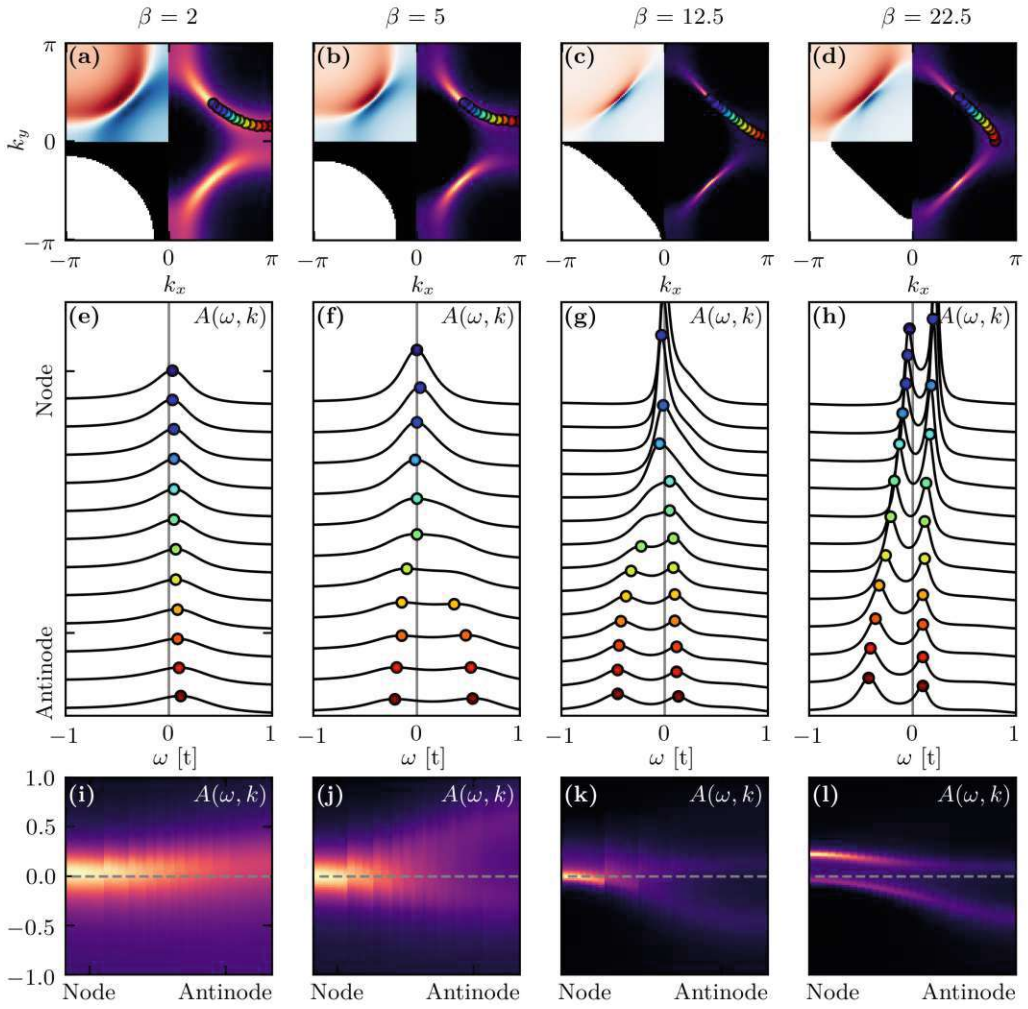

Figure 4.17: Temperature evolution of the pseudogap. Inverse temperature $\beta = \{2, 5, 12.5, 22.5\}$ from left to right. **(a)-(d)** shows the spectral function at the Fermi energy $A(\omega = 0, \mathbf{k})$ in the right half of the BZ and the real part of the Green's function $\mathrm{Re}\, G(\omega = 0, k)$ as colormap (top left) and binary image of $Re(1/G)$ (bottom left). **(e)-(h)** $A(\omega, \mathbf{k}_i)$ for selected momenta $\mathbf{k}_i$ which are also marked as same-colored dots in (a)-(d). Colored dots mark the peaks of $A(\omega, \mathbf{k}_i)$. **(i)-(l)** $A(\omega = 0, \mathbf{k})$ as colormap along the dots in (a)-(d). Parameters are: $U = 8$, $n = 0.85$, $\beta = 12.5$ and $t' = -0.2$, $t'' = 0.1$.

Violation of the Luttinger count and zeros of the Green's function — In the theory of Fermi liquids, Luttinger's theorem [249] states that the volume enclosed by the Fermi surface is equal to the particle number. Its validity has been studied in many systems and we refer the reader to Ref. [250] and references therein for further information.

Before we discuss any violation of Luttinger's theorem in the pseudogap let us first define the necessary terminology. The one-particle Green's function of the electrons in the paramagnetic state is given by,

$$G(\omega, \mathbf{k}) = [\omega - \epsilon(\mathbf{k}) + \mu - \Sigma(\omega, \mathbf{k})]^{-1}, \tag{4.6}$$

Die approbierte gedruckte Originalversion dieser Dissertation ist an der TU Wien Bibliothek verfügbar.
The approved original version of this doctoral thesis is available in print at TU Wien Bibliothek.

where ω is a real frequency, μ the chemical potential, $\Sigma(\omega, \mathbf{k})$ the fermionic self-energy and $\epsilon(\mathbf{k})$ the momentum dispersion of the non-interacting band, which for the $t - t' - t''$ approximation of the square lattice is given by,

$$\epsilon(\mathbf{k}) = -2t[\cos(k_x) + \cos(k_y)] - 4t' \cos(k_x) \cdot \cos(k_y) - 2t''[\cos(2k_x) + \cos(2k_y)]. \quad (4.7)$$

The spectral function $A(\omega, \mathbf{k})$, which is identical to the $\mathbf{k}$-resolved density of states in the non-interacting case, is directly connected to the imaginary part[24] of the Green's function via the simple relation[25],

$$A(\omega, \mathbf{k}) = -\frac{1}{\pi} G''(\omega, \mathbf{k}). \quad (4.8)$$

To set the stage let us revise the properties of the non-interacting system where we set $\Sigma''(\omega) = -i\Delta = -0.02i$, which acts as a finite scattering rate and lifetime for the states[26]. Separating the Green's function into real and imaginary part reads,

$$G(\omega, \mathbf{k}) = \frac{\omega - \epsilon(\mathbf{k}) + \mu - \Sigma'(\omega, \mathbf{k}) + i\Sigma''(\omega, \mathbf{k})}{(\omega - \epsilon(\mathbf{k}) + \mu - \Sigma'(\omega, \mathbf{k}))^2 + (\Sigma''(\omega, \mathbf{k}))^2}, \quad (4.9)$$

which simplifies to,

$$G(\omega, \mathbf{k}) = \frac{\omega - \tilde{\epsilon}(\mathbf{k}) - i\Delta}{(\omega - \tilde{\epsilon}(\mathbf{k}))^2 + (\Delta)^2}, \quad (4.10)$$

for the non-interacting case we are considering here. We furthermore absorb the chemical potential and the real part of the self-energy (which is 0 for now) into ϵ and call this the "quasiparticle dispersion" (QPD) $\tilde{\epsilon}(\mathbf{k}) = \epsilon(\mathbf{k}) - \mu + \Sigma'(\omega, \mathbf{k})$. Combining Eq. 4.10 and Eq. 4.8 we see that the momentum resolved spectrum is a collection of Lorentzian distributions centered around ω^*, defined as the solution to

$$\omega - \tilde{\epsilon}(\mathbf{k}) = 0, \quad (4.11)$$

and a peak height of $1/\Delta$. The real part of the Green's function, on the other hand, is exactly zero at ω^*. In the simple case, we consider here, and quite generally as long as Σ' does not depend on ω, G' will also have an opposite sign above and below ω^*. Furthermore, a local maximum (minimum) of magnitude $1/(2\Delta)$ will appear Δ above (below) ω^*. As a results G' has a pole at ω^* in the limit of $\Delta \to 0$ and the allowed states are simply given by $\omega = \epsilon(\tilde{\mathbf{k}})$. What we just described is, of course, a rather trivial example, but will serve as a perfect starting point for the following discussion and the

[24] In the following we will always write complex quantities as $C = C' + iC'' \equiv \mathrm{Re}(C) + i\,\mathrm{Im}(C)$. This should not be confused with the hopping parameters $t - t' - t''$, which are still real numbers.
[25] See also Section 3.1 for further information on the single-particle Green's function.
[26] We use a finite $\Sigma''(\omega)$ merely to avoid complications in numeric evaluations of the Green's function.

Die approbierte gedruckte Originalversion dieser Dissertation ist an der TU Wien Bibliothek verfügbar.
The approved original version of this doctoral thesis is available in print at TU Wien Bibliothek.
TU Bibliothek Your knowledge hub WIEN

type of plots we use. For the non-interacting case described we show the real part of the Green's function along a high-symmetry path in the Brillouin zone (BZ) in Fig. 4.18(a). Here and in the following, the special momentum points are defined as $\Gamma = (0,0,0)$, $X = (\pi,0,0)$ and $M = (\pi,\pi,0)$. Fig. 4.18(a) also shows the spectral function $A(\omega,\mathbf{k})$ as a scatter plot (yellow dots) for all points that satisfy Eq. 4.11. The size and the color is proportional to the respective value of $A(\omega,\mathbf{k})$. Unsurprisingly, for our simple case of a frequency and momentum-independent self-energy, depicted in panel (b), all dots have the same color and size. Fig. 4.18(d) and (e) display the frequency dependence of G' and A at selected momenta, which are indicated in (a) by lines of the same color as A in (d)-(e). Dots of the same color mark ω^*. Fig. 4.18(c) shows G' at $\omega = 0$, which in our convention is identical to the Fermi energy. In the lower left quadrant of the BZ we mark in green the momentum region which satisfies $-0.2 < \mathrm{Re}(1/G) < 0.2$, i.e. a small region around the Fermi surface. And finally, panel (f) shows the spectral function $A(\omega,\mathbf{k})$ integrated over three parts of the BZ, which are marked in color (blue, green, red) and match the colorcode of Fig. 4.18(c). Generally speaking we split all points of the first BZ (1BZ) into one of three sets defined by,

$$\Omega_1 = \{(k_x,k_y) \in 1\mathrm{BZ} : \mathrm{Re}(1/G(\omega=0,k_x,k_y)) > 0.2\}; \quad \text{blue}, \tag{4.12}$$

$$\Omega_2 = \{(k_x,k_y) \in 1\mathrm{BZ} : 0.2 >= \mathrm{Re}(1/G(\omega=0,k_x,k_y)) >= -0.2\}; \quad \text{green}, \tag{4.13}$$

$$\Omega_3 = \{(k_x,k_y) \in 1\mathrm{BZ} : -0.2 > \mathrm{Re}(1/G(\omega=0,k_x,k_y))\}; \quad \text{red}. \tag{4.14}$$

As we can see from Fig. 4.18(f) these disjointed sets of momenta also separate the corresponding spectral function $A_i(\omega) = \int_{\Omega_i} d\mathbf{k} A(\omega,\mathbf{k})$ for $i \in \{1,2,3\}$ in frequency space[27]. Indeed, A_1 (blue) corresponds to the spectrum below the Fermi energy (E_F), A_2 (green) to the one at (or close to) E_F and A_3 (red) to those above. It is from this picture that we can easily understand the terminology of hole-like and electron-like Fermi surfaces (FS). In our present case, the Fermi surface (four arcs of high contrast in Fig. 4.18(c)) encloses empty states (red) and one speaks of a hole-like FS. Furthermore, the red (blue) region contains exclusively empty (occupied) states[28]. Here the equivalence of the Luttinger count (LC), defined by

$$\mathrm{LC} = \int_{1\mathrm{BZ}} d\mathbf{k}\Theta(G'(\omega=0,\mathbf{k})) \simeq \frac{1}{N_k}\sum_{\mathbf{k}}^{1\mathrm{BZ}} \Theta(G'(\omega=0,\mathbf{k})), \tag{4.15}$$

where Θ is the Heaviside step function, and the particle number per spin n,

$$n = \int d\omega \mathrm{n_F}(\omega) A(\omega) \overset{\mathrm{T\ small}}{\simeq} \int_{-\infty}^{0} d\omega A(\omega), \tag{4.16}$$

becomes quite intuitive[29].

[27] Aside from some small overlap due to the finite width of the Lorentzian peaks.
[28] Again ignoring the small width of the Lorentzians.
[29] In his seminal paper [249] J. M. Luttinger did not show that this relation holds in the non-interacting

Die approbierte gedruckte Originalversion dieser Dissertation ist an der TU Wien Bibliothek verfügbar.
The approved original version of this doctoral thesis is available in print at TU Wien Bibliothek.

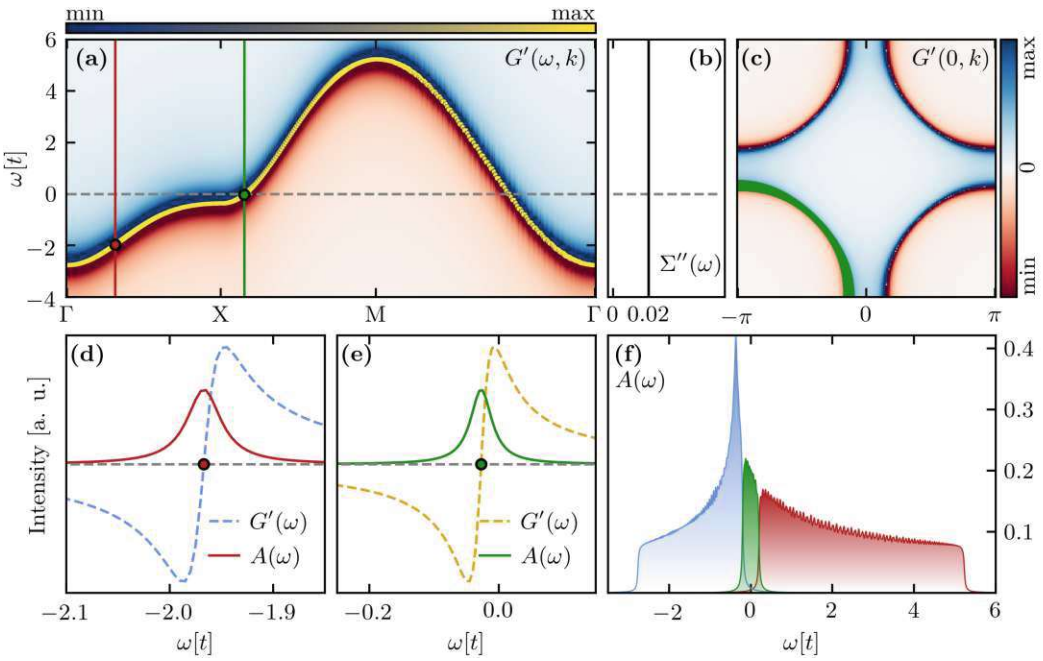

Figure 4.18: Visualization of the spectrum and real part of the Green's function G' for a simple frequency and momentum independent self-energy $\Sigma = -0.02\,i$. For a more detailed discussion see the main text. **(a)** G' along a high symmetry path in the BZ. On top (yellow dots) we show the spectral function $A(\omega, \mathbf{k})$ at all locations that satisfy $\mathrm{Re}(1/G) = 0$. Color and marker size is proportional to the respective value of $A(\omega, \mathbf{k})$; which, for the constant model self-energy is however always the same and just follows the non-interacting energy-momentum dispersion. **(b)** imaginary part of the self-energy Σ''. **(c)** G' at $\omega = 0$. Green region in the lower left quadrant marks where $-0.2 <= \mathrm{Re}(1/G) <= 0.2$. **(d)** frequency dependence of G' and A at a selected $\mathbf{k}$-vector, which is also indicated in (a) by a red vertical line. **(e)** same as (e) but for $\mathbf{k}$ marked by the green line in (a). **(f)** $A_i(\omega) = \int_{\Omega_i} d\mathbf{k} A(\omega, \mathbf{k})$ for $i \in \{1, 2, 3\}$ corresponding to blue, green and red, respectively. Ω_i is defined in Eq. 4.14. Parameters of the model are: $t = 1$, $t' = -0.2$, $t'' = 0.1$ and the filling is set to 0.9.

After revising the non-interacting case to set the stage, let us now turn on interactions. Fig. 4.19 shows conceptually the same plots as Fig. 4.18, but for the DMFT solution of the same tight-binding model with an on-site Hubbard interaction $U = 8t$ and at inverse temperature $\beta/t = 17.5$. The obtained local self-energy, displayed in Fig. 4.19(b), displays a strong frequency dependence, with large peaks both above and below the Fermi energy. It remains, however, small around $\omega = 0$. While the self-energy looks unassuming at first glance, the structure of the Green's function in Fig. 4.19 has changed quite dramatically. In addition to a band, somewhat resembling the non-interacting one, though with a considerably reduced bandwidth, new structures appear at much higher energies. These are commonly called Hubbard bands and are better visible as the satellites in the $\mathbf{k}$-integrated spectrum displayed in Fig. 4.19.

case (which was well known), but rather that the volume enclosed by the Fermi surface does not change in the presence of interactions, as long as the self-energy vanishes at the Fermi energy $\lim_{\omega\to 0} \Sigma(\omega, \mathbf{k}) = 0$. For a more detailed discussion see Ref. [250].

Die approbierte gedruckte Originalversion dieser Dissertation ist an der TU Wien Bibliothek verfügbar.
The approved original version of this doctoral thesis is available in print at TU Wien Bibliothek.

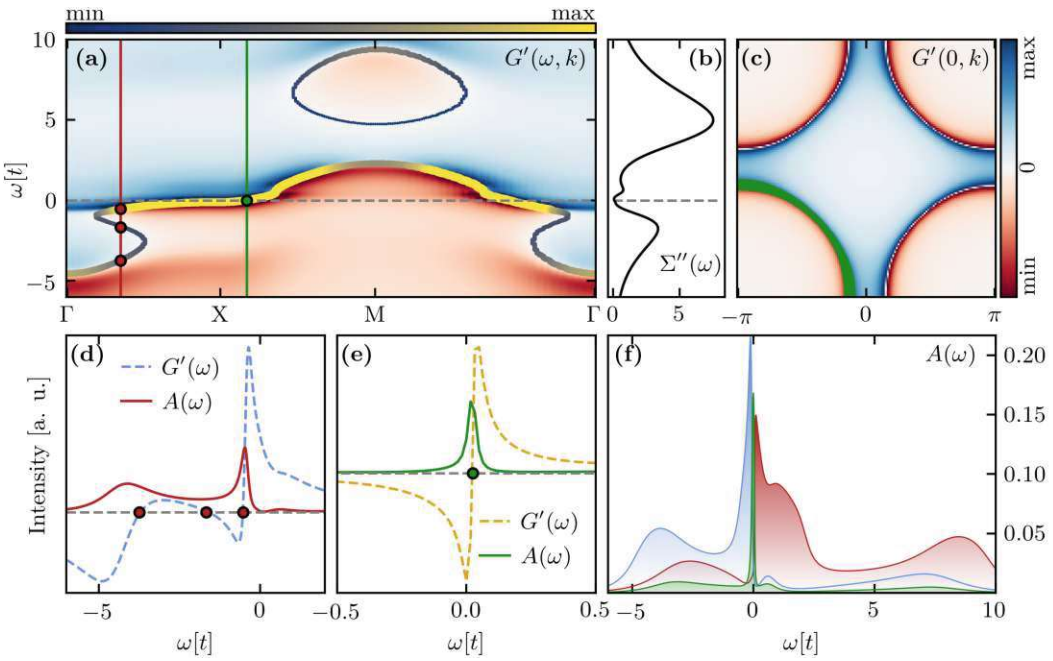

Figure 4.19: Visualization of the DMFT spectrum and real part of the Green's function G' similar as in Fig. 4.18. For a more detailed discussion see the main text. **(a)** G' along a high symmetry path in the BZ. On top (yellow dots) we show the spectral function $A(\omega, \mathbf{k})$ at all locations that satisfy $\mathrm{Re}(1/G) = 0$. Color and marker size is proportional to the respective value of $A(\omega, \mathbf{k})$. **(b)** imaginary part of the self-energy Σ''. **(c)** G' at $\omega = 0$. Green region in the lower left quadrant marks where $-0.2 <= \mathrm{Re}(1/G) <= 0.2$. **(d)** frequency dependence of G' and A at a selected $\mathbf{k}$-vector, which is also indicated in (a) by a red vertical line. **(e)** same as (e) but for $\mathbf{k}$ marked by the green line in (a). **(f)** $A_i(\omega) = \int_{\Omega_i} d\mathbf{k} A(\omega, \mathbf{k})$ for $i \in \{1, 2, 3\}$ corresponding to blue, green and red, respectively. Ω_i is defined in Eq. 4.14. Parameters of the model are: $t = 1$, $t' = -0.2$, $t'' = 0.1$, $U = 8$, the filling is set to 0.85 and the calculation performed at inverse temperature $\beta = 22.5$.

Let us state several observations and then discuss them in more detail: (i) Eq. 4.11 can have more then a single solution for a given momentum vector, as seen in panel (d). (ii) the Hubbard bands do not span the entire momentum region for the considered parameters, i.e. the number of solutions for Eq. 4.11 can differ for different $\mathbf{k}$-vectors. (iii) the real part of the Green's function not only changes its sign via a pole[30], but also by smoothly going through zero as for the middle red dot in panel (d). The first observation is a direct result of the frequency dependence of the self-energy, which results in a frequency-dependent quasiparticle dispersion $\tilde{\epsilon}(\omega, \mathbf{k})$. While this is per se certainly not surprising, it does complicate the interpretation of $\tilde{\epsilon}$. In the non-interacting case $\tilde{\epsilon}(\mathbf{k})$ was simply the energy associated with a certain momentum state, which is clearly no longer the case. Through the poles in the self-energy one gets several excitations where Eq. 4.11. The central one (close to $\omega = 0$) with $\Sigma'' \sim 0$ is a quasiparticle excitation, while the additional one(s) are the excitations in the Hubbard bands with a large Σ'', i.e.. a short lifetime. These additional solutions to Eq. 4.11 make the broad oval structures below the Γ- and above the M point in Fig. 4.19(a), known as Hubbard bands. The

[30] Strictly speaking G' only has a true pole at $T = 0$, or when the self-energy is zero at an energy-momentum location that satisfies $\omega - \tilde{\epsilon}(\omega, \mathbf{k}) = 0$. Nevertheless, we will refer to the structure in Fig. 4.18(d)-(e) as "poles" and the one for the middle red dot in Fig. 4.19(d) as "zeros".

Die approbierte gedruckte Originalversion dieser Dissertation ist an der TU Wien Bibliothek verfügbar.
The approved original version of this doctoral thesis is available in print at TU Wien Bibliothek.
TU Bibliothek Your knowledge hub WIEN

large ω side of the Hubbard bands corresponds to "poles" of the Green's function with an accompanying peak in the spectral weight, while the other half corresponds to "zeros" and is not visible as a distinct feature in the spectral function. While for this parameter set the "poles" of the Hubbard bands are above (below) E_F when the quasiparticle band is above (below) E_F, they still show residual incoherent weight below (above) E_F. This can be seen in Fig. 4.19(f) where we use the same three sets of momentum points as previously defined in Eq. 4.14. Consider for example the red (blue) shaded part, i.e. what would be empty (occupied) states in the non-interacting case, now acquired weight below (above) the Fermi energy. This spectral weight does not correspond to "poles" (or "zeros") in G', is smeared in frequency and thus not visible as a distinct feature in the spectral function, which is why we will refer to it as incoherent part of the spectrum in the following. Furthermore, since a positive (negative) sign in $G'(\omega = 0)$ no longer means that (almost) all of the spectral weight is concentrated below (above) E_F the equivalence of the Luttinger count (Eq. 4.15) and the particle number (Eq. 4.16) is also no longer self-evident. Nevertheless, following Luttinger's seminal paper [249] one can show that this relation still holds in the limit $\lim_{\omega\to 0}\Sigma(\omega) \to 0$, a theorem we refer to as "Luttinger's theorem". While the proof is for $T = 0$, empirically we find that as long as Σ remains small around $\omega = 0$ this relation is obeyed within the resolution of our approach.

The DΓA solution in the pseudogap regime, however, behaves quit different altogether. Fig. 4.20 shows, with small changes, plots of the same style as before, but for the DΓA solution of the same Hubbard model. Features of the pseudogap around the X momentum are clearly visible as a gapped spectrum in Fig. 4.20(d) and the momentum-integrated spectral function $A(\omega)$ shows the characteristic depression around the Fermi surface, as shown in Fig. 4.20(f) (gray shaded). This antinodal gap is a direct result of a low-frequency peak at, or slightly below, E_F in the self-energy which can be seen in Fig. 4.20(b) (red curve). Furthermore, and possibly less studied previously, is the "S"-shaped feature visible in G' around the X momentum. As a result of the gap-opening the "poles" of the Green's function are pushed above and below E_F, and "zeros" appear at $\omega = 0$ where previously poles were. For a Mott insulator this would neither be unexpected nor unusual, however for the pseudogap on the other hand "poles" at $\omega = 0$ still exist, albeit for different momenta, which are located around the node as displayed in Fig. 4.20(e). As a result we observe at $\omega = 0$ a gradual transition from "poles" at the node to "zeros" at the antinode. In a correlated metal the Fermi surface is the locus of all points satisfying Eq. 4.11, which are also "poles" of the Green's function. A Mott insulator, while clearly not having a well defined Fermi surface in the usual sense, displays "zeros" of the Green's function at $\omega = 0$ instead. This is usually referred to as "Luttinger surface" (LS). In the pseudogap we observe a connected surface satisfying Eq. 4.11, displayed in the lower two quadrants of Fig. 4.20(c). The crucial point is now that it changes its character from a Fermi surface to a Luttinger surface, corresponding to metallic and insulating behavior, respectively. It was noted in previous publications that one way to break Luttinger theorem is the appearance of Luttinger surfaces [250, 251]. Indeed, here we observe that the Luttinger count (LC ~ 0.75) underestimates the number of electrons in the system ($n = 0.85$) by about ~ 0.1. This is because around the X-momentum the "pole" of the Green's function is deformed into three zero crossings of G', which induces an additional sign change slightly below E_F (see panel (d)). As a

Die approbierte gedruckte Originalversion dieser Dissertation ist an der TU Wien Bibliothek verfügbar.
The approved original version of this doctoral thesis is available in print at TU Wien Bibliothek.
TU Bibliothek Your knowledge hub WIEN

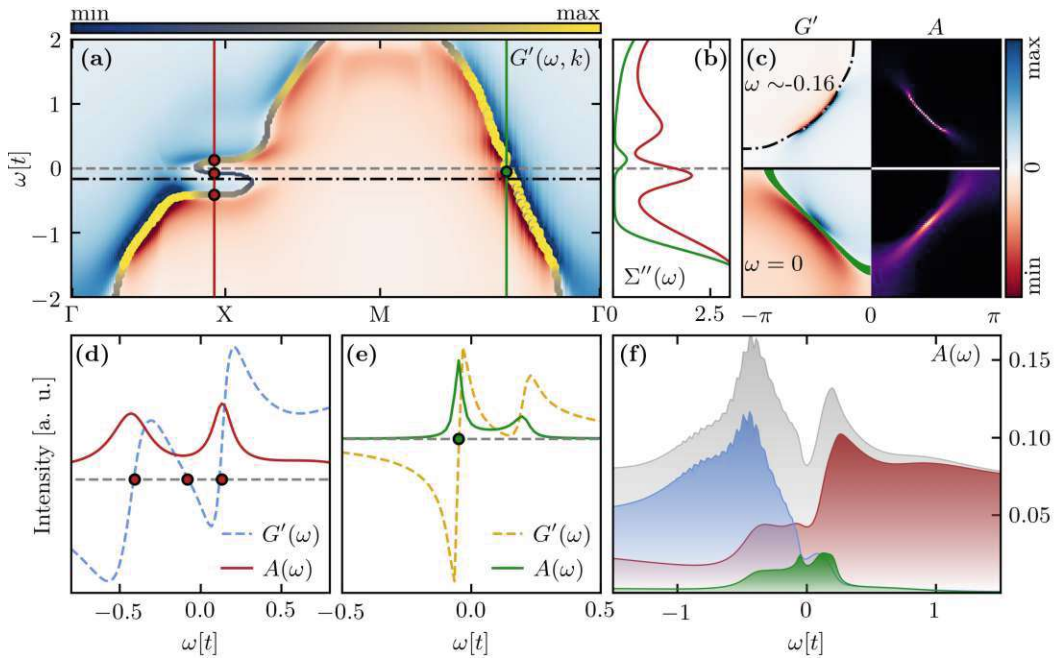

Figure 4.20: Visualization of the DΓA spectrum and real part of the Green's function G'. For a more detailed discussion see the main text. **(a)** G' along a high symmetry path in the BZ. On top (yellow dots) we show the spectral function $A(\omega, \mathbf{k})$ at all locations that satisfy $\mathrm{Re}(1/G) = 0$. Color and marker size is proportional to the respective value of $A(\omega, \mathbf{k})$. **(b)** imaginary part of the self-energy Σ'' at the same momenta picked for (d) (red) and (e) (green). **(c)** Lower half of the BZ displays A (left) G' (right) at $\omega = 0$, while top shows the same but for $\omega = -0.16$. Green region in the lower left quadrant marks where $-0.2 <= \mathrm{Re}(1/G) <= 0.2$. **(d)** frequency dependence of G' and A at a selected $\mathbf{k}$-vector, which is also indicated in (a) by a red vertical line. **(e)** same as (e) but for $\mathbf{k}$ marked by the green line in (a). **(f)** $A_i(\omega) = \int_{\Omega_i} d\mathbf{k} A(\omega, \mathbf{k})$ for $i \in \{1, 2, 3\}$ corresponding to blue, green and red, respectively. Ω_i is defined in Eq. 4.14. Parameters of the model are: $t = 1$, $t' = -0.2$, $t'' = 0.1$, $U = 8$, the filling is set to 0.85 and the calculation performed at inverse temperature $\beta = 22.5$.

result, the sign of the Green's function is negative and the LC counts the momentum as empty, even though roughly half of the spectral weight is occupied. In Fig. 4.20(c) upper part, we can see that a hole-like "Fermi surface" is recovered just below the Fermi energy which is also accompanied by Fermi arcs in the spectrum. Next, we will discuss a simple self-energy that qualitatively captures the pseudogap and the violation of Luttinger's theorem.

Simple self-energy to break Luttinger's theorem — The main features which distinguished the PG in Fig. 4.20 from a strongly correlated metal as in Fig. 4.19 were a (i) strong momentum anisotropy and (ii) a peak in Σ'' just below E_F. To model this behavior we use the following self-energy:

$$\Sigma''_{LC}(\omega, \mathbf{k}) = \frac{-\Sigma_0}{1 + \sigma|\omega - \omega_0|^2} \cdot (\cos k_x - \cos k_y)^2 - \Delta, \tag{4.17}$$

where $\Sigma_0 = 0.6$ determines the magnitude and $\omega_0 = -0.3$ the shift of the peak, $a = 10$ the width of the peak and $\Delta = 0.02$ a constant isotropic scattering rate. The first

Die approbierte gedruckte Originalversion dieser Dissertation ist an der TU Wien Bibliothek verfügbar.
The approved original version of this doctoral thesis is available in print at TU Wien Bibliothek.
TU Bibliothek Your knowledge hub WIEN

factor of the first addend captures (ii), while the second factor captures the momentum anisotropy (i). Furthermore, to obtain the real part we use the Kramers-Kronig relations. Let us note that the precise form of Eq. 4.17 does not matter for the following discussion as long as it satisfies (i) and (ii); Σ'' in Eq 4.17 is the imaginary part of a pole-like self-energy with momentum dependent weight plus a constant scattering rate Δ. The latter is not important for the discussion and only ensures that G is numerically well defined[31].

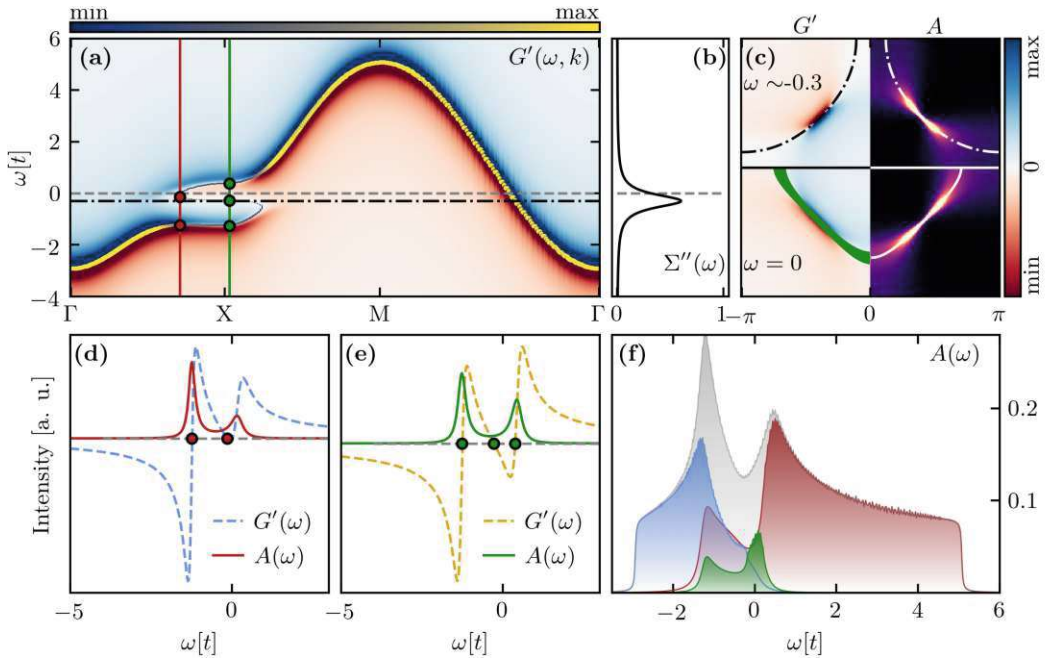

Figure 4.21: Visualization of the spectrum and real part of the Green's function G' for the LC violating self-energy of Eq. 4.17. For a more detailed discussion see the main text. **(a)** G' along a high symmetry path in the BZ. On top (yellow dots) we show the spectral function $A(\omega, \mathbf{k})$ at all locations that satisfy $\mathrm{Re}(1/G) = 0$. Color and marker size is proportional to the respective value of $A(\omega, \mathbf{k})$. **(b)** imaginary part of the self-energy Σ'' at the same momenta picked for (d) (red) and (e) (green). **(c)** Lower half of the BZ displays A (right) and G' (left) at $\omega = 0$, while top left shows G' for $\omega = -0.3$. Green region in the lower left quadrant marks where $-0.2 <= \mathrm{Re}(1/G) <= 0.2$. **(d)** frequency dependence of G' and A at a selected $\mathbf{k}$-vector, which is also indicated in (a) by a red vertical line. **(e)** same as (e) but for $\mathbf{k}$ marked by the green line in (a). **(f)** $A_i(\omega) = \int_{\Omega_i} d\mathbf{k} A(\omega, \mathbf{k})$ for $i \in \{1, 2, 3\}$ corresponding to blue, green and red, respectively. Ω_i is defined in Eq. 4.14. Parameters of the model are: $t = 1$, $t' = -0.2$, $t'' = 0.1$, and the filling is set to 0.85. Parameters of the self-energy (Eq. 4.17) are $\Delta = 0.02$, $\Sigma_0 = 0.6$, $\sigma = 10$ and $\omega_0 = -0.3$.

We display the frequency-dependent part of Σ''_{LC} in Fig. 4.21(b) and the corresponding real part of the Green's function $G'(\omega, \mathbf{k})$ in Fig. 4.21(a). For large frequencies $\Sigma''_{LC} \to -0.2i$, we recover the tight-binding solution as in Fig. 4.18, i.e. the Wannier band with a finite broadening. Close to the Fermi energy and around the X momentum, Fig. 4.18(a) and momentum cuts in Fig. 4.18(d)/(e), where $(\cos k_x - \cos k_y)^2$ is largest we see the

[31] The momentum dependent part of Eq. 4.17 goes to 0 at the node the Green's function develops an actual pole. While this is fine on paper, it creates problems for numerical calculations and thus we introduce Δ to avoid this issue.

Die approbierte gedruckte Originalversion dieser Dissertation ist an der TU Wien Bibliothek verfügbar.
The approved original version of this doctoral thesis is available in print at TU Wien Bibliothek.
TU Bibliothek Your knowledge hub WIEN

same pseudogap structure as before for the DΓA result in Fig. 4.20, which is also visible as the characteristic dip in the spectral function in Fig. 4.21(f). Moreover, Luttinger's theorem is violated by 0.22 electrons and we observe a transition from "poles" to "zeros" at $\omega = 0$.

Discussion — The appearance of Fermi arcs, i.e. disconnected Fermi surface segments, has puzzled many researchers in the last decades. Specifically, from a simple non-interacting point of view, the Fermi surface simply cannot abruptly end and Fermi surface reconstruction in the form of nodal hole pockets has been proposed as a solution, see e.g. [252]. However, ARPES experiments repeatedly failed to find the "hidden" backside of the pockets[32]. Here by studying the Hubbard model for parameters relevant to cuprates using DΓA, we found that the pseudogap can be understood as a momentum-selective insulator. The gap originates from antiferromagnetic spin fluctuations and is significantly smaller than the Mott-Hubbard gap. Furthermore, we find that the Fermi surface at the node gradually transitions into a Luttinger surface at the antinode, which resolves the conceptual need for a connected Fermi surface. Additionally, we observed that the Luttinger theorem (LT) is violated and constructed a simple self-energy that reproduces this observation. The key here is that the momenta which are gapped (i.e. close to the antinode), can be viewed as not particle-hole symmetric insulators, which are prone to violate Luttinger's theorem. Nevertheless, one should note that the formation of Fermi arcs does not imply the violation of Luttinger's theorem (LT). In particular, if $\omega_0 = 0$, i.e. the peak of the self-energy is centered directly at E_F and the spectral function is particle-hole symmetric, we still find Fermi arcs and a transition from a Fermi surface to a Luttinger surface, but no violation of LT. We display this scenario in Fig. 4.22.

[32] One should note that Fermi pockets together with a Fermi arc were measured by Kunisada *et al.* [15]. The authors attribute the pockets to antiferromagnetic order and argue that the Fermi arc is real since they fail to measure its supposed backside as well.

Die approbierte gedruckte Originalversion dieser Dissertation ist an der TU Wien Bibliothek verfügbar.
The approved original version of this doctoral thesis is available in print at TU Wien Bibliothek.
TU Bibliothek Your knowledge hub WIEN

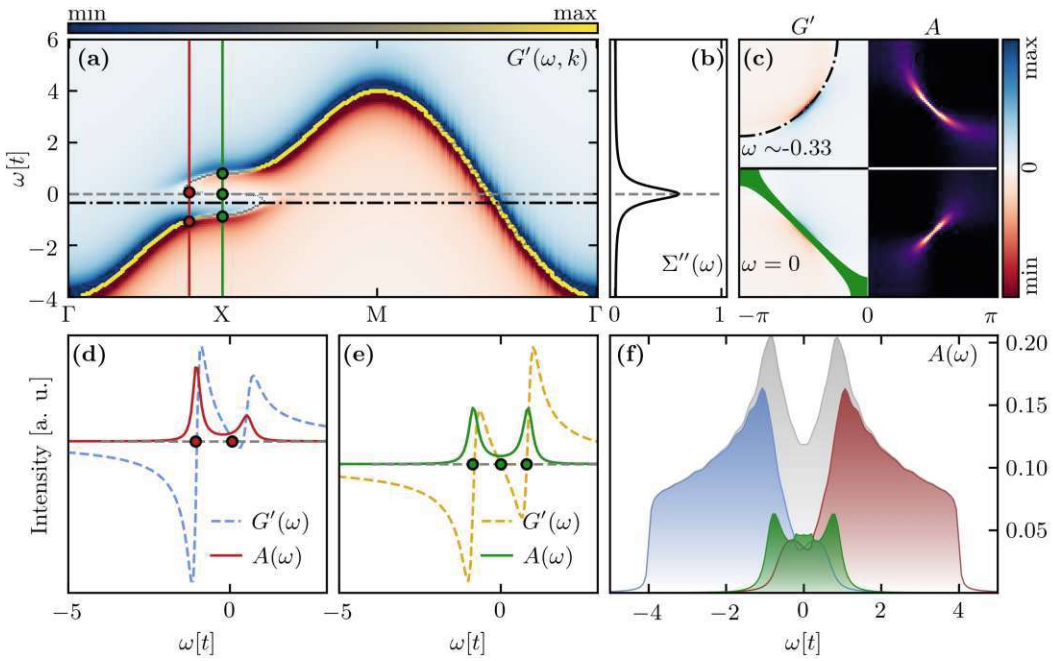

Figure 4.22: Visualization of the spectrum and real part of the Green's function G' using the self-energy of Eq. 4.17, but for the particle-hole symmetric case. **(a)** G' along a high symmetry path in the BZ. On top (yellow dots) we show the spectral function $A(\omega, \mathbf{k})$ at all locations that satisfy $\mathrm{Re}(1/G) = 0$. Color and marker size is proportional to the respective value of $A(\omega, \mathbf{k})$. **(b)** imaginary part of the self-energy Σ'' at the same momenta picked for (d) (red) and (e) (green). **(c)** Lower half of the BZ displays A (right) and G' (left) at $\omega = 0$, while top left shows G' for $\omega = -0.33$. Green region in the lower left quadrant marks where $-0.2 <= \mathrm{Re}(1/G) <= 0.2$. **(d)** frequency dependence of G' and A at a selected $\mathbf{k}$-vector, which is also indicated in (a) by a red vertical line. **(e)** same as (e) but for $\mathbf{k}$ marked by the green line in (a). **(f)** $A_i(\omega) = \int_{\Omega_i} d\mathbf{k} A(\omega, \mathbf{k})$ for $i \in \{1, 2, 3\}$ corresponding to blue, green and red, respectively. Ω_i is defined in Eq. 4.14. Parameters of the model are: $t = 1$, $t' = -0.0$, $t'' = 0.0$, and the filling is set to 1.0. Parameters of the self-energy (Eq. 4.17) are $\Delta = 0.02$, $\Sigma_0 = 0.6$, $\sigma = 10$ and $\omega_0 = -0.0$.

4.3.3 Nesting as origin of the "s-wave" structure of the pseudogap

Moving on, we turn back to the discussion of the "s-wave" structure of the pseudogap. As displayed in Fig. 4.17(h)/(l), the pseudogap we observe for the Hubbard model using DΓA develops, at sufficiently low temperatures, a gap-like behavior for all momenta along the arc. This "s-wave" structure has already previously been observed for the Hubbard model, albeit using a different method, namely CDMFT [142]. This observation prompted the authors of Ref. [142] to argue for a "s-wave" pseudogap. Here we would like to refine this picture and discuss the origin of this behavior.

It is important to note that the energy location of the gap is momentum dependent. This leads to a gap above E_F for the node, while below E_F at the antinode. As a result, the pseudogap *at the Fermi energy* displays a "d-wave" structure consistent with ARPES measurements, see e.g. [14–16]. From a theoretical perspective, since the gap is at $\omega > 0$, it is not directly visible on the Matsubara axis, at least not like the characteristic downturn of the antinodal pseudogap in Fig. 4.14(d) [126]. Furthermore, while a gap appears for all momenta along the node its magnitude still shows a strong momentum

Die approbierte gedruckte Originalversion dieser Dissertation ist an der TU Wien Bibliothek verfügbar.
The approved original version of this doctoral thesis is available in print at TU Wien Bibliothek.
TU Bibliothek Your knowledge hub WIEN

dependence. This is even more pronounced at higher temperatures, where a gap is clearly visible at the antinode, but still absent around the node (Fig. 4.17(f)/(g)). Consequently, this "s-wave" structure only appears below a certain temperature T_s (see Fig. 4.17). At $T > T_s$ we observe a "true" d-wave structure of the pseudogap.

Considering all of the observations above, the pseudogap below T_s is not purely "d-wave" like, since a gap exists at all momenta. At the same time, however, the magnitude of the gap as well as its location in frequency space is strongly momentum anisotopic, which are not properties typically attributed to an "s-wave" gap. The pseudogap is hence somewhere in between. Further research is required to determine whether the pseudogap is a combination of a *frequency-dependent* "s-wave" gap combined with a frequency-independent "d-wave" gap.

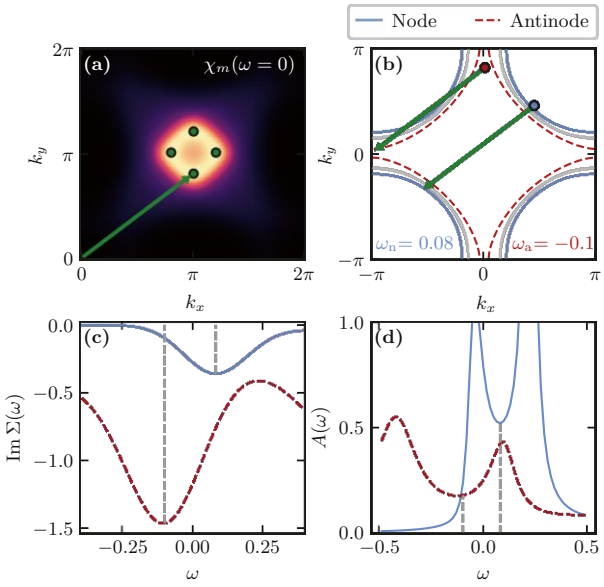

Figure 4.23: Connection of the "s-wave" pseudogap with the peak in the self-energy. **(a)** incommensurate zero-frequency magnetic susceptibility $\chi_\mathrm{m}(\omega = 0)$. Green dots mark the maxima. **(b)** contour lines which correspond to $\mathrm{Re}(1/G^\mathrm{DMFT}) = 0$ for three frequencies $\omega = 0$ (gray), $\omega = 0.08$ (blue) and $\omega = -0.1$ (red). The latter frequencies correspond to the position of the pseudogap in the self-energy at the note and antinode, respectively. Green arrows show the nesting vectors which connect the DΓA node/antinode (dot) with the DMFT spectrum. **(c)** Imaginary part of the self-energy at the antinode (red) and node (blue). Vertical dashed gray lines mark the peak locations. **(d)** DΓA Spectral function $A(\omega)$ at the antinode (red) and node (blue). Vertical dashed gray lines mark the energy of the self-energy peak from (c).

Regarding the origin of this momentum structure, we find that nesting plays a key role, which we display in Fig. 4.23. To obtain the momentum vector corresponding to antiferromagnetic fluctuations we display the magnetic susceptibility $\chi_\mathrm{m}(\omega = 0)$ in Fig. 4.23(a) and mark the peak locations by a green dot. Due to the relatively large doping of 15% the spin-fluctuations are already incommensurate and the peak is no longer located at $\mathbf{k} = (\pi, \pi)$, but at $\mathbf{k}_\mathrm{peak} \simeq (3.16, 2.5)$. To connect $\mathbf{k}_\mathrm{peak}$ with the peak in the self-energy responsible for the pseudogap we plot the imaginary part of the DΓA self-energy at the node (blue) and antinode (red) in Fig. 4.23(c) and the DΓA spectral function $A(\omega)$ in Fig. 4.23(d). The vertical dashed gray lines mark the frequency of the peak location of the self-energy which are at $\omega_\mathrm{n} = 0.08$ (node), $\omega_\mathrm{a} = -0.1$ (antinode). Fig. 4.23(b) displays a contour where $\mathrm{Re}(1/G^\mathrm{DMFT}(\omega)) = 0$ for the previously determined frequencies. At this point, it is important to note that λ-corrected DΓA performs no self-consistency for the propagators and it is the DMFT Green's function that enters the Schwinger-Dyson equation Eq. 3.72, solved to obtain the self-energy. We additionally mark the momenta of the node (blue) and antinode (red) in DΓA with colored dots and draw the vector $\mathbf{k}_\mathrm{peak}$ of the antiferromagnetic correlations originating from them. As we can see the arrows connect the DΓA node/antinode with

Die approbierte gedruckte Originalversion dieser Dissertation ist an der TU Wien Bibliothek verfügbar.
The approved original version of this doctoral thesis is available in print at TU Wien Bibliothek.
TU Bibliothek Your knowledge hub WIEN

the DMFT spectrum. This shows that the frequency of the peak in the self-energy coincides with the frequency at which the nesting condition is satisfied.

While this analysis shows that the frequency location of the gap along the arc is directly connected to the frequency where the nesting condition is satisfied, one should note that the lack of self-consistency in DΓA is expected to overestimate nesting physics. Nonetheless, a similar behavior was found in CMDFT [142] which does not exhibit this bias.

4.4 Possibility of cuprates without two-dimensionality

Almost all known cuprate superconductors display a set of common features: (i) vicinity to a Cu $3d^9$ configuration; (ii) separated CuO_2 planes; (iii) superconductivity for doping $\delta \sim 0.1-0.3$. Recently the authors of Ref. [253] discovered an exception to this "rule", namely "highly overdoped" superconducting Ba_2CuO_{3+y}. Using DFT + DMFT we reveal a bilayer structure of $Ba_2CuO_{3.2}$ of alternating quasi-2D and quasi-1D character. Correlations tune an inter-layer self-doping leading to an almost half-filled, strongly nested quasi-1D $d_{b^2-c^2}$ band, which is prone to strong antiferromagnetic fluctuations, possibly at the origin of superconductivity in Ba_2CuO_{3+y}.

The following section, marked by a vertical bar, has already been published in Physical Review B 105 (8), 085110 (2022) [143].

4.4.1 Introduction

Even 35 years after the discovery of high-temperature superconductivity in cuprates [11], the pairing mechanism remains highly controversial. In this respect, the recently discovered cuprate $Ba_2CuO_{3.2}$ [253] is supremely exciting as it puts into question common wisdom for cuprate high-temperature superconductivity. The oxygen reduction from Ba_2CuO_4 to polycrystalline Ba_2CuO_{3+y} was achieved by synthesizing the samples at extremely high pressure ($\sim$ 18 GPa) and high temperature ($\sim$ 1000° C). Unusual is, first of all, the hole concentration in the superconducting $y \sim 0.2$ phase which has $\delta = 2y = 0.4$ holes with respect to a Cu $3d^9$ electronic configuration. This is twice as many holes as in other superconducting cuprates. Despite this unusual doping the critical temperature $T_c = 70$ K is high [253].

Second, a La_2CuO_4-type structure with space group I4/mmm was suggested by the authors of [253], with a compressed oxygen octahedron, contrary to an elongated one. This compression also pushes the $3z^2 - r^2$ orbital, that is fully occupied in other cuprates, up in energy. More recent experiments [254] report, however, x-ray absorption (XAS) and resonant inelastic x-ray scattering (RIXS) data, incompatible with the La_2CuO_4 structure. These results [254] require two inequivalent Cu sites, proposing a bilayer structure. Unfortunately, single crystals have not yet been synthesized. This leaves quite an uncertainty even for the crystal structure and different ones have been suggested [253–

Die approbierte gedruckte Originalversion dieser Dissertation ist an der TU Wien Bibliothek verfügbar.
The approved original version of this doctoral thesis is available in print at TU Wien Bibliothek.
TU Bibliothek Your knowledge hub WIEN

259].

Guided by the experimental results and previous density-functional theory (DFT) calculations [255], we investigate the electronic structure of the three crystal structures of Fig. 4.24: (a) the parent compound Ba_2CuO_4, (b) the fully reduced material Ba_2CuO_3, and (c) a bilayer-structure $Ba_2CuO_{3.25}$. The last structure has an oxygen deficiency (excess) of 0.75 ($y = 0.25$) compared to the structure of panel Fig. 4.24(a) ((b)). It is close to $y = 0.2$ but can be realized in a smaller 2×2×1 unit cell by removing three oxygens (adding one oxygen). To find the ground state structure of Ba_2CuO_{3+y} near y=0.2, we consider all variations proposed in previous studies [255, 259] and find the bilayer structure of Fig. 4.24(c) to be the energetically most favorable among all possible 2×2×1 super cells with 8 Cu sites [a].

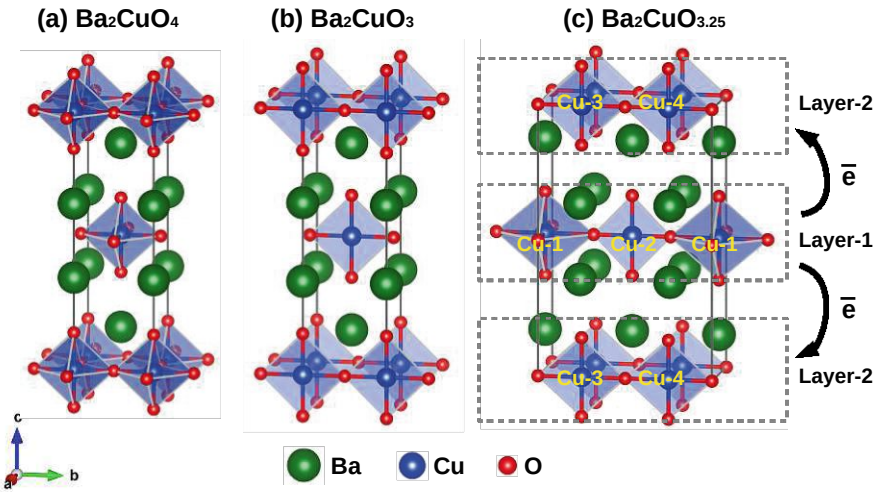

Figure 4.24: Crystal structure of (a) the parent compound Ba_2CuO_4 and (b) the ideal, fully reduced Ba_2CuO_3, where the planar oxygen atoms in a direction are vacant. (c) Energetically favorable crystal structure for $Ba_2CuO_{3.25}$ [255] close to the superconducting doping $y = 0.2$. Note (c) forms a bilayer structure, layer-2 has as (b) the in-plane oxygens in the a direction removed, in layer-1 every second one is removed. This leads in layer-2 to 1D Cu-3—O—Cu-4—O–⋯ chains. Arrows indicate the inter-layer charge transfer that is driven by electronic correlations.

The primitive cell Fig. 4.24(c) can be obtained from Ba_2CuO_3 [Fig. 4.24(b)] by inserting one oxygen into the empty spaces in the "layer-1" CuO_2 planes at the Cu-1 sites. This yields a $Ba_8Cu_4O_{13}$ supercell that contains four Cu sites, resulting in the chemical formula $Ba_2CuO_{3.25}$. It is composed of two different layers: in layer-1 we have Cu-1 sites with a six-fold octahedral CuO_6 coordination, and Cu-2 sites with planar CuO_4 squares. In layer-2 both Cu-3&4 sites are equivalent and the same as in Ba_2CuO_3 [Fig. 4.24(b)] with planar CuO_4 squares. They form 1-dimensional (1D) CuO chains in the b direction. If we compare to the parent compound Ba_2CuO_4, oxygen reduction has removed the planar O in the a direction for Cu-2, Cu-3, and Cu-4 sites. Please note that removing parts of the oxygen atoms from the CuO_2 planes and forming the 1D CuO chains, will result in an orthorhombic distortion of $Ba_2CuO_{3.2}$, if all CuO chains

Die approbierte gedruckte Originalversion dieser Dissertation ist an der TU Wien Bibliothek verfügbar.
The approved original version of this doctoral thesis is available in print at TU Wien Bibliothek.
TU Bibliothek Your knowledge hub WIEN

point in the same direction, as discussed previously for Ba_2CuO_3 [261]. However, the synthesizing process of oxygen reduced Ba_2CuO_{3+y} under high temperature and high pressure might stabilize an undistorted crystal where the CuO chains in different layers point in alternating directions. The structure is further stabilized by the fact that every other layer still contains a-b symmetric CuO_6 octahedra.

In this paper, we present DFT and DFT+dynamical mean-field theory (DMFT) [26, 37, 262] calculations for all three crystal structures of Fig. 4.24 as well as for the superconducting $Ba_2CuO_{3.2}$. To obtain the hole doping of the latter, we employ a rigid (bandstructure) doping. We find that the physics is completely different for the three structures: Ba_2CuO_4 is a two-orbital system, while Ba_2CuO_3 is a one-orbital 1D system. The $Ba_2CuO_{3.25}$ supercell inherits aspects of both parent compounds in its two inequivalent layers. Crucially, correlations induce a charge transfer so that layer-2 of $Ba_2CuO_{3.25}$ is doped close to half-filling and thus prone to strong antiferromagnetic spin-fluctuations.

4.4.2 Methods

DFT-level computations are performed by WIEN2K [55, 263] using the Perdew-Burke-Ernzerhof [264] version of the generalized gradient approximation (GGA-PBE) on a dense momentum grid with 2000 k-points totally. The structural parameters of ideal Ba_2CuO_4 and Ba_2CuO_3 are adopted from Refs. [253, 265], and the crystal structure of the bilayer $Ba_2CuO_{3.25}$ phase was optimized within DFT-PBE (see Supplemental Material of Ref. [260] for details on computation and other structures including additional references Ref. [49, 84, 266–272].). As an input for the DMFT calculations a low-energy effective Hamiltonian is generated by projecting the WIEN2K bands around the Fermi level onto Wannier functions [67, 74] using WIEN2WANNIER [77, 273]. These are supplemented by a local Kanamori interaction and the fully localized limit as double counting [274]. Constrained random phase approximation (cRPA) [80] calculations motivate an intraorbital Hubbard interaction $U = 2.6\,\text{eV}$ and a Hund's exchange $J = 0.3\,\text{eV}$ (see Supplemental Material of Ref. [260]). For the interorbital interaction we use $U' = U - 2J$. In our calculations we used slightly enhanced Hubbard interactions $U = 3.0\,\text{eV}$ to mimic the disregarded frequency dependence of U, along the lines of [50] and many other publications [b].We solve the resulting many-body Hamiltonian at room temperature (300 K) within DMFT employing a continuous-time quantum Monte Carlo solver in the hybridization expansions [120] using `w2dynamics` [277, 278]. Real-frequency spectra are obtained with the `ana_cont` code [122] via analytic continuation using the maximum entropy method (MaxEnt).

[a] Details on lattice relaxation and a table containing all energies can be found in the Supplemental Material of Ref. [260].

[b] While the bandwidth-narrowing from $U(\omega)$ is counteracted by exchange contributions to the self-energy [275, 276] that we neglect, the enhanced static U mimics the loss of low-energy spectral weight to plasmon-like satellites [81].

4.4.3 DFT electronic structure

Die approbierte gedruckte Originalversion dieser Dissertation ist an der TU Wien Bibliothek verfügbar.
The approved original version of this doctoral thesis is available in print at TU Wien Bibliothek.

Let us first review the DFT electronic structure for the three different crystal structures. For Ba_2CuO_4 the Fermi surface (FS) in Fig. 4.25(a) is composed of two Cu-d bands of $d_{x^2-y^2}$ and d_{z^2} orbital character, consistent with previous results [253, 279] and hinting toward multi-orbital physics. Instead, Ba_2CuO_3 in Fig. 4.25(b) hosts only one Fermi surface sheet of $d_{b^2-c^2}$ orbital character [255] (this orbital is like a $x^2 - y^2$ orbital only in the bc plane as the missing oxygen in the a direction dictates the local symmetry). Because the Cu layers are well separated in the c direction, this leads to a quasi-1D character of the bandstructure in the b direction. Superconductivity was, however, observed in neither of these two parent compounds, but at an oxygen concentration $y = 0.2$ for $Ba_2CuO_{3.2}$. A rigid band shift of the Ba_2CuO_3 or Ba_2CuO_4 bandstructure to this $y = 0.2$ doping results in two profoundly different FSs (see Fig. 4.26 and 4.28 below), electronic structures and even orbital occupations. This naturally prompts the question: Does the FS of $Ba_2CuO_{3.2}$ show Ba_2CuO_3 or Ba_2CuO_4 character? To address this question, we perform a supercell calculation, which allows for non-uniform oxygen reduction [255]. We identify the most promising structure for $Ba_2CuO_{3.25}$ (which is reasonably close to one of the experimental oxygen concentrations) to be the one in Fig. 4.24(c), based on the DFT total energy (see, Supplemental Material Section 1 of Ref. [260]). This structure has two inequivalent layers, each of which is similar to the two parent compounds: The Cu-1 sites in layer-1 have the same local octahedra as in Ba_2CuO_4, and its low-energy excitations in Fig. 4.25(c) are hence similarly described by a Cu-$d_{x^2-y^2}$ and a Cu-d_{z^2} orbital. The Cu-2 site in layer-1 has an oxygen removed and hosts a $d_{b^2-c^2}$ band, which does not cross the Fermi level in Fig. 4.25(c). The Cu-3&4 sites in layer-2, on the other hand, display the same local surroundings as Ba_2CuO_3 and their low-energy electronic structure as in Fig. 4.25(d) is described by a single $d_{b^2-c^2}$ orbital [280, 281]. This band is similar to Fig. 4.25(b), see also hopping elements in Table 5.2.3.

Die approbierte gedruckte Originalversion dieser Dissertation ist an der TU Wien Bibliothek verfügbar.
The approved original version of this doctoral thesis is available in print at TU Wien Bibliothek.

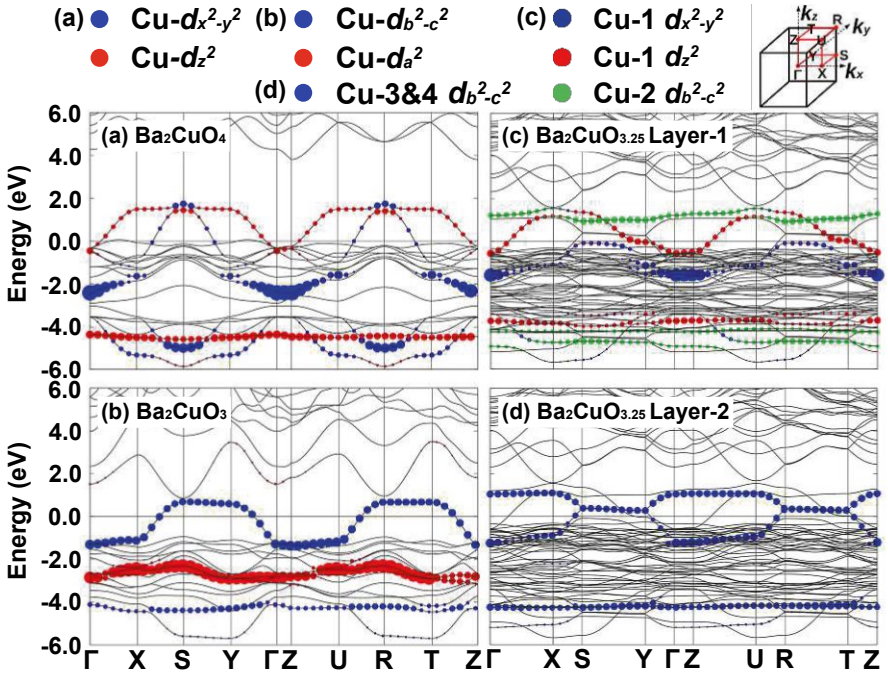

Figure 4.25: DFT bandstructure and orbital character for (a) Ba_2CuO_4, (b) Ba_2CuO_3, (c) $Ba_2CuO_{3.25}$ layer-1 and (d) $Ba_2CuO_{3.25}$ layer-2 along a high symmetry path through the Brillouin zone (see top right).

Table 4.1: Major hopping elements in meV for the $d_{b^2-c^2}$ orbital in Ba_2CuO_3 and layer-2 of $Ba_2CuO_{3.25}$. t_{abc} indicates the hopping along real space vector R_{abc}, and a, b, c are the number of unit cells along x, y and z direction.

Structure	t_{100}	t_{200}	t_{010}	t_{020}	t_{110}
Ba_2CuO_3	-18.5	-1.3	-470.2	-84.6	-6.8
$Ba_2CuO_{3.25}$	-25.8	1.4	-518.1	-89.4	-11.9

4.4.4 DFT+DMFT electronic structure

Since cuprates are known for strong correlation effects, we expect significant corrections to the DFT results. To address these we perform DFT+DMFT calculations in the paramagnetic phase at room temperature (300 K). The DMFT momentum-integrated spectral function $A(\omega)$ is displayed in Fig. 4.26. We show the spectrum both for the stoichiometric parent compound (inset) and an adjusted particle number (main panel) to reach an oxygen concentration of $y = 0.2$. The arguably simplest system is undoped Ba_2CuO_3 [Fig. 4.26(b) inset] which shows a single low-energy orbital with the typical three-peak spectrum of correlated electron systems. Besides a lower and an upper Hubbard band, there is a central quasiparticle peak with mass enhancement $m^*/m \equiv 1/Z \sim 3.85$. Please note that we are considering the paramagnetic solution, even though without doping Ba_2CuO_3 has a strong tendency to antiferromagnetism [255]. Upon doping, see Fig. 4.26(b), correlation effects become much weaker as evidenced by a reduced mass enhancement of $m^*/m \sim 1.45$. The other parent compound,

Die approbierte gedruckte Originalversion dieser Dissertation ist an der TU Wien Bibliothek verfügbar.
The approved original version of this doctoral thesis is available in print at TU Wien Bibliothek.
TU Bibliothek Your knowledge hub WIEN

Ba_2CuO_4 in Fig. 4.26(a), hosts two orbitals: a moderately correlated $d_{x^2-y^2}$ orbital close to half-filling ((spin-summed) occupation $n \sim 0.87$, $m^*/m \sim 1.39$) and a weakly correlated d_{z^2} orbital ($n \sim 0.13$, $m^*/m \sim 1.15$). A metallic behavior at this doping was also reported previously in [282]. Removing $1 - y = 0.8$ oxygen per formula, electrons dope both orbitals, slightly increase the mass enhancement in the $d_{x^2-y^2}$ orbital ($n \sim 1.56$, $m^*/m \sim 1.47$) while dramatically boosting it for the d_{z^2} orbital ($n \sim 1.04$, $m^*/m \sim 3.12$).

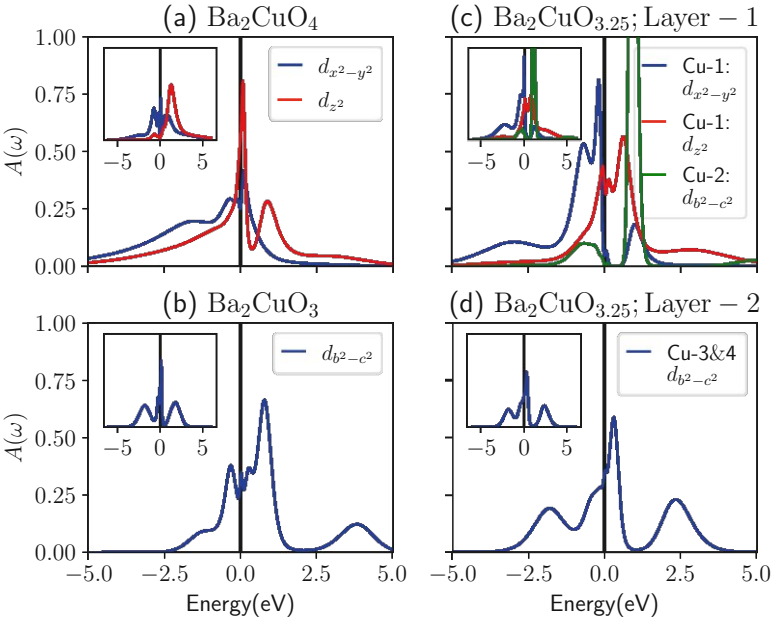

Figure 4.26: DMFT spectral function $A(\omega)$ using the Wannier-projected low-energy bands of Fig. 4.25 for the three crystal structures: (a) Ba_2CuO_4, (b) Ba_2CuO_3, (c) $Ba_2CuO_{3.25}$ layer-1 and (d) $Ba_2CuO_{3.25}$ layer-2. The inset shows results for the stoichiometric parent compound, the main panel corresponds to the hole doping of $Ba_2CuO_{3.2}$. Insets have the same scale as main panels.

We now assess how these trends survive in the structurally akin Cu-O planes of the bilayer compound $Ba_2CuO_{3.25}$. Let us thus turn to Fig. 4.26(c) and (d) which show layer-1 and layer-2 spectra of the bilayer structure $Ba_2CuO_{3.25}$, respectively. Here, correlations play a crucial role: they drive a charge transfer from layer-1 to layer-2. As a consequence the occupation of the $d_{b^2-c^2}$ orbital in layer-2 is increased towards half-filling ($n \sim 0.91$). This leads to a strongly correlated spectrum in Fig. 4.26(d) with $m^*/m \sim 2.40$. For Ba_2CuO_3, we would have a similar $m^*/m \sim 2.63$, if the occupation is fixed at 0.9 electrons per $d_{b^2-c^2}$ orbital. Hence, we conclude that the strongly correlated, half-filled, single $d_{b^2-c^2}$ band physics is preserved in the $Ba_2CuO_{3.2}$ structure. As superconductivity is known to be extremely sensitive to doping [147, 283], let us now discuss this important charge transfer in more detail.

4.4.5 Discussion

Correlation-induced charge transfer — One common ingredient for cuprate and recently observed nickelate superconductors [17, 50] has been the CuO_2 or NiO_2 plane, whose low-energy physics is dominated by a $d_{x^2-y^2}$ orbital close to half-filling [11, 167]. Neither Ba_2CuO_3 nor Ba_2CuO_4 fits into this CuO_2 plane category. The former hosts an overdoped, quasi-1D $d_{b^2-c^2}$ band, while the latter displays two-orbital, $d_{x^2-y^2}$ and d_{z^2} physics. Both compounds have been studied theoretically and several mechanisms for

Die approbierte gedruckte Originalversion dieser Dissertation ist an der TU Wien Bibliothek verfügbar.
The approved original version of this doctoral thesis is available in print at TU Wien Bibliothek.

the superconductivity have already been proposed [257, 259, 279, 282, 284–286]. Let us stress, that a rigid bandstructure doping from either parent compound will always be plagued by the ambiguity of which structure is realized for the experimental $Ba_2CuO_{3.2}$ compound, especially since both parent compounds are far away from the superconducting oxygen content. This problem is resolved by turning to a supercell calculation. Here, the stabilization of a bilayer structure is crucial. However, a naive electron count for the three inequivalent Cu sites of Fig. 4.24(c) would be Cu-1: d^7, Cu-2: d^9 and Cu-3&4: d^9 when considering the local CuO_6 and CuO_4 configurations. A charge transfer between Cu-1 and Cu-2 can be expected, as they are located in the same layer and connected by oxygen. Somewhat less straight-forward, but arguably more interesting is the interlayer charge transfer. In DFT, for $Ba_2CuO_{3.25}$, about ~ 0.44 electrons will relocate from layer-2 into layer-1, which results in an occupation of ~ 0.78 for the Cu-3&4 $d_{b^2-c^2}$ orbitals.

Local DMFT correlations counteract this charge transfer. They favor an even distribution of electrons among the orbitals, see Table 4.2. Specifically, ~ 0.12 electrons relocate back to the Cu-3&4 in layer-2, leading to 0.84 electron per $d_{b^2-c^2}$. As the oxygen content of $Ba_2CuO_{3.25}$ is already close to the experimental compound $Ba2CuO_{3.2}$, a rigid doping to $Ba_2CuO_{3.2}$ is more justified here, and the occupation of the various orbitals are also listed in Table 4.2. Of particular interest are the Cu-3&4 orbitals in layer-2, which are now unexpectedly close to typical doping levels of common quasi 2D cuprate superconductors.

Dependence on the interaction value U — We used $U = 3.0\,\text{eV}$ as Hubbard interaction, which represents an enhanced value of $U(\omega = 0)$ obtained by cRPA to account for the neglected frequency dependence. This enhancement is guided by the success of previous works like Ref. [50] and many others. Nevertheless, additionally to $U = 3.0\,\text{eV}$, we performed calculations for several interaction values starting with the $\omega = 0$ value of cRPA 2.6 eV and larger values U=3.2, 3.3 and 3.6 eV. We show the orbital occupation for the low energy bands in the $Ba_2CuO_{3.25}$ structure as a function of this interaction strength U in Fig. 4.27. As the interaction strength increases more electrons are relocated from layer-1 (a,b) to layer-2 (c), clearly indicating that the charge transfer is driven by electronic correlations. Fig. 4.27 further shows that the presented scenario is qualitatively stable with respect to reasonable variations in the interaction parameters.

Table 4.2: DFT and DMFT electron occupations for the Cu sites of $Ba_2CuO_{3.25}$ and its rigid doping to $Ba_2CuO_{3.2}$.

Site	Orbital	$Ba_2CuO_{3.25}$		$Ba_2CuO_{3.20}$	
		DFT	DMFT	DFT	DMFT
Cu-1	$d_{x^2-y^2}$	1.70	1.65	1.75	1.73
Cu-1	d_{z^2}	0.50	0.50	0.64	0.63
Cu-1	$d_{x^2-y^2}+d_{z^2}$	2.20	2.15	2.40	2.37
Cu-2	$d_{b^2-c^2}$	0.23	0.21	0.24	0.23
Cu-3&4	$d_{b^2-c^2}$	0.78	0.84	0.88	0.91

FS and nesting: a connection to high-T_c — With the discussion above we demonstrated, that the bilayer structure of $Ba_2CuO_{3.25}$ satisfies one of the common ingredients

Die approbierte gedruckte Originalversion dieser Dissertation ist an der TU Wien Bibliothek verfügbar.
The approved original version of this doctoral thesis is available in print at TU Wien Bibliothek.
TU Bibliothek Your knowledge hub WIEN

for cuprates: Namely the low-energy physics of layer-2 is described by a single, almost half-filled orbital. However, contrary to the conventional CuO_2 planes, we have a CuO chain structure with a quasi-1D low-energy orbital, as can be seen from the FS in Fig. 4.28(f). Already the parent compound Ba_2CuO_3 in Fig. 4.28(c) has such a 1D character, but at quite a different filling. The Cu-1 FS of layer-1 in Fig. 4.28(d,e) has instead a two-orbital character. However it differs from Ba_2CuO_4 in Fig. 4.28(a,b) — not only by the filling (volume of the FS) but also because the Cu-2 sites are insulating. The latter cuts off, among others, the hopping of the Cu-1 d_{z^2} orbital in the y direction.

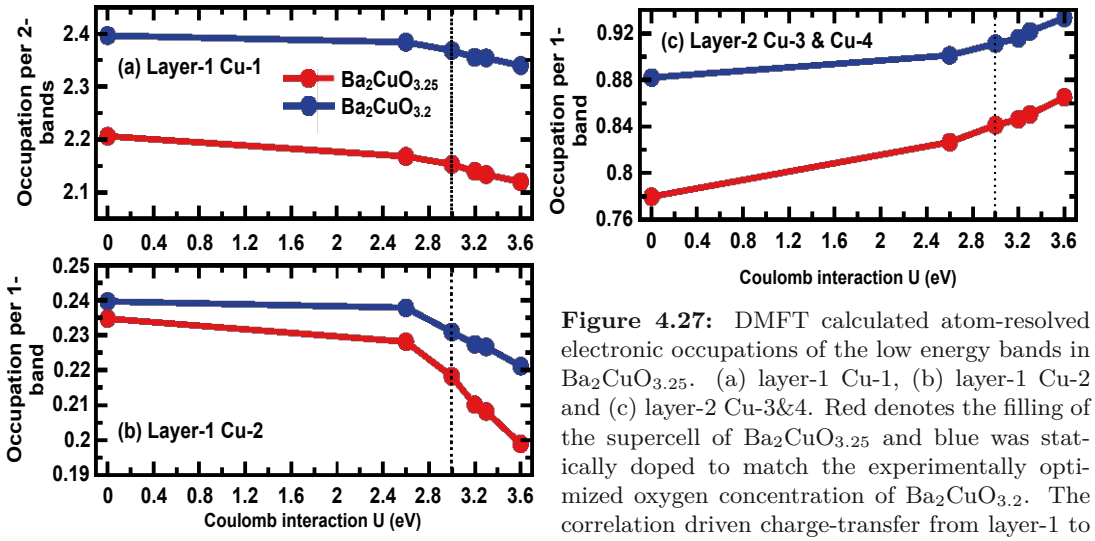

Figure 4.27: DMFT calculated atom-resolved electronic occupations of the low energy bands in $Ba_2CuO_{3.25}$. (a) layer-1 Cu-1, (b) layer-1 Cu-2 and (c) layer-2 Cu-3&4. Red denotes the filling of the supercell of $Ba_2CuO_{3.25}$ and blue was statically doped to match the experimentally optimized oxygen concentration of $Ba_2CuO_{3.2}$. The correlation driven charge-transfer from layer-1 to layer-2 is clearly visible. Dashed lines mark $U = 3.0\,\text{eV}$, which was used for the results presented in the main text. Reformatted from Ref. [143]

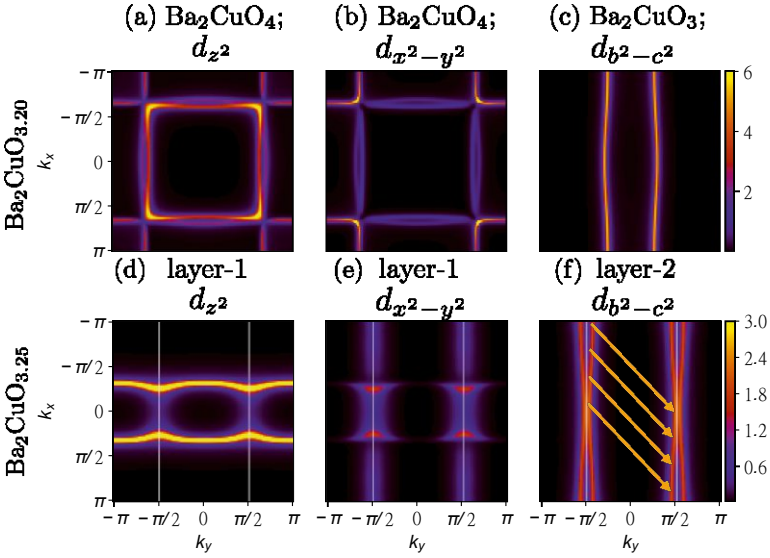

Figure 4.28: DMFT FS at $k_z = 0$ for the nominal doping of $Ba_2CuO_{3.2}$ realized in the three crystal structures of Fig. 4.24: Ba_2CuO_4 [(a) and (b) for d_{z^2} and $d_{x^2-y^2}$], Ba_2CuO_3 (c), $Ba_2CuO_{3.25}$ layer-1 [(d) and (e) for d_{z^2} and $d_{x^2-y^2}$ of Cu-1; Cu-2 is not shown because of its tiny occupation and insulating nature] and $Ba_2CuO_{3.25}$ layer-2 (f) where we also plotted the antiferromagnetic nesting vector.

Fig. 4.28(f) shows that the correlation-induced charge transfer results not only in a

Die approbierte gedruckte Originalversion dieser Dissertation ist an der TU Wien Bibliothek verfügbar.
The approved original version of this doctoral thesis is available in print at TU Wien Bibliothek.

$d_{b^2-c^2}$ orbital closer to half-filling but also in an almost perfectly nested FS. The nesting vector of $\mathbf{k}_N \simeq \{\pi, \pi - \delta, 0\}$, is similar to the dominant vector for commensurate, antiferromagnetic fluctuations ($\mathbf{k}_{AF} = \{\pi, \pi, 0\}$), and takes through its k_x component also the slight warping of the FS into account.

4.4.6 Conclusion

High temperature superconductivity remains one of the most puzzling phenomena in condensed matter physics and an overarching understanding is still missing. Hence, identifying common traits among superconductors, which help us to focus on the essential ingredients is of vital importance. The recently discovered $Ba_2CuO_{3.2}$ superconductor challenges the current picture of cuprate superconductivity. Its high hole doping concentration, compressed octahedra, and putative multi-band physics baffled the scientific community. In this work, we provide a resolution to the high doping of the compound by identifying a charge transfer process, which ultimately leads to one layer hosting a single-orbital Fermi surface which is close to half-filling and almost perfectly nested. This bilayer structure also resolves the ambiguity, whether a Ba_2CuO_3 or Ba_2CuO_4 structure is realized at the superconducting oxygen concentration of $Ba_2CuO_{3.2}$. Structural motives of both exist in the two layers, but the bilayer structure results in different dopings than previously thought.

Due to its strong nesting, layer-2 with its single orbital appears to be the natural candidate to host superconductivity. Layer-1, instead, serves more as a charge carrier reservoir/sink. This new insight shifts the focus from a highly overdoped to a quasi-1D superconductor, which is still in contrast to all other known cuprate superconductors that are 2D. Fluctuation exchange (FLEX) calculations predict p-wave superconductivity or the pair density wave state for such an almost perfectly nested 1D system [a]. A T_c as high as 70 K would, however, be unparalleled for a p-wave superconductor, calling for further theoretical work on such quasi-1D systems.

Hopefully, future single crystals will allow for a better crystallographic analysis, so that one can verify whether the bilayer structure is truly realized. Let us emphasize that the precise, in our case alternating, oxygen arrangement in layer-1 is of less relevance since this layer is not the one driving the system superconducting. Even with the ideal, ordered oxygen arrangement Cu-1 and Cu-2 have a similar $3d^{8.3}$ and $3d^{8.2}$ [b] electronic configuration, respectively, whereas the equivalent Cu-3&4 sites in layer-2 have a distinct $3d^{8.9}$ filling. This may explain the two-peak structure of the x-ray spectrum in [254]. Last but not least the prospects of a p-wave symmetry of the superconducting order parameter at an unprecedented high T_c calls for further experiments.

[a] This 1D chain is included in [141, 287] as the extreme case of the anisotropic triangular lattice with hopping $t_2 = 0$.

[b] Note that, on top of Table 4.2, 2 electrons fill the the d_{a^2} of Cu-2 sites

Die approbierte gedruckte Originalversion dieser Dissertation ist an der TU Wien Bibliothek verfügbar.
The approved original version of this doctoral thesis is available in print at TU Wien Bibliothek.
TU Bibliothek Your knowledge hub WIEN

Chapter 5

Nickelates

If it looks like a duck and quacks like a duck, we have at least to consider the possibility that we have a small aquatic bird of the family Anatidae on our hands.
— D. Adams

After the discovery of cuprates, the search for other superconducting compounds began. One obvious candidate were the nickelates, suggested by the close proximity of nickel to copper in the periodic table. Specifically, $NdNiO_2$ is isostructural and isoelectronic to the well-known $CaCuO_2$ superconductor[1]. Both are built of Cu(Ni)-O_2 planes and Ca(Nd) insulating blocking layers, which act as charge reservoirs. They host a nominal $3d^9$ configuration and superconductivity emerges upon hole doping[2]. Despite all those similarities the synthesis of a superconducting nickelate proved extremely difficult and only recently did Li *et al.* [17] succeed in synthesizing the first superconducting nickelate $Nd_{1-x}Sr_xNiO_2$.

Furthermore, despite their similarities regarding the structure and electronic configuration, band structures calculations by DFT show notable differences [50, 51] (see also Box 3 and Box 4). Among those are (i) the appearance of Nd-derived pockets, (ii) the larger Ni-O charge-transfer energy, (iii) the closer proximity of the Ni-d_{z^2} orbital to the Fermi surface, (iv) the oxygen p states are on the other hand further away from the Fermi energy and the Ni-O hybridization is weaker than the respective Cu-O one. As a result, multi-orbital physics involving the whole Ni e_g shell has been suggested for superconductivity [290, 291] as well as the possibility of Hund's physics [292].

However, our view on the superconductivity in nickelates so far is a much simpler one, namely that of a single-band Hubbard model. While the pockets will certainly contribute to properties like transport, as also evidenced by Hall measurements [293], it seems they are merely bystanders for superconductivity. Indeed, as we discuss below DΓA calculations based on a single band Hubbard model describe the superconducting dome well and yield (para)-magnon dispersions close to experiment.

In Section 5.1, we discuss our view on the minimal model for superconductivity in nickelates and discuss our reasoning behind the single-band Hubbard model in detail. Following this, we present a DFT+DMFT study, Ref. [237], on the pentalayer nickelate $Nd_6Ni_5O_{12}$ in Section 5.2. Contrary to infinite-layer nickelates the rare earth pocket bands are fully depleted, giving rise to "superconductivity in nickelates without rare earth pockets". Magnetic response, specifically the paramagnon dispersion, of the effective single-band Hubbard model is compared to resonant inelastic X-ray scattering (RIXS) measurements in Section 5.3. Within this context, we also discuss the sub-

[1] See also Box 1.
[2] Cuprates also show superconductivity upon electron doping [288, 289]. An "analogous" superconducting electron-doped nickelate has not yet been synthesized.

Die approbierte gedruckte Originalversion dieser Dissertation ist an der TU Wien Bibliothek verfügbar.
The approved original version of this doctoral thesis is available in print at TU Wien Bibliothek.

strate dependence of the superconducting transition temperature T_c, which varies about a factor of two between samples grown on STO and those grown on LSAT. Since the microscopic parameters of the effective Hubbard model change relatively little, we argue that (experimentally observed [59]) differences in sample quality are at the origin of this discrepancy. This interpretation is consistent with the observed dependence of T_c on the normal state resistivity $\rho_{300\,K}/\rho_{20\,K}$ [294]. Section 5.5 is based on our publication Ref. [295] and discusses phonon modes as a possible way to experimentally identify intercalated hydrogen in nickelates.

5.1 Minimal model for superconductivity

The following section, marked by a vertical bar, has already been published in Frontiers in Physics 9 (2022) [20].

We review the electronic structure of nickelate superconductors with and without effects of electronic correlations. As a minimal model we identify the one-band Hubbard model for the Ni $3d_{x^2-y^2}$ orbital plus a pocket around the A-momentum. The latter however merely acts as a decoupled electron reservoir. This reservoir makes a careful translation from nominal Sr-doping to the doping of the one-band Hubbard model mandatory. Our dynamical mean-field theory calculations, in part already supported by experiment, indicate that the Γ pocket, Nd $4f$ orbitals, oxygen $2p$ and the other Ni $3d$ orbitals are not relevant in the superconducting doping regime. The physics is completely different if topotactic hydrogen is present or the oxygen reduction is incomplete. Then, a two-band physics hosted by the Ni $3d_{x^2-y^2}$ and $3d_{3z^2-r^2}$ orbitals emerges. Based on our minimal modeling we calculated the superconducting T_c vs. Sr-doping x phase diagram prior to experiment using the dynamical vertex approximation. For such a notoriously difficult to determine quantity as T_c, the agreement with experiment is astonishingly good. The prediction that T_c is enhanced with pressure or compressive strain, has been confirmed experimentally as well. This supports that the one-band Hubbard model plus an electron reservoir is the appropriate minimal model.

5.1.1 Introduction

Twenty years ago, Anisimov, Bukhvalov, and Rice [296] suggested high-temperature (T_c) superconductivity in nickelates based on material calculations that showed apparent similarities to cuprates. Subsequent calculations [297–299] demonstrated the potential to further engineer the nickelate Fermi surface through heterostructuring. Two years ago Li, Hwang and coworkers [17] discovered superconductivity in Sr-doped $NdNiO_2$ films grown on a $SrTiO_3$ substrate and protected by a $SrTiO_3$ capping layer. These novel $Sr_xNd_{1-x}NiO_2$ films are isostructural and formally isoelectric to the arguably simplest, but certainly not best superconducting cuprate: infinite-layer $CaCuO_2$ [300–303].

However, the devil is in the details, and here cuprates and nickelates differ. For revealing such material-specific differences, band-structure calculations based on density-

Die approbierte gedruckte Originalversion dieser Dissertation ist an der TU Wien Bibliothek verfügbar.
The approved original version of this doctoral thesis is available in print at TU Wien Bibliothek.

functional theory (DFT) are the method of choice. They serve as a starting point for understanding the electronic structure and subsequently the phase diagram of nickelate superconductors. Following the experimental discovery of nickelate superconductivity, and even before that, numerous DFT studies have been published [19, 21, 304–312].

We already displayed the crystal structure and DFT band-structure in Box 1, while the orbital character was displayed in Box 3 and Box 4.

Based on these DFT calculations, various models for the low-energy electronic structure for nickelates and the observed superconductivity have been proposed. Besides the cuprate-like Ni $3d_{x^2-y^2}$ band, DFT shows an A and a Γ pocket which originate from Nd $5d_{xy}$ and $5d_{3z^2-r^2}$ bands, but with major Ni $3d$ admixture in the region of the pocket. The importance of the Ni $3d_{3z^2-r^2}$ orbital has been suggested in some studies [313–315] and that of the Nd-$4f$ orbitals in others [312, 316]. Further there is the question regarding the relevance of the oxygen $2p$ orbitals. For cuprates these are, besides the Cu $3d_{x^2-y^2}$ orbitals, the most relevant. Indeed, cuprates are generally believed to be charge-transfer insulators [317]. This leads to the three-orbital *Emery model* [318] visualized in Fig. 5.1A,C as the minimal model for cuprates. The much more frequently investigated Hubbard model [83, 319, 320] may, in the case of cuprates, only be considered as an effective Hamiltonian mimicking the physics of the Zhang-Rice singlet [71].

At first glance, nickelates appear to be much more complicated with more relevant orbitals than in the case of the cuprates. In this paper, we review the electronic structure of nickelates in comparison to that of cuprates, and the arguments for a simpler description of nickelate superconductors: namely a *Hubbard model* for the Ni $3d_{x^2-y^2}$ band plus a largely decoupled reservoir corresponding to the A pocket. This A pocket is part of the Nd $5d_{xy}$ band which has however a major admixture of Ni $3d_{xz/yz}$ and O $2p_z$ states around the momentum A. This leaves us with Fig. 5.1B,D as the arguably simplest model for nickelates [50, 51]. This (our) perspective is still controversially discussed in the literature. However, as we will point out below, a number of experimental observations already support this perspective against some of the early suggestions that other orbitals are relevant. Certainly, other perspectives will be taken in other articles of this series on "Advances in Superconducting Infinite-Layer and Related Nickelates". The simple picture of a one-band Hubbard model, whose doping needs to be carefully calculated since part of the holes in Sr-doped $Sr_xNd_{1-x}NdO_2$ go to the A pocket, allowed us [50] to calculate T_c, see Fig. 5.5 below, at a time when only the T_c for a single doping $x = 20\%$ was experimentally available. To this end, state-of-the-art dynamical vertex approximation (DΓA) [38, 95, 123], a Feynman diagrammatic extension of dynamical mean-field theory (DMFT) [37, 111, 321, 322] has been used. For such a notoriously difficult to calculate physical quantity as T_c, the agreement of the single-orbital Hubbard model calculation with subsequent experiments [258, 323] is astonishingly good. This further supports the modelling by a single-orbital Hubbard model which thus should serve at the very least as a good approximation or a starting point.

Die approbierte gedruckte Originalversion dieser Dissertation ist an der TU Wien Bibliothek verfügbar.
The approved original version of this doctoral thesis is available in print at TU Wien Bibliothek.

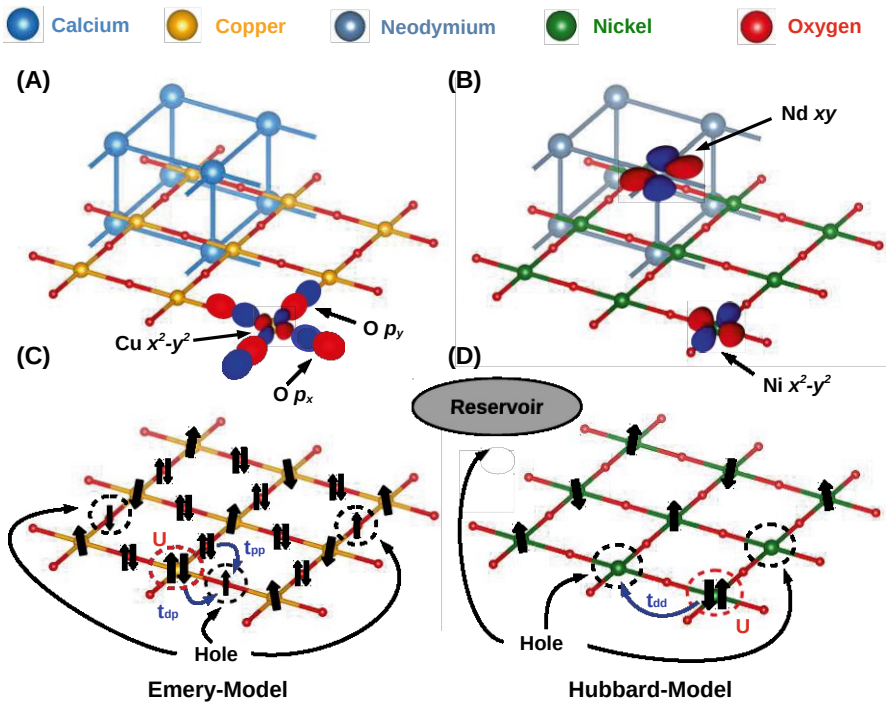

Figure 5.1: Crystal lattice and most important orbitals for (A) cuprates and (B) nickelates. (C) For cuprates the arguably simplest model is the *Emery model* with a half-filled copper $3d_{x^2-y^2}$ band and holes in the oxygen $2p$ orbitals that can hop to other oxygen (t_{pp}) and copper sites (t_{pd}) where double occupations are suppressed by the interaction U. (D) For nickelates we have a Ni-$3d_{x^2-y^2}$-band *Hubbard model* which however only accommodates part of the holes induced by Sr-doping. The others go to the A pocket stemming from the Nd $5d_{xy}$ band and acting as a decoupled *reservoir*.

The outline of this article is as follows: In Section 5.1.2 we first compare the electronic structure of nickelates to that of cuprates, starting from DFT but also discussing effects of electronic correlations as described, e.g., by DMFT. Subsequently, we argue in Section 5.1.3, orbital-by-orbital, that the other orbitals besides the Ni $3d_{x^2-y^2}$ and the A pocket are, from our perspective, not relevant. This leaves us with the one-$3d_{3z^2-r^2}$-band Hubbard model plus an electron reservoir representing the A pocket of Fig. 5.1B,D, which is discussed in Section 5.1.4 including the translation of Sr-doping to the filling in the Hubbard model and the reservoir. In Section 5.1.5, we discuss the effect of non-local correlations as described in DΓA and the calculated superconducting phase diagram. Section 5.1.6 shows that topotactic hydrogen, which is difficult to detect in experiment, completely overhauls the electronic structure and the prevalence of superconductivity. Finally, Section 5.1.7 summarizes the article.

5.1.2 Electronic structure: Nickelates vs. cuprates

Let us start by looking into the electronic structure in more detail and start with the DFT results. On a technical note, the calculations presented have been done using the WIEN2K [55, 263], VASP [324], and FPLO [325] program packages, with the PBE [49]

Die approbierte gedruckte Originalversion dieser Dissertation ist an der TU Wien Bibliothek verfügbar.
The approved original version of this doctoral thesis is available in print at TU Wien Bibliothek.
TU Bibliothek Your knowledge hub WIEN

version of the generalized gradient approximation (GGA). For further details see the original work [50]. Fig. 5.2 compares the bandstructure of the two simple materials: $CaCuO_2$ and $LaNiO_2$. Here, we restrict ourselves to only the Brillouin zone path along the most relevant momenta for these compounds: Γ (0,0,0), X (π,0,0), and A (π,π,π). In DFT both the cuprate and nickelate parent compounds are metals with a prominent Cu or Ni $3d_{x^2-y^2}$ band crossing the Fermi energy. In other aspects both materials differ (for a review cf. [326]): In the case of *cuprates*, the oxygen bands are much closer to the Fermi energy. Hence, if electronic correlations split the DFT bands into two Hubbard bands as indicated in Fig. 5.2 by the arrows and the spectral function in the left side panel, we get a charge-transfer insulator [317]. For this charge-transfer insulator, the oxygen $2p$ orbitals are the first orbitals below the Fermi level (E_F) and receive the holes that are induced by doping. The Cu $3d_{x^2-y^2}$ lower Hubbard band is below these oxygen orbitals, and the Cu $3d_{x^2-y^2}$ upper Hubbard band is above the Fermi level. Let us note that we here refer to oxygen $2p$ orbitals and Cu $3d_{x^2-y^2}$ orbitals even though the hybridization between both is very strong. Indeed, the two sets of orbitals strongly mix in the resulting effective DFT bands of Fig. 5.2.

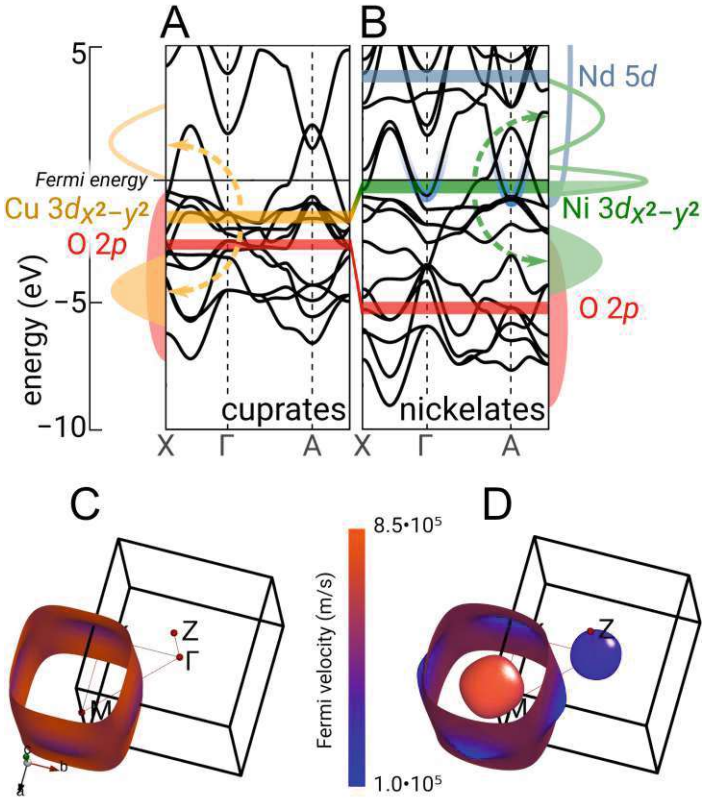

Figure 5.2: Electronic structures of $CaCuO_2$ (A) and $LaNiO_2$ (B), exemplifying superconducting cuprates and nickelates. Top: The bars indicate the center of energy for the most important DFT bands. The dashed arrows indicate the correlation-induced splitting of the Cu or Ni $3d_{x^2-y^2}$ band into Hubbard bands, leading to the (schematic) spectral function at the side. Cuprates are charge-transfer insulators with a gap between the O $2p$ and the upper Cu $3d_{x^2-y^2}$ Hubbard band, as the lower Cu $3d_{x^2-y^2}$ Hubbard band is below the O $2p$ band. For nickelates, bands with a large La(Nd) $5d$ contribution cross the Fermi energy at Γ and A, self-doping the Ni $3d_{x^2-y^2}$ band away from half-filling. C and D: Corresponding DFT Fermi surface. For cuprates DFT shows a single Cu $3d_{x^2-y^2}$ hole-like Fermi surface; for nickelates there is a similar, slightly more warped Cu $3d_{x^2-y^2}$ Fermi surface and additional small pockets around the Γ and A momentum.

Because cuprates are charge-transfer insulators, the one-band Hubbard model can only be considered as an effective Hamiltonian mimicking the Zhang-Rice singlet [71]. As already pointed out in the Introduction, more appropriate is the *Emery model* of Fig. 5.1. The correlation-induced splitting into the Hubbard bands [322] as well as the Zhang-Rice singlet [327] can be described already by DMFT [37, 111, 322]. Two-dimensional

Die approbierte gedruckte Originalversion dieser Dissertation ist an der TU Wien Bibliothek verfügbar.
The approved original version of this doctoral thesis is available in print at TU Wien Bibliothek.
TU Bibliothek Your knowledge hub WIEN

spin-fluctuations and superconductivity, however, cannot. For describing such physics, non-local correlations beyond DMFT are needed.

For the nickelates, the oxygen bands are at a much lower energy. Hence, as indicated in the right side panel of Fig. 5.2, the lower Ni $3d_{x^2-y^2}$ Hubbard band can be expected to be closer to the Fermi energy than the oxygen p orbitals [50, 51]. Consequently, undoped nickelates would be Mott-Hubbard insulators if it was not for two additional bands that cross E_F around the Γ- and A-momentum. These form electron pockets as visualized in Fig. 5.2 (bottom right) and self-dope the Ni $3d_{x^2-y^2}$ band away from half-filling. As the $3d_{x^2-y^2}$ is doped, it develops, even when the Coulomb interaction is large, a quasiparticle peak at the Fermi energy as displayed in the right side panel of Fig. 5.2.

5.1.3 Irrelevance of various orbitals

Next, we turn to various orbitals that may appear relevant at first glance but turn out to be irrelevant for the low energy physics when taking electronic correlations properly into account. To account for the latter, we use DFT+DMFT [26–28, 113, 328] which is the state of the art for calculations of correlated materials.

Oxygen orbitals. For nickelates the oxygen $2p$ orbitals are approximately 3 eV lower in energy than in cuprates within DFT. Hence, some DFT+DMFT calculations did not include these from the beginning [50, 51], and those that did [313] also found the oxygen $2p$ orbitals at a lower energy than the lower Ni $3d_{x^2-y^2}$ Hubbard. Hence, while there is still some hybridization and mixing between the O $2p$ states and the Ni $3d_{x^2-y^2}$ states, a projection onto a low-energy set of orbitals without oxygen appears possible.

Ni $3d_{3z^2-r^2}$ and t_{2g} orbitals. Instead of the oxygen $2p$ orbitals, the DFT calculation in Fig. 5.2 and elsewhere [21, 307, 308, 326] show other Ni $3d$ orbitals closely below the Ni $3d_{x^2-y^2}$ band. In fact, these other $3d$ orbitals are somewhat closer to the Fermi level than in the case of cuprates. Electronic correlations can strongly modify the DFT band structure. In particular, the Hund's exchange J tends to drive the system toward a more equal occupation of different orbitals, especially if there is more than one hole (more than one unpaired electron) in the Ni $3d$ orbitals. This is not only because a larger local spin is made possible, but also because the inter-orbital Coulomb interaction U' between two electrons in two different orbitals is smaller than the intra-orbital Coulomb interaction $U = U' + 2J$ for two electrons in the same orbital. This tendency is countered by the crystal field splitting (local DFT potentials) which puts the $3d_{x^2-y^2}$ orbital above the Ni $3d_{3z^2-r^2}$ orbital and the other (t_{2g}) Ni $3d$ orbitals because of the absence of apical O atoms in NiO_4 squares .

Fig. 5.3 shows the DFT+DMFT spectral function for $Sr_xLa_{1-x}NiO_2$ from 0% to 30% Sr-doping. In these calculations [50] all Ni $3d$ and all La $5d$ orbitals have been taken into account in a WIEN2WANNIER [77] projection supplemented by interactions calculated

Die approbierte gedruckte Originalversion dieser Dissertation ist an der TU Wien Bibliothek verfügbar.
The approved original version of this doctoral thesis is available in print at TU Wien Bibliothek.
TU Bibliothek Your knowledge hub WIEN

within the constrained random phase approximation (cRPA) [64] to be $U' = 3.10\,\text{eV}$ ($2.00\,\text{eV}$) and Hund's exchange $J = 0.65\,\text{eV}$ ($0.25\,\text{eV}$) for Ni (La). On a technical note, the DMFT self-consistency equations [37] have been solved here at room temperature ($300\,\text{K}$) by continuous-time quantum Monte Carlo simulations in the hybridization expansions [120] using the W2DYNAMICS implementation [277, 278] and the maximum entropy code of ANA_CONT [122] for analytic continuation.

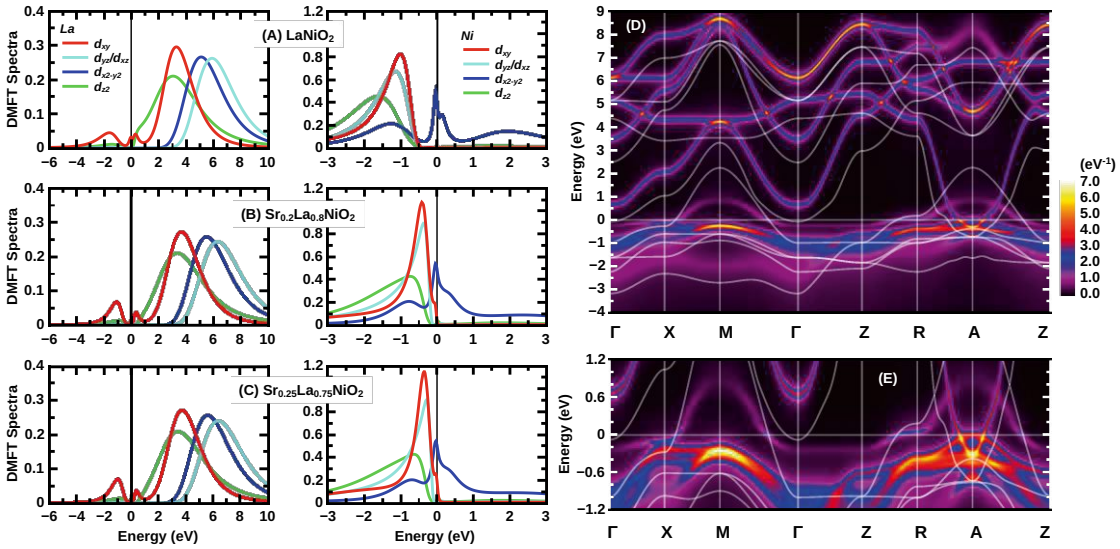

Figure 5.3: DMFT k-integrated (A-C) and k-revolved (D-E) spectral functions $A(\omega)$ and $A(k,\omega)$ of undoped $LaNiO_2$ (A), 20%Sr-doped $LaNiO_2$ ($Sr_{0.2}La_{0.8}NiO_2$) (B), and 25%Sr-doped $LaNiO_2$ ($Sr_{0.25}La_{0.75}NiO_2$) (C). The k-resolved spectral function $A(k,\omega)$ of $La_{0.8}Sr_{0.2}NiO_2$ is shown in (D); (E) is a zoom-in of (D). Data partially from [50, 64].

Clearly, Fig. 5.3 indicates that for up to 20% Sr-doping the other Ni $3d$ orbitals besides the $3d_{x^2-y^2}$ orbital are not relevant for the low-energy physics of $Sr_xLa_{1-x}NiO_2$: they are fully occupied below the Fermi energy. With doping, these other Ni $3d$ orbitals however shift more and more upwards in energy. At around 25% Sr-doping they touch the Fermi energy and hence a multi-orbital Ni description becomes necessary at larger dopings. That is, between 20% and 30% Sr-doping the physics of $Sr_xLa_{1-x}NiO_2$ turns from single- to multi-orbital. In the case of $Sr_xNd_{1-x}NiO_2$, this turning point is at slightly larger doping [50]. Later, in Section 5.1.6, we will see that for the Ni $3d^8$ configuration, which in Section 5.1.6 is induced by topotactic hydrogen and here would be obtained for 100% Sr doping, the two holes in the Ni $3d$ orbitals form a spin-1 and occupy two orbitals: $3d_{x^2-y^2}$ and $3d_{3z^2-r^2}$. In Fig. 5.3 we see at 30% doping the first steps into this direction. Importantly, within the superconducting doping regime which noteworthy is *below* 24% Sr-doping for $Sr_xNd_{1-x}NiO_2$ [258, 323] and 21% for $Sr_xLa_{1-x}NiO_2$ [18], a single $3d_{x^2-y^2}$ Ni-orbital is sufficient for the low-energy modelling. A one-band Hubbard model description based on DMFT calculations was also concluded in [51] for the undoped parent compound.

Die approbierte gedruckte Originalversion dieser Dissertation ist an der TU Wien Bibliothek verfügbar.
The approved original version of this doctoral thesis is available in print at TU Wien Bibliothek.
TU Bibliothek Your knowledge hub WIEN

DFT+DMFT calculations by Lechermann [313, 314] stress, on the other hand, the relevance of the $3d_{3z^2-r^2}$ orbital. Let us note that also in [313] the number of holes in the $3d_{3z^2-r^2}$ orbital is considerably less than in the $3d_{x^2-y^2}$. However, for low Sr-doping also a small quasiparticle peak develops for the $3d_{3z^2-r^2}$ band [313, 314]. An important difference to [50, 64] is that the $5d$ Coulomb interaction has been taken into account in [50, 64] and that the Coulomb interaction of [313] is substantially larger. The $5d$ Coulomb interaction pushes the Γ pocket above the Fermi energy (see next paragraph). As much of the holes in the $3d_{3z^2-r^2}$ orbital stem from the admixture of this orbital to the Γ pocket, this difference is very crucial for the occupation of the $3d_{3z^2-r^2}$ orbital. First experimental hints on the (ir)relevance of the $3d_{3z^2-r^2}$ can also be obtained from resonant inelastic x-ray scattering (RIXS) experiments [32, 329]. Higashi *et al.* [330] analyzed these RIXS data by comparison with DFT+DMFT and obtained good agreement with experiment. They conclude that $NdNiO_2$ is slightly doped away from $3d^9$ because of a small self-doping from the Nd $5d$ band, that only the $3d_{x^2-y^2}$ Ni orbital (not the $3d_{3z^2-r^2}$ orbital) is partially filled, and that the Ni-O hybridization plays a less important role than for the cuprates.

Γ pocket. A feature clearly present in DFT calculations for the nickelate parent compounds $LaNiO_2$ and $NdNiO_2$ is the Γ pocket, see Fig. 5.2(D). However, when the Coulomb interaction on the La or Nd sites is included, it is shifted upwards in energy. Furthermore, Sr-doping depopulates the Ni $3d_{x^2-y^2}$ orbital as well as the A and Γ pocket, and thus also helps pushing the Γ pocket above the Fermi energy. Clearly in the DFT+DMFT k-resolved spectrum of Fig. 5.3, the Γ pocket is above the Fermi energy. To some extent the presence or absence of the Γ pocket also depends on the rare-earth cation. For $NdNiO_2$ we obtain a Γ pocket for the undoped compound [50] which only shifts above the Fermi energy with Sr-doping in the superconducting region, whereas for $LaNiO_2$ it is already above the Fermi level without Sr-doping. We can hence conclude that while there might be a Γ pocket without Sr-doping, DFT+DMFT results suggest that it is absent in the superconducting doping regime.

Briefly after the discovery of superconductivity in nickelates, it has also been suggested that the Nd $5d$ orbitals of the pockets couple to the Ni $3d_{x^2-y^2}$ spin, giving rise to a Kondo effect [312, 331]. However, Table 5.1 shows that the hybridization between the relevant Ni $3d_{x^2-y^2}$ and the most important La or Nd $5d_{xy}$ and $5d_{3z^2-r^2}$ vanishes by symmetry. Also the full 5 Ni and 5 Nd band DMFT calculation in Fig. 5.3 does not show a hybridization (gap) between A pocket and Ni bands. This suggests that the Γ and A pocket are decoupled from the $3d_{x^2-y^2}$ orbitals. There is no hybridization and hence no Kondo effect.

Die approbierte gedruckte Originalversion dieser Dissertation ist an der TU Wien Bibliothek verfügbar.
The approved original version of this doctoral thesis is available in print at TU Wien Bibliothek.
TU Bibliothek Your knowledge hub WIEN

$LaNiO_2$	La $5d_{xy}$	La $5d_{yz}$	La $5d_{xz}$	La $5d_{x^2-y^2}$	La $5d_{z^2}$
Ni $3d_{x^2-y^2}$ (10-bands)	0.000	0.084	-0.084	-0.017	0.0000
Ni $3d_{x^2-y^2}$ (17-bands)	0.000	0.085	-0.085	-0.037	0.0000
$NdNiO_2$	Nd $5d_{xy}$	Nd $5d_{yz}$	Nd $5d_{xz}$	Nd $5d_{x^2-y^2}$	Nd $5d_{z^2}$
Ni $3d_{x^2-y^2}$ (10-bands, OC)	0.0000	0.0701	-0.0701	-0.0388	0.0000
Ni $3d_{x^2-y^2}$ (10-bands)	0.0000	0.0775	-0.0775	-0.0066	0.0000
Ni $d_{x^2-y^2}$ (17-bands)	0.0000	0.0811	-0.0811	-0.0239	0.0000

Table 5.1: Hybridization (hopping amplitude in eV) between the partially occupied Ni $3d_{x^2-y^2}$ and the La/Nd $5d$ orbitals [50]. Here, the results are obtained from Wannier projections onto 17-bands (La/Nd-$4f$+La/Nd-$5d$+Ni-$3d$) and 10-bands (La/Nd-$5d$+Ni-$3d$).

Nd $4f$ orbitals. Finally, the importance of the Nd $4f$ orbitals has been suggested in the literature. Treating these $4f$ orbitals in DFT is not trivial, because DFT puts them in the vicinity of the Fermi level. This neglects that electronic correlations split the Nd $4f$ into upper and lower Hubbard bands, as they form a local spin. This effect is beyond DFT. One way to circumvent this difficulty is to put the Nd $4f$ orbitals in the core instead of having them as valence states close to the Fermi energy. This is denoted as open-core (OC) in Table 5.1. The localized Nd $4f$ spins might in principle be screened through a Kondo effect. However, the hybridization of the Nd $4f$ with the Ni $3d_{x^2-y^2}$ orbital at the Fermi energy is extremely small, see Table 5.2 and [332]. Hence, the Kondo temperature is zero for all practical purposes . In spin-polarized DFT+U there is instead a local exchange interaction between the Nd $4f$ and the predominately Nd $5d$ Γ pocket [333]. However, as pointed out in the previous paragraph, the Γ pocket is shifted above the Fermi level in the superconducting Sr-doping regime. Hence in [50], we ruled out that the Nd $4f$ are relevant for superconductivity. This has been spectacularly confirmed experimentally by the discovery of superconductivity in nickelates without f electrons: $Ca_xLa_{1-x}NiO_2$ [334] and $Sr_xLa_{1-x}NiO_2$ [18] have a similar T_c.

$LaNiO_2$	f_{xz^2}	f_{yz^2}	f_{z^3}	$f_{x(x^2-3y^2)}$	$f_{y(3x^2-y^2)}$	$f_{z(x^2-y^2)}$	f_{xyz}
Ni-$d_{x^2-y^2}$	-0.0300	0.0300	0.0000	-0.0851	-0.0851	-0.0203	-0.0000
$NdNiO_2$	f_{xz^2}	f_{yz^2}	f_{z^3}	$f_{x(x^2-3y^2)}$	$f_{y(3x^2-y^2)}$	$f_{z(x^2-y^2)}$	f_{xyz}
Ni-$d_{x^2-y^2}$	-0.0215	0.0215	0.0000	-0.0612	-0.0612	0.0160	-0.0000

Table 5.2: Hybridization (hopping amplitude in eV) between the Ni $3d_{x^2-y^2}$ and the Nd(La) $4f$ orbitals, as obtained from Wannier projections onto 17-bands (La/Nd-$4f$+La/Nd-$5d$+Ni-$3d$) including the $4f$ as valence states in DFT(GGA) [50].

5.1.4 One-band Hubbard model plus reservoir

Altogether this leaves us with Fig. 5.1 B,D as the arguably simplest model for nickelate superconductors, consisting of a strongly correlated Ni $3d_{x^2-y^2}$ band and an A pocket. This A pocket is derived from the Nd $5d_{xy}$ band which however crosses the Ni $3d$ orbitals and hybridizes strongly with the Ni t_{2g} orbitals so that at the bottom of the A pocket, i.e., at the momentum A, it is made up primarily from Ni t_{2g} whereas the Nd $5d_{xy}$

Die approbierte gedruckte Originalversion dieser Dissertation ist an der TU Wien Bibliothek verfügbar.
The approved original version of this doctoral thesis is available in print at TU Wien Bibliothek.
TU Bibliothek Your knowledge hub WIEN

contribution is here at a lower energy. This makes the A pocket much more resistive to shifting up in energy than the Γ pocket.

On the other hand the A pocket does not interact with the Ni $3d_{x^2-y^2}$ band; i.e., does not hybridize in Table 5.1. Hence, we can consider the A pocket as a mere hole reservoir which accommodates part of the holes induced by Sr doping, whereas the other part goes into the correlated Ni $3d_{x^2-y^2}$ band which is responsible for superconductivity. Fig. 5.4 shows the thus obtained Ni $3d_{x^2-y^2}$ occupation as a function of Sr-doping in the DFT+DMFT calculation with 5 Ni and 5 Nd(La) orbitals. Note that $NdNiO_2$ shows for Sr-doping below about 10% more holes in the Ni $3d_{x^2-y^2}$ orbital and a weaker dependence on the Sr-doping, since here the Γ pocket is still active, taking away electrons from Ni but also first absorbing some of the holes from the Sr-doping until it is completely depopulated (shifted above the Fermi energy) before superconductivity sets in.

In the subsequent one-band calculation, presented in the next paragraph, we employ the occupation from the Ni $3d_{x^2-y^2}$ orbital as calculated in this full DMFT calculation with 5 Ni and 5 Nd orbitals, since the main band across the Fermi level has almost pure Ni $3d_{x^2-y^2}$ character. This accounts for the electron pocket in the DMFT calculation but also for minor hybridization effects between the Ni $3d_{x^2-y^2}$ and $3d_{3z^2-r^2}$ orbital, e.g., along the Γ-X direction. This hybridization puts a small number ($\sim$0.02-0.03) of holes from the $3d_{x^2-y^2}$ to the $3d_{3z^2-r^2}$ orbital whose effect is not considered in the current treatment.

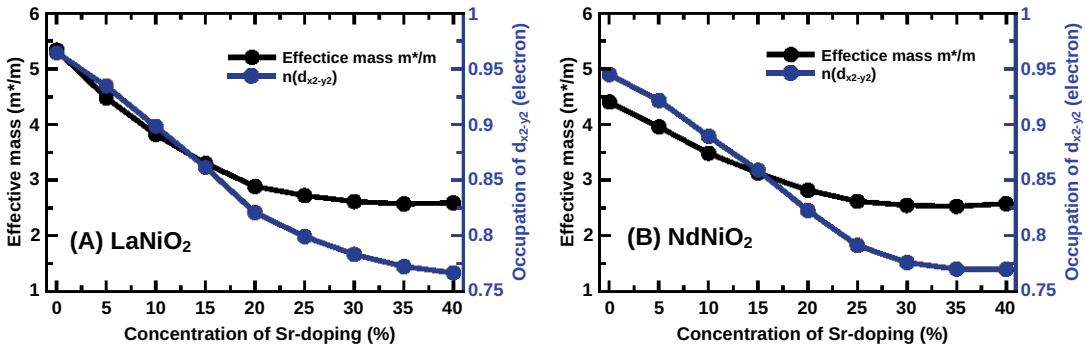

Figure 5.4: Occupation of the Ni $3d_{x^2-y^2}$ orbital [blue; right y-axis] and its effective mass enhancement $m^*/m = 1/Z$[black ; left y-axis in panels] vs. Sr-doping for $LaNiO_2$ (A) and $NdNiO_2$ (B) as calculated in DFT+DMFT. From [50] (Supplemental material)

The hopping parameters for the Ni-$3d_{x^2-y^2}$ model from a one-band Wannier projection are shown in Table 5.3, and compared to that of the same orbital in a 10-band and 17-band Wannier projection. Here t_{R_x,R_y,R_z} denotes the hopping by R_i unit cells in the i direction. That is, t_{000} is the on-site potential, $t = -t_{100}$, $t' = -t_{110}$ and $t'' = -t_{200}$ are the nearest, next-nearest and next-next-nearest neighbor hopping; $t_z = -t_{001}$ is the hopping in the z-direction perpendicular to the NiO_2 planes. The hopping parameters are strikingly similar for $LaNiO_2$ and $NdNiO_2$ and the different Wannier projections.

Besides the doping from Fig. 5.4 and the hopping for the one-band Wannier projection from Table 5.3, we only need the interaction parameter for doing realistic one-band

Die approbierte gedruckte Originalversion dieser Dissertation ist an der TU Wien Bibliothek verfügbar.
The approved original version of this doctoral thesis is available in print at TU Wien Bibliothek.
TU Bibliothek Your knowledge hub WIEN

Hubbard model calculations or nickelates. In cRPA for a single $3d_{x^2-y^2}$ orbital one obtains $U = 2.6\,\text{eV}$ [307, 311] at zero frequency. But the cRPA interaction has a strong frequency dependence because of the screening of all the other Ni and Nd(La) orbitals close by. To mimic this frequency dependence, the static U parameter needs to be slightly increased. Expertise from many DFT+DMFT calculations for transition metal oxides shows that it typically needs to be about 0.5 eV larger, so that $U = 3.2\,\text{eV} = 8t$ is reasonable. Altogether, this defines a one-band Hubbard model for nickelates at various dopings. For the conductivity and other transport properties, the A pocket may be relevant as well, but superconductivity should arise from the correlated $3d_{x^2-y^2}$ band that is hardly coupled to the A pocket.

$LaNiO_2$ (GGA)	t_{000}	t_{100}	t_{001}	t_{110}	t_{200}	t_{210}
1-band (Ni-$d_{x^2-y^2}$)	0.2689	-0.3894	-0.0362	0.0977	-0.0465	-0.0037
10-bands (La-d+Ni-d)	0.2955	-0.3975	-0.0458	0.0985	-0.0491	0.0000
17-bands (La-f+La-d+Ni-d)	0.3514	-0.3943	-0.0239	0.0792	-0.0422	-0.0008
$NdNiO_2$ (GGA open core)	t_{000}	t_{100}	t_{001}	t_{110}	t_{200}	t_{210}
1-band (Ni-$d_{x^2-y^2}$)	0.3058	-0.3945	-0.0336	0.0953	-0.0471	-0.0031
10-bands (Nd-d+Ni-d)	0.3168	-0.3976	-0.0389	0.0949	-0.0480	-0.0008

Table 5.3: Major hopping elements (in units of eV) of the Ni-$3d_{x^2-y^2}$ orbital from 1-band (Ni-$3d_{x^2-y^2}$), 10-bands (La/Nd-d+Ni-d) and 17-bands (La/Nd-f+La/Nd-d+Ni-d) Wannier projections. The DFT-relaxed lattice parameters are: $LaNiO_2$ ($a = b = 3.88\,\text{Å}$, $c = 3.35\,\text{Å}$), $NdNiO_2$ ($a = b = 3.86\,\text{Å}$, $c = 3.24\,\text{Å}$) [50].

5.1.5 Non-local correlations and superconducting phase diagram

DFT provides a first picture of the relevant orbitals, and DMFT adds to this effects of strong local correlations such as the splitting into Hubbard bands, the formation of a quasiparticle peak and correlation-induced orbital shifts such as the upshift of the Γ pocket. However, at low temperatures non-local correlations give rise to additional effects. Relevant are here: the emergence of strong spin fluctuations and their impact on the spectral function and superconductivity.

For including such non-local correlations, diagrammatic extensions of DMFT such as the dynamical vertex approximation (DΓA) [38, 94, 95, 123] have been proven extremely powerful. Such calculations are possible down to the temperatures of the superconducting phase transition, in the correlated regime and for very large lattices so that the long-range correlations close to a phase transition can be properly described. Even (quantum) critical exponents can be calculated [140, 335–337]. DΓA has proven reliable compared with numerically exact calculations where these are possible [126], and in particular provide for a more accurate determination of T_c [12] since the full local frequency dependence of the two-particle vertex is included. Such local frequency dependence can affect even the non-local pairing through spin fluctuations. In, e.g., RPA this frequency dependence and the suppression of the pairing vertex for small frequencies can only be

Die approbierte gedruckte Originalversion dieser Dissertation ist an der TU Wien Bibliothek verfügbar.
The approved original version of this doctoral thesis is available in print at TU Wien Bibliothek.
TU Bibliothek Your knowledge hub WIEN

improperly mimicked by (quite arbitrarily) adjusting the static U.

This simple one-band Hubbard model in DΓA has been the basis for calculating the phase diagram T_c vs. Sr-doping in Fig. 5.5 [50]. At the time of the calculation only a single experimental T_c at 20% Sr-doping was available [17]. The physical origin of the superconductivity in these calculations are strong spin fluctuations which form the pairing glue for high-temperature superconductivity. Charge fluctuations are much weaker; the electron-phonon coupling has not been considered and is also too weak for transition metal oxides to yield high-temperature superconductivity. The theoretical T_c in Fig. 5.5 at 20% doping was from the very beginning slightly larger than in experiment. Most likely this is because in the ladder DΓA [95, 123] calculation of T_c the spin fluctuations are first calculated and then enter the superconducting particle-particle channel [12]. This neglects the feedback effect of these particle-particle fluctuations on the self-energy and the spin fluctuations, which may in turn suppress the tendency towards superconductivity somewhat. Such effects would be only included in a more complete parquet DΓA calculation [127, 234, 338]. Also, the ignored weak three-dimensional dispersion will suppress Tc. Let us note that antiferromagnetic spin fluctuations have recently been observed experimentally [32, 339].

Given the slight overestimation of T_c from the very beginning, the agreement with the subsequently obtained experimental T_c vs. Sr-doping x phase diagram [258, 323] in Fig. 5.5 is astonishingly good. We further see that the superconducting doping regime also concurs with the doping regime where a one-band Hubbard model description is possible for $Sr_xNd_{1-x}NiO_2$, as concluded from a full DFT+DMFT calculation for 5 Ni plus 5 Nd bands. This regime is marked dark blue in Fig. 5.5 and, as already noted, extends to somewhat larger dopings [50] than for $Sr_xLa_{1-x}NiO_2$ shown in Fig. 5.3. Concomitant with this is the fact that the experimental superconducting doping range for $Sr_xLa_{1-x}NiO_2$ extends to a larger x than for $Sr_xNd_{1-x}NiO_2$. For dopings larger than the dark blue regime in Fig. 5.5, two Ni $3d$ bands need to be included. As we will show in the next Section, this completely changes the physics and is not favorable for superconductivity. For dopings smaller than the dark blue regime in Fig. 5.5, on the other hand, the Γ pocket may become relevant for $Sr_xNd_{1-x}NiO_2$, as well as its exchange coupling to the $4f$ moments.

Our theoretical calculations also reveal ways to enhance T_c. Particularly promising is to enhance the hopping parameter t. This enhances T_c because (i) t sets the energy scale of the problem and a larger t means a larger T_c if U/t, t'/t, t''/t and doping are kept fixed. Further the ratio $U/t = 8$ for nickelates is not yet optimal. Indeed, (ii) a somewhat smaller ratio U/t would imply a larger T_c at fixed t [50]. Since the interaction U is local it typically varies much more slowly when, e.g., applying compressive strain or pressure and can be assumed to be constant as a first approximation (for secondary effects, see [148, 340]). Thus compressive strain or pressure enhance (i) t and reduce (ii) U/t. Both effects enhance T_c. This prediction made in [50] has been confirmed experimentally: applying pressure of 12 GPa increases T_c from 18 K to 31 K in $Sr_{0.18}Pr_{0.82}NiO_2$ [341]. This is so far the record T_c for nickelates, and there are yet no signs for a saturation or maximum, indicating even higher T_c's are possible at higher pressures.

Die approbierte gedruckte Originalversion dieser Dissertation ist an der TU Wien Bibliothek verfügbar.
The approved original version of this doctoral thesis is available in print at TU Wien Bibliothek.
TU Bibliothek Your knowledge hub WIEN

Alternatives to enhance t are (1) to substitute the $SrTiO_3$ substrate by a substrate with smaller in-plane lattice constants since the nickelate film in-plane axis parameters will be locked to that of the substrate. Further, one can (2) replace $3d$ Ni by $4d$ Pd, i.e. try to synthesize $Nd(La)PdO_2$ [308]. Since the Pd $4d$ orbitals are more extended than the $3d$ Ni orbitals this should enhance t as well.

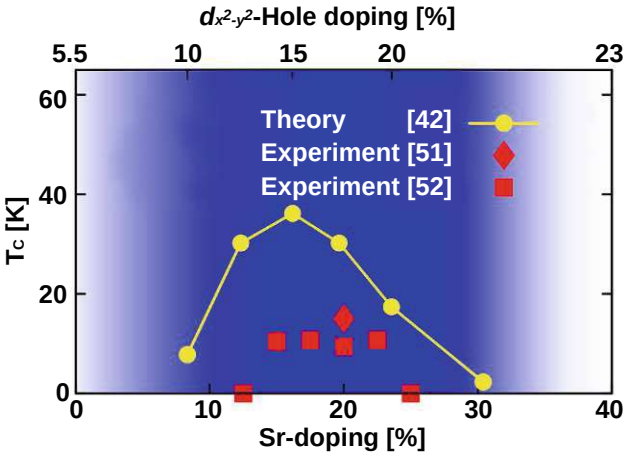

Figure 5.5: Superconducting phase diagram T_c vs. x for $Sr_xNd_{1-x}NiO_2$ as predicted by DΓA [50] and experimentally confirmed *a posteriori* in [258] and [323]. *A* priori, i.e., at the time of the calculation only one experimental data point [17] was available. For such a difficult to determine quantity as the superconducting T_c and without adjusting parameters, the accuracy is astonishing. The bottom x-axis shows the Sr-doping and the top x-axis the calculated hole doping of the $3d_{x^2-y^2}$ band according to Fig. 5.4. Adjusted from [50].

Next, we turn to the DΓA spectra, more precisely Fermi surfaces, in Fig. 5.6. Here, beyond quasiparticle renormalizations of DMFT, non-local spin fluctuations can further impact the spectrum. Shown is only the spectral function of the Hubbard model, describing the $3d_{x^2-y^2}$ band. Please keep in mind, that on top of the Fermi surface in Fig. 5.6, there is also a weakly correlated A pocket. As one can see in Fig. 5.6 antiferromagnetic spin-fluctuations lead to a pseudogap at the antinodal momenta $(\pm\pi, 0)$ $(0, \pm\pi)$ if the filling of the $3d_{x^2-y^2}$ band is close to half-filling. Indeed $n_{3d_{x^2-y^2}} = 0.95$ is the filling for the undoped parent compound $NdNiO_2$ where the A- and Γ pocket have taken 5% of the electrons away from the Ni $3d_{x^2-y^2}$ band. A Sr-doping of 20% is in-between $n_{3d_{x^2-y^2}} = 0.85$ and $n_{3d_{x^2-y^2}} = 0.8$, see Fig. 5.4. Comparing these theoretical predictions with the experimental Fermi surface, even the **k**-integrated spectrum, is very much sought after. However, here we face the difficulty that the superconducting samples require a $SrTiO_3$ capping layer or otherwise may oxidize out of vacuum. This hinders photoemission spectroscopy (PES) experiments as these are extremely surface sensitive. Hitherto PES is only available without capping layer for $Sr_xPr_{1-x}NiO_2$ [342]. These show a surprisingly low spectral density at the Fermi energy despite the metallic behavior of the doped system, raising the question of how similar these films are to the superconducting films.

Die approbierte gedruckte Originalversion dieser Dissertation ist an der TU Wien Bibliothek verfügbar.
The approved original version of this doctoral thesis is available in print at TU Wien Bibliothek.
TU Bibliothek Your knowledge hub WIEN

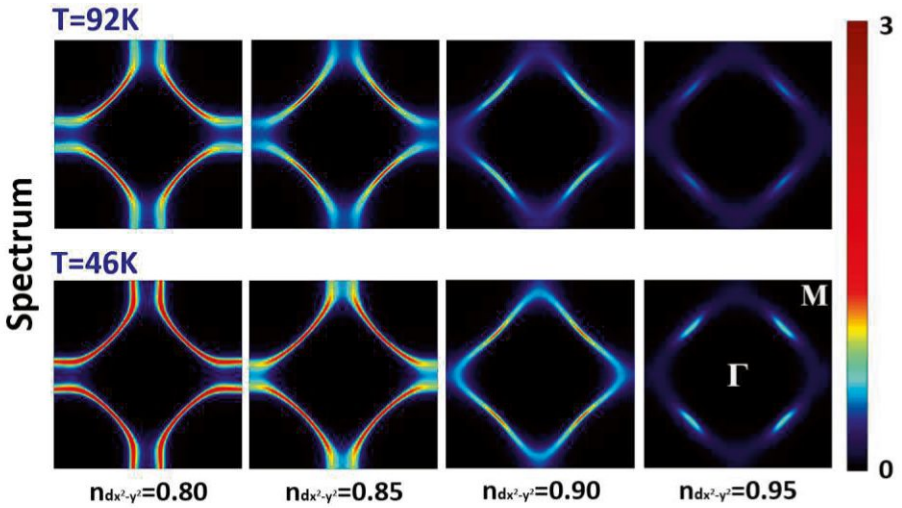

Figure 5.6: DΓA k-resolved spectrum at the Fermi energy for $T = 0.02t = 92\,\mathrm{K}$ (upper panels) and $T = 0.01t = 46\,\mathrm{K}$ (lower panels) and four different dopings $n_{d_{x^2-y^2}}$ of the Ni-3$d_{x^2-y^2}$ band (left to right). From [50].

5.1.6 Topotactic hydrogen: turning the electronic structure upside down

The fact that it took 20 years from the theoretical prediction of superconductivity in rare earth nickelates to the experimental realization already suggests that the synthesis is far from trivial. This is because nickel has to be in the unusually low oxidation state Ni^{+1}. The recipe of success for nickelate superconductors is a two step process [22]: First doped perovskite films $Sr(Ca)_xNd(La,Pr)_{1-x}NiO_3$ films are deposited on a $SrTiO_3$ substrate by pulsed laser deposition. Already this first step is far from trivial, not least because the doped material has to be deposited with homogeneous Sr(Ca) concentration. Second, $Sr(Ca)_xNd(La,Pr)_{1-x}NiO_3$ needs to be reduced to $Sr(Ca)_xNd(La,Pr)_{1-x}NiO_2$. To this end, the reducing agent CaH_2 is employed. Here, the problem is that this reduction might be incomplete with excess oxygen remaining or that hydrogen from CaH_2 is topotactically intercalated in the $Sr(Ca)_xNd(La,Pr)_{1-x}NiO_2$ structure. A particular difficulty is that the light hydrogen is experimentally hard to detect, e.g., evades conventional x-ray structural detection.

In [64], we studied the possibility to intercalate hydrogen, i.e., to synthesize unintendedly $Sr_xNd(La)_{1-x}NiO_2H$ instead of $Sr_xNd(La)_{1-x}NiO_2$. For the reduction of, e.g., $SrVO_3$ with CaH_2 it is well established that $SrVO_2H$ may be obtained as the end product [343]. Both possible end products are visualized in Fig. 5.7. The extra H, takes away one more electron from the Ni sites. Hence, we have two holes on the Ni sites which in a local picture are distributed to two orbitals and form a spin-1, due to Hund's exchange.

Die approbierte gedruckte Originalversion dieser Dissertation ist an der TU Wien Bibliothek verfügbar.
The approved original version of this doctoral thesis is available in print at TU Wien Bibliothek.
TU Bibliothek Your knowledge hub WIEN

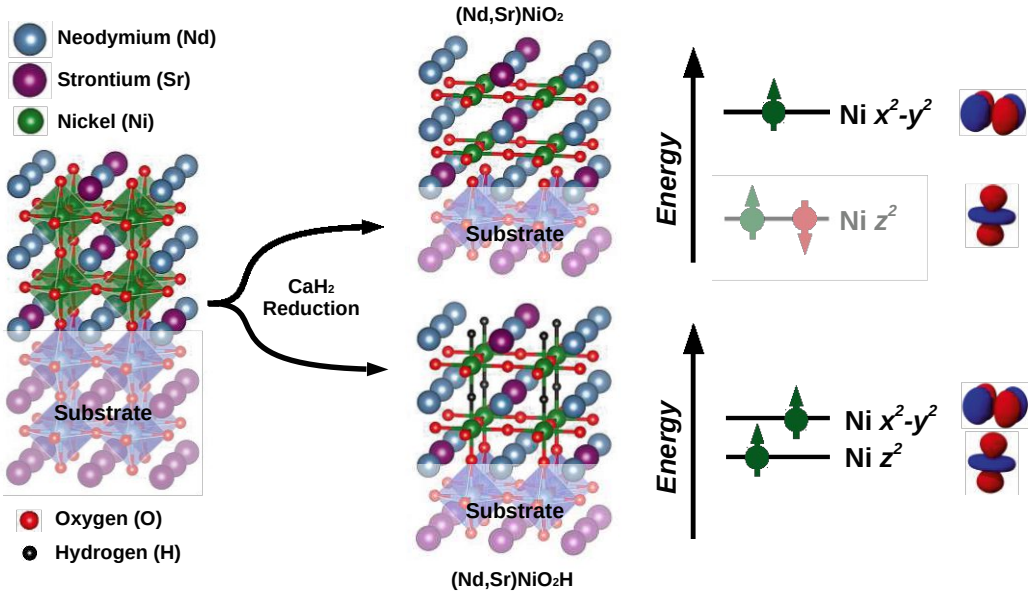

Figure 5.7: The reduction of $Sr_xNd(La)_{1-x}NiO_3$ with CaH_2 may result not only in the pursued end product $Sr_xNd(La)_{1-x}NiO_2$ but also in $Sr_xNd(La)_{1-x}NiO_2H$, where H atoms occupy the vacant O sites between the layers. This has dramatic consequences for the electronic structure. In a first, purely local picture, visualized on the right side, we have instead of Ni $3d^9$ with one hole in the $3d_{x^2-y^2}$ orbital two holes in the $3d_{x^2-y^2}$ and $3d_{3z^2-r^2}$ orbital forming a local spin-1.

The first question is how susceptible the material is to bind topotactic H. To answer this question, one can calculate the binding energy $E(ABNiO_2) + 1/2\ E(H_2)$- $E(ABNiO_2H)$ in DFT [64, 344]. The result is shown in Fig. 5.8, which clearly shows that early transition metal oxides are prone to intercalate hydrogen, whereas for cuprates the infinite-layer compound without H is more stable. Nickelates are in-between. For the undoped compounds $NdNiO_2$, and even a bit more for $LaNiO_2$, it is favorable to intercalate H. However for the Sr-doped nickelates the energy balance is inverted. Here, it is unfavorable to bind hydrogen.

Let us emphasize that this is only the enthalpy balance. In the actual synthesis also the reaction kinetics matter and the entropy which is large for the H_2 gas. Nonetheless, this shows that undoped nickelates are very susceptible to topotactic H. This possibly means that, experimentally, not a complete H-coverage as in $ABNiO_2H$ of Fig. 5.8 is realized, but some hydrogen may remain in the nickelates because of an incomplete reduction with CaH_2. Indeed hydrogen remainders have later been detected experimentally by nuclear magnetic resonance (NMR) spectroscopy, and they have even been employed to analyze the antiferromagnetic spin fluctuations [339].

Die approbierte gedruckte Originalversion dieser Dissertation ist an der TU Wien Bibliothek verfügbar.
The approved original version of this doctoral thesis is available in print at TU Wien Bibliothek.
TU Bibliothek Your knowledge hub WIEN

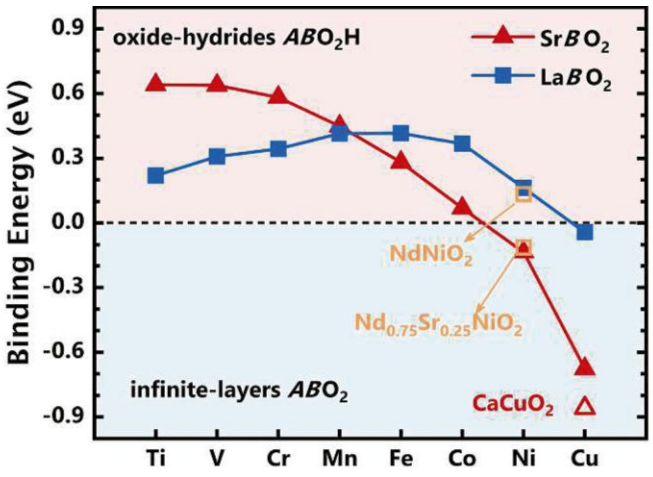

Figure 5.8: Binding energy for topotactical H as calculated by DFT for various transition metals B (x-axis). Positive binding energies indicate $AB\mathrm{NiO_2H}$ is energetically favored; for negative binding energies $AB\mathrm{NiO_2}$ is more stable. From [64].

Now that we have established that remainders of hydrogen can be expected for nickelates at low doping, the question is how this affects the electronic structure. The local picture of Fig. 5.7 already suggested a very different electronic configuration. This is further corroborated by DFT+DMFT calculations for $\mathrm{LaNiO_2H}$ presented in Fig. 5.9. Here, the DFT band structure shows a metallic behavior with two orbitals, Ni $3d_{x^2-y^2}$ and $3d_{3z^2-r^2}$, crossing the Fermi level. There are no rare-earth electron pockets any longer. Thus we have an undoped Ni $3d^8$ configuration without Sr-doping. If electronic correlations are included in DMFT, the DFT bands split into two sets of Hubbard bands. Above the Fermi level one can identify the upper $3d_{x^2-y^2}$ and $3d_{3z^2-r^2}$ Hubbard band in Fig. 5.9, with quite some broadening because of the electronic correlations. The lower Hubbard bands intertwine with the Ni t_{2g} orbitals, so that in the total spectral function individual bands are hardly discernible.

Even if we dope $\mathrm{LaNiO_2H}$ this electronic structure is not particularly promising for superconductivity. First, it is not two-dimensional because of the $3d_{3z^2-r^2}$ orbitals, which make the system more three-dimensional. More specifically, there is a considerable hopping process from Ni $3d_{3z^2-r^2}$ via H to the Ni $3d_{3z^2-r^2}$ on the vertically adjacent layer, as evidenced in Fig. 5.9 by the DFT dispersion of this band in the Γ-Z direction, the other $3d_{x^2-y^2}$ band is (as expected) flat in this direction. Second, the tendency to form local magnetic moments of spin-1 counteracts the formation of Cooper pairs from two spin-1/2's. Hence, altogether, we expect topotactic H to prevent high-temperature superconductivity.

Die approbierte gedruckte Originalversion dieser Dissertation ist an der TU Wien Bibliothek verfügbar.
The approved original version of this doctoral thesis is available in print at TU Wien Bibliothek.

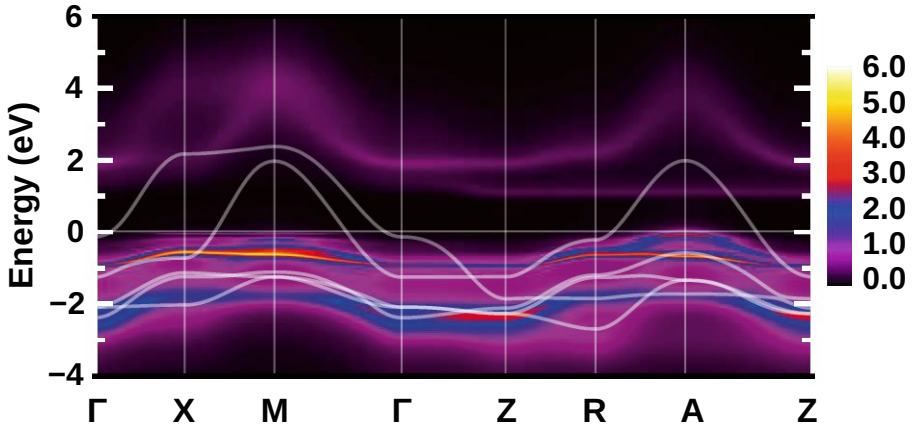

Figure 5.9: DFT (white lines) and DMFT (color bar) k-resolved spectral function for $LaNiO_2H$. From [64].

5.1.7 Conclusion

In this paper, we have discussed the physics of nickelate superconductors from the perspective of a one-band Hubbard model for the Ni $3d_{x^2-y^2}$ band plus an A pocket. Because of symmetry, this A pocket does not hybridize with the $3d_{x^2-y^2}$ band and merely acts as a decoupled electron reservoir. Hence, once the filling of the $3d_{x^2-y^2}$ band is calculated as a function of Sr or Ca doping in $Sr(Ca)_xNd(La,Pr)_{1-x}NiO_3$, we can, for many aspects, concentrate on the physics of the thus doped Hubbard model. This includes antiferromagnetic spin fluctuations and the onset of superconductivity. Other physical properties such as transport and the Hall conductivity depend as a matter of course also on the A pocket. This is in stark contrast to the cuprates, where the oxygen p orbitals are much closer to the Fermi level so that we have a charge-transfer insulator that needs to be modeled by the more complex Emery model.

The one-band Hubbard model picture for nickelates was put forward early on for nickelates [50, 51, 308, 310] and its proper doping including correlation effects has been calculated in [50]. This picture has been confirmed by many experimental observations so far. The Nd $4f$ states are from the theoretical perspective irrelevant because they form a local spin and barely hybridize with the $3d_{x^2-y^2}$ band. This has been confirmed experimentally by the observation of superconductivity in $Sr(Ca)_xLa_{1-x}NiO_2$. The minor importance of the other Ni $3d$ orbitals, in particular the $3d_{3z^2-r^2}$ orbital, is indicated through the careful analysis [330] of RIXS data [32, 329]. Not confirmed experimentally is hitherto the prediction that the Γ pocket is shifted above the Fermi level in the superconducting doping regime.

Strong evidence for the one-band Hubbard model picture is the prediction of the superconducting phase diagram [50], confirmed experimentally in [258] and [323]. A further prediction was the increase of T_c with pressure or compressive strain [50] which was subsequently found in experiment with a record $T_c = 31\,\mathrm{K}$ for nickelates under pressure [341]. The strength of antiferromagnetic spin-fluctuations as obtained in RIXS [32]

Die approbierte gedruckte Originalversion dieser Dissertation ist an der TU Wien Bibliothek verfügbar.
The approved original version of this doctoral thesis is available in print at TU Wien Bibliothek.
TU Bibliothek Your knowledge hub WIEN

also roughly agrees with that of the calculation [50]. Altogether, this gives us quite some confidence in the one-band Hubbard model scenario, which even allowed for a rough calculation of T_c. Notwithstanding, further theoretical calculations, in particular including non-local correlations also in a realistic multi-orbital setting [29, 94, 95], are eligible. On the experimental side more detailed, e.g., **k**-resolved information is desirable as are further close comparisons between experiment and theory.

A good analysis of the quality of the samples is also mandatory, especially against the background that superconducting nickelates have been extremely difficult to synthesize. Incomplete oxygen reduction and topotactic hydrogen [64, 344] are theoretically expected to be present because this is energetically favored, at least for low Sr-doping. This leads to two holes in two orbitals forming a high-spin state and a three dimensional electronic structure, thus obstructing the intrinsic physics of superconducting nickelates.

5.2 Finite layer nickelates

In the previous section, we discussed our view on the minimal low-energy model for infinite-layer nickelates, which consists of a Ni-3$d_{x^2-y^2}$ orbital and the so-called A-pocket, a hybrid of Nd-5d_{xy} and Ni-3$d_{xy/yz}$. While both orbitals are certainly relevant for transport quantities, e.g. resistivity or Hall-coefficient [258], we argued that the A-pocket is merely a passive bystander for superconductivity. Consequently, it only entered the low-energy effective Hamiltonian for superconductivity as an effective doping, and a doping-adjusted one-band Hubbard model for the Ni $3d_{xy/yz}$ orbital was used to compute the superconducting transition temperature within the dynamical vertex approximation (DΓA). With the synthesis of the first finite-layer nickelate, $Nd_6Ni_5O_{12}$ [345], it was only natural to ask how our current model generalizes. As discussed in more detail below, tight-binding parameters and transition temperature in the pentalayer nickelate $Nd_6Ni_5O_{12}$ are quite similar to its relative $NdNiO_2$ from the infinite-layer family. However, DFT+DMFT calculations show the A-pocket to be shifted above the Fermi level, thus providing evidence in favor of neglecting it for superconductivity.

The following section, marked by a vertical bar, has already been published in Physical Review Materials 6, L091801 (2022) [237].

5.2.1 Introduction

Even 35 years after the discovery of high temperature (T_c) superconductivity in cuprates [11], understanding the microscopic mechanism and identifying the necessary ingredients for a minimal model remains one of the arguably biggest challenges of solid state theory. The recent synthesis of nickelate superconductors $Sr(Ca)_xNd(La,Pr)_{1-x}NiO_2$ [17, 18, 293, 323, 334] provides a new perspective and has awoken new hope for this quest, not least because nickelates are very similar, but, at the same time, also very distinct from cuprates. In conjuncture with the cuprates they are hence ideally suited to distinguish the essential from the incidental for high-T_c superconductivity. That is, $Nd(La,Pr)NiO_2$

Die approbierte gedruckte Originalversion dieser Dissertation ist an der TU Wien Bibliothek verfügbar.
The approved original version of this doctoral thesis is available in print at TU Wien Bibliothek.
TU Bibliothek Your knowledge hub WIEN

shares the same infinite-layer structure and formal $3d^9$ valence with the simple cuprate superconductor $CaCuO_2$ [51, 57, 303]. However, besides the $d_{x^2-y^2}$ band, additional electron pockets are present at the Nd(La,Pr)NiO_2 Fermi surface, as identified in electronic structure calculations [21, 50, 64, 305–312, 332] and evidenced by a negative Hall coefficient [17, 323].

Since infinite-layer cuprates are not the best superconductors, finding superconductivity in a finite layer nickelate, the undoped pentalayer $Nd_6Ni_5O_{12}$ [345], must be considered a breakthrough for nickelate superconductivity. In contrast to infinite-layer nickelates, it has a positive Hall coefficient [345], although density-functional theory (DFT) predicts large electron pockets [345, 346]. The trilayer nickelate $Nd_4Ni_3O_8$ is, on the other hand, not superconducting [345]. This finding naturally leads to the question which finite-layer nickelates can be made superconducting and how to dope them.

In this letter, we analyze the superconducting pentalayer $Nd_6Ni_5O_{12}$ and the arguably simplest finite-layer compound, bilayer $Nd_3Ni_2O_6$ [a], by state-of-the-art density-functional theory (DFT) plus dynamical mean-field theory (DMFT) [26–28, 37, 262]. We show that local, dynamical correlations as included within DMFT push the Nd pockets (that exist in DFT [345]) above the Fermi level, thereby leaving only one correlated $d_{x^2-y^2}$ orbital per layer to form the Fermi surface—reminiscent of cuprate superconductors. The main differences between pentalayer and infinite-layer nickelates emerging from our simulations are: (i) When dynamical correlations are accounted for, Nd-pockets are present (absent) in the infinite (five-layer) compound. This indicates that the Nd-pockets are not important for superconductivity in nickelates. (ii) Our full-orbital DFT+DMFT calculations strongly suggest that the Hubbard model with a single (in-plane) orbital per Ni is the minimal setting for the pentalayer: The fluorite buffer-layers mainly suppress the already weak c-axis Ni-hopping; the tight-binding parameters and effective masses of the pentalayer's minimal $d_{x^2-y^2}$ model are very similar to the infinite nickelates. (iii) Further, neglecting the weak inter-layer hopping within the pentalayer slabs results in a 2D one-band Hubbard model, which we study by including non-local correlations within the dynamical vertex approximation (DΓA) [38, 216]. We find that spin fluctuations are dominant and give rise to superconductivity with a T_c comparable to experiment.

In the (undoped) bilayer $Nd_3Ni_2O_6$ with formal Ni valence $d^{8.5}$, instead, local correlations drive a charge transfer from the Ni $d_{xz/yz}$ to the $d_{x^2-y^2}$ orbitals that results in a *per se* multi-orbital system with a three-dimensional electronic structure. However, we predict that upon doping to a nominal valence of $d^{8.8}$, the $d_{xz/yz}$ orbitals become fully populated again and one-orbital physics, desirable for superconductivitiy, is recovered: The *doped* bilayer system shows properties similar to the infinite and pentalayer superconductors. As a dopant we propose Zr, specifically $La_{2+\delta}Zr_{1-\delta}Ni_2O_6$ with $\delta \lesssim 0.4$.

[a] Most recently, related $La_3Ni_2O_6$ crystals have been synthesized [347]

Die approbierte gedruckte Originalversion dieser Dissertation ist an der TU Wien Bibliothek verfügbar.
The approved original version of this doctoral thesis is available in print at TU Wien Bibliothek.

5.2.2 Methods

Structural relaxations for both lattice constants and all internal atomic positions are performed with the VASP code [348], while the WIEN2K package is used for the DFT electronic structures [55]. For both, the PBE [49] and PBESol [264, 349] versions of the generalized gradient approximation (GGA) are employed on a dense momentum grid with 3000 k-points. (See Appendix A.1 Section A.1.2 for detailed information or results with the modified Becke-Johnson (mBJ) [60] and DFT+U functionals.)

For the DMFT calculations, the WIEN2K bands around the Fermi level are projected onto maximally localized Wannier functions [67, 74] using WIEN2WANNIER [77, 273], visualization by Xcrysden [350] and supplemented by local Kanamori interactions for the sites shown in Fig. 5.10(a-c), taking the fully localized limit [274] as double counting. For $Nd_3Ni_2O_6$ a projection onto only the Ni-3d orbitals is sufficient, since the Nd-5d bands are well separated and above the Fermi level, as shown in Fig. 5.10(d) [discussed below]. Instead, for $Nd_6Ni_5O_{12}$ a projection onto both, the Ni-3d and Nd-5d shell, is necessary to account for the electron pocket around the M- and A-points, that are present in DFT. Expecting only minor variations of the local interaction with the number of nickel-layers, we use the same interaction parameters as were obtained for $LaNiO_2$ [64] by constrained random phase approximation (cRPA): inter-orbital interaction $U' = 3.10\,\text{eV}$ ($2.00\,\text{eV}$) and Hund's exchange $J = 0.65\,\text{eV}$ ($0.25\,\text{eV}$) for Ni (Nd). The intra-orbital Hubbard interaction follows as $U = U' + 2J$. These interaction parameters are close to those of previous studies [351, 352] for 3d oxides. The resulting Hamiltonian is then solved at room temperature ($300\,\text{K}$) in DMFT using continuous-time quantum Monte Carlo simulations in the hybridization expansions [120] implemented in W2DYNAMICS [277, 278]. The maximum entropy method [122, 280, 281, 353, 354] is employed for an analytic continuation of the spectra.

As justified below, a one-band per Ni site description based on the Ni-$d_{x^2-y^2}$ orbital is possible at low energies. Hence, we also perform a Wannier projection onto this $d_{x^2-y^2}$ orbital only [see Appendix A.1 for further information]. We supplement this effective tight-binding one-band model with the same on-site interaction U=8t as in [50], motivated by cRPA. This one-band model for five isolated layers can then be treated by more involved many-body techniques. We use the dynamical vertex approximation (DΓA) [38, 216], employing an additional, admittedly crude, approximation: neglecting the interlayer hopping. We perform calculations ranging from $300\,\text{K}$ to $40\,\text{K}$ and estimate the critical temperature T_c along the lines of [12, 355].

5.2.3 DFT crystal and electronic structure.

We consider the series $Nd_{n+1}Ni_nO_{2n+2}$ which can be synthesized from the Ruddlesden-Popper perovskite parent compound by oxygen reduction. Specifically, we concentrate on $Nd_3Ni_2O_6$ (n=2), $Nd_6Ni_5O_{12}$ (n=5, experimentally realized in [345]) and $NdNiO_2$ (n=∞, experimentally realized in [17, 258, 323]). Their crystal structures are shown in Fig. 5.10. Note the interface NdO-NdO layers between the n NiO_2 layers are transformed to fluorite-like Nd-O_2-Nd blocking slabs, which we find to be energetically favorable in

Die approbierte gedruckte Originalversion dieser Dissertation ist an der TU Wien Bibliothek verfügbar.
The approved original version of this doctoral thesis is available in print at TU Wien Bibliothek.
TU Bibliothek Your knowledge hub WIEN

DFT(+U) compared to the octahedral rock salt interface (see Appendix A.1).

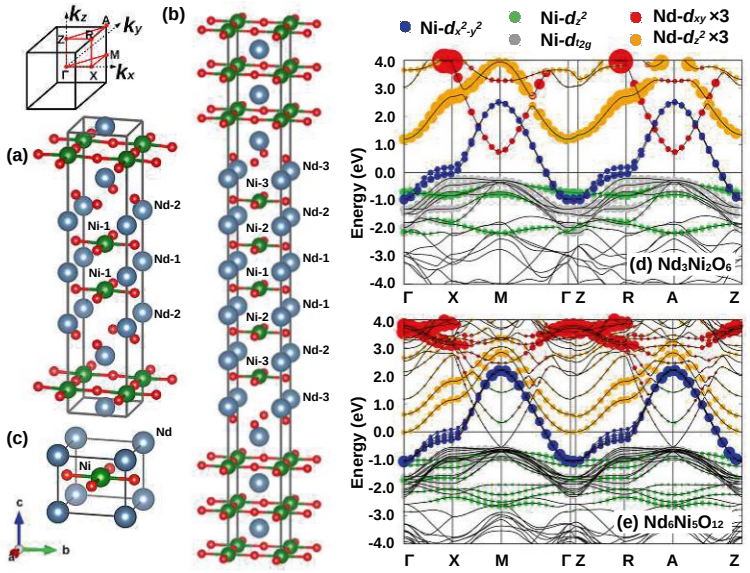

Figure 5.10: Crystal structure of the reduced Ruddlesden-Popper perovskites $Nd_{n+1}Ni_nO_{2n+2}$: (a) $Nd_3Ni_2O_6$ (n=2), (b) $Nd_6Ni_5O_{12}$ (n=5) and (c) $NdNiO_2$ (n=∞). From the center to the interface layer, the inequivalent Nd (Ni) atoms are labeled as Nd-1, 2, 3 (Ni-1, 2, 3). Nd, Ni and O atoms are shown as blue, green and red balls, respectively. The top-left panel shows the Brillouin zone and the notation for the high-symmetry momenta. DFT bandstructure and orbital character for (d) $Nd_3Ni_2O_6$ and (e) $Nd_6Ni_5O_{12}$ along a high symmetry path through the Brillouin zone.

A natural question is: how do the electronic bands in general [346] and the presence of the Nd pocket in particular change with the number of layers n? DFT studies of $NdNiO_2$ [307, 311, 312, 316, 331] show an electron pocket at the A- and Γ-point originating from the Nd-5d orbitals. Electronic correlations and Sr-doping may push the Γ-pocket above E_F. However, the A-pocket remains present in the superconducting doping region and acts as an electron reservoir [50] that (self)dopes the Ni 3d bands away from the nominal $3d^9$ configuration. In contrast, Fig. 5.10(d) for $Nd_3Ni_2O_6$ shows no electron pockets; the Nd-bands are clearly above E_F and well separated from the Ni bands. This indicates a weaker hybridization between Nd and Ni in $Nd_3Ni_2O_6$, i.e., the fluorite interface makes both NiO_2 and Nd-O_2-Nd layers more 2-dimensional (2D). For $Nd_6Ni_5O_{12}$ in Fig. 5.10(e), the DFT bandstructure shows a tube-like pocket (composed of Ni-d_{z^2} and Nd-d_{xy} character) that encompasses the momenta A and M (see Appendix A.1 for a plot). Similar to $NdNiO_2$ [307, 311, 331], a band of Nd-d_{z^2} character touches E_F at Γ.

To further investigate prospective similarities between infinite and finite layers, we list the electronic hopping terms from a Wannier projection in Table 5.2.3: infinite-layer $NdNiO_2$[20] and pentalayer $Nd_6Ni_5O_{12}$ have almost identical in-plane hopping parameters. Also the out-of-plane t_z hopping is almost the same within the five layers of the pentalayer nickelate, while it is practically zero across the fluorite spacing layer. Additionally both systems have very similar ratios of t'/t and t''/t. The bilayer $Nd_3Ni_2O_6$ has a ∼5% larger t which can be attributed to the increased two-dimensionality caused by the fluorite interface, which cuts of z-direction hopping after every second layer, rather than every fifth in the pentalayer.

While differences in hopping parameters are much smaller than between infinite and finite layer cuprates [304], the filling of the $d_{x^2-y^2}$-band, a key factor for superconductivity, differs considerably: $Nd_3Ni_2O_6$ hosts a nominal $d^{8.5}$ configuration which is far

Die approbierte gedruckte Originalversion dieser Dissertation ist an der TU Wien Bibliothek verfügbar.
The approved original version of this doctoral thesis is available in print at TU Wien Bibliothek.
TU Bibliothek Your knowledge hub WIEN

away from the optimal hole doping $\delta \lesssim 0.2$ ($d^{9-\delta}$). Also the doping of $Nd_6Ni_5O_{12}$, as predicted by DFT, is not within the superconducting region. Indeed, the A-M-pocket takes electrons away, leading to $\delta \sim 0.24$ holes (see Appendix A.1 Section A.1.5 and Table A.1) in the effective Ni-$d_{x^2-y^2}$ band, compared to the formal valency $\delta = 0.2$ ($d^{8.8}$). As we will see next, however, electronic correlations shift the tube-like pocket around A and M above the Fermi energy, and restore the doping to a level that is in line with the observed superconductivity.

System	t	t'	t''	t_z	t'/t	t''/t
$NdNiO_2$	-0.395	0.095	-0.047	-0.034	-0.242	0.119
$Nd_3Ni_2O_6$	-0.414	0.092	-0.055	-0.055	-0.223	0.132
$Nd_6Ni_5O_{12}$: Ni-1	-0.395	0.098	-0.050	-0.031	-0.249	0.127
$Nd_6Ni_5O_{12}$: Ni-2	-0.392	0.097	-0.050	———	-0.249	0.127
$Nd_6Ni_5O_{12}$: Ni-3	-0.398	0.097	-0.049	-0.026	-0.245	0.122

Table 5.4: Major tight-binding hopping parameters (in units of eV) for the Ni-$d_{x^2-y^2}$ orbital as obtained from a single-band Wannier projection; t, t', t'' and t_z indicate 1st [hopping along the direction R =(100)], 2nd [R=(010)], 3rd nearest neighbor [R=(200)] and z-direction [R=(001)] hopping, respectively. For $Nd_6Ni_5O_{12}$, Ni-1 is the central layer, Ni-3 denotes the two equivalent interface layers, and Ni-2 the two layers in-between, see Fig. 5.10(b).

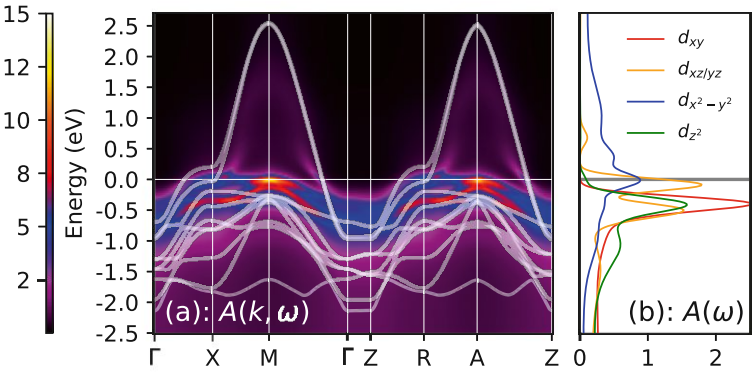

Figure 5.11: (a) DMFT k-resolved spectral function $A(k,\omega)$ for $Nd_3Ni_2O_6$. White lines are the DFT Wannier bands. (b) Corresponding k-integrated spectral function $A(\omega)$. Local correlations push the $d_{xz/yz}$ orbitals up in energy, which now contribute to the Fermi-surface at the M-point (cf. Appendix A.1).

5.2.4 DMFT results.

Some correlations, defined by the difference to a one-particle Hartree-Fock solution, are already taken into account on the level of DFT (spin-polarized or not) and further static ones in DFT+U (shown in the Appendix A.1). However, for the pentalayer we find prevalent dynamical correlations including a strong quasiparticle renormalization, which requires a method such as DMFT. For both, $Nd_3Ni_2O_6$ and $Nd_6Ni_5O_{12}$, electronic correlations dramatically change the electronic structure, see Figs. 5.11 and 5.23. In bilayer $Nd_3Ni_2O_6$, Hund's exchange favors a more equal occupation of orbitals since this way a spin-1 can be formed and also the Coulomb repulsion is lower ($U' = U - 2J$ instead of U). As a result, there is an electron transfer from the $d_{xz/yz}$ into the $d_{x^2-y^2}$ orbital (see Appendix A.1 Table A.1). The now partially depopulated $d_{xz/yz}$ orbitals are

Die approbierte gedruckte Originalversion dieser Dissertation ist an der TU Wien Bibliothek verfügbar.
The approved original version of this doctoral thesis is available in print at TU Wien Bibliothek.
TU Bibliothek Your knowledge hub WIEN

pushed up in energy, and both $d_{x^2-y^2}$ and $d_{xz/yz}$ form quasiparticle peaks in Fig. 5.11 and contribute to the Fermi surface (see Appendix A.1 Section A.1.7-A.1.8). This multi-orbital, three-dimensional electronic structure is, according to common wisdom, not favorable for superconductivity.

For the pentalayer, $Nd_6Ni_5O_{12}$, dynamical correlations have a different game-changing effect, see Fig. 5.23: The Nd-pocket around A- and M-momentum is pushed above the Fermi level, which only leaves the Ni $d_{x^2-y^2}$ contributing to the Fermi-surface (cf. Appendix A.1 Section A.1.7-A.1.8). We thus have a one-orbital system that is essentially two-dimensional and prone to strong antiferromagnetic fluctuations. The predominant Ni $d_{x^2-y^2}$ orbitals now host $\delta = 0.19$, 0.21, and 0.20 holes in the three inequivalent layers, compared to $\delta = 0.24$, 0.27, and 0.26 in DFT. As seen below, this pushes $Nd_6Ni_5O_{12}$ into the superconducting doping regime. Further, electronic correlations enhance the effective mass to $m^*/m_b \sim 2.5$ (see Appendix A.1 Section A.1.6). Altogether, our results hence show a clear similarity of the pentalayer and the infinite-layer system, with the noteworthy difference being the presence (absence) of the Nd A-pocket in $NdNiO_2$ ($Nd_6Ni_5O_{12}$). This evidences/supports that the pocket is not essential for superconductivity in nickelates as argued in [50].

This brings us back to the bilayer compound $Nd_3Ni_2O_6$ and the question: can we tune its electronic structure to one that is favorable for superconductivity? We believe one can do so through chemical doping/substitution: Here, we consider $La_{2+x}Zr_{1-x}Ni_2O_6$ which has a nominal valency $3d^{9-x/2}$. Indeed, at $x = 0.4$ no electron pockets are present within DFT+DMFT anymore, and the Fermi surface is composed only of a single Ni $d_{x^2-y^2}$ orbital (see Appendix A.1 Section A.1.10), hosting $\delta = \frac{x}{2} = 0.2$ holes, akin to the penta-layer and doped infinite-layer nickelates.

Die approbierte gedruckte Originalversion dieser Dissertation ist an der TU Wien Bibliothek verfügbar.
The approved original version of this doctoral thesis is available in print at TU Wien Bibliothek.
TU Bibliothek Your knowledge hub WIEN

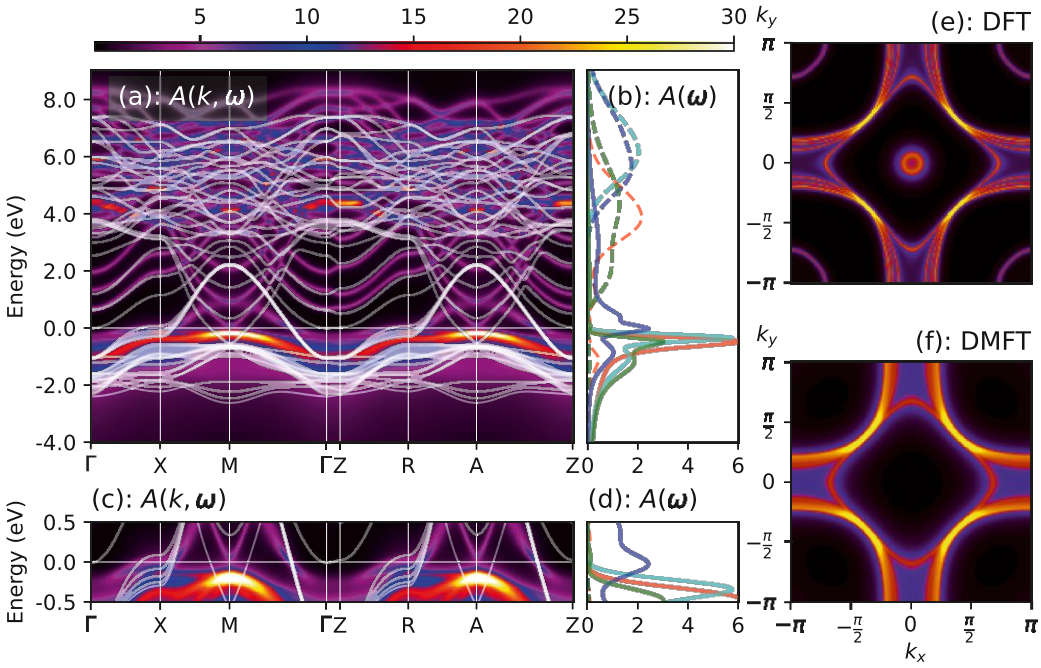

Figure 5.12: DMFT k-revolved spectral functions $A(k,\omega)$ (a) and k-integrated A(ω) (b) of $Nd_6Ni_5O_{12}$; (c) and (d) are a zoom-in around E_F=0; solid lines in (a, c) are the DFT Wannier-bands. Fermi surface for (e) DFT and (f) DMFT. The colorbar at the top is for all plots. The DMFT Fermi surface has been multiplied by two for better visibility. Colorcode for the k-integrated spectral function is the same as in Fig.5.11, with solid lines for Ni and dashed for Nd. Adapted from [237].

5.2.5 Estimating T_c with DΓA.

The DMFT calculation with all Ni and Nd-d orbitals for $Nd_6Ni_5O_{12}$ suggests single orbital physics. Indeed, one-band DMFT (Appendix A.1 Section A.1.7-A.1.8) agrees well with the full-orbital calculation, including effective masses (compare Appendix A.1 Table A.1 and A.3), justifying a projection onto only the $d_{x^2-y^2}$-orbital. Since interlayer hoppings are as small as in the infinite-layer system, for what follows, we treat the layers as independent as done previously for $NdNiO_2$ [50].

This allows us to calculate T_c as a function of the $d_{x^2-y^2}$ orbital-filling in an effective two-dimensional Hubbard model. To this end, we include non-local spin and superconducting fluctuations with DΓA: The thus calculated superconducting dome is displayed as the red-shaded region in Fig.5.13, experiment for $Nd_6Ni_5O_{12}$ [345] as a diamond. Also shown is the experimental phase diagram for $NdNiO_2$ (violet-shaded region, translated to the $d_{x^2-y^2}$ filling according to [50]) which thanks to higher quality films with less defects [59] now agrees much better with DΓA than previously [17, 293, 323]. As we can see, the doping of the pentalayer parent compound $Nd_6Ni_5O_{12}$ is indeed already in the doping range for superconductivity. This was not the case without correlations: DFT (gray lines in Fig.5.13) would predict a doping outside of the superconducting dome, due to the

Die approbierte gedruckte Originalversion dieser Dissertation ist an der TU Wien Bibliothek verfügbar.
The approved original version of this doctoral thesis is available in print at TU Wien Bibliothek.
TU Bibliothek Your knowledge hub WIEN

presence of the Fermi surface tube around A- and M. Also the proposed $La_{2.4}Zr_{0.6}Ni_2O_6$ has a very similar doping (blue line), but it has slightly different hopping parameters, in particular a larger t which should result in a slightly larger T_c as (i) t sets the unit of energy and (ii) according to DΓA, a smaller U/t is favorable for T_c.

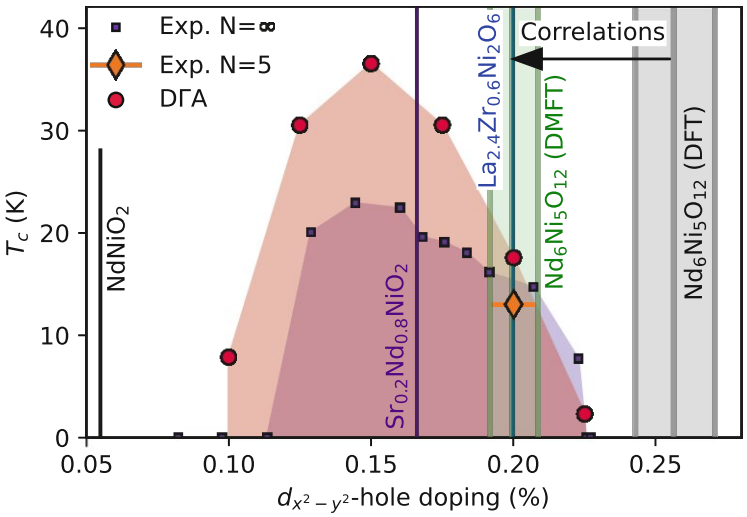

Figure 5.13: Phase diagram T_c vs. hole doping of the Ni $d_{x^2-y^2}$ band as calculated by DΓA. For $Nd_6Ni_5O_{12}$, the doping of the inequivalent layers is marked by three green (DMFT) and gray lines (DFT) and the experimental T_c (diamond) is from [345]. For Sr-doped $NdNiO_2$, experimental data are from [59].

5.2.6 Conclusion.

We have seen that electronic correlations decisively alter the electronic structure of finite layer nickelates, beyond a mere effective mass renormalization of the bands. In the case of the pentalayer nickelate $Nd_6Ni_5O_{12}$, DFT predicts an electron pocket around the A and M momenta and thus a doping which is not in line with the observed superconductivity. However, electronic correlations push this electron pocket above the Fermi energy so that there are 0.2 holes per Ni (with only a tiny variation of ~ 0.02 holes between the layers). This way the Ni $d_{x^2-y^2}$ orbital is placed in the optimal superconducting doping range; it also has virtually the same hopping terms as $NdNiO_2$. Hence, electronic correlations are key to explaining the experimental observation of superconductivity in $Nd_6Ni_5O_{12}$ [345]. These predictions also call for a careful angular photoemission spectroscopy (ARPES) study of this pentalayer system to experimentally confirm the absence of the Nd-derived pockets.

While the A-pocket in $NdNiO_2$ is possibly only a passive bystander for superconductivity [50], it will certainly contribute to the Hall coefficient. We therefore suggest the very different Hall coefficient for $n = \infty$ [345] and $n = 5$ [17, 323] to be explained by the presence ($NdNiO_2$) or absence ($Nd_6Ni_5O_{12}$) of these electron pockets. Further, it is tempting to attribute (at least part of) the unusually broad superconducting transition to the layer-dependent doping of $Nd_6Ni_5O_{12}$.

According to our phase diagram in Fig. 5.13, pentalayer nickelate is overdoped. Without electron pockets, $Nd_{n+1}Ni_nO_{2n+2}$ has a hole doping $\delta = 1/n$, suggesting that T_c will increase with a few more Ni-layers and the parent compounds will likely remain inside

Die approbierte gedruckte Originalversion dieser Dissertation ist an der TU Wien Bibliothek verfügbar.
The approved original version of this doctoral thesis is available in print at TU Wien Bibliothek.

the superconducting dome up to about $n = 10$. For $n < 5$, we have instead too many holes. Then, electron-doping with a tetravalent cation as, e.g., in $La_{2+\delta}Zr_{1-\delta}Ni_2O_6$ with $\delta \lesssim 0.4$ is needed.

5.3 Magnetic response in nickelate superconductors

In the previous sections 5.1 and 5.2 we discussed the possibly minimal model for superconductivity in nickelate superconductors: a single-band Hubbard model[3]. Subsequently, we solved this model within DΓA and used the results to obtain the critical temperature T_c, see Section 3.9 for details. This procedure is, in principle, parameter-free. However, since we (currently) cannot treat frequency-dependent interactions $U(\omega)$ within DΓA, a static approximation of $U_{\mathrm{cRPA}}(\omega)$ has to be used. A natural first choice would be to simply use $U = U_{\mathrm{cRPA}}(\omega = 0)$, which is about 2.6 eV for the single-band approximation of $LaNiO_2$[311]. However, previous studies [81, 356, 357] showed that cRPA overscreens the interaction. To compensate for this, the authors of Ref. [50] proposed a range of reasonable interaction values for the single-band model $7t \lesssim U \lesssim 9t$ and argued that $U = 8\,\mathrm{t}$ (3.11 eV) is likely to be most appropriate. Since the following discussion focuses more on the Hubbard mode we will use the nearest-neighbor hopping t, which is 0.389 eV for the single-band model of $LaNiO_2$, as unit of energy. $U_{\mathrm{cRPA}}(\omega = 0) = 2.6\,\mathrm{eV}$ for $LaNiO_2$.

Estimating the superconducting transition temperature of the effective single-band Hubbard model using DΓA[4] [50] yields a dome structure similar to that measured in experiments [59, 258] for $8t \lesssim U \lesssim 9t$[5]. The pairing symmetry obtained in DΓA is d-wave, reminiscent of that in cuprate [3]. On the experimental side, the pairing symmetry remains an open question and results are still inconclusive. The authors of Ref. [358] measure both s-wave and d-wave gaps using scanning tunneling microscopy (STM), depending on the location of the sample. Measurements based on the London penetration depth are both reported to be "consistent with d-wave pairing" [359] and "inconsistent with a dominant $d_{x^2-y^2}$-wave gap" [360].

Also, the minimal model which captures superconductivity in nickelates is controversial and, among others, the relevance of multi-orbital physics [290, 306, 361], Kondo physics [362], or even phonons [363] have been suggested. It is natural to ask what makes the single band Hubbard model, which we use in this thesis to model superconductivity in nickelates, superconducting, or phrased differently: what is the dominant contribution to the "pairing glue"? This question can be answered by performing a fluctuation diagnostic of the pairing vertex, see e.g. [364]. Analyses of DΓA [12] or dynamical cluster approximation (DCA) [161] solutions of the Hubbard model reveal antiferromagnetic spin-fluctuations to be the primary source contributing to the "pairing glue"[6]. While

[3] One should note that the correct doping translation from Sr doping to filling in the single-band model is important.

[4] For a detailed description of the procedure, we refer the reader to Section 3.8 and Section 3.9 as well as Ref. [355], where the authors also comment on estimating T_c in 2D systems.

[5] For $U = 7\,\mathrm{t}$ the superconducting dome extends towards very low doping which is not observed in measurements [50].

[6] One should note that, while spin fluctuations mediate superconductivity in our calculations, the topic

Die approbierte gedruckte Originalversion dieser Dissertation ist an der TU Wien Bibliothek verfügbar.
The approved original version of this doctoral thesis is available in print at TU Wien Bibliothek.
TU Bibliothek Your knowledge hub WIEN

performing a "fluctuation diagnostic" in an experiment is much less straightforward, the strength or characteristics of different fluctuations can be measured, e.g., using resonant inelastic X-ray scattering (RIXS) or neutron scattering. So far, long-range antiferromagnetic order is absent in infinite-layer nickelates [367, 368]. This absence of AFM order is one of the notable differences between cuprates and nickelates. One natural explanation is the self-doping in nickelates induced by the A- and Γ-pocket bands. Consequently, the $d_{x^2-y^2}$ orbital of the parent compound is *not* half-filled and thus less prone to AFM order. Indeed, also in cuprates AFM order vanishes upon hole-doping see e.g. Ref. [3, 369]. Nevertheless, signatures of AFM fluctuations have been measured in several probes. These include RIXS [32], which report paramagnon dispersion with a sizeable effective spin-interaction J, while nuclear magnetic resonance (NMR) indicates the existence of AFM fluctuations [339]. More recently, the authors of Ref. [370] performed μSR measurements and observed signatures of short-range magnetic correlations, which for some samples is reported to be consistent with the formation of a static order on the timescale of the muon.

In the following section, we discuss the paramagnetic susceptibility for the Hubbard model as obtained within DΓA and compare it to the experimentally measured spectra from Ref. [32]. We find they are overall similar, especially since model biases are expected both from theory and experiment. Possible origins of systematic deviations, most notably an overestimated magnon bandwidth in theory, and implications for the superconducting transition temperature are discussed.

5.3.1 Models and Methods

Antiferromagnetic (AFM) fluctuations in the paramagnetic state constitute the major contribution to the pairing glue in our DΓA + Eliashberg calculations. Hence, a critical check is whether or not AFM fluctuations with similar characteristics are also observed in experimental measurements. To this end, we compare the paramagnon dispersion calculated in DΓA with the one extracted from RIXS measurements by the authors of Ref. [32]. To understand how those respective paramagnon dispersions are obtained, let us briefly review what is exactly computed in DΓA and the model that is used to extract the magnon dispersion from measurements.

Single-band model for nickelates —- We consider a single-band Hubbard model as the effective model for superconductivity and the paramagnon dispersion of nickelates. The rare-earth-derived bands enter as an effective doping [50]. For a detailed discussion of our reasoning behind this model we refer the reader to the previous Section 5.1, which is based on Ref. [20]. The Hamiltonian of this model is

$$\mathcal{H}_{\text{Hubbard}} = \sum_{\mathbf{k},\sigma} \epsilon_{\mathbf{k}} \hat{c}^{\dagger}_{\mathbf{k}\sigma} \hat{c}_{\mathbf{k}\sigma} + U \sum_{i} \hat{n}_{i\uparrow} \hat{n}_{i\downarrow} + \mu \hat{n}, \tag{5.1}$$

where $U = 8\,\text{t}$ (3.1 eV) is the Hubbard interaction μ the chemical potential to fix the

remains highly controversial and many different mechanisms have been proposed [3, 162, 365, 366].

Die approbierte gedruckte Originalversion dieser Dissertation ist an der TU Wien Bibliothek verfügbar.
The approved original version of this doctoral thesis is available in print at TU Wien Bibliothek.
TU Bibliothek Your knowledge hub WIEN

number of particles[7] and $\epsilon_{\mathbf{k}}$ the energy-momentum dispersion given by

$$\epsilon_{\mathbf{k}} = -2t[\cos(k_x) + \cos(k_y)] - 4t'\cos(k_x)\cos(k_y) - 2t''[\cos(2k_x) + \cos(2k_y)]$$

where $t = 1\,\mathrm{t}$ (0.389 eV), $t' = -0.25\,\mathrm{t}$ (0.097 eV) and $t'' = 0.12\,\mathrm{t}$ (0.046 eV)[8] [50].

Paramagnon dispersion in DΓA —- The magnetic susceptibility $\chi_{\mathrm{m}} = \sum_{kk'} \chi_{\mathrm{m}}^{qkk'}$ for the model of Eq. 5.1 given by the solution to the Bethe-Salpeter equation (Eq. 3.57), which we reproduce here for the single-band SU(2) symmetric case[9],

$$\chi_{\mathrm{m}}^{qkk'} = \chi_0^{qkk'} - \frac{1}{\beta^2} \sum_{k_1 k_2} \chi_0^{qkk_1} \Gamma_{\mathrm{m}}^{qk_1k_2} \chi_{\mathrm{m}}^{qk_2k'}, \tag{5.2}$$

where $\chi_0^{qkk'} = \beta G^k G^{k-q}$ and G is the one-particle Green's function of the system. Within DΓA for Eq. 5.2 $G \equiv G^{\mathrm{DMFT}}$ is the DMFT propagator and $\Gamma_{\mathrm{m}}^{qkk'} \equiv \Gamma_{\mathrm{m}}^{\mathrm{AIM};\omega\nu\nu'}$ is approximated by that of the corresponding Anderson impurity model (AIM). Subsequently, a λ correction is used

$$\chi_{\mathrm{m}}^{\lambda_{\mathrm{m}};q} = \frac{1}{\frac{1}{\chi_{\mathrm{m}}^{q}} + \lambda_{\mathrm{m}}}, \tag{5.3}$$

which can be understood as adding an effective mass to the paramagnon [89], or equivalently as decreasing the (antiferromagnetic) correlations length[10].

Analytic continuation — To compare with RIXS measurements χ_{m} is required for *real* frequencies. For analytic continuation we use the maximum entropy method (*MaxEnt*) [122, 280, 281, 353, 354] as implemented in `ana_cont` [122]. We use the "chi2kink" method [122, 353] starting from a flat default model to reduce bias and avoid any free parameters[11]. Since *MaxEnt* tends to broaden spectra [122], we expect the theoretical dispersion to be broader, especially at higher frequencies.

Paramagnon dispersion from RIXS — RIXS measurements do not probe magnetic excitations exclusively, but rather elementary excitations in general [371]. To extract the magnon excitation, the authors of Ref. [32] used a Gaussion for the elastic peak, a damped harmonic oscillator (DHO) for the magnon, an anti-symmetrized Lorentzian for phonons and the tail of an anti-symmetrized Lorentzian for the high-energy background. For detailed information regarding the fitting procedure, we refer the reader to the supplementary information of Ref. [32].

[7] The translation between Sr doping and effective Ni-$3d_{x^2-y^2}$ occupation can be found in Fig. 3 in the supplementary material of Ref. [50].
[8] See also Box 5.
[9] For a general discussion see Section 3.4 and Section 3.5.
[10] For a detailed discussion on DΓA and the λ correction see Section 3.8 and Refs. [89, 134].
[11] We checked the results against using a broad Gaussian as starting model and obtained essentially the same results.

Die approbierte gedruckte Originalversion dieser Dissertation ist an der TU Wien Bibliothek verfügbar.
The approved original version of this doctoral thesis is available in print at TU Wien Bibliothek.
TU Bibliothek Your knowledge hub WIEN

5.3.2 Paramagnon dispersion compared between RIXS and DΓA

Parent compound: DΓA and RIXS — The paramagnon dispersion for the parent compound ($x = 0$) of $Nd_{1-x}Sr_xNiO_2$ is shown in Fig. 5.14. Fig. 5.14(a) displays $\chi''_m(\omega, q)$ as computed in DΓA using a filling of $n = 0.95$, which mimics the self-doping due to the rare-earth pockets [50], along a high-symmetry path in the Brillouin zone (BZ), shown as an inset. The data in Fig. 5.14(b) was extracted from the RIXS measurements of Ref. [32][12]. Given that we performed a parameter-free calculation, the agreement between our model calculations and the DHO magnon energy extracted from RIXS is quite good. This indicates that experimental spin fluctuations are similar to those leading to superconductivity in DΓA calculations. Yet they also show some systematic differences, which are discussed in the following. While both show a dispersing paramagnon with a linear slope close to the Γ point, the slope is overestimated in DΓA. This is also connected to the magnitude of the bandwidth, which is larger in our DΓA calculations. To compare, the peak of $\chi_m(q = X, \omega)$ is at $\sim 260\,\text{meV}$ in DΓA, while the measured one is close to $\sim 190\,\text{meV}$. This corresponds to an overestimation of the effective spin coupling J, which we discuss in more detail below. Furthermore, the "dip" observed in the dispersion around the M/2 momentum, which corresponds to higher-order couplings in a spin-wave picture, is more pronounced in theory compared to the experiment.

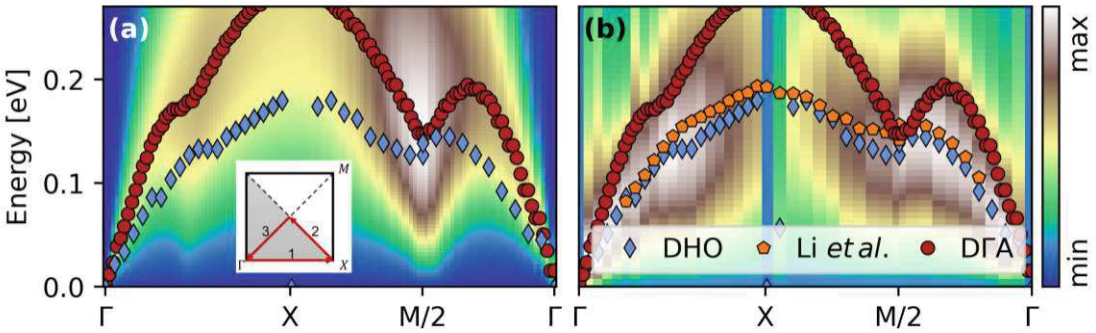

Figure 5.14: Paramagnon dispersion in $Nd_{1-x}Sr_xNiO_2$ for $x = 0$ ($n = 0.95$). **(a)** colormap of the dispersion within DΓA at $T \simeq 60K$. **(b)** colormap of the magnon dispersion extracted from RIXS measurements at $T = 15\,\text{K}$. Raw data was taken from [32]. The author of this thesis performed subsequent fits to extract the magnon from the experimental raw data. Red dots mark the maximum of the peak in DΓA and blue diamonds are those of the extracted DHO, orange pentagons mark the peak position reported in Ref. [32]. Inset in (a) shows the k-path in the BZ, where $\Gamma = (0, 0, 0)$, $X = (\pi, 0, 0)$ and $M/2 = (\pi/2, \pi/2, 0)$. Tight-binding parameters are $t = 0.389$, $t' = -0.25t$ and $t'' = 0.1t$. Hubbard interaction $U = 3.11\,\text{eV}$ ($8t$).

Let us now turn toward the doped compounds. Results for $x = 0.125$ ($n = 0.875$) and $x = 0.225$ ($n = 0.80$) are displayed in Fig. 5.15(a) and Fig. 5.15(b), respectively. Consistent with experiment (blue diamonds in Fig. 5.15), we observe a shift towards lower energies around the M/2 momentum. Furthermore, the amplitude of χ_m decreases as

[12] We plot the fitted damped harmonic oscillator, which is used as a model to describe the magnon. The fit was performed by us as described by the authors of Ref. [32] in their supplemental material.

Die approbierte gedruckte Originalversion dieser Dissertation ist an der TU Wien Bibliothek verfügbar.
The approved original version of this doctoral thesis is available in print at TU Wien Bibliothek.
TU Bibliothek Your knowledge hub WIEN

$q \to$X, which was also observed in Ref. [32][13]. However, similar to the parent compound (Fig. 5.14), the bandwidth remains overestimated in DΓA at finite doping. Particularly the peak position at the X momentum shows a large deviation compared to the one extracted from RIXS. This may, however, be partially attributed to the bias introduced both on the theoretical and experimental sides.

On the one hand, we expect a worse performance of the numerical analytic continuation for large frequencies. A spectrum already relatively flat at the X momentum might be additionally broadened. On the other hand, the intensity of the magnon peak is also reduced in RIXS [32], making the experimental fitting procedure more difficult.

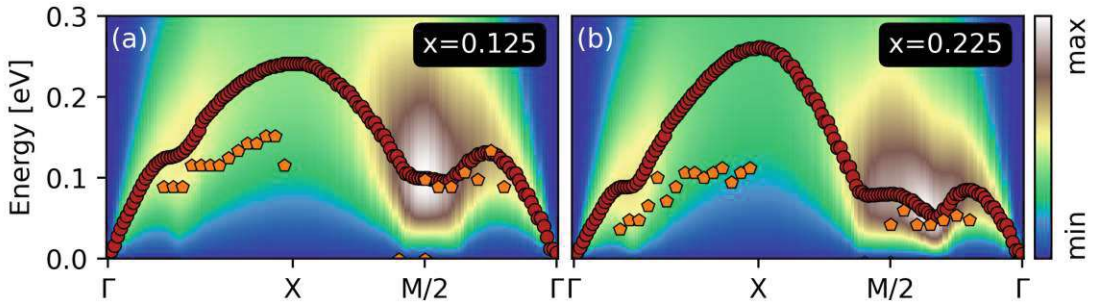

Figure 5.15: Paramagnon dispersion in $La_{1-x}Sr_xNiO_2$ for $x = 0.125$ (left) and $x \simeq 0.225$ (right). The red dots mark the maximum of the dispersion at each k-point, while the orange pentagons are the corresponding RIXS peak locations taken from Ref. [32]. Tight-binding parameters are $t = 0.389\,\text{eV}$, $t' = -0.25t$ and $t'' = 0.12t$. Hubbard interaction $U = 3.11\,\text{eV}$ $(8t)$.

5.3.3 Effective spin-wave picture

Spin exchange coupling J —— In the limit of large Hubbard interactions U the Hubbard model (Eq. 5.1) reduces to an effective Heisenberg Hamiltonian. This mapping has already been performed and we refer the reader to Ref. [372] for an extensive discussion. While this mapping provides a direct relation between t, U and the effective spin couplings J, temperature and occupation do not enter this discussion. Furthermore, this mapping becomes rather tedious in the presence of t' and t'' [372]. One should also note that $LaNiO_2$ is not Mott insulating, and a spin-wave picture is less appropriate compared to cuprates. Nevertheless, it still provides a somewhat intuitive picture for understanding the characteristics of spin fluctuations. For those reasons, we employ a more "experimentalist" approach, starting from the Heisenberg Hamiltonian and then fit the corresponding spin-wave to our DΓA results in order to extract information about J and J'. The effective classical spin-wave dispersion for a spin-1/2 system including only the nearest J and next-nearest spin-spin J' spin-spin interaction is given by [148, 372, 373],

$$\omega_{\mathbf{k}} = Z_C \sqrt{\mathrm{A}_{\mathbf{k}}^2 - \mathrm{b}_{\mathbf{k}}^2}, \tag{5.4}$$

[13] See supplementary material of [32] Fig. S6(b).

Die approbierte gedruckte Originalversion dieser Dissertation ist an der TU Wien Bibliothek verfügbar.
The approved original version of this doctoral thesis is available in print at TU Wien Bibliothek.
TU Bibliothek Your knowledge hub WIEN

U [t]	8	8	9	10	Exp. [32]
T [K]	361	60	60	60	20
J [meV]	76	62	64	44	63.6 ± 3.3
J' [meV]	-13	-23	-12	-12	-10.3 ± 2.3

Table 5.5: Effective spin-coupling J and J' for $NdNiO_2$ obtained with DΓA and measured in RIXS [32] given in units of meV. We list results for different interaction values $U = \{8, 9, 10\}$ in units of the hopping $t = 0.389\,\text{eV}$ and two different temperatures $T = \{300\,\text{K}, 60\,\text{K}\}$ for $U = 8\,t$.

where Z_C is the spin-wave renormalization factor to account for the effects of quantum fluctuations and

$$\begin{aligned} \mathrm{A}_{\mathbf{k}} &= 2J + 2J'[\cos(k_x)\cos(k_y) - 1], \\ \mathrm{B}_{\mathbf{k}} &= J[\cos(k_x) + \cos(k_y)]. \end{aligned} \tag{5.5}$$

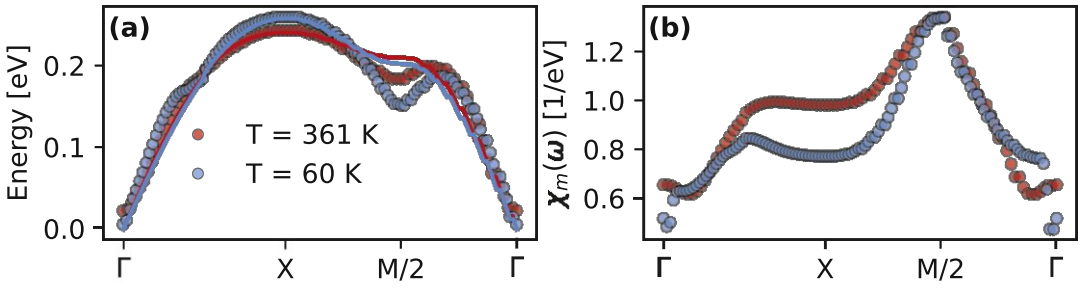

Figure 5.16: Paramagnon dispersion obtained in DΓA for $LaNiO_2$ as a function of temperature. **(a)** dispersion (dots) and spin-wave fit (lines) using Eq.5.4. **(b)** value of the magnetic susceptibility $\chi_m(\omega_{\text{peak}})$ at the peak location ω_{peak}. Red corresponds to 361 K and blue to 60 K.

To better compare with the values obtained in experiment, we fix $Z_C = 1.18$ as in Ref. [32]. Fig. 5.16 shows the paramagnon dispersion and the corresponding value of the magnetic susceptibility $\chi_m(\omega_{\text{peak}})$. First let us note that the reduced dispersion around the M/2-point ($\mathbf{k} = (\pi/2, \pi/2, 0)$) is not well captured by the (J-J') spin-wave fit. We presume that higher-order couplings in the effective spin Hamiltonian would need to be included to capture it. While this would be interesting for further research, it is out of scope for this thesis.

Similar to the cuprate superconductor La_2CuO_4 [373] we can observe that the dispersion along the antiferromagnetic zone boundary (AFZ) becomes more pronounced as temperature is lowered. This is mimicked by an increasing *ferromagnetic* next-nearest spin-coupling J' of $\sim -13\,\text{meV}$ at 361 K to $\sim -23\,\text{meV}$ at 60 K. For J the trend is opposite and its value gets reduced from $\sim 76\,\text{meV}$ at 361 K to $\sim 62\,\text{meV}$ at 60 K. Experimentally $J = 63.6 \pm 3.3\,\text{meV}$ and $J' = -10.3 \pm 2.3\,\text{meV}$ at 20 K were reported in Ref. [32]. We list the effective couplings below in Table 5.5, for different temperatures and interaction values.

The effective spin-coupling of a Hubbard model with $t' = t'' = 0$ is to zeroth order

Die approbierte gedruckte Originalversion dieser Dissertation ist an der TU Wien Bibliothek verfügbar.
The approved original version of this doctoral thesis is available in print at TU Wien Bibliothek.
TU Bibliothek Your knowledge hub WIEN

$J = \frac{4t^2}{U} + \mathcal{O}(\frac{t^4}{U^3})$ [373][14]. Since the (para)magnon bandwidth scales with J, the overestimation of DΓA compared to RIXS would suggest that either (i) the hopping amplitude t is overestimated, (ii) that U is too small, that contributions outside the single-band Hubbard model, most notably defects (iii) or multi-band physics (iv) are relevant, (v) DΓA does not capture the magnon dispersion of the single-band Hubbard model correctly. Since tight-binding parameters are typically more reliable than the interaction strength, scenario (ii) is more likely than (i) and we discuss results for $U = 9t$ in the subsection below. Subsequently, we briefly comment on (iv) and then delve into scenario (iii). Possibility (v) is not further discussed since (a) T_c was obtained using DΓA and (b) currently, no exact solutions of the Hubbard model at the parameters considered exist.

5.3.4 Connection to T_c and parameter dependencies

Results for $U = 9\,\mathrm{t}$ — Fig. 5.17 shows the magnetic susceptibility calculated the same way as in Fig. 5.14 and Fig. 5.15, but for an interaction value $U = 9\,\mathrm{t}$. The colormaps in (a,b,c) shows $\chi_{\mathrm{m}}^{q,\omega}$ along the same high-symmetry path as shown in the inset of Fig. 5.14(a). The red dots mark the maximum at each momentum, while the blue diamonds correspond to the peak maxima reported in Ref. [32]. Fig. 5.17(d) compares the peak location of the paramagnon dispersion for several interaction values.

The width of the dispersion is reduced, as expected from the spin-wave picture discussed in the previous subsection. Subsequently, the agreement with experimental measurements is improved compared to the results of $U = 8\,\mathrm{t}$ in Fig. 5.14 and Fig. 5.15. While this suggests that $U = 9\,\mathrm{t}$ is more appropriate, we might, however, instead overcompensate for the influence of the other factors outlined above.

[14] Let us note that this mapping is justified in the large interaction limit for $t' = t'' = 0$. For a detailed discussion on the influence of t' and t'' we refer the reader to Ref. [372].

Die approbierte gedruckte Originalversion dieser Dissertation ist an der TU Wien Bibliothek verfügbar.
The approved original version of this doctoral thesis is available in print at TU Wien Bibliothek.
TU Bibliothek Your knowledge hub WIEN

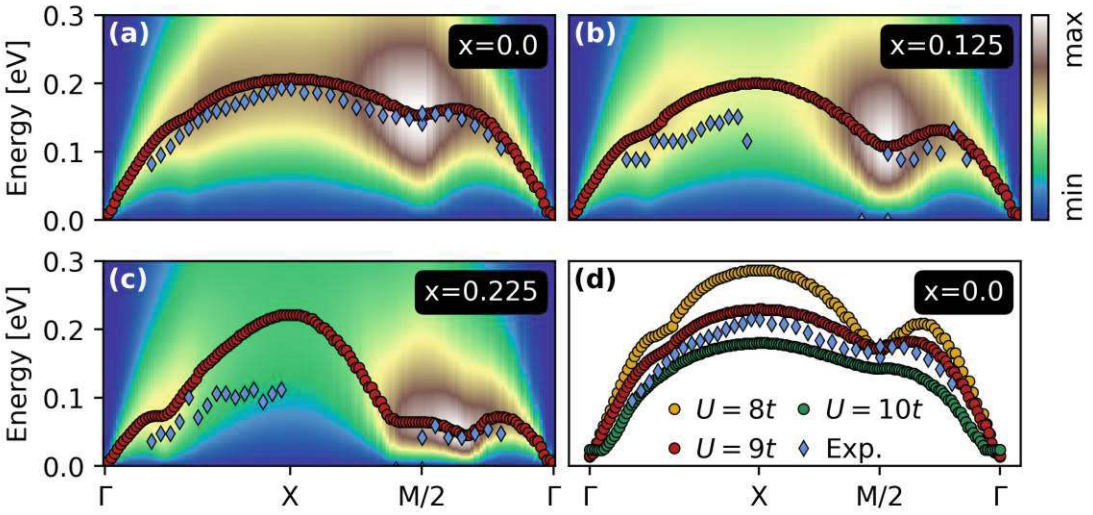

Figure 5.17: Paramagnon dispersion of $La_{1-x}Sr_xNiO_2$ using $U = 9t \simeq 3.5\,\text{eV}$. **(a)** parent compound $x \sim 0.0$ ($n = 0.95$) at $T \simeq 60K$. **(b)** $x \sim 0.125$ ($n = 0.875$). **(c)** $x \sim 0.225$ ($n = 0.8$). The red dots mark the maximum of the dispersion at each k-point, while the blue dots are the corresponding peak locations measured using RIXS and taken from Ref. [32]. **(d)** paramagnon dispersion of the parent compound for different values of the interaction U. Tight-binding parameters are $t = 0.389$, $t' = -0.25t$ and $t'' = 0.12t$.

Let us recall the superconducting transition temperature and discuss it in combination with the paramagnon dispersion. Fig. 5.18 shows the DΓA phase diagram for two interaction values $U = 8t$ (light red) and $U = 9t$ (dark red) together with two experimentally measured domes (blue curves). The theoretical values are taken from Ref. [50] and the experimental from Ref. [59] for the $(LaAlO_3)_{0.3}(Sr_2TaAlO_6)_{0.7}$ (LSAT) substrate and from Ref. [258] for those on $SrTiO_3$ (STO).

It is worth noting that measurements for the same nickelate $NdNiO_2$ on different substrates, one on STO [258] (light blue) and one on LSAT [59] (dark blue), show about a factor of two difference in the superconducting transitions temperatures. The higher transition temperature is measured for the LSAT substrate and the authors of [59] attribute the difference to cleaner films with fewer lattice defects. This conclusion is supported by STM measurements that show fewer stacking defaults and a significant reduction in resistivity of samples grown on LSAT in the same article. A dependence of T_c on the residual resistivity, which was taken as a proxy measure of disorder and lattice defects, was also reported in Ref. [294] and cleaner films show a larger T_c in a manner "not too different from cuprate superconductors". Indeed cuprates show a decrease in T_c for increasing in-plane [374], out-of-plane [375–377] resistivity and when magnetic or non-magnetic impurities are induced [378].

On the theoretical side, we observe a similar difference in transition temperature between calculations using $U = 8\,\text{t}$ and $U = 9\,\text{t}$, respectively. However, from a DFT-PBE perspective, the respective Wannier tight-binding parameters of $LaNiO_2$[15] with in-plane

[15] It is common practice to use La instead of Nd to avoid the (wrong) appearance of f-bands around the Fermi energy. For treating Nd directly the Nd f-shell electrons are usually considered as core

Die approbierte gedruckte Originalversion dieser Dissertation ist an der TU Wien Bibliothek verfügbar.
The approved original version of this doctoral thesis is available in print at TU Wien Bibliothek.
TU Bibliothek Your knowledge hub WIEN

lattice constants fixed to those of STO and LSAT are quite similar. We find that the nearest-neighbor hopping t increases by about $\sim 4\%$ from STO to LSAT, while the ratio of t'/t and t''/t remains essentially the same. An increase of t is not surprising as the smaller in-plane lattice constant of LSAT increases the orbital overlap and thus also t [50]. On the other hand, the Hubbard interaction ($U_{\mathrm{cRPA}} = 2.6\,\mathrm{eV}$) essentially does not change when performing constrained random phase approximation calculations for $LaNiO_2$ with the $a-b$ lattice parameters fixed to those corresponding to LSAT and STO, respectively [379].

Considering these changes of the effective single-band Hamiltonian, we expect samples grown on LSAT to have an intrinsically larger T_c, since t sets the energy scale and a smaller U/t is also beneficial [50]. That being said the expected difference in T_c, as a result of the slightly different intrinsic models, is closer to $10-15\%$[16], but almost certainly not a factor of two. For this reason, we conclude that changes in our effective single-band Hubbard model do not explain differences in the measured T_c.

As a consequence, the origin is presumed to be beyond the single-band Hubbard model, which brings us back to the points from the previous subsection: disorder (iv) and multi-orbital effects (iii). Since our DFT calculations show overall no major change in the band structure between the substrates, we attribute the difference in T_c to disorder and lattice defects. Following this argument, the appropriate Hubbard interaction for the effective single-band description of infinite-layer nickelates is close to $U = 8\,\mathrm{t}$ (possibly slightly enhanced) with an intrinsic $T_c^{\mathrm{max}} \simeq 30\,\mathrm{K}$, comparable to that measured on LSAT[17]. Consequently, we would expect the T_c of samples grown on STO to be similar once comparable sample qualities are realized in experiment. What remains to be understood is how defects and lattice disorder influence the magnon dispersion.

Disorder, defects and magnon dispersions — To fully address the influence of impurities and lattice defects on the paramagnon dispersion would require large-scale calculations for supercells that include them. Such calculations are, however, not feasible at the moment[18] and we will content ourselves with qualitative considerations instead.

One possibility is that defects, e.g. intercalated topotactic hydrogen [64, 295], induce local ferromagnetic couplings [368], which in turn would reduce the effective antiferromagnetic coupling strength J and presumably also T_c. While estimating the absolute influence of such local defects in RIXS is very difficult, if not impossible, samples that show a different T_c can be compared. Such a study would include measurements of several samples of the same "species", e.g. $Nd_{0.8}Sr_{0.2}NiO_2$ on STO, which show a sample-to-sample variation in T_c. Along the same lines, comparing paramagnon dispersions for samples grown on different substrates (e.g. STO and LSAT) would yield valuable information about the connection between the paramagnon dispersion and T_c. A study similar to the latter has already been performed for the related $PrNiO_2$ compound [380]. The measurements suggest that the paramagnon dispersion and J are

electrons.

[16] About $\sim 4\,\%$ because of a change in t and another $5-10\,\%$ because of the change in U/t.

[17] Effects beyond the single-band model will always lead to some discrepancy. For this reason, we refrain from fine-tuning parameters.

[18] At least not for DΓA calculations or similar many-body methods that include non-local fluctuations.

Die approbierte gedruckte Originalversion dieser Dissertation ist an der TU Wien Bibliothek verfügbar.
The approved original version of this doctoral thesis is available in print at TU Wien Bibliothek.
TU Bibliothek Your knowledge hub WIEN

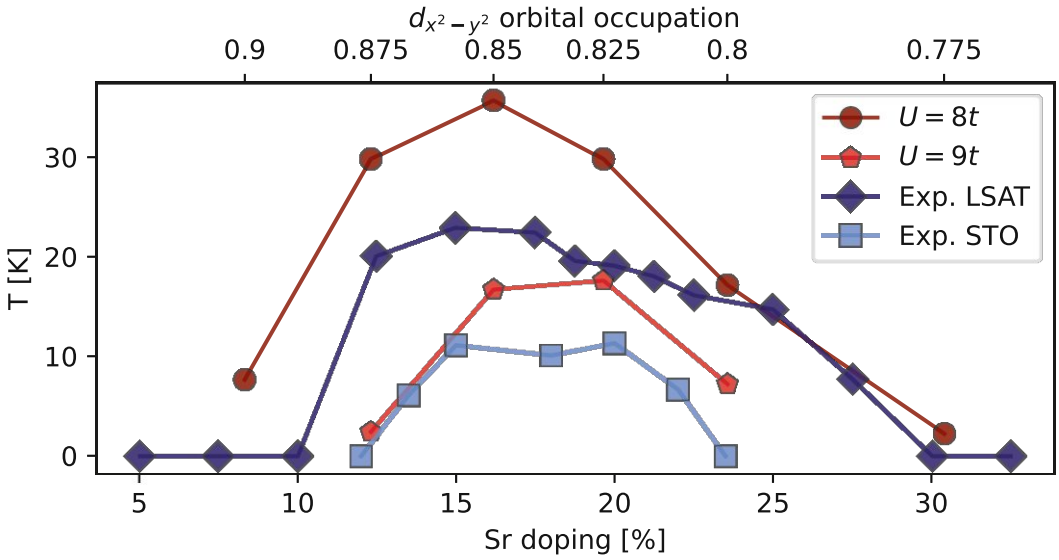

Figure 5.18: Superconducting phase diagram T_c as a function of Sr doping for $NdNiO_2/LaNiO_2$. Blue lines are calculated with the dynamical vertex approximation for $U = 8t$ (dark-red) and $U = 9t$ (light-red), taken from Ref. [50]. Red lines are the experimentally measured T_c (for 90% residual resistivity) for $NdNiO_2$ grown on LSAT (dark blue) and STO (light blue). The values were taken from Ref. [59] and [258], respectively.

similar for samples grown on LSAT and STO. However, those measurements were done on the non-superconducting parent compound. Hence, it would be interesting to check if the reported results remain unchanged if samples with different T_c's are measured directly.

Another way how lattice defects might influence T_c is by decreasing the magnetic correlation length ξ. Particularly if lattice stacking faults and similar defects introduce artificial "grain boundaries"[19] ξ might be suppressed without directly changing the effective antiferromagnetic coupling strength J. An enhancement of the effective mass would result in a similar effect[20]. Though conceptually somewhat different[21], the λ-correction in DΓA has a similar effect in the sense that λ decreases the magnetic correlation length. Such a reduced correlation length (added mass), however, essentially does not change the paramagnon dispersion (see Fig. 5.19 and discussion in the next subsection). Furthermore, the intensity primarily changes around the M momentum, where the susceptibility is the largest. As a result, such an effective paramagnon mass enhancement is difficult to extract from the available RIXS data, which cannot access the M point. Yet, it is precisely the strength of the susceptibility around that momentum, which, at least from a spin fluctuation or DΓA perspective, is most important for T_c. We thus propose to perform measurements of the magnetic correlation length ξ for superconducting samples grown on different substrates. A suppressed ξ for samples grown on STO compared to those grown on LSAT would support the scenario outlined here.

[19] See for examples Fig. 1 in Ref. [59].
[20] This is because effective mass enhancement and suppression of the correlation length are related [89].
[21] The λ-correction was introduced to enforce exact sum-rules (see Section 3.8) and not to treat disorder.

Die approbierte gedruckte Originalversion dieser Dissertation ist an der TU Wien Bibliothek verfügbar.
The approved original version of this doctoral thesis is available in print at TU Wien Bibliothek.
TU Bibliothek Your knowledge hub WIEN

DMFT and DΓA —— To investigate the influence of suppressing the correlation length on the paramagnon dispersion, we compare χ_m between DMFT and DΓA in Fig. 5.19 on a high-symmetry path in the BZ including the M momentum (see inset in panel (d)). We choose the overdoped compound ($x = 0.225$) since DMFT shows no antiferromagnetic order for this doping. Hence, we can directly compare χ_m between DMFT (no λ correction) and DΓA (with λ correction). The former is shown in panel (c), while we display the latter in panel (a).

We draw the location of the peak in χ_m at each momentum in Fig. 5.19(b). It remains essentially unchanged in the presence of a λ correction, i.e. ξ suppression. The magnitude of the susceptibility at the peak is, however, drastically different around the M momentum, as displayed in Fig. 5.19(d). This suppression is strongest when the susceptibility is large, which is no surprise since $\chi^\lambda = \frac{1}{1/\chi_m+\lambda}$. Hence a reduction of the correlation length for antiferromagnetic fluctuations is expected to be virtually invisible in RIXS measurements, which do not access the M point. At the same time, a reduction of T_c is expected.

Let us further note that we observe incommensurate antiferromagnetic fluctuations (evidenced by the shift of the maximum slightly away from M), which is typical for overdoped cuprates [104, 105][22]. For nickelates, measurements that could distinguish commensurate from incommensurate spin fluctuations have, to the best of our knowledge, not been performed at the time of writing this thesis.

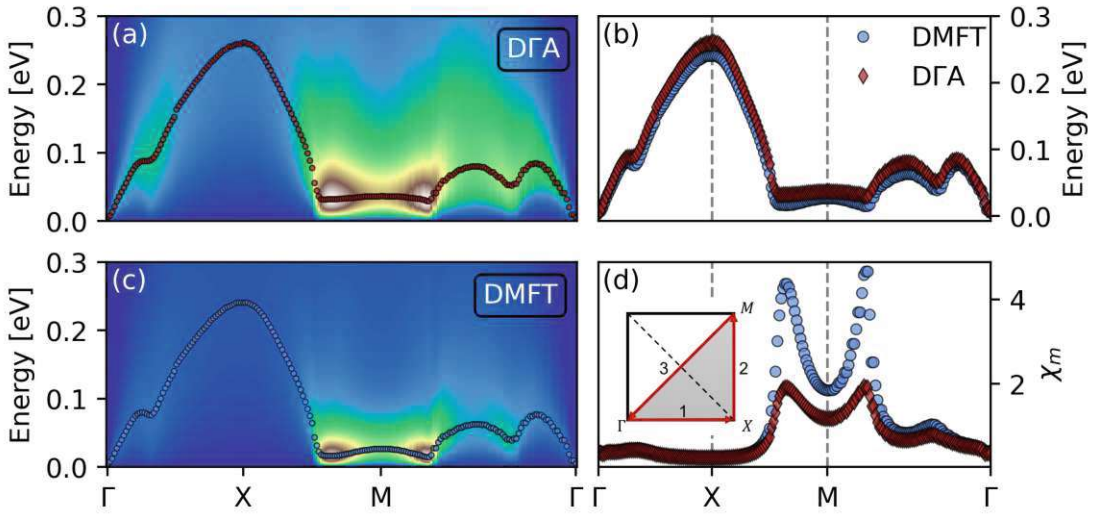

Figure 5.19: Paramagnon dispersion of $La_{1-x}Sr_xNiO_2$ for $x \sim 0.225$ at a temperature of 60 K within the effective single-orbital Hubbard model description. **(a)** colormap of $\chi_\mathrm{m}^{q,\omega}$ as in DΓA. **(c)** colormap of $\chi_\mathrm{m}^{q,\omega}$ as in DMFT. **(b)** maximum of the dispersion corresponds to the lines on top of the colormaps. **(d)** value of the magnetic susceptibility at the peak maximum. The inset in (d) shows the k-path in the BZ, where $\Gamma = (0,0,0)$, $\mathrm{X} = (\pi,0,0)$ and $\mathrm{M} = (\pi,\pi,0)$. Corresponding tight-binding parameters are $t = 0.389$, $t' = -0.25t$ and $t'' = 0.12t$. Hubbard interaction $U = 3.11$ eV ($8t$).

[22] Let us note that the prototypical cuprate L_2CuO_4 is a 214 layered system compared to the 112 layer structure of nickelates.

Die approbierte gedruckte Originalversion dieser Dissertation ist an der TU Wien Bibliothek verfügbar.
The approved original version of this doctoral thesis is available in print at TU Wien Bibliothek.
TU Bibliothek Your knowledge hub WIEN

5.4 Hydrogen defects

The previous chapters focused on how to construct a minimal low-energy effective Hamiltonian and the approximate solution of it. In order to treat the material with methods like DFT+DMFT and subsequently DΓA we can neither treat lattice defects nor non-stoichiometry. However, in experiments, deviations from the perfect crystal are a real concern; indeed, the growth of superconducting samples has proven to be extremely challenging. Not only did it take roughly twenty years from the first theoretical predictions [296] till Li et al. [17] reported the first results, but it also took roughly a year until those results were reproduced by other groups [323].

To understand this inherent difficulty in manufacturing samples that are indeed superconducting, let us quickly outline how the synthesis works [17]. In the first step, a doped sample in the perovskite phase $Sr_xNd_{1-x}NiO_3$ is grown on a $SrTiO_3$ substrate. Oxygen reduction to the infinite-layer phase $Sr_xNd_{1-x}NiO_2$ is performed by using calcium hydrate CaH_2 as a reagent [17].

Si *et al.* [64] noticed that contrary to cuprates, hydrogen intercalation and thus the creation of $Nd(La)NiO_2H$ is energetically favorable. The intercalated hydrogen will destroy the quasi-2D nature of the electronic structure and change the valence of Ni from a $3d^9$ to a $3d^8$ configuration. Compared with known compounds of the nickelate and cuprate family, both effects seem to be unfavorable for superconductivity[23].

However, hydrogen is rather hard to detect with common experimental techniques and hence assessing the quality of samples is difficult. Below we discuss this intercalation process in more detail and identify a hydrogen phonon mode, which is well separated, to be a possible candidate to experimentally detect intercalated hydrogen defects.

The following section, marked by a vertical bar, has already been published in Crystals 12(5), 656 (2022) [382].

5.4.1 Introduction

Computational materials calculations predicted superconductivity in nickelates [296] and heterostructures thereof [297–299] since decades, mainly based on apparent similarly to cuprate superconductors. Three years ago, superconductivity in nickelates was finally discovered in experiment by Li, Hwang and coworkers [17], breaking the grounds for a new age of superconductivity, the nickel age. It is marked by an enormous theoretical and experimental activity, including but not restricted to [17, 18, 21, 50, 51, 64, 187, 237, 293, 305–316, 323, 334, 345, 361, 383, 384]. Superconductivity has been found by now, among others, in $Nd_{1-x}Sr_xNiO_2$ [17, 323], $Pr_{1-x}Sr_xNiO_2$ [293], $La_{1-x}Ca_xNiO_2$ [334], $La_{1-x}Sr_xNiO_2$ [18], and most recently in the pentalayer nickelate $Nd_6Ni_5O_{12}$ [345]. Fig. 5.20 shows some of the hallmark experimental critical temperatures (T_c's) for the nickelates in comparison with the preceding copper [11] and iron age [385] of uncon-

[23] As an example La_2NiO_4, which hosts a formal Ni $3d^8$ configuration, is insulating and does not display superconductivity, see e.g. [381].

Die approbierte gedruckte Originalversion dieser Dissertation ist an der TU Wien Bibliothek verfügbar.
The approved original version of this doctoral thesis is available in print at TU Wien Bibliothek.
TU Bibliothek Your knowledge hub WIEN

ventional superconductivity. Also shown are some other noteworthy superconductors, including the first superconductor, solid Hg, technologically relevant NbTi, and hydride superconductors [145]. The last are superconducting close to room temperature, albeit only at a pressure of 267GPa exerted in a diamond anvil cell. All of these compounds are marked in gray in Fig. 5.20 as they are conventional superconductors. That is, the pairing of electrons originates from the electron-phonon coupling, as described in the theory of Bardeen, Cooper, and Schrieffer (BCS) [2].

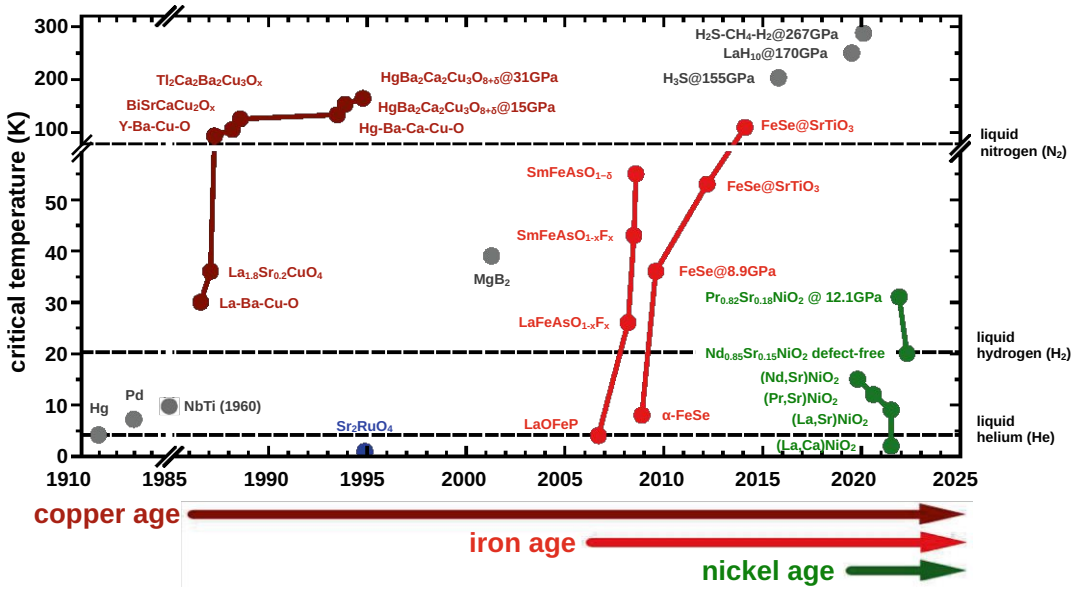

Figure 5.20: Superconducting T_c vs. year of discovery for selected superconductors. The discovery of cuprates, iron pnictides and nickelates led to enormous experimental and theoretical activities. Hence one also speaks of the copper, iron and nickel age of superconductivity.

In contrast, cuprates, nickelates, and, to a lesser extent, iron pnictides are strongly correlated electron systems with a large Coulomb interaction between electrons because of their narrow transition metal orbitals. Their T_c is too high for BCS theory [9, 386], and the origin of superconductivity in these strongly correlated systems is still hotly debated. One prospective mechanism are antiferromagnetic spin fluctuations [12, 162–165] stemming from strong electronic correlations. Another mechanism is based on charge density wave fluctuations and received renewed interest with the discovery of charge density wave ordering in cuprates [171, 172]. Dynamical vertex approximation [38, 95, 123, 387] calculations for nickelates [50], that are unbiased with respect to charge and spin fluctuations, found that spin fluctuations dominate and successfully predicted the superconducting dome prior to experiment in $Nd_{1-x}Sr_xNiO_2$ [59, 258, 323].

Why did it take 20 years to synthesize superconducting nickelates that have been so seemingly predicted on a computer? To mimic the cuprate Cu $3d^9$ configuration, as in $NdNiO_2$, nickel has to be in the uncommon oxidation state Ni^{1+} which is rare and prone to oxidize further. Only through a complex two step procedure, Lee, Hwang and coworkers [22] were able to synthesize superconducting nickelates. In a first step,

Die approbierte gedruckte Originalversion dieser Dissertation ist an der TU Wien Bibliothek verfügbar.
The approved original version of this doctoral thesis is available in print at TU Wien Bibliothek.
TU Bibliothek Your knowledge hub WIEN

modern pulsed laser deposition (PLD) was used to grow a $Sr_xNd_{1-x}NiO_3$ film on a $SrTiO_2$ substrate. This nickelate is still in the 3D perovskite phase, see Fig. 5.21 (left), with one oxygen atom too much and will thus not show superconductivity. Hence, this additional oxygen between the layers needs to be removed in a second step. The reducing agent CaH_2 is used to this end, within a quite narrow temperature window [22]. If all goes well, one arrives at the superconducting $Sr_xNd_{1-x}NiO_2$ film (top center). However, this process is prone to incomplete oxidation or to intercalate hydrogen topotactically, i.e., at the position of the removed oxygen, see Fig. 5.21 (bottom center). Both of those unwanted outcomes are detrimental for superconductivity.

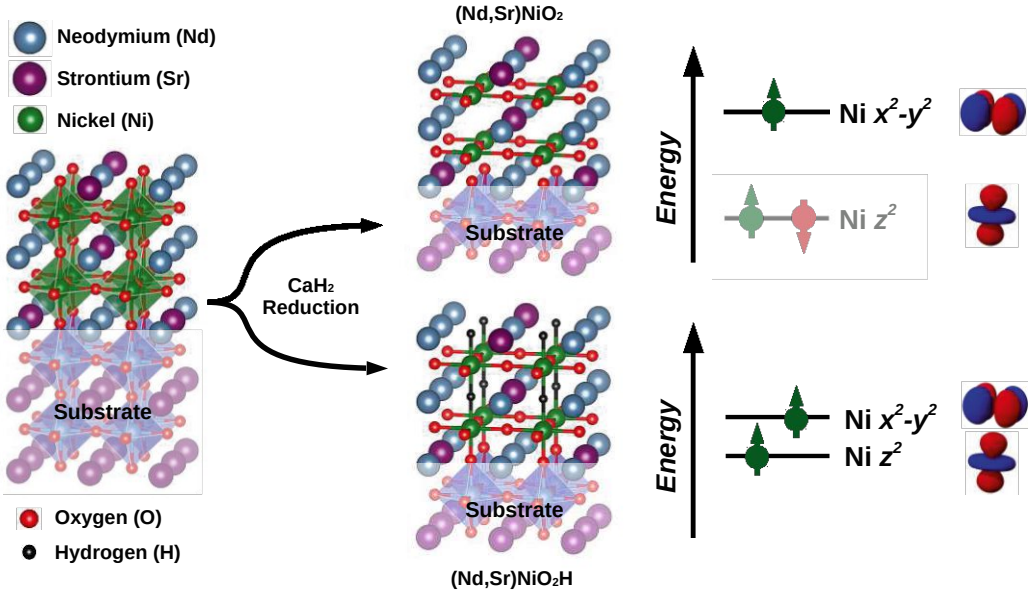

Figure 5.21: For synthesizing superconducting nickelates (1, left) a perovskite film of $Nd(La)_{1-x}Sr_xNiO_3$ is grown on a $SrTiO_3$ substrate and (2, center) the O atoms between the planes are removed by reduction with CaH_2. Besides the pursued nickelate $Nd(La)_{1-x}Sr_xNiO_2$ (top center) also excess oxygen or topotactic H may remain in the film, yielding $Nd(La)_{1-x}Sr_xNiO_2H$ (bottom center). The excess hydrogen results in two holes instead of one hole within the topmost two Ni $3d$ orbitals (right). Adapted from [20].

In [64, 344, 388] it was shown by density-functional theory (DFT) calculations that $NdNiO_2H$ is indeed energetically favorable to $NdNiO_2$ + 1/2 H. For the doped system, on the other hand, $Nd_{0.8}Sr_{0.2}NiO_2$ without the hydrogen intercalated is energetically favorable. The additional H or likewise an incomplete oxidation to $SrNdNiO_{2.5}$ alters the physics completely. Additional H or $O_{0.5}$ will remove an electron from the Ni atoms, resulting in Ni^{2+} instead of Ni^{1+}. The formal electronic configuration is hence $3d^8$ instead of $3d^9$, or two holes instead of one hole in the Ni d-shell. Dynamical mean-field theory (DMFT) calculations [64] evidence that the basic atomic configuration is the one of Fig. 5.21 (lower right). That is, because of Hund's exchange the two holes in $NdNiO_2H$ occupy two different orbitals, $3d_{x^2y^2}$ and $3d_{3z^2-r^2}$, and form a spin-1. A

Die approbierte gedruckte Originalversion dieser Dissertation ist an der TU Wien Bibliothek verfügbar.
The approved original version of this doctoral thesis is available in print at TU Wien Bibliothek.
TU Bibliothek Your knowledge hub WIEN

consequence of this is that DMFT calculations predict $NdNiO_2H$ to be a Mott insulator, whereas $NdNiO_2$ is a strongly correlated metal with a large mass enhancement of about five [64].

To the best of our knowledge, such a two-orbital, more 3D electronic structure is unfavorable for high-T_c superconductivity. The two-dimensionality of cuprate and nickelate superconductors helps to suppress long-range antiferromagnetic order, while at the same time retaining strong antiferromagnetic fluctuations that can act as a pairing glue for superconductivity. In experiment, we cannot expect ideal $NdNiO_2$, $NdNiO_2H$ or $NdNiO_{2.5}$ films, but most likely some H or additional O will remain in the $NdNiO_2$ film, after the CaH_2 reduction. Additional oxygen can be directly evidenced in standard x-ray diffraction analysis after the synthesis step. However, hydrogen, being very light, evades such an x-ray analysis. It has been evidenced in nickelates only by nuclear magnetic resonance (NMR) experiments [339] which, contrary to x-ray techniques, are very sensitive to hydrogen. Ref. [389] suggested hydrogen in $LaNiO_2$ to be confined at grain boundaries or secondary-phase precipitates. Given these difficulties, it is maybe not astonishing that it took almost one year before a second research group [323] was able to reproduce superconductivity in nickelates. Despite enormous experimental efforts, only a few groups succeeded hitherto.

In this paper, we present additional DFT results for topotactic hydrogen and incomplete oxygen reduction in nickelate superconductors: In Section 5.4.3 we provide technical information on the DFT calculations. In Section 5.4.3 we analyze the energy gain to topotactically intercalate hydrogen in $LaNiO_2$ and $NdNiO_2$. In Section 5.4.4, we analyze the phonon spectrum and identify a high-energy mode originating from the Ni-H-Ni bond as a characteristic feature of intercalated hydrogen. In Section 5.4.5 we show the changes of the charge distribution caused by topotactic hydrogen. Finally, Section 5.4.6 provides a summary and outlook.

5.4.2 Method

Computational details on E_b. In both our previous theoretical study [64] and this article, the binding energy E_b of hydrogen atoms is computed as:

$$E_b = E[ABO_2] + \mu[H] - E[ABO_2H]. \tag{5.6}$$

Here, $E[ABO_2]$ and $E[ABO_2H]$ are the total energy of infinite-layer ABO_2 and hydride-oxides ABO_2H, while $\mu[H] = E[H_2]/2$ is the chemical potential of H. Note that H_2 is a typical byproduct for the reduction with CaH_2 and also emerges when CaH_2 is in contact with H_2O. Hence it can be expected to be present in the reaction. A positive (negative) E_b indicates the topotactic H process is energetically favorable (unfavorable) to obtain ABO_2H instead of ABO_2 and $H_2/2$.

In the present paper, we go beyond [64] that reported E_b of various ABO_2 compounds by investigating E_b of $La_{1-x}Ca_xNiO_2$ systems for many different doping levels. Here,

Die approbierte gedruckte Originalversion dieser Dissertation ist an der TU Wien Bibliothek verfügbar.
The approved original version of this doctoral thesis is available in print at TU Wien Bibliothek.

the increasing Ca-doping is achieved by using the virtual crystal approximation (VCA) [390, 391] from $LaNiO_2$ (x=0) to $CaNiO_2$ (x=1). For each Ca concentration, structure relaxation and static total energy calculation is carried out for $La_{1-x}Ca_xNiO_2$ and $La_{1-x}Ca_xNiO_2H$ within the tetragonal space group $P4/mmm$. To this end, we use density-functional theory (DFT) [35, 46] with the VASP code [348, 392] and the generalized gradient approximations (GGA) of Perdew, Burke, and Ernzerhof (PBE) [49] and PBE revised for solids (PBEsol) [264]. For undoped $LaNiO_2$, the GGA-PBEsol relaxations predict its in-plane lattice constant as 3.890 Å whichis close to that of the STO substrate: 3.905 Å. The computations for $La_{1-x}Ca_xNiO_2$ and $LaCoO_2$, $LaCuO_2$, $SrCoO_2$ and $SrNiO_2$ are performed without spin-polarization and a DFT+U treatment [274], as the inclusion of Coulomb U and spin-polarization only slightly decreases the E_b by ∼5% for $LaNiO_2$ [20] . For $NdNiO_2$, an inevitably computational issue are the localized Nd-4f orbitals. These f-orbitals are localized around the atomic core, leading to strong correlations. In non-spin-polarized DFT calculations this generates flat bands near the Fermi level E_F and leads to unsuccessful convergence. To avoid this, we employed DFT+U [U_f(Nd)=7 eV and U_d(Ni)=4.4 eV] and initialize a G-type antiferromagnetic ordering for both Nd- and Ni-sublattice in a $\sqrt{2} \times \sqrt{2} \times 2$ supercell of $NdNiO_2$. For the $Nd_{0.75}Sr_{0.25}NiO_2$ case, 25% Sr-doping is achieved by replacing one out of the four Nd atoms by Sr in a $\sqrt{2} \times \sqrt{2} \times 2$ $NdNiO_2$ supercell.

Computational details on phonons. The phonon computations for $LaNiO_2$, $LaNiO_2H$, $LaNiO_2H_{0.125}$, $LaNiO_{2.125}$ are performed with the frozen phonon method using the PHONONY [393] code interfaced with VASP. Computations with density-functional perturbation theory (DFPT) method [394] are also carried out for double check. For $LaNiO_2$ and $LaNiO_2H$, the unit cells shown in Fig. 5.23(a,b) are enlarged to a 2×2×2 supercell, while for $LaNiO_2H_{0.125}$ and $LaNiO_{2.125}$ the phonon are directly computed with the supercell of Fig. 5.23(c,d).

Computational details on electron density. The electron density distributions of $LaNiO_2$, $LaNiO_2H$, $LaNiO_2H_{0.125}$, and $LaNiO_{2.125}$ are computed using the WIEN2K code [55] while taking the VASP-relaxed crystal structure as input. The isosurfaces are plotted from 0.1 (yellow lines) to 2.0 (center of atoms) with spacing 0.1 in units of e/Å^2.

Die approbierte gedruckte Originalversion dieser Dissertation ist an der TU Wien Bibliothek verfügbar.
The approved original version of this doctoral thesis is available in print at TU Wien Bibliothek.
TU Bibliothek Your knowledge hub WIEN

5.4.3 Energetic stability

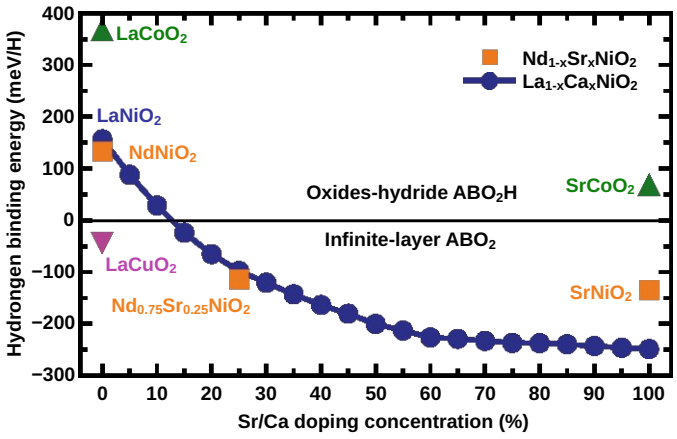

Figure 5.22: Hydrogen binding energy (E_b) per hydrogen in two nickelate superconductors, $La_{1-x}Ca_xNiO_2$ and $Nd_{1-x}Sr_xNiO_2$ vs. Sr/Ca doping concentration x; $LaCuO_2$, $LaCoO_2$, and $SrCoO_2$ are shown for comparison. Slightly above 10% (Sr,Ca)-doping infinite-layer nickelates are energetically more stable. Note that the doping changes the filling of the B-3d orbital. To study the relationship between E_b and the types of B-site elements, E_b of several other ABO_2 compounds is computed: $LaCoO_2$, $LaCuO_2$, $SrCoO_2$ and $SrNiO_2$. Note that this changes the filling of B-3d orbital within a large range: e.g. $3d^8$ for $LaCoO_2$ and $3d^9$ for $LaNiO_2$.

Fig. 5.22 shows the results of the hydrogen binding energy E_b for the infinite-layer nickelate superconductors $Nd_{1-x}Sr_xNiO_2$ [17, 258, 323] and $La_{1-x}Ca_xNiO_2$ [334]. To reveal the evolution of E_b when the B-site band filling deviates from their original configurations ($3d^9$ in $LaNiO_2$ when x=0 and $3d^8$ in $CaNiO_2$ when x=1), we also show the binding energy of $LaCoO_2$ ($3d^8$), $LaCuO_2$ ($3d^{10}$), $SrCoO_2$ ($3d^7$) and $SrNiO_2$ ($3d^8$).

Let us start with the case of $La_{1-x}Ca_xNiO_2$ [334]. Here, the unoccupied La-4f orbitals make the computation possible even without spin-polarization and Coulomb U for La-4f, whereas for $NdNiO_2$ this is not practicable due to Nd-4f flat bands near E_F. Positive (negative) E_b above (below) the horizontal line in Fig. 5.22 indicates topotactic H is energetically favorable (unfavorable). When x=0, i.e. for bulk $LaNiO_2$, the system tends to confine H atoms, resulting in oxide-hydride ABO_2H with $E_b = 157$ meV/H. As the concentration of Ca increases, E_b monotonously decreases, reaching -248 meV for the end member of the doping series, $CaNiO_2$. The turning point between favorable and unfavorable topotactic H inclusion is around 10% to 15% Ca-doping. Let us note that $E_b = 0$ roughly agrees with the onset of superconductivity, which for Ca-doped $LaNiO_2$ emerges for x>15% Ca-doping [334].

To obtain E_b in $NdNiO_2$ a much higher computational effort is required: firstly, the Nd-4f orbitals must be computed with either treating them as core-states or including spin-splitting. Secondly, for the spin-polarized DFT(+U) calculations, an appropriate (anti-)ferromagnetic ordering has to be arranged for both Ni- and Nd-sublattices. In oxide-hydride ABO_2H compounds, the δ-type bond between Ni and H stabilizes a G-type anti-ferromagnetic order by driving the system from a quasi two-dimensional (2D) system to a three dimensional (3D) one [64]. Given the large computational costs of E_b for $Nd_{1-x}Sr_xNiO_2$ by using anti-ferromagnetic DFT+U calculations for both Nd-4f (U ~7 eV) and Ni-3d (U=4.4 eV) orbitals, we merely show here the results of $NdNiO_2$

Die approbierte gedruckte Originalversion dieser Dissertation ist an der TU Wien Bibliothek verfügbar.
The approved original version of this doctoral thesis is available in print at TU Wien Bibliothek.
TU Bibliothek Your knowledge hub WIEN

(x=0), $Nd_{0.75}Sr_{0.25}NiO_2$ (x=0.25) and $SrNiO_2$ (x=1), which are adopted from [64]. With 25% Sr-doping, the E_b of $NdNiO_2$ is reduced from 134 meV to -113 meV. Please note that E_b of (Nd,Sr)NiO_2 is slightly smaller than in (La,Ca)NiO_2, at least in the low doping range. This can be explained by shorter lattice constants in $NdNiO_2$, in agreement with the finding [64] that compressive strain plays an important role at reducing E_b.

One can speculate that this suppression of topotactic hydrogen may also play a role when comparing the recently synthesized (Nd,Sr)NiO_2 films on a $(LaAlO_3)_{0.3}(Sr_2TaAlO_6)_{0.7}$ (LSAT) substrate [59] with the previously employed $SrTiO_3$ (STO) substrate [258]. Lee *et al.* [59] reported cleaner films without defects and also a higher superconducting transition temperature $T_c \sim 20$ K for the LSAT film, as compared to $T_c = 15$ K and plenty of stacking fault defects for the STO substrate [258]. As for (La,Ca)NiO_2, $E_b = 0$ falls in the region of the onset of the superconductivity for (Sr,Nd)NiO_2, which is $x \sim$10% Sr-doping in LSAT-strained defect-free films [59] and $x \sim$12.5% at $SrTiO_3$-substrate states [258]. Topotactic hydrogen might play a role in suppressing superconductivity in this doping region.

In Fig. 5.22, we further show additional infinite-layer compounds $LaCoO_2$, $LaCuO_2$, $SrCoO_2$ and $SrNiO_2$ for comparison. Their E_b is predicted to be 367, -42, 69 and -134 meV, respectively. Combining the results of $LaNiO_2$ and $CaNiO_2$, we summarize several tendencies on how to predict E_b of ABO_2: (1) the strongest effect on E_b is changing the B-site element. However this seems unpractical for nickelate superconductors as the band filling is strictly restricted to be $3d^{9-x}$ ($x \sim 0.2$). For both trivalent (La, Nd) and bivalent (Sr, Ca) cations, E_b decreases when the B-site cation goes from early to late transition metal elements, e.g. from $LaCoO_2$ ($3d^8$) to $LaNiO_2$ ($3d^9$) to $LaCuO_2$ ($3d^{10}$). (2) Compressive strains induced by either substrate or external pressure can effectively reduce E_b and we believe that this might be used for growing defect-free films. (3) According to our theoretical calculations, E_b mainly depends on lattice parameters and band filling of the B-site 3d-orbitals, but much less on magnetic ordering and Coulomb interaction U.

Die approbierte gedruckte Originalversion dieser Dissertation ist an der TU Wien Bibliothek verfügbar.
The approved original version of this doctoral thesis is available in print at TU Wien Bibliothek.
TU Bibliothek Your knowledge hub WIEN

5.4.4 Phonon dispersion

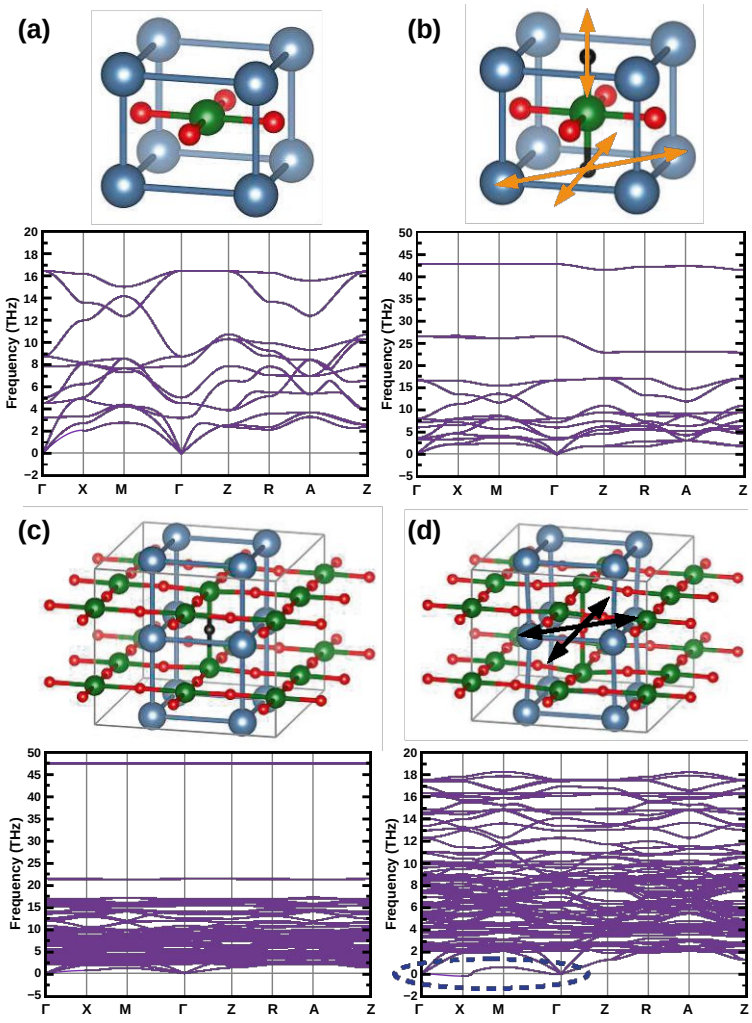

Figure 5.23: Phonon spectra of (a) $LaNiO_2$, (b) $LaNiO_2H$ and in a 2×2×2 $LaNiO_2$ supercell doped with a single (c) H and (d) O atom [i.e. $LaNiO_2H_{0.125}$ in (c) and $LaNiO_{2.125}$ in (d)]. The orange and black arrows in (b) and (d) represent vibrations of H and O atoms. The blue dashed oval in (d) labels the unstable phonon modes induced by intercalating additional O atoms in $LaNiO_2$.

As revealed by previous DFT phonon spectra calculations [311], $NdNiO_2$ is dynamically stable. One of the very fundamental question would be whether topotactic H from over-reacted reduction and/or O from unaccomplished reductive reactions affect the lattice stability. To investigate this point, we perform DFT phonon calculations and analyze the lattice vibration induced by H/O intercalation, as shown in Fig. 5.23.

The phonon spectrum of $LaNiO_2$ [5.23(a)] is essentially the same as in Ref. [311], all the phonon frequencies are positive, indicating it is dynamically stable. In Fig. 5.23(b), the oxides-hydride $LaNiO_2H$ is also predicted to be dynamically stable. Please note

Die approbierte gedruckte Originalversion dieser Dissertation ist an der TU Wien Bibliothek verfügbar.
The approved original version of this doctoral thesis is available in print at TU Wien Bibliothek.

that the phonon dispersions between 0 and 20 THz are basically the same as those in $LaNiO_2$ [Fig. 5.23(a); note the different scale of the y-axis]. However, one can see new, additional vibration modes from the light H-atoms at frequencies of ∼27 THz and ∼43 THz. Among these vibrations, the double degenerate mode at lower frequency is generated by an in-plane (xy-plane) vibration of the topotactic H atom. There are two such in-plane vibrations of H atoms, either along the (100) or (110) direction (and symmetrically related directions), as indicated by the orange arrows in Fig. 5.23(b). The mode located at the higher frequency ∼43 THz is, on the other hand, formed by an out-of-plane (z-direction) vibration and is singly degenerate.

We explain these phonon modes in detail by computing the bonding strength between H-1s–Ni-d_{z^2} and H-1s–La-d_{xy} orbitals. Our tight-binding calculations yields an electron hopping term of -1.604 eV between H-1s and Ni-d_{z^2} while it is -1.052 eV from La-d_{xy} to H-1s. That is, the larger H-1s–Ni-d_{z^2} overlap leads to a stronger δ-type bonding and, together with the shorter c-lattice constant, to a higher phonon energy. Additionally, the shorter c-lattice in $LaNiO_2$ should also play a role at forming a stronger H-1s–Ni-d_{z^2} bond.

In our previous analysis of the band character for $LaNiO_2H$ [64], the H-1s bands were mainly located at two energy regions: a very flat band that is mostly from the H-1s itself at ∼-7 to -6 eV, and a hybridized band between H-1s and Ni-d_{z^2} at ∼-2 eV. Together with the higher phonon energy this indicates that the topotactic H atoms are mainly confined by a Ni sub-lattice via bonding and anti-bonding states formed by H-1s and Ni-d_{z^2} orbitals, instead of the La(Nd) sub-lattice.

The complete (full) topotactic inclusion of H, where all vacancies induced by removing oxygen are filled by H, is an ideal limiting case. Under varying experimental conditions, such as chemical reagent, substrate, temperature, and strain, the H-topotactic inclusion may be incomplete, and thus ABO_2H_δ (δ<1) be energetically favored. Hence, we also compute the phonon spectrum at a rather low H-topotactic density: $LaNiO_2H_{0.125}$, achieved by including a single H into 2×2×2 $LaNiO_2$ supercells as shown in Fig. 5.23(c). Also such a local H defect, as revealed by the positive frequency at all q-vectors in the lower panel of Fig. 5.23(c), does not destroy the dynamical stability of the $LaNiO_2$ crystal. In fact, the only remarkable qualitative difference between the complete and 12.5% topotactic H case is the number of phonon bands at 0 THz to 20 THz. This is just a consequence of the larger 2×2×2 $LaNiO_2$ supercell, with eight times more phonons. Some quantitative differences can be observed with respect to the energy of the phonon mode: The out-of-plane vibration energy is enhanced from ∼43 THz in $LaNiO_2H$ [Fig. 5.23(b)] to ∼47 THz in $LaNiO_2H_{0.125}$ [Fig. 5.23(b)], and the in-plane vibration mode frequency is reduced from ∼27 THz in $LaNiO_2H$ [Fig. 5.23(b)] to ∼21 THz $LaNiO_2H_{0.125}$ [Fig. 5.23(c)]. This is because the H-intercalation shrinks the local c-lattice, i.e., the distance between two Ni atoms separated by topotactic H, from 3.383 Å in [$LaNiO_2H$: Fig. 5.23(b)] to 3.327 Å [$LaNiO_2H_{0.125}$: Fig. 5.23(c)]. The bond length between H and La is, on the other hand, slightly increased from 2.767 Å in [$LaNiO_2H$: Fig. 5.23(b)] to 2.277 Å [$LaNiO_2H_{0.125}$: Fig. 5.23(c)]. This lattice compression (enlargement) explains the enhancement (reduction) for the out-of-plane (in-plane) phonon frequencies (energies).

Die approbierte gedruckte Originalversion dieser Dissertation ist an der TU Wien Bibliothek verfügbar.
The approved original version of this doctoral thesis is available in print at TU Wien Bibliothek.
TU Bibliothek Your knowledge hub WIEN

These results pave a new way to detect the formation of topotactic H in infinite nickelate superconductors: by measuring the phonon modes. The existence of localized phonon modes with little dispersion at ∼25 THz and ∼45 THz indicates the presence of topotactic hydrogen, which otherwise would be extremely hard to detect. These frequencies correspond to energies of 103 meV and 186 meV, respectively, beyond the range <80 meV measured for $La_{1-x}Sr_xNiO_2$ in [395].

Lastly, we further study the case representing an incompleted reduction process: $LaNiO_{2.125}$, achieved by intercalating a single O into a 2×2×2 $LaNiO_2$ supercell [$LaNiO_{2.125}$: Fig. 5.23(d)]. As the same consequence of employing a supercell in phonon computation, the number of phonon bands is multiplied by a factor of 8 in the frequency region between 0 THz to 20 THz. One obvious difference between undoped $LaNiO_2$ [Fig. 5.23(a)] and $LaNiO_{2.125}$ [Fig. 5.23(d)] is, that the additional O leads to an unstable phonon mode near q=X(π,0,0) [blue region in Fig. 5.23(d)]. This phonon mode is formed by an effective vibration of the additional O along the xy plane in the (001) or (110) direction (and symmetrically related directions depending on the exact q-vector) of locally cubic coordinate. Such a mode is related to the structural transition from cubic Pm-3m to a R-3c rhombohedral phase as in bulk $LaNiO_3$, with the Ni-O-Ni bond along the z-direction deviating from 180°. Our simulations for other concentrations of additional O atoms (not shown) also indicate that incomplete oxygen reduction reactions generally result in local instabilities of $LaNiO_{2+\delta}$ with δ>0.

5.4.5 Charge distribution

In this Section, we perform electron density calculations for $LaNiO_2$, $LaNiO_2H$, $LaNiO_2H_{0.125}$ and $LaNiO_{2.125}$ compounds to investigate the bond types resulting from intercalated H and O atoms. Fig. 5.24 (a) and (b) show the electron density of $LaNiO_2$ at the NiO-plane and La-plane (light green planes of the top panels). In Fig. 5.24(a), a strong Ni-O bond is observed while the low electron density between each Ni-O layers reveals a very weak inter-layer coupling, indicating the strong quasi-2D nature of the infinite-layer nickelates. In Fig. 5.24(b), no bonds are formed between the La (Nd) atoms. The A-site rare-earth elements merely play the role of electron donors.

Die approbierte gedruckte Originalversion dieser Dissertation ist an der TU Wien Bibliothek verfügbar.
The approved original version of this doctoral thesis is available in print at TU Wien Bibliothek.
TU Bibliothek Your knowledge hub WIEN

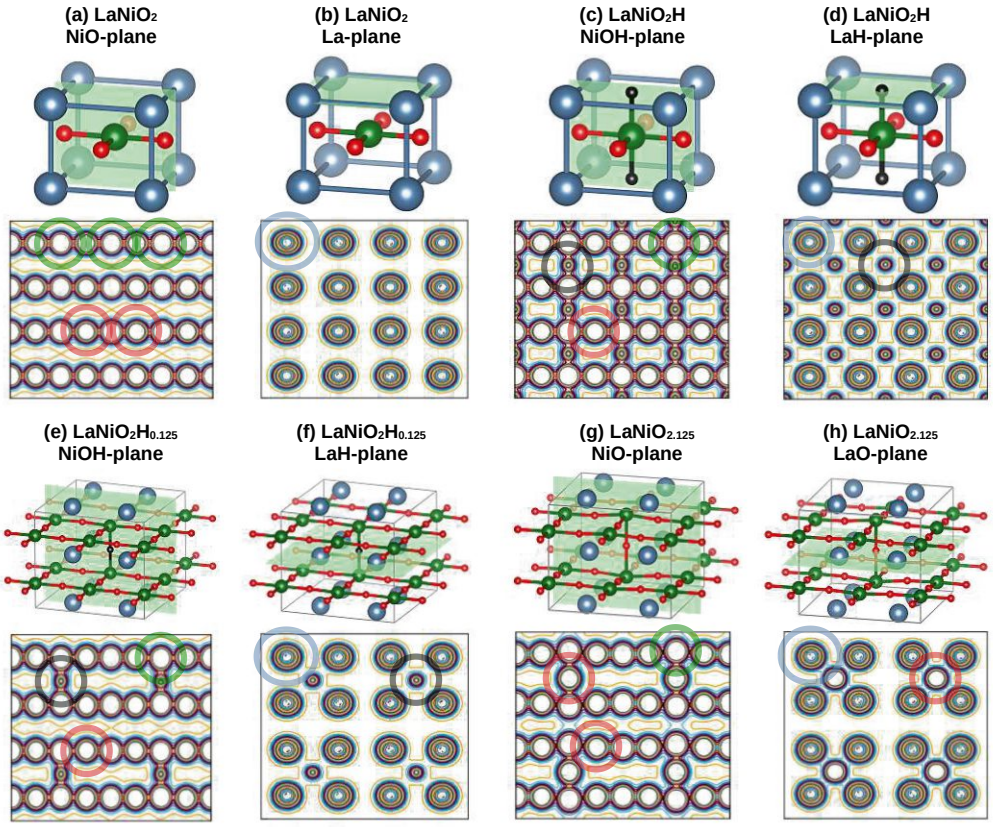

Figure 5.24: DFT calculated valence charge density of (a,b) $LaNiO_2$, (c,d) $LaNiO_2H$, and a $LaNiO_2$ supercell doped with a single (e,f) H and (g,h) O atom. For each compound, the charge density of (020) and (001) planes are shown in panels (a,c,e,g) and (b,d,f,h),respectively. The La, Ni, O and H atoms are labeled by blue, green, red and black circles, respectively.

Fig. 5.24 (c) and (d) present the electron density of $LaNiO_2H$ along the same planes. In the NiOH-plane of Fig. 5.24(c), the comparison to Fig. 5.24(c) shows that intercalated H boosts a 3D picture with an additional δ-type bond formed by Ni-d_{z^2} and H-1s orbitals (black circle). Along the LaH-plane [Fig. 5.24(d)], δ-type bonds are formed by the orbital overlap between La-d_{xy} and H-1s orbitals. For $LaNiO_2$ with partial topotactic H [$LaNiO_2H_{0.125}$ in Fig. 5.24(e,f)], the additional H atoms play similar roles at the Ni-H and the La-H bonds as in $LaNiO_2H$. The Ni and La atoms without H in-between are similar as in Fig. 5.24(a-b) and those with H are akin to Fig. 5.24(c-d). This indicates that the effects induced by topotactic H are indeed very local, i.e., they only affect the the nearest Ni and La atoms.

In Fig. 5.24 (g) and (h), for $LaNiO_{2.125}$, the additional O increases the local c-lattice (Ni-Ni bond length via the additional O) from the $LaNiO_2$ value of 3.338 Å to 4.018 Å which is even larger than the DFT-relaxed value of $LaNiO_3$: 3.80 Å. This lattice expansion can be clearly seen in Fig. 5.24(g). The large electron density between Ni and O along the z-direction indicates the strength of this Ni-O bond in the z-direction is comparable with

Die approbierte gedruckte Originalversion dieser Dissertation ist an der TU Wien Bibliothek verfügbar.
The approved original version of this doctoral thesis is available in print at TU Wien Bibliothek.

the ones along x/y directions. From Fig. 5.24(h), we conclude that similar La-O bonds are formed after intercalating additional O atoms, the La-La distance is shrunken by the additional O atom from 3.889 Å ($LaNiO_2$) to 3.746 Å between the La atoms pointing to the additional O. However, from the electron density plot, the La-O bond strength seems not stronger than the La-H bonding in Fig. 5.24(c,e). This can be explained by the fact that both O-p_x and -p_y orbitals do not point to orbital lobes of La-d_{xy}, leading to a comparable bond strength as the La-H bond in $LaNiO_2H_\delta$.

5.4.6 Conclusion and outlook

Our theoretical study demonstrates that the parent compounds of infinite-layer nickelate superconductors, $LaNiO_2$ and $NdNiO_2$, are energetically unstable with respect to topotactic H in the reductive process from perovskite La(Nd)NiO_3 to La(Nd)NiO_2. The presence of H, which reshapes the systems from ABO_2 to the hydride-oxide ABO_2H, triggers a transition from a quasi-2D strongly correlated single-band ($d_{x^2-y^2}$) metal, to a 2-band ($d_{x^2-y^2}$+d_{z^2}) anti-ferromagnetic 3D Mott insulator. Our predictions [64] have been reproduced by other groups using DFT+U calculations for other similar ABO_2 systems [344, 388]. The recent experimental observation [396] of Ni^{2+} ($3d^8$) in nickelates indicates the existence of topotactic H, as do NMR experiments [339]. The presence of H and its consequence of a 3D Mott-insulator is unfavorable for the emergence of superconductivity in nickelates. However, it is difficult to detect topotactic H in experiment. Three factors contribute to this difficulty: (1) the small radius of H makes it hard to be detected by commonly employed experimental techniques such as x-ray diffraction and scanning transmission electron microscopy (STEM). (2) As revealed by our phonon calculations, the dynamical stability of La(Nd)NiO_2 does not rely on the concentration of intercalated H atoms. Hence the same infinite-layer structures should be detected by STEM even in the presence of H. (3) As revealed by electron density distributions, the topotactic H does not break the local crystal structure either (e.g. bond length and angle); the H atoms merely affect the most nearby Ni atoms via a Ni-d_{z^2}-H-1s δ-bond. This is different if we have additional O atoms instead of H: O atoms do not only induce a dynamical instability but also obviously change the local crystal by enlarging the Ni-Ni bond length and angle visibly. Oxygen impurities also lead to unstable phonon modes in $LaNiO_{2+x}$ and thus a major lattice reconstruction.

The ways to avoid topotactic H revealed by our calculations are: in-plane compressive strains and bivalent cation doping with Sr or Ca. This draws our attention to the recently synthesized (Nd,Sr)NiO_2 films [59] , which has been grown on a $(LaAlO_3)_{0.3}(Sr_2TaAlO_6)_{0.7}$ (LSAT) instead of a $SrTiO_3$ (STO) substrate, inducing an additional 0.9% compressive strain. These new films were shown to be defect-free and with a considerably larger superconducting dome from 10% to 30% Sr-doping and a higher maximal T_c ∼20 K [59], compared to 12.5%-25% Sr-doping and T_c ∼15 K for nickelate films grown on STO which show many stacking faults [17, 258, 323]. The compressive strain induced by replacing the STO substrate (a=3.905 Å) by LSAT (a=3.868 Å) may tune the positive E_b to negative, thus contributing to suppressing defects and recovering a single $d_{x^2-y^2}$-band picture.

Die approbierte gedruckte Originalversion dieser Dissertation ist an der TU Wien Bibliothek verfügbar.
The approved original version of this doctoral thesis is available in print at TU Wien Bibliothek.
TU Bibliothek Your knowledge hub WIEN

Besides avoiding topotactic H, compressive strain is also predicted as an effectively way to enhance T_c. Previous dynamical vertex approximation calculations [20, 50] reveal the key to enhance T_c in nickelates is to enhance the bandwidth W and to reduce the ratio of Coulomb interaction U to W. Based on this prediction, we have proposed [20, 50] three experimental ways to enhance T_c in nickelates: (1) in-plane compressive strain, which can indeed be achieved by using other substrates having a smaller lattice than STO, such as LSAT (3.868 Å), $LaAlO_3$ (3.80 Å) or $SrLaAlO_4$ (3.75 Å). The smaller in-plane lattice shrinks the distansce between Ni atoms thus increases their orbital overlap, leading to a larger W and a smaller U/W. Recent experimental reports have confirmed the validity of this approach by growing (Nd,Sr)NiO_2 on LSAT [59] and $Pr_{0.8}Sr_{0.2}NiO_2$ on LSAT [397]. (2) Applying external pressure on the films plays the same role as in-plane strain for the, essentially 2D, nickelates. This has been experimentally realized in [341]: under 12.1 GPa pressure T_c can be enhanced monotonously to 31 K without yet showing a saturation. (3) Replacing 3*d* Ni by 4*d* Pd. In infinite-layer palladates such as $NdPdO_2$ or $LaPdO_2$ and similar compounds with 2D PdO_2 layers and separating layers between them, the more extended 4*d* orbitals of Pd are expected to reduce U/W from $U/W \sim 7$ for nickelates to $U/W \sim 6$ for palladates. Further experimental and theoretical research on the electronic and magnetic structure and the superconductive properties of palladates are thus worth to perform.

Die approbierte gedruckte Originalversion dieser Dissertation ist an der TU Wien Bibliothek verfügbar.
The approved original version of this doctoral thesis is available in print at TU Wien Bibliothek.

5.5 Chain formation of intercalated hydrogen in nickelates

The following section is a short summary of the arXiv preprint arXiv:2208.11085 (2022) [295].

As mentioned in Section 5.5, nickelate superconductors are synthesized by first growing a perovskite phase $R\mathrm{NiO_3}$, where R is a trivalent rare-earth atom, on a substrate [17]. The most common substrate is STO, but recent experiments also include LSAT [59]. Subsequently, to obtain infinite-layer $R\mathrm{NiO_2}$, $\mathrm{CaH_2}$ is used as a reduction agent to remove the apical oxygen from the samples. Contrary to cuprates, hydrogen intercalation is favorable and (local) $R\mathrm{NiO_2H}$ may form [64].

Detecting hydrogen in experiments is, however, notoriously difficult. Since hydrogen atoms are small, specifically when compared to the other atoms in $R\mathrm{NiO_2H}$, they are hard to detect in many common techniques such as X-ray powder diffraction (XRD) or scanning transmission electron microscopy (STEM). Using gas extraction of $\mathrm{LaNiO_2}$ bulk samples[24], hydrogen concentrations close to 20% were reported by the authors of Ref. [398]. Our research expands upon the ideas developed in Ref. [64] and we address two questions: (i) is there a preferred arrangement of H atoms in the crystal, or do they occupy essentially random positions? (ii) what is the influence of H on the electronic environment?

To order or not to order. — To determine the distribution of H atoms for a given δ, we compute the H binding energy E_b

$$E_b = \{E[\mathrm{LaNiO_2}] + n \times \mu[\mathrm{H}] - E[\mathrm{LaNiO_2H_\delta}]\}/n, \tag{5.7}$$

where n is the number of H atoms in the unit cell, for all possible inequivalent configurations of apical H[25]. $E[\mathrm{LaNiO_2H_\delta}]$ is defined as the DFT energy after structural relaxation of all internal atomic positions and lattice parameters. In Fig. 5.25, we show the DFT ground state structure for all possible H concentrations within a $2 \times 2 \times 2$ supercell[26]. For all hydrogen concentrations, we observe that the configuration with the lowest DFT energy shows chains of hydrogen in c-axis direction. This is most notable for $\delta = \{0.25, 0.5, 0.75\}$, corresponding to one, two and three chains in Fig. 5.25(c,e,g), respectively. This chain ordering also persists in larger supercells and the highest binding energy per hydrogen of all tested configurations was that of a single infinite chain in a $3 \times 3 \times 3$ supercell, which corresponds to $\mathrm{LaNiO_2H_{1/9}}$. Such an order of hydrogen atoms will lead to a charge modulation on the Ni and La sites with a vector of $(1/3, 1/3, 0)$, reminiscent of the charge density wave observed in infinite-layer nickelates [396, 399].

[24] One should note that so far, no superconductivity was observed in bulk infinite-layer nickelates [23, 398].

[25] Hydrogen intercalation is only favorable at the apical position between Ni atoms, see the revised version of [295].

[26] For information on all possible configurations as well as energy differences, we refer the reader to the original manuscript [295].

Die approbierte gedruckte Originalversion dieser Dissertation ist an der TU Wien Bibliothek verfügbar.
The approved original version of this doctoral thesis is available in print at TU Wien Bibliothek.
TU Bibliothek Your knowledge hub WIEN

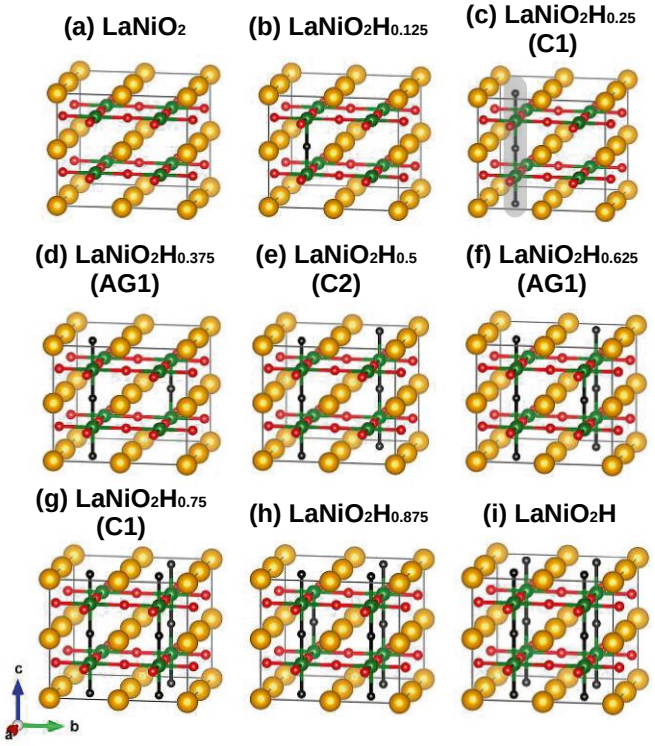

Figure 5.25: DFT ground state crystal structures of $LaNiO_2H_\delta$ for various hydrogen concentrations δ=0.0%-100%. yellow atoms: La; red: O; green: Ni; black: H). $LaNiO_2$ without H corresponds to (a), while $LaNiO_2H$ is shown in (i). The gray region in (c) marks the single hydrogen chain of $LaNiO_2H_{0.25}$. Two chains are present in $LaNiO_2H_{0.5}$ (e) and three in $LaNiO_2H_{0.75}$ (g). Calculations using larger supercells imply that the single hydrogen in (b,d,f,h) would form chains. Figure taken from Ref. [295].

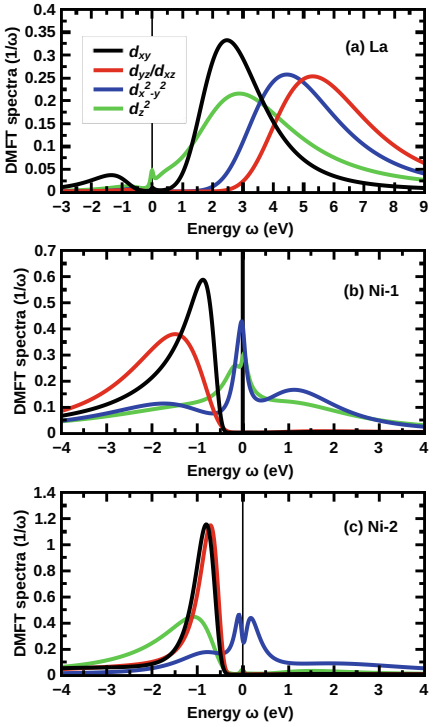

Figure 5.26: DMFT k-integrated spectral functions $A(\omega)$ of $LaNiO_2H_{0.5}$ (in units of $1/\omega$), resolved for (a) La, (b) first Ni site (Ni-1) with apical H and (c) second Ni site (Ni-2) without apical H. Figure taken from Ref. [295].

Influence of H on the electronic structure. — To investigate the influence of intercalated hydrogen atoms on the electronic structure, we performed DFT+DMFT calculations in a $2\times2\times2$ supercell for $LaNiO_2H_{0.5}$ (the structure is displayed in Fig. 5.25(e)). For the correlated subspace of the DMFT calculation, we used the full Ni-3d and La-5d shell und supplemented the Wannier Hamiltonian with a local Kanamori interaction using an intraorbital Hubbard interaction U=4.4 eV and a Hund's exchange J=0.65 eV (inter orbital U'=U-2J=3.1 eV) for Ni-3d, U=2.5 eV and J=0.25 eV (U'=2.0 eV) for La-5d orbitals in line with Ref. [50]. At topotactic hydrogen concentrations $<$ 100%, we find a finite Ni-La hybridization, which is absent in $LaNiO_2H$ [64] (see also Table 5.6). This La-Ni hybridization was also observed experimentally using inelastic X-ray scattering (RIXS) measurements [32, 329, 396, 399] and is visible in Fig. 5.26(a) as the peak around E_F and at -1.5 eV.

Die approbierte gedruckte Originalversion dieser Dissertation ist an der TU Wien Bibliothek verfügbar.
The approved original version of this doctoral thesis is available in print at TU Wien Bibliothek.
TU Bibliothek Your knowledge hub WIEN

Table 5.6: DMFT occupation n at the La-site for different concentrations δ of topotactic-H. A modified version of a similar table from Ref. [295].

$LaNiO_2H_\delta$				
δ	0.25	0.50	0.75	1.00
n(La-site)	0.32	0.24	0.20	0.00

In $LaNiO_2H_{0.5}$, there exist two inequivalent Ni sites. One with apical hydrogen chains (Ni-1) and one without (Ni-2). Fig. 5.26(b,c) displays their respective k-integrated spectral functions $A(\omega)$, which are noticeably different. The apical hydrogen removes an electron from its environment, mostly from the Ni-1 site (~ 0.8), which neighbors the topotactic hydrogen. As a result, Ni-1 is close to a $3d^8$ configuration but remains metallic, contrary to the Mott insulator $LaNiO_2H$. In comparison, only ~ 0.1 electrons are removed from the Ni-2 site, which stays close to the $3d^9$ configuration, similar to the parent compound $LaNiO_2$. Orbital occupations computed from multi-orbital DMFT calculations are listed in Table 5.7. Hence, intercalated hydrogen will naturally lead to a coexistence of Ni^{1+} ($3d^9$) and Ni^{2+} ($3d^8$) oxidation states. Such coexistence of oxidation states was also observed experimentally using resonant inelastic X-ray scattering by the authors of Ref. [396].

Table 5.7: Effective mass enhancement (m^*/m_b) and occupation n of different Ni orbitals for $LaNiO_2H_{0.5}$. A modified version of a similar table from Ref. [295].

$LaNiO_2H_{0.5}$				
orbital	Ni-1 $d_{x^2-y^2}$	Ni-1 d_{z^2}	Ni-2 $d_{x^2-y^2}$	Ni-2 d_{z^2}
m^*/m_b	4.13	2.85	2.77	1.19
n	1.05	1.11	0.83	1.96

Die approbierte gedruckte Originalversion dieser Dissertation ist an der TU Wien Bibliothek verfügbar.
The approved original version of this doctoral thesis is available in print at TU Wien Bibliothek.
TU Bibliothek Your knowledge hub WIEN

5.6 Optimizing superconductivity: from cuprates via nickelates to palladates

Prediction is very difficult, especially if it's about the future.
— N. Bohr

The following section is a short summary of the arXiv preprint arXiv:2207.14038 (2022) [400].

Motivation — Both nickelates and cuprates are layered transition metal oxides with a nominal $3d^{9-\delta}$ configuration and square planar NiO_2 (CuO_2) sheets. Furthermore, superconductivity emerges for $0.1 \leq \delta \leq 0.25$[27] and both show a band with Ni(Cu)-$3d_{x^2-y^2}$ character on the Fermi surface in electronic structure calculations[28] [21, 51]. While the description of a single-band Hubbard model is controversial for both materials[29], their similarities regarding the structure and elemental composition suggest that layered transition metal oxides with a $d^{9-\delta}$ configuration are a recipe for superconductivity. Motivated by this, we discuss the possibility of superconductivity in palladium oxides like $LaPdO_2$.

How do palladates fit into the picture? — DFT calculations of three possible palladates, $LaPdO_2$, $RbSr_2PdO_3$ and $A'_2PdO_2Cl_2$ (A'=$Ba_{0.5}La_{0.5}$), suggest that they are in-between cuprates and nickelates (Fig. 5.27). Cuprates are charge-transfer insulators [317], where the Cu-3d and O-2p bands exist at similar energies. Consequently, cuprates show a strong Cu-O hybridization with a sizeable weight of O contributing to the band that crosses the Fermi energy. Contrary, in nickelates, the Ni-3d orbitals are higher in energy and hybridize with the rare-earth elements of the "block layers", i.e. La in $LaNiO_2$. This hybridization leads to the formation of the A- and Γ pocket bands. The 4d orbitals of the palladates, however, hybridize only weakly with *both* the O-2p and the rare-earth orbitals. Hence, we anticipate that a single-band Hubbard model description is at least as justified than in either nickelates or cuprates[30].

The parameters of a single-band Hubbard model description of various palladates are listed below in Table 5.8. The tight-binding parameters were obtained from a Wannier projection onto the $4d_{x^2-y^2}$-derived band around the Fermi energy, and the interaction value was subsequently computed using cRPA.

[27] Cuprates also show superconductivity upon electron doping [288, 289]. An "analogous" superconducting electron-doped nickelate has not yet been synthesized.
[28] See also Box 2, Box 3 and Box 4.
[29] For cuprates for example the relevance of the O orbitals is discussed, see e.g. Ref. [65, 318]. For nickelates, multi-orbital effects are also under consideration [19, 256, 290, 313–315, 401–403].
[30] While $RbSr_2PdO_3$ and $A'_2PdO_2Cl_2$ are dynamically stable in the $P4/mmm$ phase $LaPdO_2$ is not. DFT predicts a structure distortion that includes a buckling of the NiO_2 planes, see the revised version of Ref. [400].

Die approbierte gedruckte Originalversion dieser Dissertation ist an der TU Wien Bibliothek verfügbar.
The approved original version of this doctoral thesis is available in print at TU Wien Bibliothek.
TU Bibliothek Your knowledge hub WIEN

	$\lvert t\rvert$(meV)	t'/t	t''/t	U_{eff}/t
$NdNiO_2$	395	-0.25	0.12	8
$NdNiO_2$(Strained)	419	-0.23	0.12	7.0–7.5
$NdPdO_2$	558	-0.17	0.13	4.5
$RbSr_2PdO_3$	495	-0.24	0.16	6
$A'_2PdO_2Cl_2$	443	-0.22	0.14	7.5
$A'_2PdO_2Cl_2$ (-1.5% strain)	470	-0.22	0.14	7.0
$A'_2PdO_2Cl_2$ (-3.0% strain)	497	-0.22	0.14	6.0

Table 5.8: Summary of the DFT-derived parameters for the single-band Hubbard model, as an effective low-energy model for the nickelate $NdNiO_2$, the palladates $NdPdO_2$, $RbSr_2PdO_3$, and $A'_2PdO_2Cl_2$. Taken from Ref. [400]

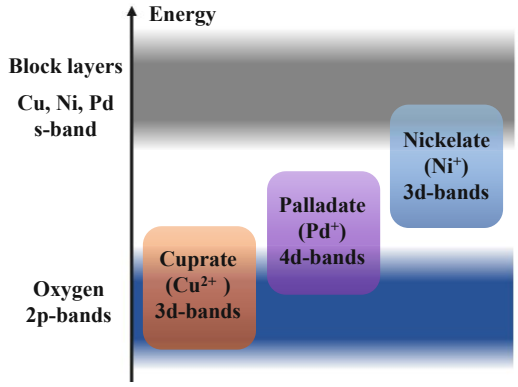

Figure 5.27: Schematic picture of the energy levels for copper (Cu^{2+}), nickel (Ni^+), palladium (Pd^+) superconductors. Taken from Ref. [400].

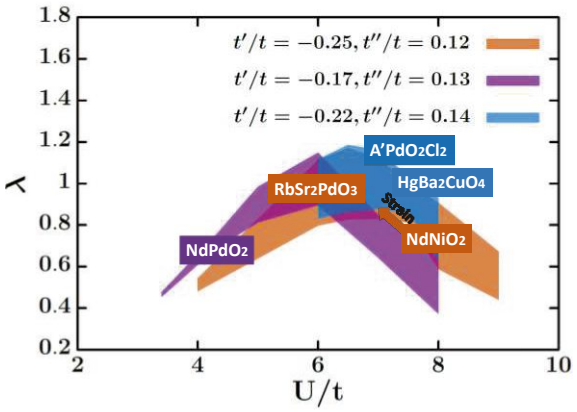

Figure 5.28: Interaction U dependence of the superconducting eigenvalues λ at $T = 0.01t$ for three different t',t'' from Table 5.8. For each U, the linewidth corresponds to the range of λ for fillings $0.80 \leq n \leq 0.90$. Materials corresponding to these models and U's are indicated. Taken from Ref. [400].

T_c of the single-band Hubbard model using DΓA. — Using the parameters of the effective single-band Hubbard model from Table 5.8, we compute the superconducting eigenvalue using DΓA[31]. We see from Fig. 5.28 that $NdNiO_2$ is not optimal, but too strongly correlated. Our calculations predict that decreasing U/t, e.g. by applying strain or changing $3d$ with $4d$ as in $RbSr_2PdO_3$, should increase T_c.

Fig. 5.29 shows the superconducting eigenvalue λ computed within DΓA as a function of interaction value U and doping δ for three sets of tight-binding parameters. The first (left panel) shows λ the simplest case where only nearest-neighbor hopping is considered and $t' = t'' = 0$. The middle panel shows λ for tight-binding parameters corresponding to a single-band approximation of $NdPdO_2$ and the right panel those corresponding to $NdNiO_2$.

[31] For details regarding DΓA see also Section 3.8. For details regarding the superconducting eigenvalues, see Section 3.9.

Die approbierte gedruckte Originalversion dieser Dissertation ist an der TU Wien Bibliothek verfügbar.
The approved original version of this doctoral thesis is available in print at TU Wien Bibliothek.
TU Bibliothek Your knowledge hub WIEN

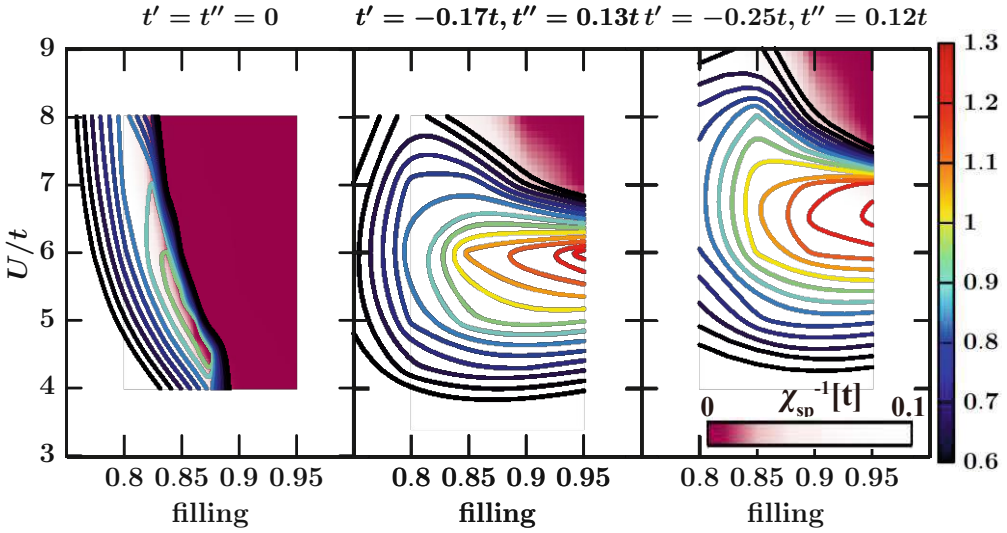

Figure 5.29: Superconducting eigenvalue λ and antiferromagnetic susceptibility $\chi_{\mathrm{sp}}(Q_{\max}, \omega = 0)$ as a function of interaction U and filling at $T = 0.01t$ for the three different t', t'' given at the top of each panel. Taken from Ref. [400]

λ shows a dome structure with filling reminiscent of the superconducting dome in cuprates [3, 5] and nickelates [258] for sufficiently high interaction values, e.g. $U/t > 6$ for the middle panel in Fig. 5.29. A similar dome of λ as a function of U is found for all fillings $0.8 \leq \delta \leq 0.95$. We understand both the U and δ dome structure as competition between pairing strength and spectral weight at the Fermi energy. As antiferromagnetic fluctuations become larger, towards half-filling and larger U, so does the effective pairing interaction. At the same time, however, strong antiferromagnetic fluctuations will open a pseudogap, thus leading to a suppression of the spectral weight at E_{F}. This is why the superconducting eigenvalue is suppressed for large U and in the vicinity of half-filling ($n = 1$) in Fig. 5.29. Balancing a large pairing vertex and a weak pseudogap gives rise to an optimum and a dome of λ as a function of doping and U.

Experimentally confirming or refuting the existence of superconductivity in infinite-layer palladates would be another big step toward identifying the necessary requirements for superconductivity in layered transition metal oxides. Furthermore, it provides an ideal scenario to test the predictive power of our theoretical framework, both qualitatively and quantitatively.

Die approbierte gedruckte Originalversion dieser Dissertation ist an der TU Wien Bibliothek verfügbar.
The approved original version of this doctoral thesis is available in print at TU Wien Bibliothek.

Die approbierte gedruckte Originalversion dieser Dissertation ist an der TU Wien Bibliothek verfügbar.
The approved original version of this doctoral thesis is available in print at TU Wien Bibliothek.

Chapter 6

Conclusion and outlook

Conclusion

They could argue for hours on almost any subject; they usually agreed on broad conclusions, but disagreed on almost every detail.

— B. Joyce

In this thesis, we discussed the electronic structure and low-temperature physics of two families of high-temperature superconductors: nickelates and cuprates. Specifically, we focused on (i) building effective low-energy models and (ii) using those models to compute observables and explain experimental measurements. Below we summarize the insights gained and conclusions reached during my Ph.D. In Section 6, we provide an overview of selected open topics for further research.

Pseudogap — As of writing this thesis, there exists no agreed-upon theory for the microscopic origin of the pseudogap (PG) in the scientific community. The PG, characterized by a depression of the density of states at the Fermi energy and the appearance of Fermi arcs in angular resolved photoemission (ARPES) experiments, appears in the underdoped regime of cuprates. Here we analyzed the origin of it in the particle-hole asymmetric doped single-band Hubbard model and compared characteristics to experiments.

In Section 4.2, we discussed the emergence of a large imaginary part of the spin-fermion vertex as a possible mechanism to explain the onset of the PG at high temperatures and when correlation lengths are still small. Specifically, this mechanism will naturally lead to an opening of the PG starting with the antinode and not the hot spots, as would be the case for weak coupling. We further explored the parameter space of a simple Ansatz for the self-energy based on antiferromagnetic fluctuations when the spin-fermion coupling vertex acquires an imaginary part. We find that the PG observed both in electron- as well as in hole-doped cuprates is qualitatively captured by this model. Furthermore, this model for the self-energy exhibits true Fermi arcs when the correlation length and strength of the AFM fluctuations are small but shows a transition to hole pockets once they become large. Whether hole pockets also appear in (numerical) solutions of the Hubbard model is an interesting direction for further research.

In Section 4.3, we studied the real-frequency structure of the PG in the Hubbard model for parameters relevant to cuprates using the dynamical vertex approximation (DΓA). Our calculations show that the PG can be understood as a momentum-selective insulator, where the antinodes are gapped while the nodes are metallic. One should note that the antinodal gap originates from antiferromagnetic fluctuations and is much smaller than the Mott gap. Furthermore, we observed a violation of Luttinger's theorem, which can be traced back to the gapped $\mathbf{k}$-points close to the antinode. For those momenta, the spectrum at low frequencies is conceptually similar to a particle-hole asymmetric insulator. Furthermore, we found an "s-wave"-like structure of the PG in DΓA at

Die approbierte gedruckte Originalversion dieser Dissertation ist an der TU Wien Bibliothek verfügbar.
The approved original version of this doctoral thesis is available in print at TU Wien Bibliothek.
TU Bibliothek Your knowledge hub WIEN

sufficiently low temperature, similar to Ref. [142], which we connected to nesting physics.

Ba_2CuO_4 — In Section 4.4 we studied a more recently discovered cuprate superconductor, which displays superconductivity at unusually high doping levels [253]. We determined, based on DFT energy calculation, a non-uniform oxygen distribution with two inequivalent CuO layers as the ground state. Charge transfer between the layers results in a doping level of the Cu-$3d_{x^2-y^2}$ orbital comparable to that of "regular" cuprates, albeit with a strong x–y anisotropy.

Nickelates: minimal model for superconductivity — In Section 5.1 we reviewed the electronic structure of infinite-layer nickelate superconductors. Based on DFT+DMFT results, we argued that a single-band Hubbard model is enough to capture the mechanism responsible for superconductivity. Calculations performed by the authors of Ref. [50] show that the theoretical superconducting dome of the effective Hubbard model agrees well with the experimentally measured one.

Superconductivity in layered nickelates — Not long after the discovery of superconductivity in infinite-layer nickelates, it was also found in a five-layer compound, $Nd_6Ni_5O_{12}$ [345]. Using DFT+DMFT, we investigated the electronic structure of this compound and found that the rare-earth pockets are depleted once (local) correlations are taken into account. Assuming that the layers can be treated independently, we find that the parameters of the resulting single-band Hubbard model are similar to that of 20 % doped infinite-layer nickelates, and calculations based on this Hubbard model yield a transition temperature close to the measured one.

Nickelates: magnetic response — One of the key features that distinguish nickelates from cuprates is the absence of long-range antiferromagnetic order. This is partially explained by the "self-doping" due to the rare-earth pockets, which results in an effective Ni-$3d_{x^2-y^2}$ occupation away from half-filling. Nevertheless, if nickelates are "cuprates analogs", signatures of antiferromagnetic fluctuations should be present. Measurements using resonant inelastic X-ray scattering (RIXS) were reported to be "consistent with a doped Mott insulator" by the authors of Ref. [32]. In Section 5.3, we compared the paramagnon dispersion obtained from the single-band Hubbard model using DΓA to the experimentally extracted one and observed a reasonable agreement without adjusting any free parameters. The most notable discrepancy is that our calculations for $U = 8\,t$ overestimate the paramagnon bandwidth and thus the effective spin-spin coupling J. Measurements on cleaner samples are required to identify whether the deviation is of theoretical or experimental nature.

Since antiferromagnetic fluctuations are, for our calculations, also connected to the superconducting transition temperature T_c, we discuss connections between the measured RIXS spectra and the observed T_c. Specifically, we show that a suppression of the antiferromagnetic correlation length ξ is not expected to visibly change J extracted from the available RIXS data. At the same time, T_c would be reduced in our theoretical framework. We conjecture that the experimental T_c is correlated with ξ and that samples of poorer quality show a reduced T_c and reduced ξ.

Nickelates: hydrogen defects — The synthesis of nickelates involves a reduction process from the perovskite $LaNiO_3$ to the infinite-layer $LaNiO_2$ phase, typically using

Die approbierte gedruckte Originalversion dieser Dissertation ist an der TU Wien Bibliothek verfügbar.
The approved original version of this doctoral thesis is available in print at TU Wien Bibliothek.
TU Bibliothek Your knowledge hub WIEN

the reduction agent CaH_2. The authors of Ref. [64] noticed that, contrary to cuprates, the intercalation of "topotactic hydrogen" is energetically favorable in nickelates. At the same time, intercalating hydrogen, which creates a local Ni-3d^8 configuration [64], is expected to be unfavorable for superconductivity[1]. However, hydrogen is notoriously hard to detect in experiments, which makes it difficult to assess the quality of the samples in this respect. In Section 5.5, we discussed hydrogen phonon modes as indicators for the presence of hydrogen in samples.

Outlook

I may not have gone where I intended to go, but I think I have ended up where I needed to be.
— D. Adams

Let us now delve deeper into questions left open and possible further research directions.

Pseudogap: Emery model — The discussion of the PG within this thesis is based on the Hubbard model. One open question concerning cuprates is whether the key physics is (qualitatively) captured by the Hubbard model or if other (more complicated) models are necessary. One such model is the Emery model [318], consisting of one Cu-3d and two O-p orbitals. How the structure and temperature/doping dependence of the PG differs in the Emery model compared to the Hubbard model would be an important step forward to understanding cuprates.

Pseudogap: "s-wave" structure — Evidence for an "s-wave" structure of the PG at sufficiently low temperatures was found in two independent methods: CDMFT [142] and DΓA (this work). Let us stress that "s-wave" means that the gap never closes in momentum space. Its frequency location does, however, have a strong momentum dependence and the gap is above E_F for the node. Hence a metallic behavior and the "d-wave" structure at the Fermi energy is retained. Interesting further research would be to check (i) if this is intrinsic to the Hubbard model, i.e. other methods can reproduce these results, and (ii) if this is also observed in cuprates, e.g. in inverse ARPES.

Nickelates: T_c enhancement by pressure — The authors of Ref. [404] reported a monotonic increase of T_c in infinite-layer nickelates when applying pressure. Promising further research would be to estimate how T_c changes if hydrostatic pressure is applied[2].

DΓA phase diagram of cuprates — Calculating the superconducting dome using DΓA also for cuprates would be an interesting prospect. Using a small hopping in z-direction would allow for an estimation of the Néel order, which was experimentally measured for underdoped cuprates. This would allow drawing a phase diagram including the Néel temperature, the region where the PG is present and the d-wave superconducting dome. Comparing this theoretical phase diagram to the experimental one would be a large step forward in understanding how much of cuprates is already contained in the

[1] Consider for example La_2NiO_4, which hosts a nominal Ni-3d^8 configuration and does not display superconductivity even when doped, see e.g. Ref. [381]. Contrary, the cuprate "sibling" La_2CuO_4 hosts a Cu-3d^9 configuration and displays d-wave superconductivity upon doping. For the superconducting dome, see, e.g., [5].

[2] For a recent theoretical study concerning uniaxial pressure, see Ref. [291].

Die approbierte gedruckte Originalversion dieser Dissertation ist an der TU Wien Bibliothek verfügbar.
The approved original version of this doctoral thesis is available in print at TU Wien Bibliothek.
TU Bibliothek Your knowledge hub WIEN

DΓA solution of the Hubbard model.

Superconductivity: Emery model — Similarly as for the PG, it is controversial whether superconductivity in cuprates is captured by the Hubbard model. Consequently, studying superconductivity in the Emery model can give further insights into what is essential and what is incidental to high-temperature superconductivity. Furthermore, the oxygen orbitals are further away from the Fermi energy in band-structure calculations for nickelates. Studying the differences between the Hubbard and Emery models might yield further insight into the dissimilarities of cuprates and nickelates.

Die approbierte gedruckte Originalversion dieser Dissertation ist an der TU Wien Bibliothek verfügbar.
The approved original version of this doctoral thesis is available in print at TU Wien Bibliothek.
TU Bibliothek Your knowledge hub WIEN

Appendix

A.1 Supplemental Material: Finite layer nickelates

Parts of the following section, marked by a vertical bar, have already been published Physical Review Materials 6, L091801 (2022) [237].

A.1.1 Outline

This Supplementary Material presents additional information as well as density-functional theory (DFT) and dynamical mean-field theory (DMFT) results supporting our conclusions in the main text: Section A.1.2 provides computational details regarding DFT, DMFT and analytic continuation, while Section A.1.3 provides results for different DFT functionals. Details on the Wannier projection are provided in Section A.1.4, and in Section A.1.5 on the calculation of the occupation of the *effective* Ni $3d_{x^2-y^2}$ orbital. Section A.1.6 compares the effective mass for different nickelates and different Wannier projections. Section A.1.7 supplements the information of the main text by showing the DMFT spectral functions for other Wannier function projections. Section A.1.8 shows the corresponding Fermi surfaces, while the self-energy is displayed and discussed in Section A.1.9. Finally, Section A.1.10 presents results for $La_{2+\delta}Zr_{1-\delta}Ni_2O_6$ at $\delta = 0$ and 0.4.

A.1.2 Computational details and analytic continuation

PBEsol has proven to be very effective for lattice constants relaxation [349]. Hence in our DFT calculations, we used the GGA-PBEsol exchange potential to relax both lattice constants and atomic positions including spin-polarization. DFT calculations without spin-polarization do not converge because the Nd-f orbitals are treated as valence orbitals in VASP: that is, the fact that a large number of very flat bands crossing E_f makes it difficult to converge the DFT self-consistency loops. A solution to avoid this issue is to switch on spin-polarization in DFT and/or DFT+U calculations, which allows for a spin-splitting of the Nd-f bands. This spin-splitting $\Delta(\mathrm{Nd}-f)$ is proportional to $U_f(\mathrm{Nd})$, which is set to 7 eV in our study.

After obtaining the crystal structure, spin-polarized DFT and DFT+U calculations with GGA-PBEsol were performed to investigate the total energy of both bilayer $Nd_3Ni_2O_6$ and penta-layers $Nd_6Ni_5O_{12}$ with rock-salt and fluorite type as possible interfaces. Both calculations predict crystal structures with fluorite-like interface to be energetically favorable by 2.019 eV and 2.242 eV [per supercell as in Fig.1(a,b) of main text] for $Nd_3Ni_2O_6$ and $Nd_6Ni_5O_{12}$, respectively. The DFT bands in Fig. 1 (d,e) were obtained

Die approbierte gedruckte Originalversion dieser Dissertation ist an der TU Wien Bibliothek verfügbar.
The approved original version of this doctoral thesis is available in print at TU Wien Bibliothek.
TU Bibliothek Your knowledge hub WIEN

from non-spin-polarized DFT calculations with DFT-PBE functional using `Wien2k`. To avoid computational instability and convergence problems, we employed the so-called "open-core" approximation implemented in `Wien2k` that allows treating the Nd-f orbitals as core states without participating in computations. Lastly, let us note that with the spin-polarized DFT-PBEsol relaxed crystal structures, both the PBE and the PBEsol functional predict basically the same electronic band-structure. For the small differences see Fig. A.1.

Additionally, to investigate what role dynamical correlations play with regard to the electronic structure and superconductivity in nickelates, we have performed (non-spin-polarized) band calculations with the modified Becke-Johnson (mBJ) potential [60], as well as non-spin-polarized and spin-polarized DFT+U calculations. The mBJ potential allows the calculation of band gaps (i.e., the d-d and d-p energetic distance in our study) with an accuracy similar to very expensive GW calculations, performing better at treating local correlations and exchanges. To simulate multi-band correlations and exchange effects, both orbital-dependent Coulomb interaction U=4.4 eV and Hund's exchange J=0.65 eV on Ni-3d orbitals are included in DFT+U calculations. We also performed antiferromagnetic (AFM) DFT+U calculations to show that the pockets are robust against choice of U and magnetic orders. For the results, see Section A.1.3.

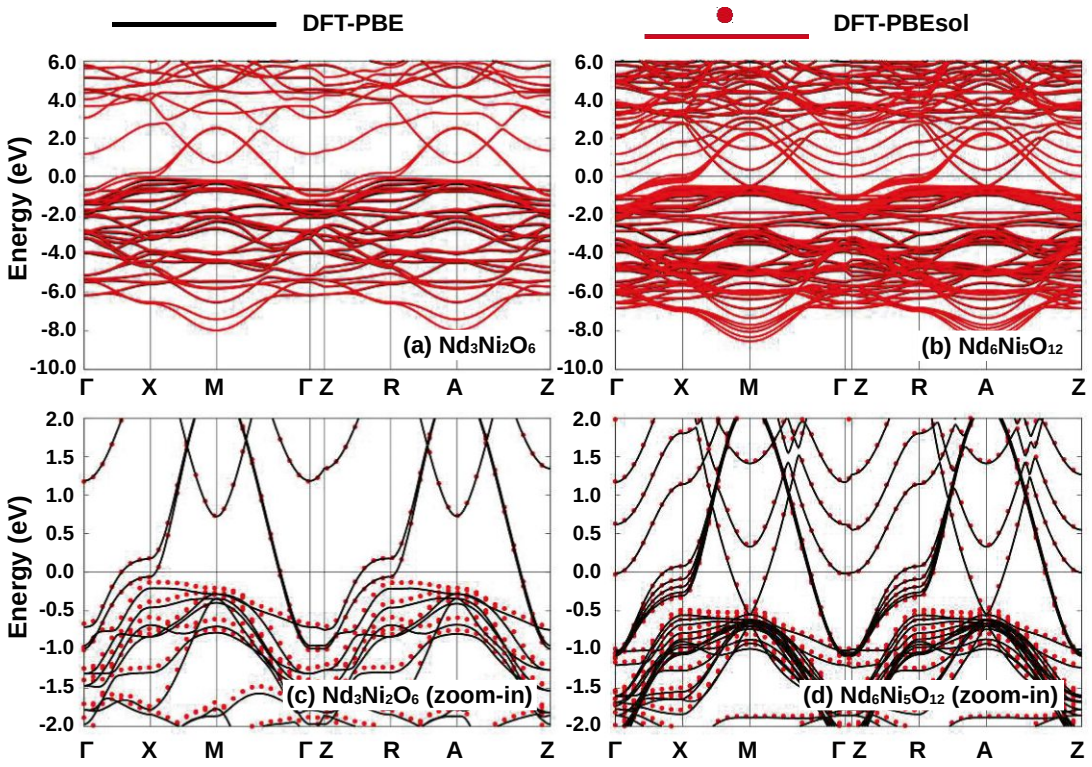

Figure A.1: Comparison between the DFT-PBE (black) and DFT-PBEsol (red) bandstructure. Left panels show results for $Nd_3Ni_2O_6$, while $Nd_6Ni_5O_{12}$ is displayed on the right. Bottom panels are a zoom-in around the Fermi energy of the respective top panels.

Die approbierte gedruckte Originalversion dieser Dissertation ist an der TU Wien Bibliothek verfügbar.
The approved original version of this doctoral thesis is available in print at TU Wien Bibliothek.

As noted in the method section of the main text, all DMFT calculations were performed using the `w2dynamics` code [278], which solves the Anderson impurity model using continuous-time quantum Monte Carlo simulations in the hybridization expansions [120]. We construct a separate impurity problem for each Nd and Ni site, which are connected via the DMFT bath (Dyson equation). For equivalent sites only one impurity problem is solved; the supercell is precisely as in Fig. 1 (a-c) of the main paper, which labels the inequivalent sites. For example, for $Nd_6Ni_5O_{12}$ there are three inequivalent Ni and three inequivalent Nd sites, so that we have have to solve six impurity problems with altogether 30 d-orbitals. After converging the DMFT iteration, we perform an additional high-statistic run to improve our analytical continuation. For this run we perform of the order $5 \cdot 10^9$ and $2 \cdot 10^8$ measurements for the $d_{x^2-y^2}$-only and full-d projection, respectively.

Analytic continuation is performed by the Maximum entropy method [280, 281] using the ana-cont package [122]. To determine the hyperparameter α, which is one of the most crucial parameters in the fitting procedure, we employ the "chi2kink" [353, 354] method. Additionally, we employ a "preblur" width of $b = 0.1$ to avoid unphysical artifacts around the Fermi energy. This corresponds to smearing the kernel with a Gaussian of width b.

A.1.3 DFT with more evolved potentials

One of the main conclusions in the main text was that electronic correlations depopulate the Nd pockets. Thereby the occupation in the superconducting Ni $d_{x\check{s}-y\check{s}}$ band shifts to values that are inside the predicted dome for superconductivity. Specifically, when looking at the DFT occupation the system would not be expected to be superconducting based on previous similar nickelates. In the main text we compared DFT-GGA-PBE to DFT+DMFT, which allows us to track the changes in the bandstructure as dynamic electronic correlations are included. In this section we show results for the modified Becke-Johnson (mBJ) potential, as well as non-spin-polarized and spin-polarized DFT+U calculations. The mBJ functional is known to yield very accurate electronic band structures and gaps (in this study: distances between Ni-d to O-p and Ni-$d_{x^2-y^2}$ to other Ni-d bands) for various types of materials including 3d strongly correlated transition-metal oxides [60]. Hence we perform mBJ band calculations as benchmarks to investigate whether an evolved treatment for the exchange leads to changes in the orbital occupations and a different physical picture. To study the roles of orbital-dependent potential from Coulomb U and Hund's exchange J, DFT+U calculations are performed for the same reason.

We chose interaction values identical to the ones described in the main text and used for DFT+DMFT to ensure best comparability. Those results are displayed in Fig. A.3 for the bilayer system and in Fig. A.2 for the pentalayer one. In both figures, panel (a) displays the bandstructure for DFT-mBJ, (b) the same for non-spinpolarized DFT+U and the bottom two panels correspond to spin-polarized DFT+U for (c) spin-up and (d) spin-down. While more elaborate than DFT-GGA, nevertheless, none of those approaches predicts the depopulation of the Nd-pocket for $Nd_6Ni_5O_{12}$ and thereby places the Ni $d_{x^2-y^2}$ band outside the region where superconductivity would be expected. Sim-

Die approbierte gedruckte Originalversion dieser Dissertation ist an der TU Wien Bibliothek verfügbar.
The approved original version of this doctoral thesis is available in print at TU Wien Bibliothek.
TU Bibliothek Your knowledge hub WIEN

ilarly, for $Nd_3Ni_2O_6$ there are no pockets in all of these DFT variants and a single Ni-$d_{x^2-y^2}$ band crossing the Fermi energy. That is, while there is an additional Hartree-like shift and the spin-up and -down bands are split in DFT+U, no qualitative differences are found when comparing the bands of standard DFT, mBJ and DFT+U calculations. Such differences are found in DFT+DMFT (see main text), and point to the importance of dynamic correlations in nickelates.

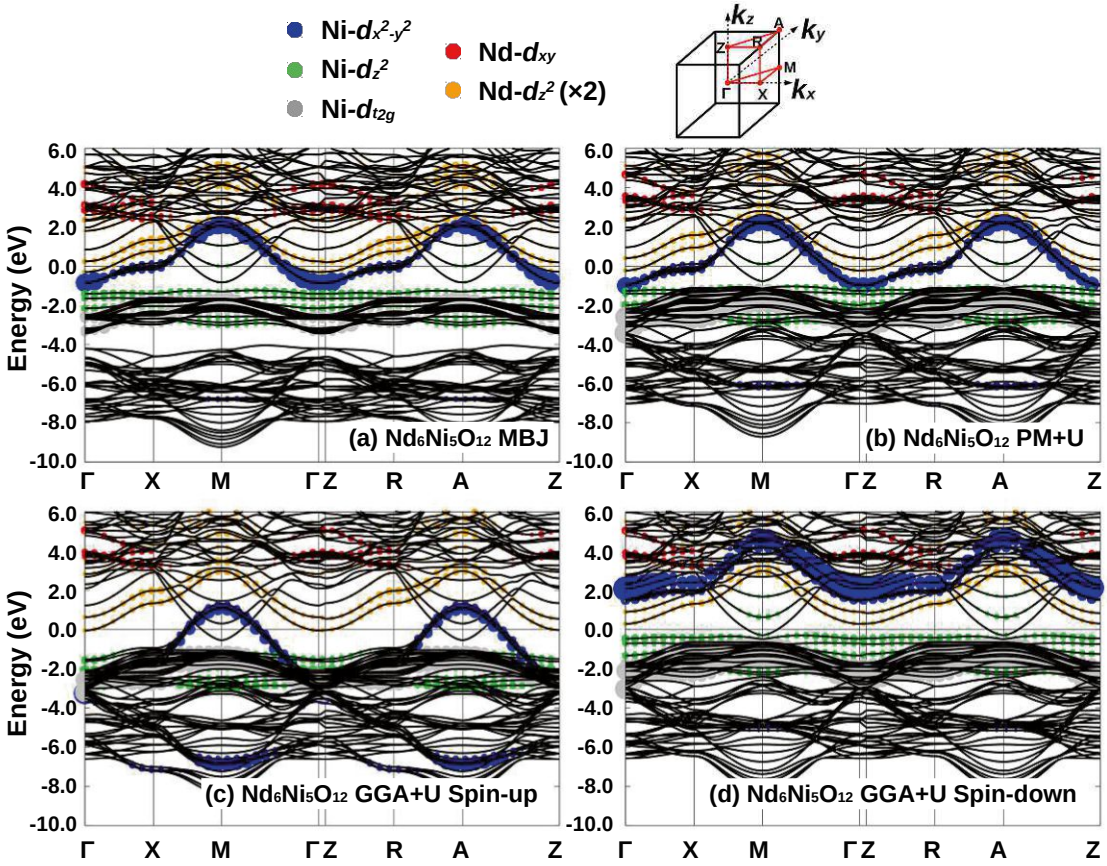

Figure A.2: DFT bandstructure calculations for $Nd_6Ni_5O_{12}$. (a) mBJ potential, (b) paramagnetic DFT+U and (c,d) spin-polarised DFT+U for spin (up,down).

To prove the robustness of Γ- and M/A-pocket, we further perform DFT+U calculations with a G-type AFM order for both Nd and Ni sites. As the Nd-f orbitals are treated as core states and excluded from band plotting, the finite magnetic moments on Nd are merely from Nd-5d orbitals/bands. Here, to test whether these pockets are robust against different U parameters, we perform AFM band calculations with four different setups: (1) with U on both Nd-5d (U=2.5 eV and J=0.25 eV) and Ni-3d (U=4.4 eV and J=0.65 eV); (2) with same U on Ni-3d (U=4.4 eV and J=0.65 eV) but doubled interaction parameters on Nd-5d (U=5.0 eV and J=0.5 eV); (3) with U only on Ni-3d (U=4.4 eV and J=0.65 eV); (4) with U on Nd-5d (U=2.5 eV and J=0.25 eV) but a smaller U on Ni-3d (U=2.4 eV and J=0.65 eV). Please note that these AFM band calculations are carried out with adopting a $\sqrt{2} \times \sqrt{2} \times 1$ supercell that allows G-AFM order, a k-space

Die approbierte gedruckte Originalversion dieser Dissertation ist an der TU Wien Bibliothek verfügbar.
The approved original version of this doctoral thesis is available in print at TU Wien Bibliothek.
TU Bibliothek Your knowledge hub WIEN

(first BZ) reduction and rotation is hence induced by the process of enlarging cell. On the top of this fact, the original Γ and M points now are shifted to the Γ-point. As one can see from Fig. A.4(a-d), in these Γ points there are multi bands leading to pockets, indicating static orbital/electron correlation fails at removing the pockets and recovering their single-band $d_{x^2-y^2}$ cuprate-like picture and Fermi surface. Among all these four setups, cases (2) and (4), which are with enhanced U on Nd or reduced U on Ni, makes the electrons energetically favorable to transfer from Nd to Ni, i.e., it reduces the self-doping effect and helps removing the pockets. However, as in Fig. A.4(b,d) one can see the pockets are still reserved, indicating the necessity of dynamical correlations (cf. Section A.1.9) when computing the electronic structures of nickelates.

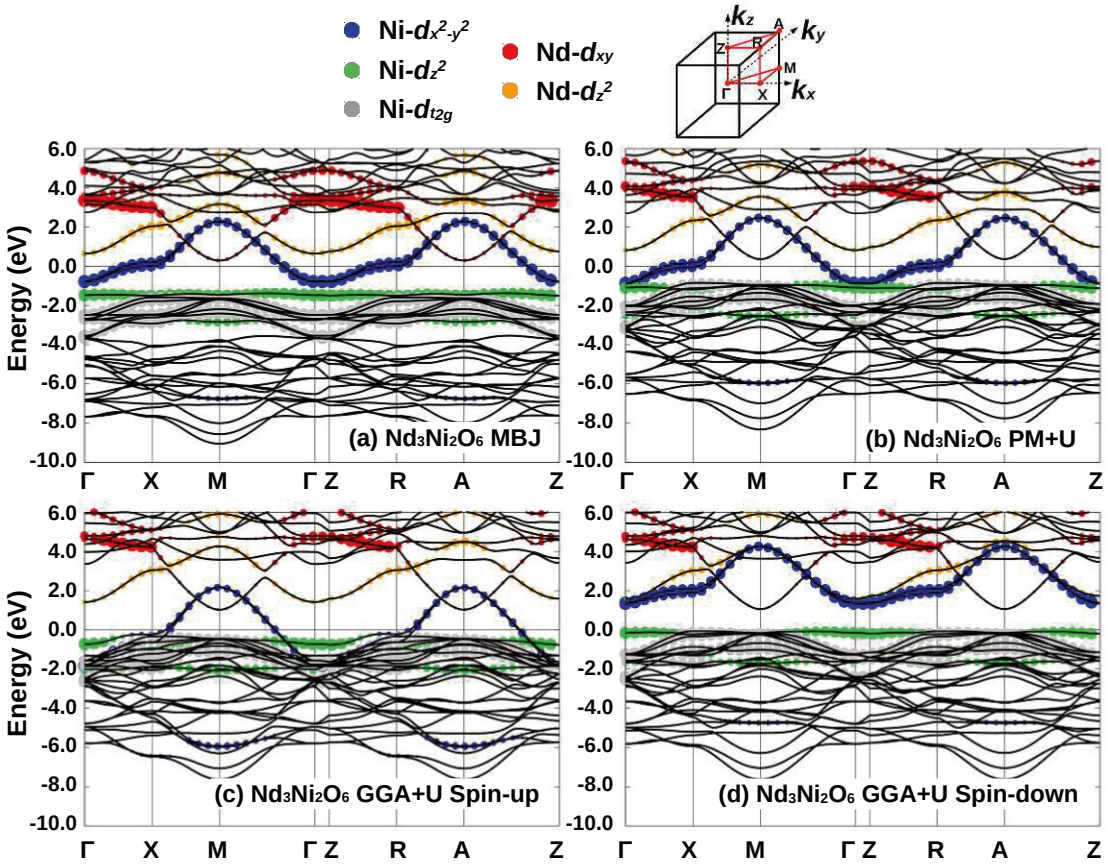

Figure A.3: DFT bandstructure calculations for $Nd_3Ni_2O_6$. (a) mBJ potential, (b) paramagnetic DFT+U and (c,d) spin-polarised DFT+U for spin (up,down).

Die approbierte gedruckte Originalversion dieser Dissertation ist an der TU Wien Bibliothek verfügbar.
The approved original version of this doctoral thesis is available in print at TU Wien Bibliothek.
TU Bibliothek Your knowledge hub WIEN

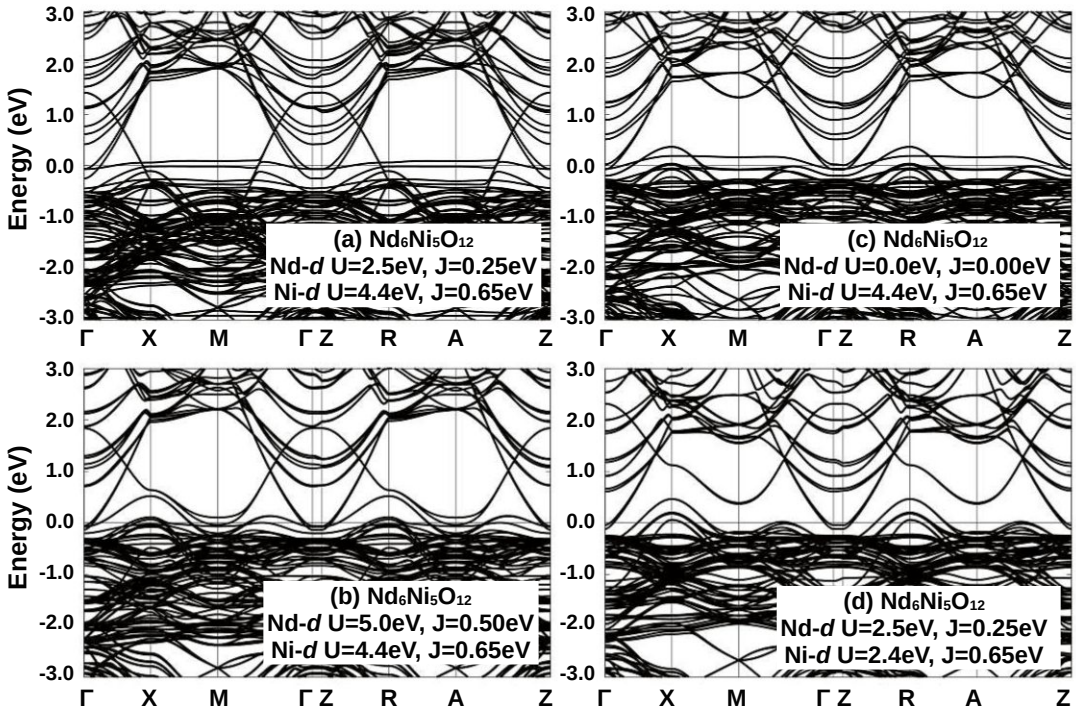

Figure A.4: Antiferromagnetic (AFM) DFT+U bandstructure calculations for $Nd_6Ni_5O_{12}$. (a) cRPA U=2.5 eV, J=0.25 eV for Nd-5d and cRPA U=4.4 eV, J=0.65 eV for Ni-3d; (b) enhanced U=5.0 eV, J=0.50 eV for Nd-5d and cRPA U=4.4 eV, J=0.65 eV for Ni-3d; (c) U=0.0 eV, J=0.00 eV for Nd-5d and cRPA U=4.4 eV, J=0.65 eV for Ni-3d; (d) cRPA U=2.5 eV, J=0.25 eV for Nd-5d and reduced U=2.4 eV, J=0.65 eV for Ni-3d.

A.1.4 Wannier projections

In this section of the supplementary material we provide additional information concerning the Wannier projection of the main text. Specifically, we use the following Wannier projections: (i) projection of the full d-shell for Ni and Nd ($Nd_6Ni_5O_{12}$) and Ni-d only ($Nd_3Ni_2O_6$); (ii) projection onto the Ni $3d_{x^2-y^2}$ bands only. We use the $d_{x^2-y^2}$-only projection as basis for our single-band low-energy effective Hamiltonian. Such a Ni $d_{x^2-y^2}$-only projection reproduces the corresponding DFT bands well (Fig. A.5), hence justifying our single-band per layer approximation. Fig. A.5 displays both the DFT bands (black lines), as well as the tight-binding bands from the Wannier projection. The full-d projection is displayed in red and the $d_{x^2-y^2}$-only one in blue, respectively. The energy windows of DFT bands for Wannier projections are set as: -1.0 eV to 3.0 eV, -3.0 eV to 3.0 eV, -1.5 eV to 2.5 eV and -3.0 eV to 8.0 eV for $Nd_3Ni_2O_6$ $d_{x^2-y^2}$ only, $Nd_3Ni_2O_6$ Ni-d, $Nd_6Ni_5O_{12}$ $d_{x^2-y^2}$ only, and $Nd_6Ni_5O_{12}$ Nd-d+Ni-d projections. The agreement between DFT and Wannier bands is remarkable for both $d_{x^2-y^2}$, Ni-d and Nd-d+Ni-d projections, even for bands with a van-Hove singularity around the Fermi energy.

Die approbierte gedruckte Originalversion dieser Dissertation ist an der TU Wien Bibliothek verfügbar.
The approved original version of this doctoral thesis is available in print at TU Wien Bibliothek.
TU Bibliothek Your knowledge hub WIEN

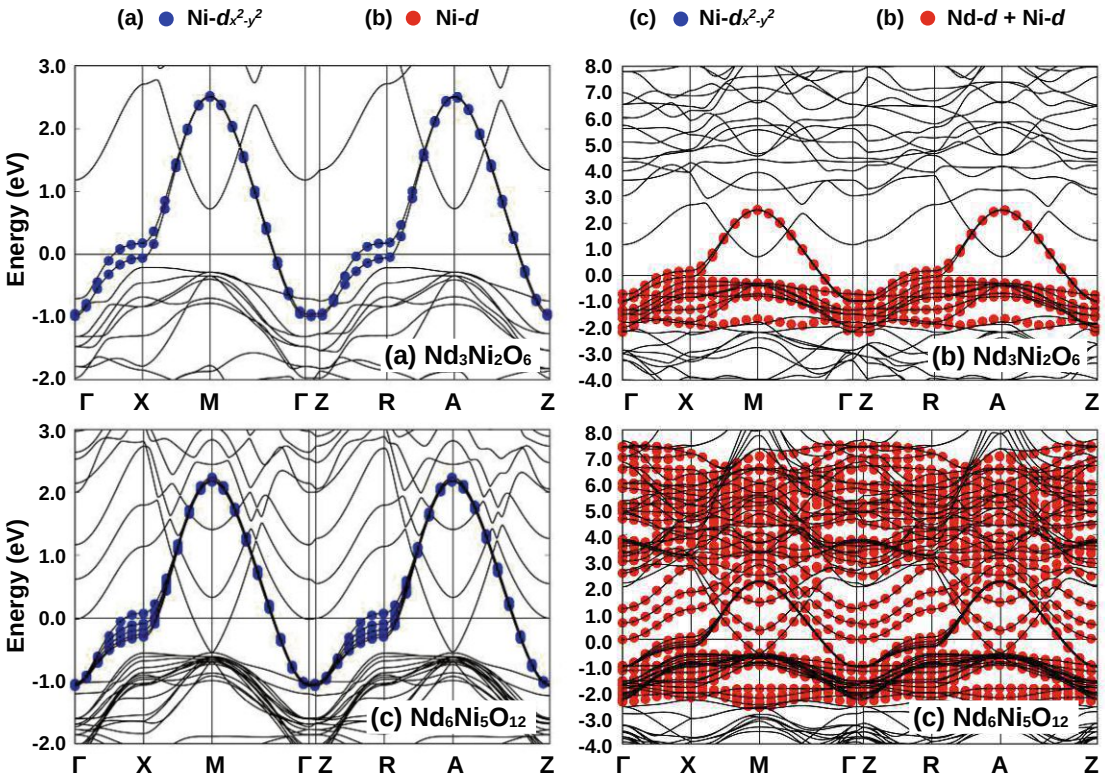

Figure A.5: DFT bands (black lines) and Wannier projection bands for the full d-shell (red, right) and the $d_{x^2-y^2}$ band only (blue, left), $Nd_3Ni_2O_6$ (a, b) and $Nd_6Ni_5O_{12}$ (c, d).

A.1.5 Orbital occupation

With the exception of the undoped bilayer system $Nd_3Ni_2O_6$ where also the Ni $3d_{xz/yz}$ bands form a quasiparticle peak at the Fermi energy, all nickelates considered only have one strongly correlated band crossing the Fermi energy: the Ni $3d_{x^2-y^2}$ band. In some cases there are additional pockets (bands) that are however only very weakly renormalized compared to the DFT bands. They also do not show a strong broadening nor any formation of (Hubbard) side peaks. This strongly suggests that strong correlations –and thus most likely the mechanism for high-temperature superconductivity– resides in these effective Ni $3d_{x^2-y^2}$ band. If pockets are present as e.g. for the infinite layer nickelate system, they do not hybridize with this Ni $3d_{x^2-y^2}$ band. All those reasons indicate that the minimal model for superconductivity is the effective Ni $3d_{x^2-y^2}$ band with an appropriate filling.

In the multi-orbital Hamiltonian, this *effective* single Ni $3d_{x^2-y^2}$ band is made up out of predominately Ni $3d_{x^2-y^2}$ character with some admixtures of the other Ni and Nd orbitals, due to hybridization effects. If we would include the oxygen p orbitals in the multi-orbital calculation they would also contribute to this band. Hybridization with orbitals lying in energy above the Ni $3d_{x^2-y^2}$ orbital such as the Nd states will decrease the occupation of the $3d_{x^2-y^2}$ orbital in the multi-orbital calculation, while hybridization

Die approbierte gedruckte Originalversion dieser Dissertation ist an der TU Wien Bibliothek verfügbar.
The approved original version of this doctoral thesis is available in print at TU Wien Bibliothek.
TU Bibliothek Your knowledge hub WIEN

with orbitals lying below such as the other Ni orbitals (or oxygen orbitals if included) will enhance the occupation of the Ni $3d_{x^2-y^2}$ orbital. If we consider a single-band effective low-energy Hamiltonian, such hybridization effects must not be included since it would give the wrong occupation of the *effective* orbital and the wrong Fermi surface.

On the other hand, all bands that are completely below (above) the Fermi energy are fully occupied (empty), and the occupation of the effective low-energy Hamiltonian is simply given by the electrons remaining after filling all orbitals below the Fermi energy. If there are, however, pockets present, which do not hybridize noticeable with the target band and are hence not included in the low-energy effective Hamiltonian, their occupation has to be accounted for.

For transition metal oxides, this procedure to set the orbital occupation of the effective orbitals is the established DFT+DMFT procedure for projections onto only the five d-orbitals or onto three t_{2g} or two e_g orbitals [26, 262]. In our case, the hybridization of the Ni $3d_{x^2-y^2}$ with the other Ni and Nd orbitals is rather weak so that the difference of the occupation of the $3d_{x^2-y^2}$ orbital in the calculation with all orbitals as employed in [50] and the occupation of the *effective* Ni $3d_{x^2-y^2}$ with all other orbitals filled or empty (except for pockets) is of only a few percent.

In the following we explicitly describe how we calculated the occupation of the *effective* single orbital Hamiltonian (Ni $3d_{x^2-y^2}$ orbital) using the latter procedure without the aforementioned hybridization effects.

In Table A.1 we list both the occupation as well as the quasi-particle weight as obtain within DFT and DFT+DMFT for the full calculation with all orbitals. Hybridization is clearly present within the Ni d-shell, as illustrated by the occupation of the Ni d_{z^2} orbital. This hybridization is not a consequence of correlations, but already present within DFT. For a comparison, we further list the layer dependent occupation for the $d_{x^2-y^2}$-only model in Table A.2 for different average occupations.

In the case, where pockets are present which do not hybridize with the correlated Ni $d_{x^2-y^2}$ and hence are not included in the DΓA calculation, the extraction of the correct filling becomes more involved. Below we outline the corresponding approach used for all compounds:

Occupation $Nd_6Ni_5O_{12}$

Once local correlations are taken into account the Nd derived pockets are shifted above the Fermi surface and can be considered as empty. Thus there is an average filling of 0.8 electrons per Ni layer for the effective $d_{x^2-y^2}$ orbitals in DMFT. For DFT, on the other hand, there is a pocket. Here, the occupation of the Ni $d_{x^2-y^2}$ orbitals has been obtained by adjusting the chemical potential of the $d_{x^2-y^2}$-only projection to lie on top of the full-d projection, and subsequently integrating the spectral function from $-10\,\mathrm{eV}$ to $0\,\mathrm{eV}$. Due to the presence of Nd derived pockets within DFT, this occupation is lower than 0.8 on average.

Die approbierte gedruckte Originalversion dieser Dissertation ist an der TU Wien Bibliothek verfügbar.
The approved original version of this doctoral thesis is available in print at TU Wien Bibliothek.
TU Bibliothek Your knowledge hub WIEN

Occupation $Sr_xNd_{1-x}NiO_2$

For the infinite layer case, we have employed for Fig. 4 of the main text and Fig. A.6, for consistency with the previously published phase diagram, the procedure of [50]. That is, the $d_{x^2-y^2}$ occupation from the DFT+DMFT calculation with all five Ni and five Nd d-orbitals has been used.

We further performed the following calculation of the orbtial occupation: First, we do a Wannier projection onto the Ni $d_{x^2-y^2}$, Nd d_{xy} and Nd d_{z^2} orbital, which do not hybridize notably. We then fix the position of the pocket bands to their respective location within the DMFT calculation and again integrate the resulting spectral function of the two pockets from $-10\,\mathrm{eV}$ to $0\,\mathrm{eV}$ to obtain the number of electrons in the pockets n_{pockets}. The occupation of the Ni $d_{x^2-y^2}$ orbital is then given by $1 - x - n_{\mathrm{pockets}}$. This is the only case, where we have to employ an approximation, namely that the shape of the pocket and its spectral weight do not change by electronic correlations. For the pocket this is indeed a good approximation. We also cross-checked our result by computing the DMFT Fermi-surface and using Luttinger's sum rule [249, 405, 406] to obtain the particle density.

The difference of these two variations to calculate the occupation of the $d_{x^2-y^2}$-orbital for subsequent single-orbital Hubbard model calculations is about 1% doping for $Sr_{0.2}Nd_{0.8}NiO_2$. We can consider this as the uncertainty in our calculations, it is of a similar magnitude as the differences between experimental and theoretical doping range in Fig. 5.13 of the main text. Let us also note that the new defect-free $Sr_xNd_{1-x}NiO_2$ films [59] have been grown on a (La,Sr)(Al,Ta)O_3 (LSAT) substrate with a slightly smaller lattice constant of $a = 3.868\,\text{Å}$ than the previously used [17, 293, 323] $SrTiO_3$ substrate with $a = 3.905\,\text{Å}$. This may also lead to some minor changes of the phase diagram.

Occupation $La_{2+\delta}Zr_{1-\delta}Ni_2O_6$

For $\delta = 0.4$ the pockets are pushed above the Fermi surface by local correlations within DMFT. Hence the corresponding filling is simply given by the nominal valence $3d^{9-\delta/2}$ ($3d^{8.8}$ when $\delta = 0.4$) and correspondingly the occupation of Ni $d_{x^2-y^2}$ is $n = 0.8$.

Die approbierte gedruckte Originalversion dieser Dissertation ist an der TU Wien Bibliothek verfügbar.
The approved original version of this doctoral thesis is available in print at TU Wien Bibliothek.

Table A.1: Full-d DMFT and DFT orbital-resolved occupation, renormalization factor Z, and effective mass m^*/m_b of Ni-$d_{x^2-y^2}$ Wannier orbital for the fully fledged calculation with all 3d-orbitals (and for the pentalyer and infinite layer Nd 5d orbitals).

System	Atom	n d_{xy}	n $d_{yz/xz}$	n $d_{x\check{s}-y\check{s}}$	n $d_{z\check{s}}$	n *total*	Z $d_{x^2-y^2}$	m^*/m_b
$NdNiO_2$	Nd	0.252	0.009	0.012	0.101	0.385		
(DMFT)	Ni	1.961	1.927	0.945	1.854	8.615	0.227	4.404
$Nd_{0.8}Sr_{0.2}NiO_2$	Nd	0.247	0.009	0.012	0.083	0.362		
(DMFT)	Ni	1.957	1.917	0.822	1.824	8.438	0.355	2.812
$Nd_3Ni_2O_6$ (n_d=8.5; DMFT)	Ni	1.994	1.850	0.824	1.980	8.500	0.348	2.867
$Nd_3Ni_2O_6$ (n_d=8.5; DFT)	Ni	2.000	1.995	0.534	1.977	8.500		
$Nd_3Ni_2O_6$ (n_d=8.8; DMFT)	Ni	1.995	1.990	0.836	1.987	8.800	0.327	3.061
$Nd_3Ni_2O_6$ (n_d=8.8; DFT)	Ni	2.000	1.997	0.814	1.992	8.800		
$Nd_6Ni_5O_{12}$	Nd-1	0.212	0.009	0.011	0.067	0.310		
(DMFT)	Nd-2	0.248	0.016	0.010	0.083	0.375		
	Nd-3	0.041	0.011	0.003	0.016	0.083		
	Ni-1	1.965	1.929	0.828	1.835	8.488	0.351	2.844
	Ni-2	1.966	1.929	0.821	1.849	8.496	0.352	2.838
	Ni-3	1.966	1.929	0.848	1.823	8.497	0.333	2.997
$Nd_6Ni_5O_{12}$	Nd-1	0.275	0.012	0.015	0.095	0.410		
(DFT)	Nd-2	0.315	0.022	0.014	0.114	0.487		
	Nd-3	0.066	0.016	0.004	0.025	0.128		
	Ni-1	1.958	1.921	0.773	1.805	8.380		
	Ni-2	1.960	1.919	0.762	1.828	8.388		
	Ni-3	1.960	1.920	0.806	1.789	8.395		

Table A.2: DMFT occupation of the Ni 3 $d_{x^2-y^2}$ orbital of $Nd_6Ni_5O_{12}$, for a projection on only the Ni-$d_{x^2-y^2}$ band.

occupation	0.75	0.8	0.82	0.83	0.84	0.85	0.9	0.95	1
Ni-1 (center)	0.746	0.801	0.817	0.829	0.841	0.851	0.9	0.95	1.004
Ni-2 (middle)	0.739	0.791	0.812	0.823	0.832	0.843	0.891	0.941	0.994
Ni-3 (outer)	0.764	0.808	0.827	0.838	0.847	0.857	0.91	0.958	1.004

A.1.6 Effective mass

DMFT allows us to compute the mass renormalization created by local correlations. As discussed in the main text, the quasi-particle weight Z and thus also the effective mass $m^*/m_b = 1/Z$ are quite similar for the infinite layer and the pentalayer compound. We display this effective mass m^*/m_b as a function of the occupation in the Ni $d_{x^2-y^2}$ orbital

Die approbierte gedruckte Originalversion dieser Dissertation ist an der TU Wien Bibliothek verfügbar.
The approved original version of this doctoral thesis is available in print at TU Wien Bibliothek.

in Fig. A.6 for all systems considered in the main text and the strontium doped infinite layer nickelate from [50]. In case of the pentalayer system we display the values for the layer at the center, but the ratio between m^*/m_b and occupation is almost the same for all layers. We find it quite remarkable, that both known superconducting nickelates (the doped infinite layer and the quintuple layer) exhibit almost the same effective mass $m^*/m_b \sim 2.85$ at the same Ni $3d_{x^2-y^2}$ occupation. $La_{2+\delta}Zr_{1-\delta}Ni_2O_6$ shows both qualitatively and quantitatively a similar mass renormalization as the superconducting compounds. We believe this to be one indication for the possibility of superconductivity in $La_{2+\delta}Zr_{1-\delta}Ni_2O_6$.

Let us also emphasize that the mass renormalization in the fully fledged calculation with all d-orbitals in Table A.1 are quite similar to that in the projection onto a single Ni $3d_{x^2-y^2}$ band in Table A.3.

Table A.3: DMFT quasi-particle renormalization Z of the $d_{x^2-y^2}$ orbital of $Nd_6Ni_5O_{12}$, for a projection on only the Ni-$d_{x^2-y^2}$ band.

occupation	0.75	0.8	0.82	0.83	0.84	0.85	0.9	0.95	1
Ni-1 (center)	0.443	0.393	0.378	0.368	0.356	0.348	0.306	0.274	0.281
Ni-2 (middle)	0.452	0.402	0.383	0.373	0.365	0.355	0.314	0.281	0.281
Ni-3 (outer)	0.427	0.385	0.367	0.357	0.349	0.34	0.296	0.266	0.275

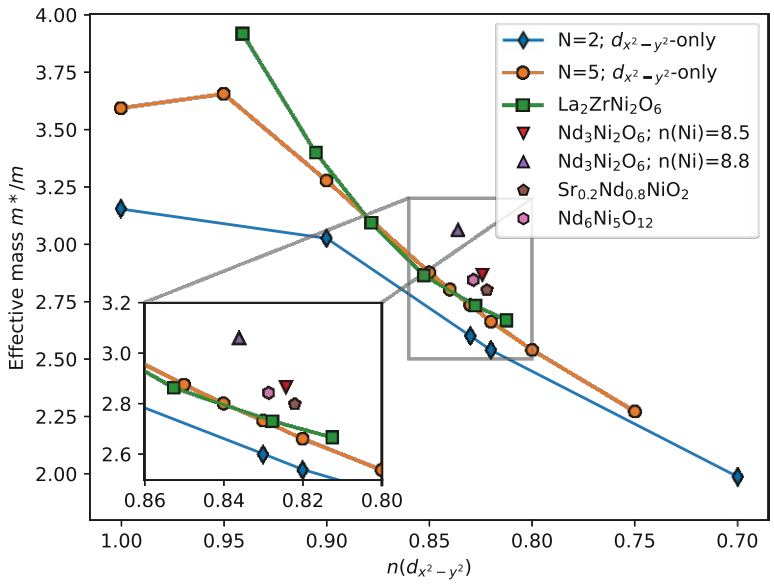

Figure A.6: Effective mass m^*/m_b as a function of the occupation of the Ni $d_{x^2-y^2}$ orbital for all systems considered. For comparison we also included the values for the infinite layer nickelate from Ref. [50].

A.1.7 DMFT spectral function

In the main text we presented the k-resolved (integrated) spectral function $A(k,\omega)$ ($A(\omega)$) for the bilayer in Fig. 2 and the pentalayer compound in Fig. 3. This section

Die approbierte gedruckte Originalversion dieser Dissertation ist an der TU Wien Bibliothek verfügbar.
The approved original version of this doctoral thesis is available in print at TU Wien Bibliothek.

supplements these results, by also providing said quantities for (i) the bilayer system at a different filling (n(Ni)=8.8) to simulate electron doping effect, (ii) the bilayer system, but for the $d_{x^2-y^2}$ only projection at n=0.8 and (iii) the quintuple layer system but for the $d_{x^2-y^2}$ only projection.

Information (i) is displayed in Fig. A.7(a)-(b) and shows two interesting features compared to the undoped (n(Ni)=8.5) case as discussed in the main text: First, the $d_{xz/yz}$ orbital is fully occupied and pushed below the Fermi surface, hence recovering the one-band physics. Second, the quasipartilce weight $Z = 0.326$ is comparable to the superconducting compounds as displayed in Fig. A.6. Thus we conclude, that the doped bilayer $Nd_3Ni_2O_6$ compound falls much more into the paradigm of known nickelate superconductors. In section A.1.10 we will propose $La_{2+\delta}Zr_{1-\delta}Ni_2O_6$ as promising candidate compound to achieve such a doping in a bilayer system.

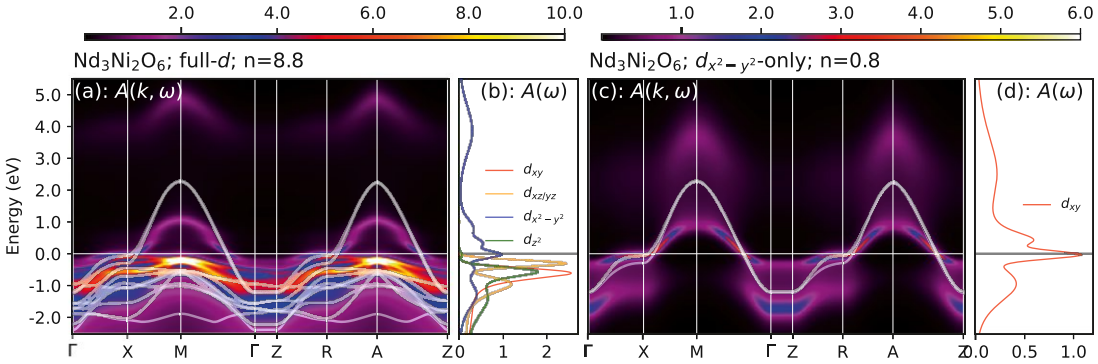

Figure A.7: (a) DMFT k-resolved spectral functions $A(k,\omega)$ of $Nd_3Ni_2O_6$. (b) k-integrate spectral function $A(\omega)$. Solid lines in (a) are DFT Wannier-bands. The average occupation per nickel site is n =8.8. The $d_{xz/yz}$ orbital is below the Fermi energy in contrast to n =8.5 from the main text.

Information (ii) is displayed in Fig.A.7(c)-(d) for completeness. The comparison to Fig. A.7(a)-(b) shows that a one-orbital description is possible at this doping level.

Information (iii) is displayed in Fig. A.8(b) and highlight how DMFT suppresses layer dependent physics. Not only do local correlations lead to a more uniform occupation, also the k-integrated spectral function $A(\omega)$ is quite similar for all layers in Fig. A.8(a). The most notable differences is (i) that the upper Hubbard band is more spread out in the full-d projection and (ii) that there is additional structure in the low-frequency part of the $d_{x^2-y^2}$-only projection. Both differences can partially be attributed to the analytic continuation. We used more statistic for the $d_{x^2-y^2}$-only projection since it contains fewer bands and is thus numerically less demanding. In turn there is less noise and more features can be resolved by the maximum entropy method. To compare this we show analytic continuation for the $d_{x^2-y^2}$-only projection, but with a higher α in the MaxEnt code for the $d_{x^2-y^2}$-only projection in Fig.A.8(c), which leads to broader features and better agreement with the calculation including all five Ni orbitals. Nevertheless, while the position of the upper Hubbard band peak depends on the MaxEnt parameters, it's weight and center of mass does not in a significant way. The corresponding spectral

Die approbierte gedruckte Originalversion dieser Dissertation ist an der TU Wien Bibliothek verfügbar.
The approved original version of this doctoral thesis is available in print at TU Wien Bibliothek.
TU Bibliothek Your knowledge hub WIEN

weights w_{uhb} and center of masses c_{uhb} are $\{w_{uhb} = 1.48, c_{uhb} = 3.3\}$ for the $d_{x^2-y^2}$-only and $\{w_{uhb} = 1.55, c_{uhb} = 4.0\}$ for the full-d projection.

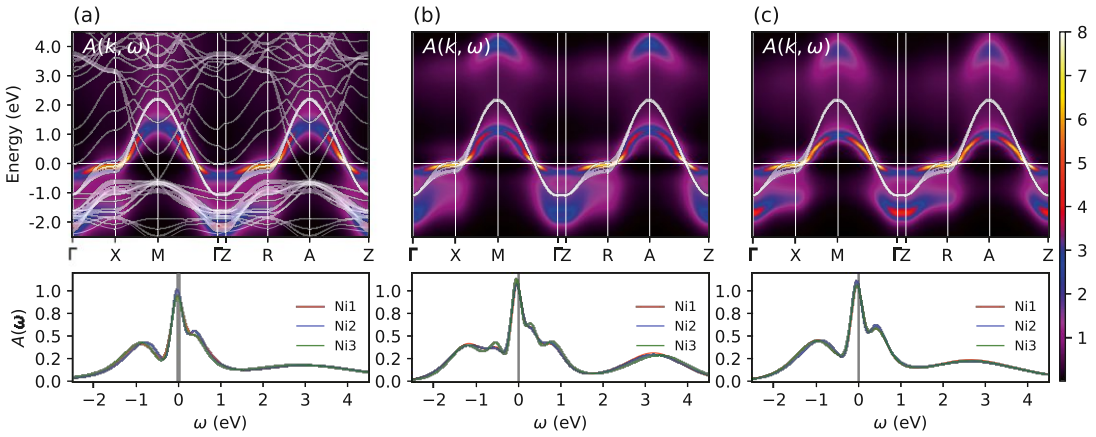

Figure A.8: DMFT k-resolved spectral functions $A(k, \omega)$ of $Nd_6Ni_5O_{12}$ (top) and k-integral $A(\omega)$ (bottom). (a) Ni $d_{x^2-y^2}$ orbital from full-d projection. (b) *effective* Ni $d_{x^2-y^2}$ orbital from $d_{x^2-y^2}$-only projection. (c) same as (b), but with a larger α for the analytic continuation.

A.1.8 Fermi surface

Since superconductivity is a low-temperature phenomenon it is most strongly influenced, if not dominated by, low-energy excitations. Hence, a lot of the system can be learned by looking at the Fermi surface, or, for finite temperatures, at the spectral function around zero energy. For simplicity we will refer to both concepts just as Fermi surface. Fig. A.9(d) displays the Fermi surface for the $Nd_6Ni_5O_{12}$ system within the DFT framework (top) and DFT+DMFT (bottom). The DFT solution still has pockets from the Nd atoms around the $\Gamma = [0, 0, 0]$ and a tube-like pocket extending around the $M = [\pi, \pi, 0]$ to the $A = [\pi, \pi, \pi]$ point. To better visualize these pockets (tubes) we also plotted the DFT Fermi-surface in a 3D fashion in Fig. A.10(a) using the Xcrysden program package [350] together with the DFT Fermi-surface of $NdNiO_2$ (b)-(c). These are, however, pushed above the Fermi surface once local correlations are included with the DMFT framework. Another point worth mentioning is the appearance of one electron-like Fermi surface and four hole-like ones, which is due to one of the five Wannier bands of the pentalayer having its van Hove singularities at $(0, \pm\pi)$, $(\pm\pi, 0)$ above the Fermi-energy (see also discussion in Section A.1.4). However, there exists no assignment of these different Fermi surfaces to a single layer; each layer contains a superposition of them all.

When discussing $Nd_3Ni_2O_6$ in the main text (Fig. 2) one feature emerging from local correlations was the $d_{xz/yz}$ orbital contribution to the Fermi surface predominantly at the M-point. In Fig. A.9(b) we display this effect by showing the system's DMFT Fermi surface. Notice, that in DFT (top) the holes reside in the $d_{x^2-y^2}$ orbital only. The recovery of a $d_{x^2-y^2}$ only Fermi surface via electron doping to n(Ni)=8.8 is displayed in Fig. A.9(c).

Die approbierte gedruckte Originalversion dieser Dissertation ist an der TU Wien Bibliothek verfügbar.
The approved original version of this doctoral thesis is available in print at TU Wien Bibliothek.
TU Bibliothek Your knowledge hub WIEN

In the main text we estimated T_c from an effective one-band model, whose Wannier projection was discussed in Section A.1.4. Here we show the corresponding Fermi surface for the $Nd_6Ni_5O_{12}$ and the $Nd_3Ni_2O_6$ system at an average $d_{x^2-y^2}$ occupation of 0.80 in Fig. A.9(d) and Fig. A.9(a), respectively.

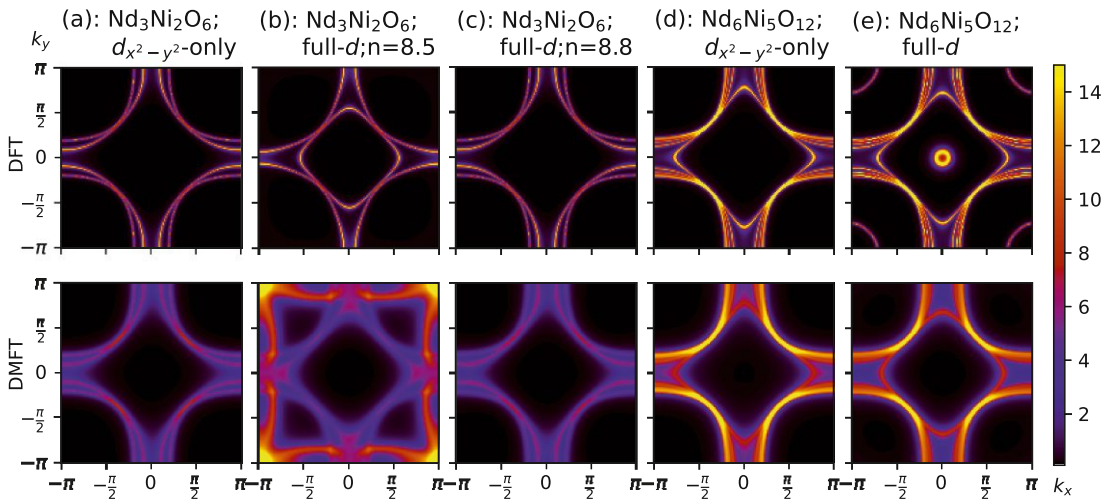

Figure A.9: Fermi surface for the DFT solution (top) and for DFT+DMFT (bottom). (a) $Nd_3Ni_2O_6$ for the $d_{x^2-y^2}$-only projection and average occupation per layer $n = 0.8$. (b) $Nd_3Ni_2O_6$ for the full-d projection and a total of 8.5 electrons. (c) same as (b) but for 8.8 electrons. (d) $Nd_6Ni_5O_{12}$ for the $d_{x^2-y^2}$-only projection and average occupation per layer $n = 0.8$. (e) $Nd_6Ni_5O_{12}$ for the full-d projection. Notice how the pockets are shifted above the Fermi surface once local correlations are taken into account in (e) [same as Fig. 3 (e,f) of the main paper, re-plotted here for better comparison].

Die approbierte gedruckte Originalversion dieser Dissertation ist an der TU Wien Bibliothek verfügbar.
The approved original version of this doctoral thesis is available in print at TU Wien Bibliothek.

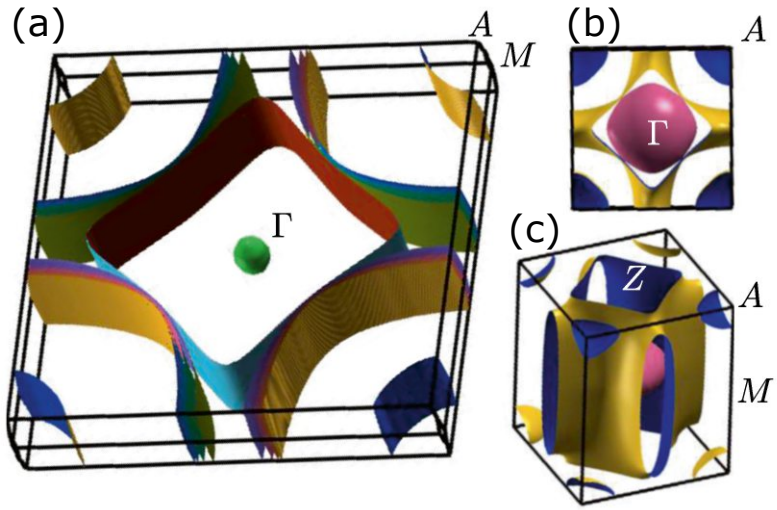

Figure A.10: (a) $Nd_6Ni_5O_{12}$ Fermi surface for the DFT solution within the 1st BZ. The pocket at the Γ-point and the small tube around the A and M point are derived from Nd-d orbitals, while the five large sheets derive from the Ni $d_{x^2-y^2}$ orbitals. (b) $NdNiO_2$ DFT Fermi surface top view and (c) side view. For this compound, the pocket at Γ-point is much more pronounced and the second pocket is only around the A-point.

A.1.9 DMFT self-energy

We further show the layer-averaged self-energy for the pentalayer compound in Fig. A.11. The slope of $\mathrm{Re}\,\Sigma$ vs. ω in Fig. A.11 (a) or that of $\mathrm{Im}\,\Sigma$ vs. $i\omega_n$ in Fig. A.11 (d) determines the quasiparticle renormalization $m^*/m = 1 - \partial\,\mathrm{Re}\,\Sigma(\omega)/\partial\omega|_{\omega=0}$. It is much larger $m^*/m \approx 3$ for the $d_{x^2-y^2}$-orbital (cf. in Table A.1) than for the other orbitals where $m^*/m \sim 1.3$. The scattering rate or (inverse) life time is in turn given by $\mathrm{Im}\,\Sigma(\omega)$ in Fig. A.11 (b). It shows strong scattering rates in the Hubbard bands. Note, only the $d_{x^2-y^2}$-orbital has an upper Hubbard band, there are no states and no scattering rate above E_F for the other orbitals.

While finite life time effects are obviously absent in a static, e.g. Hartree-Fock, kind of description, also the real part evades such an approximation. The Hartree-Fock self-energy corresponds to the large ω limit of the DMFT self-energy. For such large ω's, the self-energy for the $d_{x^2-y^2}$-orbital is larger than that of the other orbitals in Fig. A.11 (c). However, around the Fermi energy it is just vice versa. The same can be seen in Fig. A.11 (a) when comparing the $\nu = 0$ and $\nu \to \pm\infty$ behavior. Altogether this shows that the DMFT self-energy evades an approximate description by a static self-energy; its dynamics (frequency dependence) is dominating.

Die approbierte gedruckte Originalversion dieser Dissertation ist an der TU Wien Bibliothek verfügbar.
The approved original version of this doctoral thesis is available in print at TU Wien Bibliothek.
TU Bibliothek Your knowledge hub WIEN

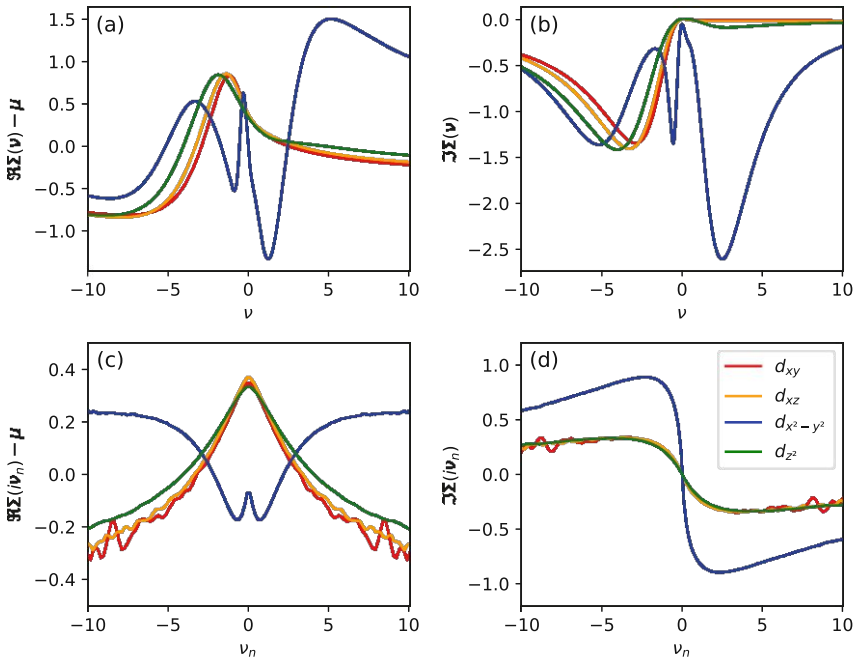

Figure A.11: Layer-averaged self-energy of the five Ni d-orbitals for $Nd_6Ni_5O_{12}$ in units of eV. Left: real part; right: imaginary part. Top: analytic continuation to real frequencies using the maximum entropy method; bottom: self-energy as a function of Matsubara frequencies.

A.1.10 The bilayer nickelate $La_2ZrNi_2O_6$

In the main text we discussed the possibility to engineer a superconducting bilayer nickelate compound. Given the results of Fig. A.14(b), one promising candidate for a nickelate superconductor is $La_{2+\delta}Zr_{1-\delta}Ni_2O_6$ for $\delta = 0.4$. In Fig. A.12 we display the orbital character of the Ni d-shell Wannier projection for the parent compound (100% Zr doping: left) and at 40% Zr doping (right). Wannier projection of the Zr d-shell is not shown here for clarity, but instead as white lines in Fig. A.13 on top of the DFT+DMFT k-resolved spectral function. For 40% Zr doping the disappearance of the pockets due to local correlations is clearly shown in Fig. A.13(c,d). This is further emphasised by the Fermi surface plots in Fig. A.14(a) for the undoped and Fig. A.14(b) for the doped compound.

Die approbierte gedruckte Originalversion dieser Dissertation ist an der TU Wien Bibliothek verfügbar.
The approved original version of this doctoral thesis is available in print at TU Wien Bibliothek.

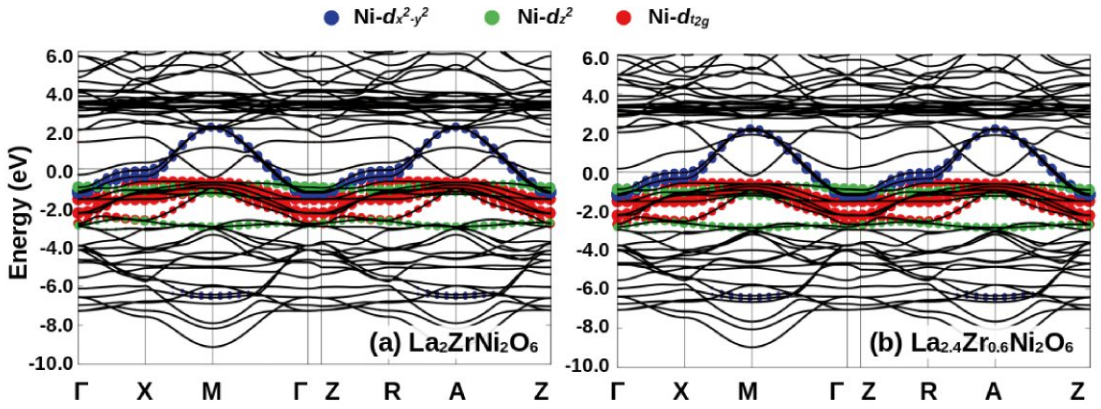

Figure A.12: DFT bands (black lines) and orbital character as indicated by color. (a) $La_2ZrNi_2O_6$ and (b) $La_{2.4}Zr_{0.6}Ni_2O_6$

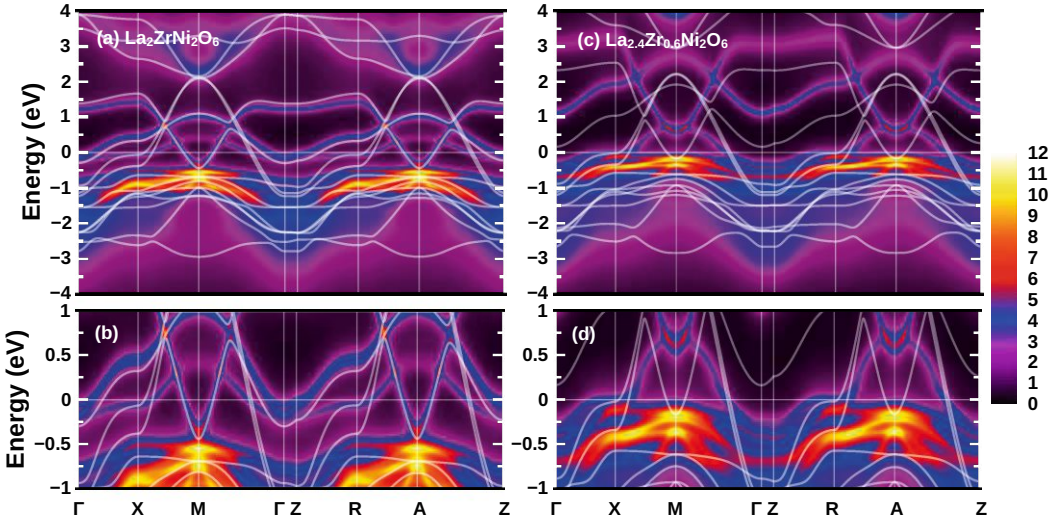

Figure A.13: DMFT k-resolved spectral function $A(\omega, k)$ for $La_2ZrNi_2O_6$ (a) and $La_{2.4}Zr_{0.6}Ni_2O_6$ (c). White lines correspond to the DFT Wannier bands. Bottom displays a zoom-in around the Fermi energy of the corresponding plot in the top.

Die approbierte gedruckte Originalversion dieser Dissertation ist an der TU Wien Bibliothek verfügbar.
The approved original version of this doctoral thesis is available in print at TU Wien Bibliothek.

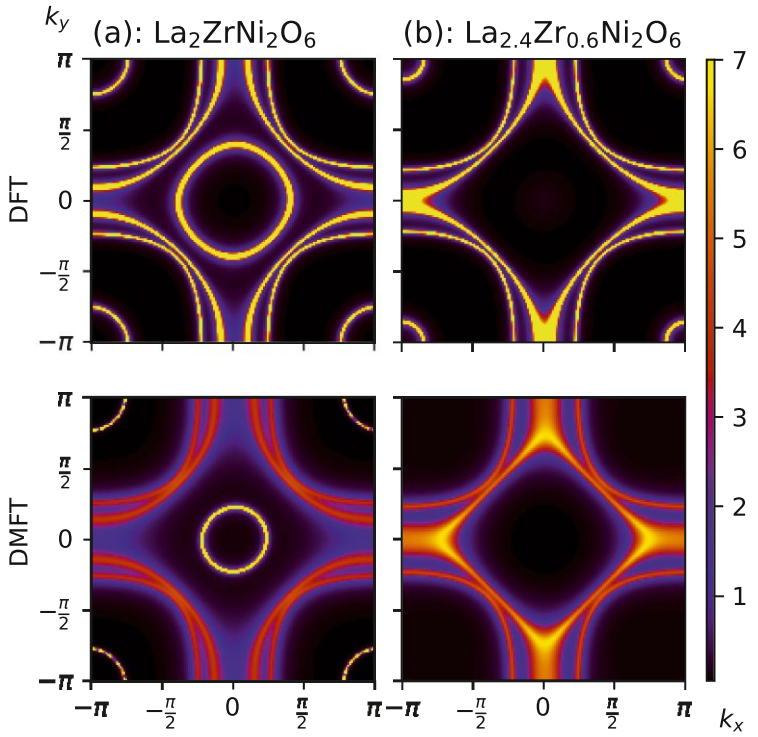

Figure A.14: Fermi surface for (a) $La_2ZrNi_2O_6$ and (b) $La_{2.4}Zr_{0.6}Ni_2O_6$, as obtained from the DFT Wannier projection (top) and DFT+DMFT (bottom).

Die approbierte gedruckte Originalversion dieser Dissertation ist an der TU Wien Bibliothek verfügbar.
The approved original version of this doctoral thesis is available in print at TU Wien Bibliothek.

A.2 Supplemental Material: Ba_2CuO_4

This Supplementary Material presents additional DFT and DMFT results supporting our conclusions in the main text. Additionally details on our computational methods are also provided. Specifically, additional information on different structures and details on the optimization procedure are included in Section A.2.1. Partial density of states for the structures discussed in the main text are provided in Section A.2.2. Section A.2.3 contains details on the Wannier function projection as well as plots to highlight the quality of our effective low-energy model. Details on the computation of interaction parameters are contained in Section A.2.4. We also list details of the DMFT calculation in Section A.2.5 and display the k-resolved spectral function in combination with the DFT bands. Finally, we compute the phonon dispersion of bilayer $Ba_2CuO_{3.25}$ supercell, demonstrating its dynamical stability in A.2.6.

A.2.1 DFT structure optimization

Structural optimization discussed in the main text has been performed within the density-functional theory (DFT) framework as a 2×2×1 supercell calculation with the Vienna *ab initio* simulation package `Vasp` [268, 269] code package using the Perdew-Burke-Ernzerhof version of the generalized gradient approximation (GGA-PBE) [49]. Results have been cross-validated with the `WIEN2K` [55, 263] code. We considered 29 different possible structures, whose energies are listed in Table A.4 and Table A.5 together with the corresponding names used in [255, 259, 407]. Crystal structures are displayed in Fig. A.15. To determine the energy, we used two procedures: (1) allow relaxation for both lattice constants and all internal atomic positions; (2) only atomic positions are allowed to relax, while fixing lattices parameters to the experimental values of Ref.[253]. Results of these two structural optimization procedures are shown in Table A.4 and Table A.5, respectively. The former approach was used in Ref.[407] while the later one was done in Ref. [255]. Crucially, both procedures yielded structure No. 25 as the energetically most favourable one, consistent with Ref. [255] where it is called 64-1*.

Die approbierte gedruckte Originalversion dieser Dissertation ist an der TU Wien Bibliothek verfügbar.
The approved original version of this doctoral thesis is available in print at TU Wien Bibliothek.

Table A.4: Relative DFT-PBE calculated total energy of fully relaxed structures of all considered possible phases of 2×2×1 supercells of $Ba_2CuO_{3.25}$ that contains 16 Ba atoms, 8 Cu atoms and 26 O atoms [in the unit of eV, the total energy of phase-2 ("BaO-2" as named in Ref.[255]) is set as zero]. Beside the 26 possible phases in [255], we also consider the Lieb-type phase proposed by [259], and the "monolayer" and "brickwall" phases in [407]. The structural parameters of "monolayer" phase are adopted from Ref. [407], whose total energy is ∼70 meV higher than that of bilayer (No. 25), being consistent with Ref. [407]. For "Lieb" structure, the supercell is composed by a Lieb-type Ba_2CuO_3 layer and a $Ba_2CuO_{3.5}$ layer that contains octahedron CuO_4 and CuO_3 1D chain, as shown in Fig. A.15. The second row contains the corresponding names of the Ref.[255, 259, 407].

Structure	No. 1	2	3	4	5	6	7
Ref. names	BaO-1	BaO-2	82-1	82-2	82-3	73-1	73-2
Rel. energy [eV]	-1.209	0.000	-5.091	-4.437	-4.490	-5.763	-5.947
Structure	8	9	10	11	12	13	14
Ref. names	64-2	64-3	64-4	64-5	64-6	55-1	55-2
Rel. energy [eV]	-6.692	-6.808	-6.898	-6.807	-6.435	-7.030	-7.364 3
Structure	15	16	17	18	19	20	21
Ref. names	55-3	55-4	64-3*	64-4*	64-5*	64-6*	55-1*
Rel. energy [eV]	-7.031	-6.939	-6.772	-7.319	-7.006	-6.64	-7.437
22	23	24	25	26	27	28	29
55-2*	55-3*	55-4*	64-1*	64-1	Lieb	monolayer	brickwall
-7.364	-7.420	-7.366	**-8.136**	-7.553	-7.774	-8.064	-6.490

Table A.5: Relative DFT-PBE calculated total energy with fixed experimental lattice constants of all considered possible phases of 2×2×1 supercells of $Ba_2CuO_{3.25}$ that contains 16 Ba atoms, 8 Cu atoms and 26 O atoms [in the unit of eV, the total energy of phase-2 ("BaO-2" as named in Ref.[255]) is set as zero]. The structural parameters of "monolayer" phase is adopted from Ref.[407]. The second row contains the corresponding names of the Ref.[255, 259, 407].

Struct.	No. 1	2	3	4	5	6	7	8
Ref. n.	BaO-1	BaO-2	82-1	82-2	82-3	73-1	73-2	64-2
R.e. [eV]	-1.515	0.000	-6.121	-5.301	-5.380	-6.783	-6.755	-7.289
Struct.	9	10	11	12	13	14	15	16
Ref. n.	64-3	64-4	64-5	64-6	55-1	55-2	55-3	55-4
R.e. [eV]	-7.892	-7.812	-7.642	-7.119	-8.183	-8.107	-8.183	-8.075
Struct.	17	18	19	20	21	22	23	24
Ref. n.	64-3*	64-4*	64-5*	64-6*	55-1*	55-2*	55-3*	55-4*
R.e. [eV]	-7.880	-7.794	-7.665	-7.179	-8.032	-7.917	-8.005	-7.949
Struct.	25	26	27	28	29	-	-	-
Ref. n.	64-1*	64-1	Lieb	monolayer	brickwall	-	-	-
R.e. [eV]	**-8.771**	-8.762	-8.564	-7.025	-7.540	-	-	-

Die approbierte gedruckte Originalversion dieser Dissertation ist an der TU Wien Bibliothek verfügbar.
The approved original version of this doctoral thesis is available in print at TU Wien Bibliothek.
TU Bibliothek Your knowledge hub WIEN

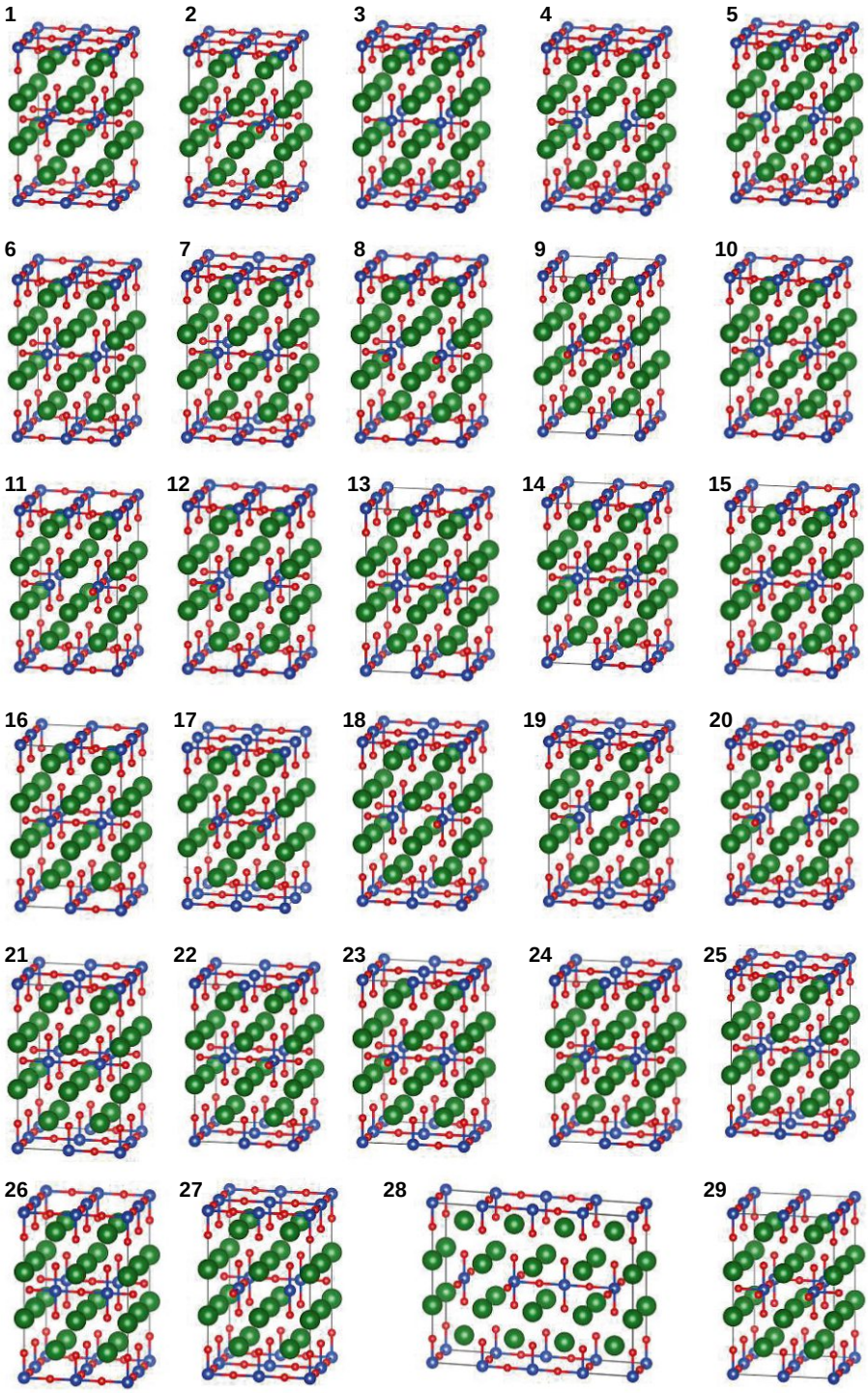

Figure A.15: 29 possible structures of 2×2×1 supercell of $Ba_2CuO_{3.25}$. The green, blue, and red balls represent the Ba, Cu, and O atoms, respectively.

Die approbierte gedruckte Originalversion dieser Dissertation ist an der TU Wien Bibliothek verfügbar.
The approved original version of this doctoral thesis is available in print at TU Wien Bibliothek.
TU Bibliothek Your knowledge hub WIEN

A.2.2 DFT density of states

In the main text we employ a minimal model for $Ba_2CuO_{3.25}$ 2×2×1 supercell, instead of the full d-shell for dynamical mean-field theory (DMFT) calculations, since the e_g orbitals are well separated from the fully occupied t_{2g} bands which are considered as unimportant bystanders for the emergence of superconductivity. Please note that in the DFT and DMFT calculations we reduced the 2×2×1 supercell of $Ba_2CuO_{3.25}$ (No. 25 in Table A.4) to a 1×2×1 one as shown in Fig. 1(c) of the main text. This is because No. 25 phase (as shown in Fig. A.15) is doubly repeated along a direction and with this reduction/simplification the computational efforts can be remarkably reduced. Furthermore, the bands in Wannier projections were also reduced by a factor of 2. We show here in Fig.A.16 the DFT density of states (DOS) for the full d-shell of all in-equivalent Cu sites discussed in the main text. As one can observe, the t_{2g} orbitals are well separated from the partially occupied e_g orbitals which we used to construct our low-energy effective model.

Our effective low-energy model from the main text did not take oxygen degrees of freedom explicitly into account, but rather included them effectively via their strong hybridization. Fig. A.17 displays the partial DOS of the d-shell and the oxygen ligands for all three structures discussed. We also included the same plot for the cuprate superconductor $CaCuO_2$ as reference in Fig. A.17(d). The comparison between Ba_2CuO_3 and $CaCuO_2$ indicates their degrees of d-p hybridization around Fermi energy are almost the same, proving the effectiveness of our minimal single-band model for Ba_2CuO_3 and $CaCuO_2$.

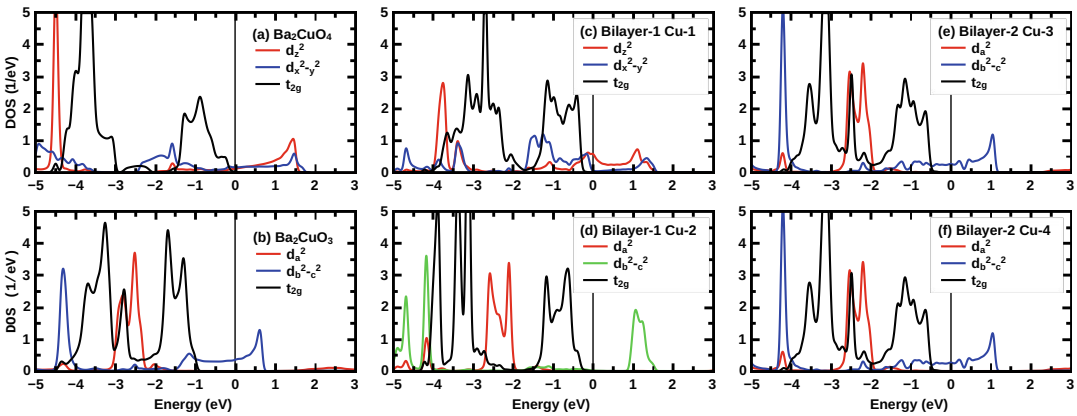

Figure A.16: DOS of the full d-shell for (a) Ba_2CuO_4, (b) Ba_2CuO_3, and for $Ba_2CuO_{3.25}$: (c) Cu-1, (d) Cu-2, (e) Cu-3 and (f) Cu-4. The Cu-3 (e) is same as Cu-4 (f) as protected by crystal symmetry.

Die approbierte gedruckte Originalversion dieser Dissertation ist an der TU Wien Bibliothek verfügbar.
The approved original version of this doctoral thesis is available in print at TU Wien Bibliothek.

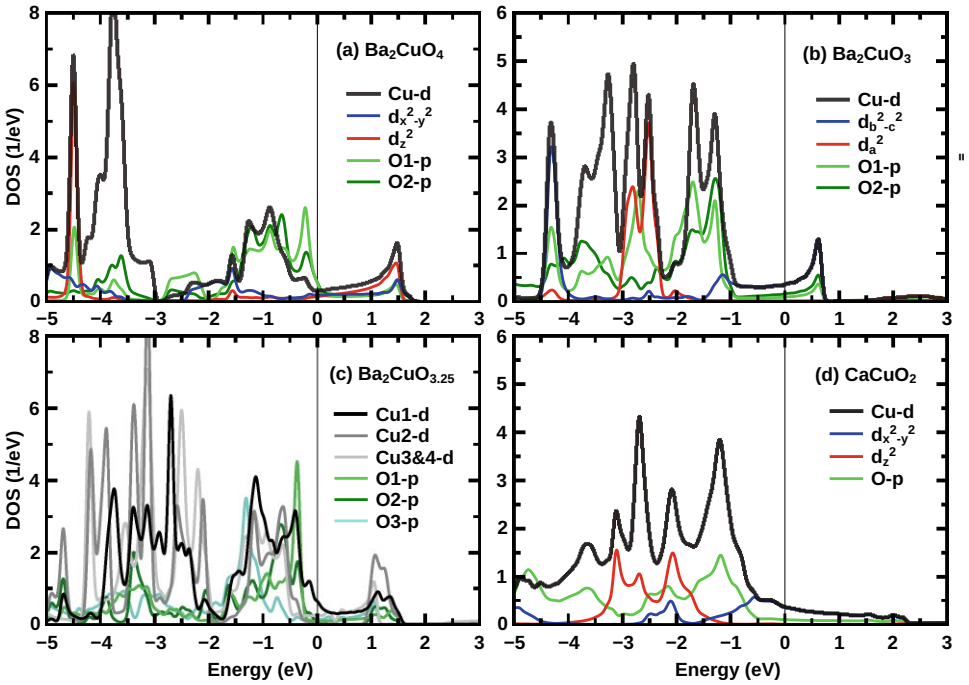

Figure A.17: Partial DOS of the d-shells and all the inequivalent oxygen ligands. (a) Ba_2CuO_4, (b) Ba_2CuO_3, (c) $Ba_2CuO_{3.25}$ and (d) $CaCuO_2$.

A.2.3 Wannier Function Projection

To construct the effective low-energy model Hamiltonian, the WIEN2K DFT bands around the Fermi level are projected onto maximally localized Wannier functions using the WANNIER90 [67, 74, 266] and WIEN2WANNIER [77] codes. Energy windows of DFT bands in the Wannier projections for the three structures discussed in main text Ba_2CuO_4, Ba_2CuO_3 and $Ba_2CuO_{3.25}$ are -3.00 to 2.00 eV, -3.00 to 0.75 eV and -3.00 to 1.75 eV, respectively. Results are compared to a larger energy window of -6.00 to 2.0 eV, but no remarkable difference in the projection and hopping terms has been observed. The corresponding Wannier bands and the comparison with DFT bands are shown in Fig. A.18. Fig. A.19 shows the orbital character of the Wannier projection for the $Ba_2CuO_{3.25}$ structure. The Wannier band characters is almost the same as that of the DFT bands in Fig.2 of main text. The Wannier band dispersion successfully captures the hybridized two-bands Cu-1, insulating Cu-2, and single-band $d_{b^2-c^2}$ nature of Cu-3&4.

Die approbierte gedruckte Originalversion dieser Dissertation ist an der TU Wien Bibliothek verfügbar.
The approved original version of this doctoral thesis is available in print at TU Wien Bibliothek.

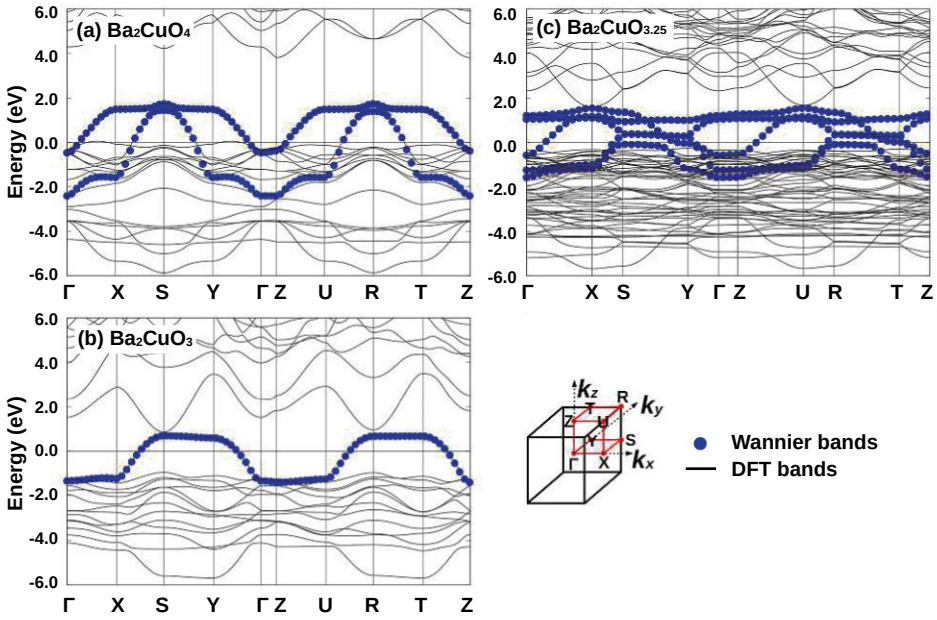

Figure A.18: Wannier bands with blue dots and DFT bands as solid black lines of the three crystal structures discussed in the main text. (a) Ba_2CuO_4, (b) $Ba_2CuO_{3.25}$ and (c) Ba_2CuO_3. The good agreement between Wannier and DFT bands indicates the quality of our Wannier projections and the low-energy effective model.

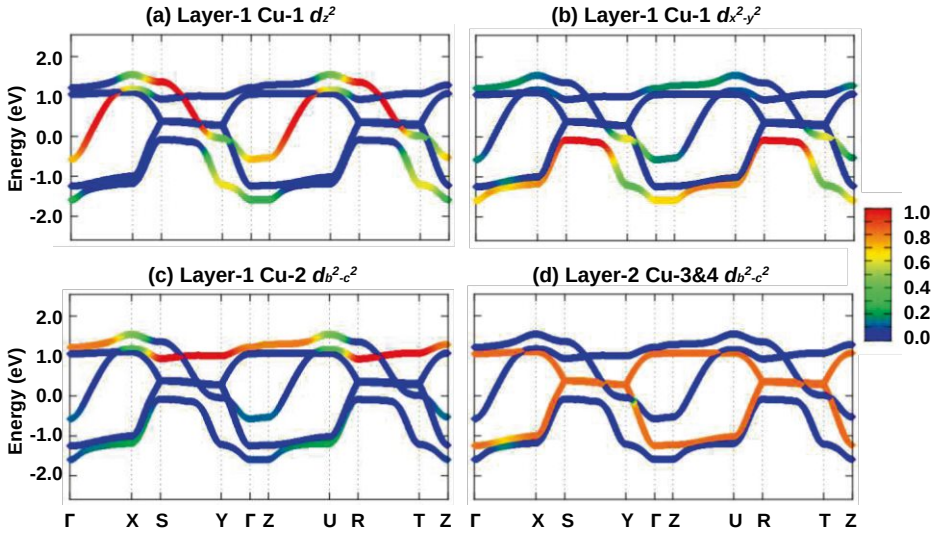

Figure A.19: Orbital characters of low-energy Wannier bands for $Ba_2CuO_{3.25}$ as indicated by color. (a) Layer-1 Cu-1 d_{z^2}, (b) layer-1 Cu-1 $d_{x^2-y^2}$, (c) layer-1 Cu-2 $d_{b^2-c^2}$ and (d) layer-2 Cu-3&4 $d_{b^2-c^2}$

Die approbierte gedruckte Originalversion dieser Dissertation ist an der TU Wien Bibliothek verfügbar.
The approved original version of this doctoral thesis is available in print at TU Wien Bibliothek.
TU Bibliothek Your knowledge hub WIEN

A.2.4 Calculation of Kanamori interaction parameters

We employ constrained random phase approximation (cRPA) [84] to obtain the Coulomb interaction matrix elements mentioned in the main text. For this we used the same Wannier-function setup from the previous section. The calculations were carried out as described in Ref. [80], using a procedure for entangled band-structures [270], and a 6×6×6 k-mesh. The screened Hubbard interaction U for the $d_{b^2-c^2}$ orbital of the Ba_2CuO_3 phase becomes 2.6 eV, while the unscreened Coulomb interaction V is 12.1 eV. In the Ba_2CuO_4 compound, also bands of characters other than $d_{x^2-y^2}$ and d_{z^2} cross the Fermi level. Including many-body renormalizations on the full 3d-shell of Cu, these are expected to depopulate and move below the Fermi level. To mimic this effect and eliminate metallic screening in a $d_{x^2-y^2} + d_{z^2}$ setup, we partially dope the system by setting the charge of Ba to $Z = 56.5$. This procedure results in $U = 2.5$ eV ($V = 12.2$ eV) for the $d_{x^2-y^2}$ orbital. The d_{z^2} orbital is significantly more delocalized: We find $U = 1$ eV ($V = 5$ eV). However, as is common practice in the DMFT community, we use the same U value for both orbitals, preserving $SU(2)$ symmetry. Nevertheless, we can also physically motivate this choice: The effective d_{z^2} orbital is strongly delocalized as it encapsulates low-energy hopping processes mediated by various other orbital characters that we eliminate in the Wannier projection. Along the above lines, however, the corresponding bands will be pushed down in energy if many-body corrections are included. Therewith, orbital hybridizations are reduced and the d_{z^2} orbital becomes more atomic-like. To anticipate this tendency, we use the same U as for the $d_{x^2-y^2}$ orbital.

Note that the above interaction values correspond to the static ($\omega = 0$) limit of the cRPA dynamically screened Hubbard interaction $U(\omega)$. Omitting the dynamics of the interaction in the DFT+DMFT calculations neglects renormalizations from and spectral weight transfers to plasmon satellites[81, 271]. At the same time, DFT+DMFT neglects non-local self-energies, in particular those arising from exchange contributions to the self-energy. The saving grace for standard DFT+DMFT is to simultaneously omit both ingredients as their effect onto the quasi-particle band-width nearly cancels[272, 275, 276]. However, there is a subtlety to note: While $U(\omega)$ leads to spectral weight transfers, exchange acts as a (non-local) one-particle potential that keeps the number of electrons in the low-energy excitations constant. A practical and time-honored approach is therefore to use interactions that are slightly enhanced with respect to the cRPA $U(\omega = 0)$ values. Crucially, we demonstrate in Fig.4 of the main text that our qualitative results are independent on the precise value of the interaction parameters.

A.2.5 Details on Dynamical Mean Field Theory calculations

All DMFT calculations presented in this study were carried out with the `w2dynamics` [278] package. This code package employs the continuous-time quantum Monte Carlo (CTQMC) solver in the hybridization expansion (CT-HYB) [408]. For the DMFT convergence we performed order 10^8 QMC measurements per iteration. After convergence had been reached we performed an additional high-statistic run with $5 \cdot 10^9$ measurements to improve the quality of our analytic continuation.

Die approbierte gedruckte Originalversion dieser Dissertation ist an der TU Wien Bibliothek verfügbar.
The approved original version of this doctoral thesis is available in print at TU Wien Bibliothek.
TU Bibliothek Your knowledge hub WIEN

To perform DMFT calculations for the bilayer $Ba_2CuO_{3.25}$ structure, we defined four impurity problems for the four Cu atoms in the supercell. The impurity sites couple to one another via a common bath, but the non-local interactions between the sites are assumed to be small and thus neglected. Fig. A.20 displays the k-resolved spectral function of DMFT (colors) and the DFT bands (white lines) on top, highlighting the importance of (local) correlations.

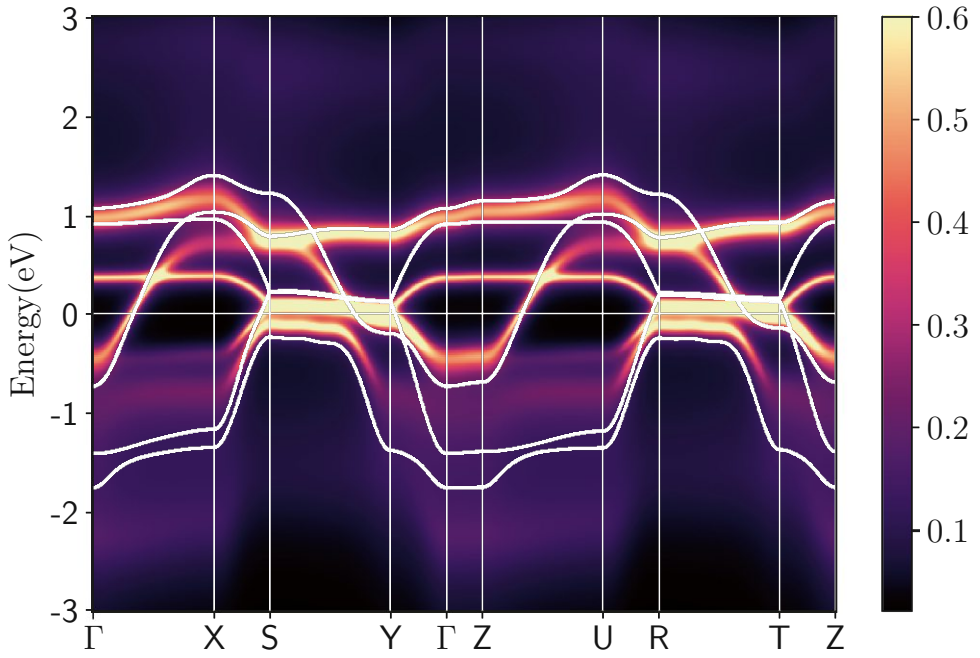

Figure A.20: Low-energy DMFT k-resolved spectral function (colorplot) and DFT Wannnier bands (white lines) for the $Ba_2CuO_{3.25}$ structure.

A.2.6 Phonon dispersion

Below in Fig. A.21 the phonon dispersion for the $Ba_2CuO_{3.25}$ structures is displayed: (a) with experimental lattices and (b) DFT relaxed lattice. The phonon dispersion confirms the dynamical stability of the proposed bilayer phase. The computations were done by enlarging the primitive cell to a 2×2×1 supercell of $Ba_2CuO_{3.25}$ structures using the `vasp` + `phonony` code framework. In (a) the numbers of phonon dispersion are two times larger than in (b), because in (b) we adopted the primitive cell as in Fig.1(c) of main text while in (a) we adopted a 2×2×1 supercell, which is two times larger than the former.

Die approbierte gedruckte Originalversion dieser Dissertation ist an der TU Wien Bibliothek verfügbar.
The approved original version of this doctoral thesis is available in print at TU Wien Bibliothek.

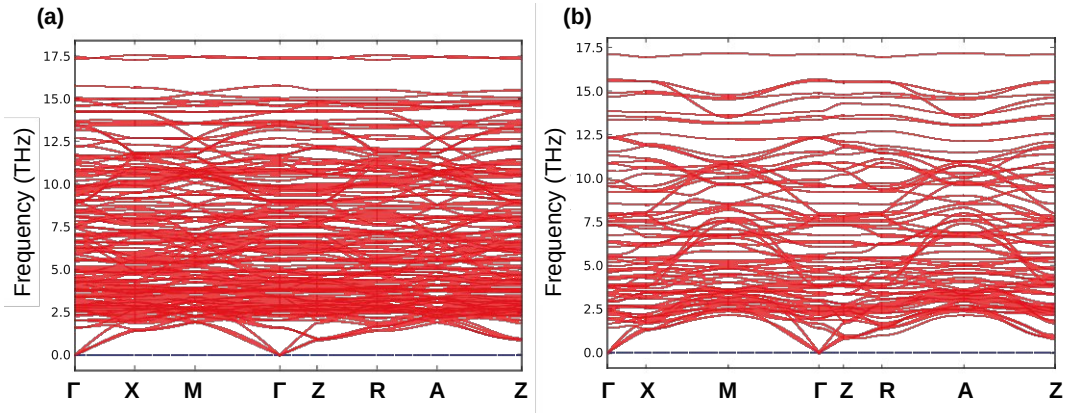

Figure A.21: DFT resulted phonon dispersion for $Ba_2CuO_{3.25}$.

Die approbierte gedruckte Originalversion dieser Dissertation ist an der TU Wien Bibliothek verfügbar.
The approved original version of this doctoral thesis is available in print at TU Wien Bibliothek.

Die approbierte gedruckte Originalversion dieser Dissertation ist an der TU Wien Bibliothek verfügbar.
The approved original version of this doctoral thesis is available in print at TU Wien Bibliothek.

References

[1] K. Onnes. "On the sudden change in the rate at which the resistance of mercury disappears." Comm. Leiden. (1911).

[2] J. Bardeen, L. N. Cooper, and J. R. Schrieffer. "Microscopic Theory of Superconductivity". Phys. Rev. 106 (1957), pp. 162–164.

[3] B. Keimer, S. A. Kivelson, M. R. Norman, S. Uchida, and J. Zaanen. "From quantum matter to high-temperature superconductivity in copper oxides". Nature 518 (2015), pp. 179–186.

[4] G. Logvenov, A. Gozar, and I. Bozovic. "High-Temperature Superconductivity in a Single Copper-Oxygen Plane". Science 326 (2009), pp. 699–702.

[5] H. Takagi, T. Ido, S. Ishibashi, M. Uota, S. Uchida, and Y. Tokura. "Superconductor-to-nonsuperconductor transition in $(La_{1-x}Sr_x)_2CuO_4$ as investigated by transport and magnetic measurements". Phys. Rev. B 40 (1989), pp. 2254–2261.

[6] A. Schilling, M. Cantoni, J. D. Guo, and H. R. Ott. "Superconductivity above 130 K in the Hg–Ba–Ca–Cu–O system". Nature 363 (1993), pp. 56–58.

[7] W. L. McMillan. "Transition Temperature of Strong-Coupled Superconductors". Phys. Rev. 167 (1968), pp. 331–344.

[8] M. L. Cohen and P. W. Anderson. "Comments on the Maximum Superconducting Transition Temperature". AIP Conference Proceedings 4 (1972), pp. 17–27.

[9] S. Y. Savrasov and O. K. Andersen. "Linear-Response Calculation of the Electron-Phonon Coupling in Doped $CaCuO_2$". Phys. Rev. Lett. 77 (1996), pp. 4430–4433.

[10] K.-P. Bohnen, R. Heid, and M. Krauss. "Phonon dispersion and electron-phonon interaction for $YBa_2Cu_3O_7$ from first-principles calculations". Europhysics Letters 64 (2003), p. 104.

[11] J. G. Bednorz and K. A. Müller. "Possible high T_C superconductivity in the Ba-La-Cu-O system". Zeitschrift für Physik B Condensed Matter 64 (1986), pp. 189–193.

[12] M. Kitatani, T. Schäfer, H. Aoki, and K. Held. "Why the critical temperature of high-T_c cuprate superconductors is so low: The importance of the dynamical vertex structure". Phys. Rev. B 99 (2019), p. 41115.

[13] H. Ding, T. Yokoya, et al. "Spectroscopic evidence for a pseudogap in the normal state of underdoped high-Tc superconductors". Nature 382 (1996), pp. 51–54.

[14] T. J. Reber, N. C. Plumb, et al. "The origin and non-quasiparticle nature of Fermi arcs in $Bi_2Sr_2CaCu_2O_{8+\delta}$". Nature Physics 8 (2012), pp. 606–610.

Die approbierte gedruckte Originalversion dieser Dissertation ist an der TU Wien Bibliothek verfügbar.
The approved original version of this doctoral thesis is available in print at TU Wien Bibliothek.

[15] S. Kunisada, S. Isono, et al. "Observation of small Fermi pockets protected by clean CuO_2 sheets of a high-Tc superconductor". Science 369 (2020), pp. 833–838.

[16] K. M. Shen, F. Ronning, et al. "Nodal Quasiparticles and Antinodal Charge Ordering in $Ca_{2-x}Na_xCuO_2Cl_2$". Science 307 (2005), pp. 901–904.

[17] D. Li, K. Lee, et al. "Superconductivity in an infinite-layer nickelate". Nature 572 (2019), pp. 624–627.

[18] M. Osada, B. Y. Wang, et al. "Nickelate Superconductivity without Rare-Earth Magnetism: $(La, Sr)NiO_2$". Advanced Materials (2021), p. 2104083.

[19] K.-W. Lee and W. E. Pickett. "Infinite-layer $LaNiO_2$: Ni^{1+} is not Cu^{2+}". Phys. Rev. B 70 (2004), p. 165109.

[20] K. Held, L. Si, et al. "Phase Diagram of Nickelate Superconductors Calculated by Dynamical Vertex Approximation". Frontiers in Physics 9 (2022).

[21] A. S. Botana and M. R. Norman. "Similarities and Differences between $LaNiO_2$ and $CaCuO_2$ and Implications for Superconductivity". Phys. Rev. X 10 (2020), p. 11024.

[22] K. Lee, B. H. Goodge, et al. "Aspects of the synthesis of thin film superconducting infinite-layer nickelates". APL Materials 8 (2020), p. 41107.

[23] Q. Li, C. He, J. Si, X. Zhu, Y. Zhang, and H.-H. Wen. "Absence of superconductivity in bulk $Nd_{1-x}Sr_xNiO_2$". Communications Materials 1 (2020), pp. 1–8.

[24] N. F. Mott. "Metal-Insulator Transition". Rev. Mod. Phys. 40 (1968), pp. 677–683.

[25] B. Klebel-Knobloch, T. Schäfer, A. Toschi, and J. M. Tomczak. "Anisotropy of electronic correlations: On the applicability of local theories to layered materials". Phys. Rev. B 103 (2021), p. 045121.

[26] K. Held. "Electronic structure calculations using dynamical mean field theory". Advances in physics 56 (2007), pp. 829–926.

[27] V. I. Anisimov, A. I. Poteryaev, M. A. Korotin, A. O. Anokhin, and G. Kotliar. "First-principles calculations of the electronic structure and spectra of strongly correlated systems: dynamical mean-field theory". Journal of Physics: Condensed Matter 9 (1997), pp. 7359–7367.

[28] A. I. Lichtenstein and M. I. Katsnelson. "Ab initio calculations of quasiparticle band structure in correlated systems: LDA++ approach". Phys. Rev. B 57 (1998), pp. 6884–6895.

[29] J. M. Tomczak, P. Liu, A. Toschi, G. Kresse, and K. Held. "Merging *GW* with DMFT and non-local correlations beyond". The European Physical Journal Special Topics 226 (2017), pp. 2565–2590.

Die approbierte gedruckte Originalversion dieser Dissertation ist an der TU Wien Bibliothek verfügbar.
The approved original version of this doctoral thesis is available in print at TU Wien Bibliothek.
TU Bibliothek Your knowledge hub WIEN

[30] L. Boehnke, F. Nilsson, F. Aryasetiawan, and P. Werner. "When strong correlations become weak: Consistent merging of *GW* and DMFT". Phys. Rev. B 94 (2016), p. 201106.

[31] F. Nilsson, L. Boehnke, P. Werner, and F. Aryasetiawan. "Multitier self-consistent *GW* + EDMFT". Phys. Rev. Mater. 1 (2017), p. 043803.

[32] H. Lu, M. Rossi, et al. "Magnetic excitations in infinite-layer nickelates". Science 373 (2021), pp. 213–216.

[33] E. Schrödinger. "Quantisierung als Eigenwertproblem". Annalen der Physik 384 (1926), pp. 361–376.

[34] P. A. M. Dirac and R. H. Fowler. "Quantum mechanics of many-electron systems". Proceedings of the Royal Society of London. Series A, Containing Papers of a Mathematical and Physical Character 123 (1929), pp. 714–733.

[35] P. Hohenberg and W. Kohn. "Inhomogeneous Electron Gas". Phys. Rev. 136 (1964), B864–B871.

[36] C. N. Varney, C.-R. Lee, Z. J. Bai, S. Chiesa, M. Jarrell, and R. T. Scalettar. "Quantum Monte Carlo study of the two-dimensional fermion Hubbard model". Phys. Rev. B 80 (2009), p. 075116.

[37] A. Georges, G. Kotliar, W. Krauth, and M. J. Rozenberg. "Dynamical mean-field theory of strongly correlated fermion systems and the limit of infinite dimensions". Rev. Mod. Phys. 68 (1996), p. 13.

[38] A. Toschi, A. A. Katanin, and K. Held. "Dynamical vertex approximation; A step beyond dynamical mean-field theory". Phys Rev. B 75 (2007), p. 45118.

[39] M. Born and R. Oppenheimer. "Zur Quantentheorie der Molekeln". Annalen der Physik 389 (1927), pp. 457–484.

[40] G. M. Eliashberg. "Temperature Green's Function for Electrons in a Superconductor". Zh. Eksp. Teor. Fiz. 38 (1960), pp. 966–976.

[41] R. M. Martin. "Electronic Structure: Basic Theory and Practical Methods". Cambridge University Press, 2004.

[42] W. Kohn, A. D. Becke, and R. G. Parr. "Density Functional Theory of Electronic Structure". The Journal of Physical Chemistry 100 (1996), pp. 12974–12980.

[43] R. G. Parr and Y. Weitao. "Density-Functional Theory of Atoms and Molecules". Oxford University Press, 1995.

[44] R. G. Parr, R. A. Donnelly, M. Levy, and W. E. Palke. "Electronegativity: The density functional viewpoint". The Journal of Chemical Physics 68 (1978), pp. 3801–3807.

[45] R. van Leeuwen. "Density Functional Approach to the Many-Body Problem: Key Concepts and Exact Functionals". Vol. 43. Advances in Quantum Chemistry. Academic Press, 2003, pp. 25–94.

Die approbierte gedruckte Originalversion dieser Dissertation ist an der TU Wien Bibliothek verfügbar.
The approved original version of this doctoral thesis is available in print at TU Wien Bibliothek.
TU Bibliothek Your knowledge hub WIEN

[46] W. Kohn and L. J. Sham. "Self-Consistent Equations Including Exchange and Correlation Effects". Phys. Rev. 140 (1965), (4A) A1133.

[47] E. M. Stoudenmire, L. O. Wagner, S. R. White, and K. Burke. "One-Dimensional Continuum Electronic Structure with the Density-Matrix Renormalization Group and Its Implications for Density-Functional Theory". Phys. Rev. Lett. 109 (2012), p. 056402.

[48] D. M. Ceperley and B. J. Alder. "Ground State of the Electron Gas by a Stochastic Method". Phys. Rev. Lett. 45 (1980), pp. 566–569.

[49] J. P. Perdew, K. Burke, and M. Ernzerhof. "Generalized Gradient Approximation Made Simple". Phys. Rev. Lett. 77 (1996), pp. 3865–3868.

[50] M. Kitatani, L. Si, O. Janson, R. Arita, Z. Zhong, and K. Held. "Nickelate superconductors – a renaissance of the one-band Hubbard model". npj Quantum Materials 5 (2020), p. 59.

[51] J. Karp, A. S. Botana, M. R. Norman, H. Park, M. Zingl, and A. Millis. "Many-Body Electronic Structure of $NdNiO_2$ and $CaCuO_2$". Phys. Rev. X 10 (2020), p. 21061.

[52] P. Villars and K. Cenzual. "CaCuO2 Crystal Structure". SpringerMaterials.

[53] A. T. Bollinger and I. Božović. "Two-dimensional superconductivity in the cuprates revealed by atomic-layer-by-layer molecular beam epitaxy". Superconductor Science Technology 29, 103001 (2016), p. 103001.

[54] K. Schwarz and P. Blaha. "Solid state calculations using WIEN2k". Computational Materials Science 28 (2003). Proceedings of the Symposium on Software Development for Process and Materials Design, pp. 259–273.

[55] P. Blaha, K. Schwarz, et al. "WIEN2k: An Augmented Plane Wave Plus Local Orbitals Program for Calculating Crystal Properties". English (US). TU Wien, 2019.

[56] K. Burke and J. Kozlowski, eds. "Lies My Teacher Told Me About Density Functional Theory: Seeing Through Them with the Hubbard Dimer". Forschungszentrum Jülich GmbH Zentralbibliothek, 20, 2021, Chapter 3 of the lecture series book: Simulating Correlations with Computers.

[57] D. Di Castro, M. Salvato, et al. "Occurrence of a high-temperature superconducting phase in $(CaCuO_2)_n/(SrTiO_3)_m$ superlattices". Phys. Rev. B 86 (2012), p. 134524.

[58] A. Ikeda, Y. Krockenberger, and H. Yamamoto. "Molecular beam epitaxy of electron-doped infinite-layer $Ca_{1-x}R_xCuO_2$ thin films". Phys. Rev. Materials 3 (2019), p. 064803.

[59] K. Lee, B. Y. Wang, et al. "Character of the "normal state" of the nickelate superconductors". arXiv:2203.02580 (2022).

Die approbierte gedruckte Originalversion dieser Dissertation ist an der TU Wien Bibliothek verfügbar.
The approved original version of this doctoral thesis is available in print at TU Wien Bibliothek.
TU Bibliothek Your knowledge hub WIEN

[60] F. Tran and P. Blaha. "Accurate Band Gaps of Semiconductors and Insulators with a Semilocal Exchange-Correlation Potential". Phys. Rev. Lett. 102 (2009), p. 226401.

[61] J. P. Perdew. "Density functional theory and the band gap problem". International Journal of Quantum Chemistry 28 (1985), pp. 497–523.

[62] M. K. Y. Chan and G. Ceder. "Efficient Band Gap Prediction for Solids". Phys. Rev. Lett. 105 (2010), p. 196403.

[63] L. F. Mattheiss. "Electronic band properties and superconductivity in $La_{2-y}X_yCuO_4$". Phys. Rev. Lett. 58 (1987), pp. 1028–1030.

[64] L. Si, W. Xiao, et al. "Topotactic Hydrogen in Nickelate Superconductors and Akin Infinite-Layer Oxides ABO_2". Phys. Rev. Lett. 124 (2020), p. 166402.

[65] N. Kowalski, S. S. Dash, P. Sémon, D. Sénéchal, and A.-M. Tremblay. "Oxygen hole content, charge-transfer gap, covalency, and cuprate superconductivity". Proceedings of the National Academy of Sciences 118 (2021), e2106476118.

[66] E. Müller-Hartmann. "Correlated fermions on a lattice in high dimensions". Zeitschrift für Physik B Condensed Matter 74 (1989), pp. 507–512.

[67] N. Marzari, A. A. Mostofi, J. R. Yates, I. Souza, and D. Vanderbilt. "Maximally localized Wannier functions: Theory and applications". Rev. Mod. Phys. 84 (2012), pp. 1419–1475.

[68] H. LaBollita. "w2kplot". https://github.com/harrisonlabollita/w2kplot. 2022.

[69] P. Hansmann. "LDA+DMFT: From bulk to heterostuctures". PhD thesis. TU Wien, 2010.

[70] S. M. O'Mahony, W. Ren, et al. "On the electron pairing mechanism of copper-oxide high temperature superconductivity". Proceedings of the National Academy of Sciences 119 (2022), e2207449119.

[71] F. C. Zhang and T. M. Rice. "Effective Hamiltonian for the superconducting Cu oxides". Phys. Rev. B 37 (1988), p. 3759.

[72] R. Arita and K. Held. "Dynamical cluster approximation study of d- and p-wave pairing in the Hubbard model at T→0". Journal of Magnetism and Magnetic Materials 310 (2007), pp. 645–647.

[73] F. Bloch. "Über die Quantenmechanik der Elektronen in Kristallgittern". Zeitschrift für Physik 52 (1928), p. 555.

[74] G. H. Wannier. "The Structure of Electronic Excitation Levels in Insulating Crystals". Phys. Rev. 52 (1937), pp. 191–197.

[75] I. Souza, N. Marzari, and D. Vanderbilt. "Maximally localized Wannier functions for entangled energy bands". Phys. Rev. B 65 (2001), p. 35109.

[76] N. Marzari and D. Vanderbilt. "Maximally localized generalized Wannier functions for composite energy bands". Phys. Rev. B 56 (1997), pp. 12847–12865.

Die approbierte gedruckte Originalversion dieser Dissertation ist an der TU Wien Bibliothek verfügbar.
The approved original version of this doctoral thesis is available in print at TU Wien Bibliothek.
TU Bibliothek Your knowledge hub WIEN

[77] J. Kuneš, R. Arita, P. Wissgott, A. Toschi, H. Ikeda, and K. Held. "Wien2wannier: From linearized augmented plane waves to maximally localized Wannier functions". Comp. Phys. Comm. 181 (2010), pp. 1888–1895.

[78] M. Springer and F. Aryasetiawan. "Frequency-dependent screened interaction in Ni within the random-phase approximation". Phys. Rev. B 57 (1998), pp. 4364–4368.

[79] F. Aryasetiawan, K. Karlsson, O. Jepsen, and U. Schönberger. "Calculations of Hubbard U from first-principles". Phys. Rev. B 74 (2006), p. 125106.

[80] T. Miyake and F. Aryasetiawan. "Screened Coulomb interaction in the maximally localized Wannier basis". Phys. Rev. B 77 (2008), p. 85122.

[81] M. Casula, P. Werner, et al. "Low-Energy Models for Correlated Materials: Bandwidth Renormalization from Coulombic Screening". Phys. Rev. Lett. 109 (2012), p. 126408.

[82] A. Georges, L. d. Medici, and J. Mravlje. "Strong Correlations from Hund's Coupling". Annual Review of Condensed Matter Physics 4 (2013), pp. 137–178.

[83] J. Kanamori. "Electron Correlation and Ferromagnetism of Transition Metals". Progress of Theoretical Physics 30 (1963), pp. 275–289.

[84] F. Aryasetiawan, M. Imada, A. Georges, G. Kotliar, S. Biermann, and A. I. Lichtenstein. "Frequency-dependent local interactions and low-energy effective models from electronic structure calculations". Phys. Rev. B 70 (2004), p. 195104.

[85] F. Simkovic, R. Rossi, and M. Ferrero. "Two-dimensional Hubbard model at finite temperature: Weak, strong, and long correlation regimes". Phys. Rev. Res. 4 (2022), p. 043201.

[86] N. E. Bickers and D. J. Scalapino. "Conserving approximations for strongly fluctuating electron systems. I. Formalism and calculational approach". Annals of Physics 193 (1989), pp. 206–251.

[87] T. Matsubara. "A new approach to quantum-statistical mechanics". Prog. Theor. Phys. 14 (1955), p. 351.

[88] G. C. Wick. "Properties of Bethe-Salpeter Wave Functions". Phys. Rev. 96 (1954), pp. 1124–1134.

[89] G. Rohringer. "New routes towards a theoretical treatment of nonlocal electronic correlations". PhD thesis. Vienna University of Technology, 2013, p. 318.

[90] D. Sénéchal, A. M. Tremblay, and C. Bourbonnais. "Theoretical Methods for Strongly Correlated Electrons (CRM Series in Mathematical Physics)". Springer, New York, 2004.

[91] G. C. Wick. "The Evaluation of the Collision Matrix". Phys. Rev. 80 (1950), p. 268.

[92] P. Worm. "Diagrammatic approach to the optical conductivity in strongly correlated systems". MA thesis. Vienna University of Technology, 2019, p. 69.

Die approbierte gedruckte Originalversion dieser Dissertation ist an der TU Wien Bibliothek verfügbar.
The approved original version of this doctoral thesis is available in print at TU Wien Bibliothek.
TU Bibliothek Your knowledge hub WIEN

[93] A. Abrikosov, L. Gorkov, I. Dzyaloshinski, and R. Silverman. "Methods of Quantum Field Theory in Statistical Physics". Dover Books on Physics. Dover Publications, 2012.

[94] A. Galler, P. Thunström, P. Gunacker, J. M. Tomczak, and K. Held. "Ab initio dynamical vertex approximation". Phys. Rev. B 95 (2017), p. 115107.

[95] G. Rohringer, H. Hafermann, et al. "Diagrammatic routes to nonlocal correlations beyond dynamical mean field theory". Rev. Mod. Phys. 90 (2018), p. 25003.

[96] M. Abbate, G. Zampieri, F. Prado, A. Caneiro, J. M. Gonzalez-Calbet, and M. Vallet-Regi. "Electronic structure and metal-insulator transition in $LaNiO_{3-\delta}$". Phys. Rev. B 65 (2002), p. 155101.

[97] N. E. Bickers and S. R. White. "Conserving approximations for strongly fluctuating electron systems. II. Numerical results and parquet extension". Phys. Rev. B 43 (1991), pp. 8044–8064.

[98] G. Rohringer, A. Valli, and A. Toschi. "Local electronic correlation at the two-particle level". Phys. Rev. B 86 (2012), p. 125114.

[99] N. E. Bickers. "Self-Consistent Many-Body Theory for Condensed Matter Systems". *Theoretical Methods for Strongly Correlated Electrons*. New York, NY: Springer New York, 2004, pp. 237–296.

[100] N. Wentzell, G. Li, et al. "High-frequency asymptotics of the vertex function: Diagrammatic parametrization and algorithmic implementation". Phys. Rev. B 102 (2020), p. 85106.

[101] P. Worm, C. Watzenböck, M. Pickem, A. Kauch, and K. Held. "Broadening and sharpening of the Drude peak through antiferromagnetic fluctuations". Phys. Rev. B 104 (2021), p. 115153.

[102] C. Watzenböck. "Vertex corrections in strongly correlated electron systems - timescales of the spin and charge response". PhD thesis. TU Wien, 2022.

[103] P. Kappl, F. Krien, C. Watzenböck, and K. Held. "Non-linear responses and three-particle correlators in correlated electron systems exemplified by the Anderson impurity model". 2022.

[104] O. J. Lipscombe, B. Vignolle, T. G. Perring, C. D. Frost, and S. M. Hayden. "Emergence of Coherent Magnetic Excitations in the High Temperature Underdoped $La_{2-x}Sr_xCuO_4$ Superconductor at Low Temperatures". Phys. Rev. Lett. 102 (2009), p. 167002.

[105] M. Fujita, H. Hiraka, et al. "Progress in Neutron Scattering Studies of Spin Excitations in High-Tc Cuprates". Journal of the Physical Society of Japan 81 (2012), p. 011007.

[106] E. E. Salpeter and H. A. Bethe. "A Relativistic Equation for Bound-State Problems". Phys. Rev. 84 (1951), pp. 1232–1242.

[107] M. Wallerberger. "Private communication". 2022.

Die approbierte gedruckte Originalversion dieser Dissertation ist an der TU Wien Bibliothek verfügbar.
The approved original version of this doctoral thesis is available in print at TU Wien Bibliothek.
TU Bibliothek Your knowledge hub WIEN

[108] A. A. Katanin. "Fulfillment of Ward identities in the functional renormalization group approach". Phys. Rev. B 70 (2004), p. 115109.

[109] F. Krien, A. Valli, and M. Capone. "Single-boson exchange decomposition of the vertex function". Phys. Rev. B 100 (2019), p. 155149.

[110] L. Hedin. "New Method for Calculating the One-Particle Green's Function with Application to the Electron-Gas Problem". Phys. Rev. 139 (1965), A796–A823.

[111] W. Metzner and D. Vollhardt. "Correlated Lattice Fermions in $d = \infty$ Dimensions". Phys. Rev. Lett. 62 (1989), pp. 324–327.

[112] A. Georges and G. Kotliar. "Hubbard model in infinite dimensions". Phys. Rev. B 45 (1992), pp. 6479–6483.

[113] G. Kotliar, S. Y. Savrasov, K. Haule, V. S. Oudovenko, O. Parcollet, and C. A. Marianetti. "Electronic structure calculations with dynamical mean-field theory". Rev. Mod. Phys. 78 (2006), p. 865.

[114] E. Pavarini, E. Koch, D. Vollhardt, and A. Lichtenstein. "DMFT at 25: Infinite Dimensions". Forschungszentrum Jülich GmbH Zentralbibliothek, 2014.

[115] E. Pavarini and E. Koch, eds. "Simulating Correlations with Computers". Forschungszentrum Jülich GmbH Zentralbibliothek, 20, 2021, p. 420.

[116] A. Tamai, M. Zingl, et al. "High-Resolution Photoemission on $SrRuO_4$ Reveals Correlation-Enhanced Effective Spin-Orbit Coupling and Dominantly Local Self-Energies". Phys. Rev. X 9 (2019), p. 021048.

[117] Y. Lu and M. W. Haverkort. "Exact diagonalization as an impurity solver in dynamical mean field theory". The European Physical Journal Special Topics 226 (2017), pp. 2549–2564.

[118] D. Medvedeva, S. Iskakov, F. Krien, V. V. Mazurenko, and A. I. Lichtenstein. "Exact diagonalization solver for extended dynamical mean-field theory". Phys. Rev. B 96 (2017), p. 235149.

[119] R. Bulla, T. A. Costi, and T. Pruschke. "Numerical renormalization group method for quantum impurity systems". Rev. Mod. Phys. 80 (2008), pp. 395–450.

[120] E. Gull, A. J. Millis, A. I. Lichtenstein, A. N. Rubtsov, M. Troyer, and P. Werner. "Continuous-time Monte Carlo methods for quantum impurity models". Rev. Mod. Phys. 83 (2011), pp. 349–404.

[121] P. Werner, A. Comanac, L. de'Medici, M. Troyer, and A. J. Millis. "Continuous-Time Solver for Quantum Impurity Models". Phys. Rev. Lett. 97 (2006), p. 076405.

[122] J. Kaufmann and K. Held. "ana_cont: Python package for analytic continuation". Computer Physics Communications 282 (2023), p. 108519.

[123] A. A. Katanin, A. Toschi, and K. Held. "Comparing pertinent effects of antiferromagnetic fluctuations in the two- and three-dimensional Hubbard model". Phys. Rev. B 80 (2009), p. 75104.

Die approbierte gedruckte Originalversion dieser Dissertation ist an der TU Wien Bibliothek verfügbar.
The approved original version of this doctoral thesis is available in print at TU Wien Bibliothek.
TU Bibliothek Your knowledge hub WIEN

[124] E. Gull, M. Ferrero, O. Parcollet, A. Georges, and A. J. Millis. "Momentum-space anisotropy and pseudogaps: A comparative cluster dynamical mean-field analysis of the doping-driven metal-insulator transition in the two-dimensional Hubbard model". Phys. Rev. B 82 (2010), p. 155101.

[125] E. Gull, O. Parcollet, and A. J. Millis. "Superconductivity and the Pseudogap in the Two-Dimensional Hubbard Model". Phys. Rev. Lett. 110 (2013), p. 216405.

[126] T. Schäfer, N. Wentzell, et al. "Tracking the Footprints of Spin Fluctuations: A MultiMethod, MultiMessenger Study of the Two-Dimensional Hubbard Model". Phys. Rev. X 11 (2021), p. 11058.

[127] A. Valli, T. Schäfer, et al. "Dynamical vertex approximation in its parquet implementation: Application to Hubbard nanorings". Phys. Rev. B 91 (2015), p. 115115.

[128] J. Kaufmann, C. Eckhardt, M. Pickem, M. Kitatani, A. Kauch, and K. Held. "Self-consistent ladder dynamical vertex approximation". Phys. Rev. B 103 (2021), p. 35120.

[129] J. Stobbe and G. Rohringer. "Consistency of potential energy in the dynamical vertex approximation". Phys. Rev. B 106 (2022), p. 205101.

[130] L. Del Re and A. Toschi. "Dynamical vertex approximation for many-electron systems with spontaneously broken SU(2) symmetry". Phys. Rev. B 104 (2021), p. 085120.

[131] K. Held, ed. "Dynamical Vertex Approximation". Forschungszentrum Jülich GmbH Zentralbibliothek, 2014, Chapter 10 of the lecture series book: DMFT at 25: Infinite Dimensions.

[132] C. Hille, F. B. Kugler, et al. "Quantitative functional renormalization group description of the two-dimensional Hubbard model". Phys. Rev. Res. 2 (2020), p. 033372.

[133] Y. M. Vilk, A.-M. Tremblay, Y.M. Vilk, and A.-M.S. Tremblay. "Non-Perturbative Many-Body Approach to the Hubbard Model and Single-Particle Pseudogap". J. Phys. I France 7 (1997), pp. 1309–1368.

[134] T. Schäfer. "Classical and quantum phase transitions in strongly correlated electron systems". PhD thesis. TU Wien, 2016.

[135] G. Rohringer and A. Toschi. "Impact of non-local correlations over different energy scales: A Dynamical Vertex Approximation study". Phys. Rev. B 94 (2016), p. 125144.

[136] N. D. Mermin and H. Wagner. "Absence of Ferromagnetism or Antiferromagnetism in One- or Two-Dimensional Isotropic Heisenberg Models". Phys. Rev. Lett. 17 (1966), p. 1307.

[137] G. Li, A. Kauch, P. Pudleiner, and K. Held. "The *victory* project v1.0: an efficient parquet equations solver". 2017.

Die approbierte gedruckte Originalversion dieser Dissertation ist an der TU Wien Bibliothek verfügbar.
The approved original version of this doctoral thesis is available in print at TU Wien Bibliothek.
TU Bibliothek Your knowledge hub WIEN

[138] C. J. Eckhardt, C. Honerkamp, K. Held, and A. Kauch. "Truncated unity parquet solver". Phys. Rev. B 101 (2020), p. 155104.

[139] F. Krien, P. Worm, P. Chalupa-Gantner, A. Toschi, and K. Held. "Explaining the pseudogap through damping and antidamping on the Fermi surface by imaginary spin scattering". Communications Physics 5 (2022), p. 336.

[140] G. Rohringer, A. Toschi, A. Katanin, and K. Held. "Critical Properties of the Half-Filled Hubbard Model in Three Dimensions". Phys. Rev. Lett. 107 (2011), p. 256402.

[141] S. Yoshida, K. Yada, and Y. Tanaka. "Theory of a pair density wave on a quasi-one-dimensional lattice in the Hubbard model". Phys. Rev. B 104 (2021), p. 094506.

[142] S. Sakai, S. Blanc, et al. "Raman-Scattering Measurements and Theory of the Energy-Momentum Spectrum for Underdoped $Bi_2Sr_2CaCuO_{8+\delta}$ Superconductors: Evidence of an s-Wave Structure for the Pseudogap". Phys. Rev. Lett. 111 (2013), p. 107001.

[143] P. Worm, M. Kitatani, J. M. Tomczak, L. Si, and K. Held. "Hidden one-dimensional, strongly nested, and almost half-filled Fermi surface in Ba_2CuO_{3+y} superconductors". Phys. Rev. B 105 (2022), p. 085110.

[144] E. Antipov, S. Putilin, et al. "Mercury-based copper mixed-oxide superconductors". Physica C: Superconductivity 235-240 (1994), pp. 21–24.

[145] A. P. Drozdov, M. I. Eremets, I. A. Troyan, V. Ksenofontov, and S. I. Shylin. "Conventional superconductivity at 203 kelvin at high pressures in the sulfur hydride system". Nature 512 (2015), p. 73.

[146] Y. Sato, S. Kasahara, et al. "Thermodynamic evidence for a nematic phase transition at the onset of the pseudogap in YBa2Cu3Oy". Nature Physics 13 (2017), pp. 1074–1078.

[147] M. Qin, T. Schäfer, S. Andergassen, P. Corboz, and E. Gull. "The Hubbard Model: A Computational Perspective". 2022.

[148] O. Ivashko, M. Horio, et al. "Strain-engineering Mott-insulating La2CuO4". Nature Communications 10 (2019), p. 786.

[149] G. Kim, K. S. Rabinovich, et al. "Optical conductivity and superconductivity in highly overdoped $La_{2-x}Ca_xCuO_4$ thin films". Proceedings of the National Academy of Sciences 118 (2021), e2106170118.

[150] F. Nilsson, K. Karlsson, and F. Aryasetiawan. "Dynamically screened Coulomb interaction in the parent compounds of hole-doped cuprates: Trends and exceptions". Phys. Rev. B 99 (2019), p. 075135.

[151] C. Hu, J. Zhao, et al. "Momentum-resolved visualization of electronic evolution in doping a Mott insulator". Nature Communications 12 (2021), p. 1356.

Die approbierte gedruckte Originalversion dieser Dissertation ist an der TU Wien Bibliothek verfügbar.
The approved original version of this doctoral thesis is available in print at TU Wien Bibliothek.
TU Bibliothek Your knowledge hub WIEN

[152] J. Saylor, L. Takacs, C. Hohenemser, J. I. Budnick, and B. Chamberland. "Néel temperature of stoichiometric La2CuO4". Phys. Rev. B 40 (1989), pp. 6854–6861.

[153] S. Mitsuda, G. Shirane, et al. "Confirmation of antiferromagnetism in La_2 CuO_{4-y} with polarized neutrons". Phys. Rev. B 36 (1987), pp. 822–825.

[154] E. Kozik, E. Burovski, V. W. Scarola, and M. Troyer. "Néel temperature and thermodynamics of the half-filled three-dimensional Hubbard model by diagrammatic determinant Monte Carlo". Phys. Rev. B 87 (2013), p. 205102.

[155] Y. Ando, Y. Kurita, S. Komiya, S. Ono, and K. Segawa. "Evolution of the Hall Coefficient and the Peculiar Electronic Structure of the Cuprate Superconductors". Phys. Rev. Lett. 92 (2004), p. 197001.

[156] I. M. Vishik. "Photoemission perspective on pseudogap, superconducting fluctuations, and charge order in cuprates: a review of recent progress". Reports on Progress in Physics 81 (2018), p. 062501.

[157] N. Barišić, M. K. Chan, et al. "Universal sheet resistance and revised phase diagram of the cuprate high-temperature superconductors". Proceedings of the National Academy of Sciences 110 (2013), pp. 12235–12240.

[158] C. C. Homes, T. Timusk, R. Liang, D. A. Bonn, and W. N. Hardy. "Optical conductivity of c axis oriented YBa_2 Cu_3 $O_{6.70}$: Evidence for a pseudogap". Phys. Rev. Lett. 71 (1993), pp. 1645–1648.

[159] W. W. Warren, R. E. Walstedt, et al. "Cu spin dynamics and superconducting precursor effects in planes above T_c in YBa_2 Cu_3 $O_{6.7}$". Phys. Rev. Lett. 62 (1989), pp. 1193–1196.

[160] C. Tsuei and J. Kirtley. "d-wave pairing symmetry in cuprate superconductors". Physica C: Superconductivity 341-348 (2000), pp. 1625–1628.

[161] X. Dong, L. D. Re, A. Toschi, and E. Gull. "Mechanism of superconductivity in the Hubbard model at intermediate interaction strength". Proceedings of the National Academy of Sciences 119 (2022), e2205048119.

[162] D. J. Scalapino. "A common thread: The pairing interaction for unconventional superconductors". Rev. Mod. Phys. 84 (2012), pp. 1383–1417.

[163] D. Vilardi, P. M. Bonetti, and W. Metzner. "Dynamical functional renormalization group computation of order parameters and critical temperatures in the two-dimensional Hubbard model". Phys. Rev. B 102 (2020), p. 245128.

[164] G. Sordi, P. Sémon, K. Haule, and A.-M. S. Tremblay. "Strong Coupling Superconductivity, Pseudogap, and Mott Transition". Phys. Rev. Lett. 108 (2012), p. 216401.

[165] E. Gull and A. Millis. "Numerical models come of age". Nature Phys. 11 (2015), p. 808.

[166] C. M. Varma. "Non-Fermi-liquid states and pairing instability of a general model of copper oxide metals". Phys. Rev. B 55 (1997), pp. 14554–14580.

Die approbierte gedruckte Originalversion dieser Dissertation ist an der TU Wien Bibliothek verfügbar.
The approved original version of this doctoral thesis is available in print at TU Wien Bibliothek.
TU Bibliothek Your knowledge hub WIEN

[167] P. W. Anderson. "The Resonating Valence Bond State in La2CuO4 and Superconductivity". Science 235 (1987), pp. 1196–1198.

[168] A. V. Chubukov, S. Sachdev, and J. Ye. "Theory of two-dimensional quantum Heisenberg antiferromagnets with a nearly critical ground state". Phys. Rev. B 49 (1994), pp. 11919–11961.

[169] C. Castellani, C. Di Castro, and M. Grilli. "Non-Fermi-liquid behavior and d-wave superconductivity near the charge-density-wave quantum critical point". Zeitschrift für Physik B Condensed Matter 103 (1996), pp. 137–144.

[170] E. Blackburn, J. Chang, et al. "X-Ray Diffraction Observations of a Charge-Density-Wave Order in Superconducting Ortho-II $YBa_2Cu_3\mathbf{O}_{6.54}$ Single Crystals in Zero Magnetic Field". Phys. Rev. Lett. 110 (2013), p. 137004.

[171] R. Comin and A. Damascelli. "Resonant X-Ray Scattering Studies of Charge Order in Cuprates". Annual Review of Condensed Matter Physics 7 (2016), pp. 369–405.

[172] T. Wu, H. Mayaffre, et al. "Magnetic-field-induced charge-stripe order in the high-temperature superconductor YBa2Cu3Oy". Nature 477 (2011), p. 191.

[173] J. Chang, E. Blackburn, et al. "Direct observation of competition between superconductivity and charge density wave order in YBa2Cu3O6.67". Nature Physics 8 (2012), pp. 871–876.

[174] D. Pelc, M. Vučković, et al. "Emergence of superconductivity in the cuprates via a universal percolation process". Nature Communications 9 (2018), p. 4327.

[175] I. K. Drozdov, I. Pletikosić, et al. "Phase diagram of Bi2Sr2CaCu2O8+δ revisited". Nature Communications 9 (2018), p. 5210.

[176] D. LeBoeuf, N. Doiron-Leyraud, et al. "Lifshitz critical point in the cuprate superconductor $YBa_2Cu_3O_y$ from high-field Hall effect measurements". Phys. Rev. B 83 (2011), p. 054506.

[177] M. Platé, J. D. F. Mottershead, et al. "Fermi Surface and Quasiparticle Excitations of Overdoped $TL_2Ba_2CuO_{6+\delta}$". Phys. Rev. Lett. 95 (2005), p. 077001.

[178] J. Ayres, M. Berben, et al. "Incoherent transport across the strange-metal regime of overdoped cuprates". Nature 595 (2021), pp. 661–666.

[179] B. Michon, C. Berthod, et al. "Planckian behavior of cuprate superconductors: Reconciling the scaling of optical conductivity with resistivity and specific heat". arXiv preprint arXiv:2205.04030 (2022).

[180] S. I. Mirzaei, D. Stricker, et al. "Spectroscopic evidence for Fermi liquid-like energy and temperature dependence of the relaxation rate in the pseudogap phase of the cuprates". PNAS 110 (2013), pp. 5774–5778.

[181] A. A. Kordyuk. "Pseudogap from ARPES experiment: Three gaps in cuprates and topological superconductivity". Low Temperature Physics 41 (2015), pp. 319–341.

Die approbierte gedruckte Originalversion dieser Dissertation ist an der TU Wien Bibliothek verfügbar.
The approved original version of this doctoral thesis is available in print at TU Wien Bibliothek.
TU Bibliothek Your knowledge hub WIEN

[182] O. Gunnarsson, T. Schäfer, et al. "Fluctuation Diagnostics of the Electron Self-Energy: Origin of the Pseudogap Physics". Phys. Rev. Lett. 114 (2015), p. 236402.

[183] O. Gunnarsson, T. Schäfer, et al. "Parquet decomposition calculations of the electronic self-energy". Phys. Rev. B 93 (2016), p. 245102.

[184] W. Wu, M. S. Scheurer, S. Chatterjee, S. Sachdev, A. Georges, and M. Ferrero. "Pseudogap and Fermi-Surface Topology in the Two-Dimensional Hubbard Model". Phys. Rev. X 8 (2018), p. 21048.

[185] W. Wu, M. S. Scheurer, M. Ferrero, and A. Georges. "Effect of Van Hove singularities in the onset of pseudogap states in Mott insulators". Phys. Rev. Research 2 (2020), p. 033067.

[186] F. Krien, A. Valli, P. Chalupa, M. Capone, A. I. Lichtenstein, and A. Toschi. "Boson-exchange parquet solver for dual fermions". Phys. Rev. B 102 (2020), p. 195131.

[187] M. Klett, P. Hansmann, and T. Schäfer. "Magnetic Properties and Pseudogap Formation in Infinite-Layer Nickelates: Insights From the Single-Band Hubbard Model". Frontiers in Physics 10 (2022).

[188] Y. M. Vilk. "Shadow features and shadow bands in the paramagnetic state of cuprate superconductors". Phys. Rev. B 55 (1997), pp. 3870–3875.

[189] N. P. Armitage, D. H. Lu, et al. "Anomalous Electronic Structure and Pseudogap Effects in $Nd_{1.85}Ce_{0.15}CuO_4$". Phys. Rev. Lett. 87 (2001), p. 147003.

[190] B. Kyung, V. Hankevych, A.-M. Daré, and A.-M. S. Tremblay. "Pseudogap and Spin Fluctuations in the Normal State of the Electron-Doped Cuprates". Phys. Rev. Lett. 93 (2004), p. 147004.

[191] A. Kanigel, M. R. Norman, et al. "Evolution of the pseudogap from Fermi arcs to the nodal liquid". Nature Physics 2 (2006), pp. 447–451.

[192] A. Eberlein, W. Metzner, S. Sachdev, and H. Yamase. "Fermi Surface Reconstruction and Drop in the Hall Number due to Spiral Antiferromagnetism in High-T_c Cuprates". Phys. Rev. Lett. 117 (2016), p. 187001.

[193] M. S. Scheurer, S. Chatterjee, W. Wu, M. Ferrero, A. Georges, and S. Sachdev. "Topological order in the pseudogap metal". Proceedings of the National Academy of Sciences 115 (2018), E3665–E3672.

[194] S. Sachdev. "Topological order, emergent gauge fields, and Fermi surface reconstruction". Reports on Progress in Physics 82 (2018), p. 14001.

[195] N. Doiron-Leyraud, C. Proust, et al. "Quantum oscillations and the Fermi surface in an underdoped high-Tc superconductor". Nature 447 (2007), pp. 565–568.

[196] A. Kaminski, S. Rosenkranz, et al. "Spontaneous breaking of time-reversal symmetry in the pseudogap state of a high-Tc superconductor". Nature 416 (2002), pp. 610–613.

Die approbierte gedruckte Originalversion dieser Dissertation ist an der TU Wien Bibliothek verfügbar.
The approved original version of this doctoral thesis is available in print at TU Wien Bibliothek.
TU Bibliothek Your knowledge hub WIEN

[197] J. Xia, E. Schemm, et al. "Polar Kerr-Effect Measurements of the High-Temperature $YBa_2Cu_3O_{6+x}$ Superconductor: Evidence for Broken Symmetry near the Pseudogap Temperature". Phys. Rev. Lett. 100 (2008), p. 127002.

[198] L. Zhao, C. A. Belvin, et al. "A global inversion-symmetry-broken phase inside the pseudogap region of YBa2Cu3Oy". Nature Physics 13 (2016), pp. 250–254.

[199] P. W. Anderson, P. A. Lee, M. Randeria, T. M. Rice, N. Trivedi, and F. C. Zhang. "The physics behind high-temperature superconducting cuprates: the "plain vanilla" version of RVB". Journal of Physics: Condensed Matter 16 (2004), R755–R769.

[200] K.-Y. Yang, T. M. Rice, and F.-C. Zhang. "Phenomenological theory of the pseudogap state". Phys. Rev. B 73 (2006), p. 174501.

[201] P. A. Lee, N. Nagaosa, and X.-G. Wen. "Doping a Mott insulator: Physics of high-temperature superconductivity". Rev. Mod. Phys. 78 (2006), pp. 17–85.

[202] M. Punk, A. Allais, and S. Sachdev. "Quantum dimer model for the pseudogap metal". Proceedings of the National Academy of Sciences 112 (2015), pp. 9552–9557.

[203] S. Sakai, M. Civelli, and M. Imada. "Hidden Fermionic Excitation Boosting High-Temperature Superconductivity in Cuprates". Phys. Rev. Lett. 116 (2016), p. 57003.

[204] F. Krien and A. Valli. "Parquetlike equations for the Hedin three-leg vertex". Phys. Rev. B 100 (2019), p. 245147.

[205] See supplemental material of [139].

[206] S. Ouazi, J. Bobroff, H. Alloul, and W. A. MacFarlane. "Correlation length in cuprate superconductors deduced from impurity-induced magnetization". Phys. Rev. B 70 (2004), p. 104515.

[207] The importance of the AZB was also demonstrated at weak-to-intermediate coupling [**Honerkamp01**, 409–411], where paramagnon scattering leads to a deformation of the FS [412].

[208] A. Kampf and J. R. Schrieffer. "Pseudogaps and the spin-bag approach to high-T_c superconductivity". Phys. Rev. B 41 (1990), pp. 6399–6408.

[209] P. Monthoux and D. Pines. "$YBa_2Cu_3O_7$: A nearly antiferromagnetic Fermi liquid". Phys. Rev. B 47 (1993), pp. 6069–6081.

[210] A. Abanov, A. V. Chubukov, and J. Schmalian. "Quantum-critical theory of the spin-fermion model and its application to cuprates: Normal state analysis". Advances in Physics 52 (2003), pp. 119–218.

[211] Z. B. Huang, W. Hanke, and E. Arrigoni. "Role of vertex corrections in the spin-fluctuation–mediated pairing mechanism". Europhysics Letters (EPL) 71 (2005), pp. 959–965.

Die approbierte gedruckte Originalversion dieser Dissertation ist an der TU Wien Bibliothek verfügbar.
The approved original version of this doctoral thesis is available in print at TU Wien Bibliothek.
TU Bibliothek Your knowledge hub WIEN

[212] Z. B. Huang, W. Hanke, E. Arrigoni, and A. V. Chubukov. "Renormalization of the electron-spin-fluctuation interaction in the $t-t'-U$ Hubbard model". Phys. Rev. B 74 (2006), p. 184508.

[213] E. G. C. P. van Loon, F. Krien, H. Hafermann, A. I. Lichtenstein, and M. I. Katsnelson. "Fermion-boson vertex within dynamical mean-field theory". Phys. Rev. B 98 (2018), p. 205148.

[214] M. Pickem, J. Kaufmann, J. M. Tomczak, and K. Held. "Particle-hole asymmetric lifetimes promoted by spin and orbital fluctuations in ultrahin SrVO3 films". arXiv preprint arXiv:2008.12227 (2020).

[215] R. W. Godby, M. Schlüter, and L. J. Sham. "Self-energy operators and exchange-correlation potentials in semiconductors". Phys. Rev. B 37 (1988), pp. 10159–10175.

[216] G. Rohringer, A. Katanin, T. Schäfer, A. Hausoel, K. Held, and A. Toschi. "LadderDΓA code". github.com/ladderDGA (2018).

[217] A. N. Rubtsov, M. I. Katsnelson, and A. I. Lichtenstein. "Dual fermion approach to nonlocal correlations in the Hubbard model". Phys. Rev. B 77 (2008), p. 33101.

[218] G. V. Astretsov, G. Rohringer, and A. N. Rubtsov. "Dual parquet scheme for the two-dimensional Hubbard model: Modeling low-energy physics of high-T_c cuprates with high momentum resolution". Phys. Rev. B 101 (2020), p. 75109.

[219] P. M. Bonetti, A. Toschi, C. Hille, S. Andergassen, and D. Vilardi. "Single-boson exchange representation of the functional renormalization group for strongly interacting many-electron systems". Phys. Rev. Res. 4 (2022), p. 013034.

[220] D. Nicoletti, O. Limaj, et al. "High-Temperature Optical Spectral Weight and Fermi-liquid Renormalization in Bi-Based Cuprate Superconductors". Phys. Rev. Lett. 105 (2010), p. 77002.

[221] S. L. Adler. "Consistency Conditions on the Strong Interactions Implied by a Partially Conserved Axial-Vector Current". Phys. Rev. 137 (1965), B1022–B1033.

[222] J. R. Schrieffer. "Ward's identity and the suppression of spin fluctuation superconductivity". Journal of Low Temperature Physics 99 (1995), pp. 397–402.

[223] A. V. Chubukov and D. K. Morr. "Electronic structure of underdoped cuprates". Physics Reports 288 (1997), pp. 355–387.

[224] P. A. Igoshev, A. A. Katanin, and V. Y. Irkhin. "Magnetic fluctuations and itinerant ferromagnetism in two-dimensional systems with Van Hove singularities". Journal of Experimental and Theoretical Physics 105 (2007), pp. 1043–1056.

[225] F. Krien, A. I. Lichtenstein, and G. Rohringer. "Fluctuation diagnostic of the nodal/antinodal dichotomy in the Hubbard model at weak coupling: A parquet dual fermion approach". Phys. Rev. B 102 (2020), p. 235133.

[226] See [413] and references therein.

Die approbierte gedruckte Originalversion dieser Dissertation ist an der TU Wien Bibliothek verfügbar.
The approved original version of this doctoral thesis is available in print at TU Wien Bibliothek.
TU Bibliothek Your knowledge hub WIEN

[227] An analysis similar to Fig. 4.8 but for $\omega = 2\pi T$ (not shown) only yields a vanishingly small contribution.

[228] S. Sachdev, M. A. Metlitski, and M. Punk. "Antiferromagnetism in metals: from the cuprate superconductors to the heavy fermion materials". Journal of Physics: Condensed Matter 24 (2012), p. 294205.

[229] J. A. Sobota, Y. He, and Z.-X. Shen. "Angle-resolved photoemission studies of quantum materials". Rev. Mod. Phys. 93 (2021), p. 25006.

[230] W. Tabis, P. Popčević, et al. "Arc-to-pocket transition and quantitative understanding of transport properties in cuprate superconductors". preprint (2021), arXiv:2106.07457.

[231] J. Mayer, K. Khairy, and J. Howard. "Drawing an elephant with four complex parameters". American Journal of Physics 78 (2010), pp. 648–649.

[232] N. P. Armitage, F. Ronning, et al. "Doping Dependence of an n-Type Cuprate Superconductor Investigated by Angle-Resolved Photoemission Spectroscopy". Phys. Rev. Lett. 88 (2002), p. 257001.

[233] S. W. Jang, H. Sakakibara, H. Kino, T. Kotani, K. Kuroki, and M. J. Han. "Direct theoretical evidence for weaker correlations in electron-doped and Hg-based hole-doped cuprates". Scientific Reports 6 (2016), p. 33397.

[234] G. Li, A. Kauch, P. Pudleiner, and K. Held. "The victory project v1.0: An efficient parquet equations solver". Comp. Phys. Comm. 241 (2019), pp. 146–154.

[235] T. Schäfer, F. Geles, et al. "Fate of the false Mott-Hubbard transition in two dimensions". Phys. Rev. B 91 (2015), p. 125109.

[236] R. S. Markiewicz, S. Sahrakorpi, M. Lindroos, H. Lin, and A. Bansil. "One-band tight-binding model parametrization of the high-T_c cuprates including the effect of k_z dispersion". Phys. Rev. B 72 (2005), p. 054519.

[237] P. Worm, L. Si, M. Kitatani, R. Arita, J. M. Tomczak, and K. Held. "Correlations tune the electronic structure of pentalayer nickelates into the superconducting regime". Phys. Rev. Materials 6 (2022), p. L091801.

[238] M. Hashimoto, E. A. Nowadnick, et al. "Direct spectroscopic evidence for phase competition between the pseudogap and superconductivity in $Bi_2Sr_2CaCu_2O_{8+\delta}$". Nature Materials 14 (2015), pp. 37–42.

[239] W. S. Lee, I. M. Vishik, et al. "Abrupt onset of a second energy gap at the superconducting transition of underdoped Bi2212". Nature 450 (2007), pp. 81–84.

[240] M. Hashimoto, I. M. Vishik, R.-H. He, T. P. Devereaux, and Z.-X. Shen. "Energy gaps in high-transition-temperature cuprate superconductors". Nature Physics 10 (2014), pp. 483–495.

Die approbierte gedruckte Originalversion dieser Dissertation ist an der TU Wien Bibliothek verfügbar.
The approved original version of this doctoral thesis is available in print at TU Wien Bibliothek.
TU Bibliothek Your knowledge hub WIEN

[241] I. M. Vishik, W. S. Lee, et al. "ARPES studies of cuprate Fermiology: superconductivity, pseudogap and quasiparticle dynamics". New Journal of Physics 12 (2010), p. 105008.

[242] I. M. Vishik, M. Hashimoto, et al. "Phase competition in trisected superconducting dome". Proceedings of the National Academy of Sciences 109 (2012), pp. 18332–18337.

[243] R.-H. He, M. Hashimoto, et al. "From a Single-Band Metal to a High-Temperature Superconductor via Two Thermal Phase Transitions". Science 331 (2011), pp. 1579–1583.

[244] T. Schäfer, A. Toschi, K. Held, T. Schafer, A. Toschi, and K. Held. "Dynamical vertex approximation for the two-dimensional Hubbard model". Journal of Magnetism and Magnetic Materials 400 (2016), pp. 107–111.

[245] P. Pudleiner, T. Schäfer, D. Rost, G. Li, K. Held, and N. Blümer. "Momentum structure of the self-energy and its parametrization for the two-dimensional Hubbard model". Phys. Rev. B 93 (2016), p. 195134.

[246] V. I. Anisimov, I. A. Nekrasov, D. E. Kondakov, T. M. Rice, and M. Sigrist. "Orbital–selective Mott–insulator transition in $Ca_{2-x}Sr_xRuO_4$". The European Physical Journal B - Condensed Matter and Complex Systems 25 (2002), pp. 191–201.

[247] L. De'Medici, A. Georges, and S. Biermann. "Orbital-selective Mott transition in multiband systems: Slave-spin representation and dynamical mean-field theory". Phys. Rev. B 72 (2005), p. 205124.

[248] F. Simkovic, R. Rossi, A. Georges, and M. Ferrero. "Origin and fate of the pseudogap in the doped Hubbard model". preprint (2022), arXiv:2209.09237.

[249] J. M. Luttinger. "Fermi Surface and Some Simple Equilibrium Properties of a System of Interacting Fermions". Phys. Rev. 119 (1960), pp. 1153–1163.

[250] J. Skolimowski and M. Fabrizio. "Luttinger's theorem in the presence of Luttinger surfaces". Phys. Rev. B 106 (2022), p. 045109.

[251] K. B. Dave, P. W. Phillips, and C. L. Kane. "Absence of Luttinger's Theorem due to Zeros in the Single-Particle Green Function". Phys. Rev. Lett. 110 (2013), p. 090403.

[252] P. M. Bonetti and W. Metzner. "SU(2) gauge theory of the pseudogap phase in the two-dimensional Hubbard model". Phys. Rev. B 106 (2022), p. 205152.

[253] W. M. Li, J. F. Zhao, et al. "Superconductivity in a unique type of copper oxide". Proceedings of the National Academy of Sciences 116 (2019), pp. 12156–12160.

[254] R. Fumagalli, A. Nag, et al. "Crystalline and magnetic structure of Ba2CuO3+δ investigated by x-ray absorption spectroscopy and resonant inelastic x-ray scattering". Physica C: Superconductivity and its Applications 581 (2021), p. 1353810.

Die approbierte gedruckte Originalversion dieser Dissertation ist an der TU Wien Bibliothek verfügbar.
The approved original version of this doctoral thesis is available in print at TU Wien Bibliothek.
TU Bibliothek Your knowledge hub WIEN

[255] K. Liu, Z.-Y. Lu, and T. Xiang. "Electronic structures of quasi-one-dimensional cuprate superconductors $Ba_2CuO_{3+\delta}$". Phys. Rev. Materials 3 (2019), p. 44802.

[256] Z. Wang, S. Zhou, W. Chen, and F.-C. Zhang. "$t - J$ model on the effective brick-wall lattice for the recently discovered high-temperature superconductor $Ba_2CuO_{3+\delta}$". Phys. Rev. B 101 (2020), p. 180509.

[257] K. Jiang, C. Le, et al. "Electronic structure and two-band superconductivity in unconventional high-T_c cuprates $Ba_2CuO_{3+\delta}$". Phys. Rev. B 103 (2021), p. 045108.

[258] D. Li, B. Y. Wang, et al. "Superconducting Dome in $Nd_{1-x}Sr_xNiO_2$ Infinite Layer Films". Phys. Rev. Lett. 125 (2020), p. 27001.

[259] K. Yamazaki, M. Ochi, et al. "Superconducting mechanism for the cuprate $Ba_2CuO_{3+\delta}$ based on a multiorbital Lieb lattice model". Phys. Rev. Research 2 (2020), p. 033356.

[260] See supplemental material of [143].

[261] H. Yamamoto, M. Naito, and H. Sato. "A new superconducting barium cuprate prepared by molecular beam epitaxy". Physica C: Superconductivity 338 (2000), pp. 29–37.

[262] G. Kotliar and D. Vollhardt. "Strongly Correlated Materials: Insights from Dynamical Mean-Field Theory". Physics Today 57 (2004), p. 53.

[263] K. Schwarz, P. Blaha, and G. K. H. Madsen. "Electronic structure calculations of solids using the WIEN2k package for material sciences". Comp. Phys. Comm. 147 (2002), pp. 71–76.

[264] J. P. Perdew, A. Ruzsinszky, et al. "Restoring the Density-Gradient Expansion for Exchange in Solids and Surfaces". Phys. Rev. Lett. 100 (2008), p. 136406.

[265] A. V. Khoroshilov and I. S. Shaplygin. "Crystal growth in the Y-Ba-Cu-O and Bi-Sr-Ca-Cu-O systems". Inorganic Materials 30 (1994).

[266] G. Pizzi, V. Vitale, et al. "Wannier90 as a community code: new features and applications". Journal of Physics: Condensed Matter 32 (2020), p. 165902.

[267] J. Kaufmann, P. Gunacker, A. Kowalski, G. Sangiovanni, and K. Held. "Symmetric improved estimators for continuous-time quantum Monte Carlo". Phys. Rev. B 100 (2019), p. 075119.

[268] G. Kresse and J. Furthmüller. "Efficient iterative schemes for ab initio total-energy calculations using a plane-wave basis set". Phys. Rev. B 54 (1996), pp. 11169–11186.

[269] G. Kresse and J. Hafner. "Norm-conserving and ultrasoft pseudopotentials for first-row and transition elements". Journal of Physics: Condensed Matter 6 (1994), pp. 8245–8257.

Die approbierte gedruckte Originalversion dieser Dissertation ist an der TU Wien Bibliothek verfügbar.
The approved original version of this doctoral thesis is available in print at TU Wien Bibliothek.
TU Bibliothek Your knowledge hub WIEN

[270] T. Miyake, F. Aryasetiawan, and M. Imada. "Ab initio procedure for constructing effective models of correlated materials with entangled band structure". Phys. Rev. B 80 (2009), p. 155134.

[271] M. Casula, A. Rubtsov, and S. Biermann. "Dynamical screening effects in correlated materials: Plasmon satellites and spectral weight transfers from a Green's function ansatz to extended dynamical mean field theory". Phys. Rev. B 85 (2012), p. 35115.

[272] A. van Roekeghem, T. Ayral, et al. "Dynamical Correlations and Screened Exchange on the Experimental Bench: Spectral Properties of the Cobalt Pnictide $BaCo_2As_2$". Phys. Rev. Lett. 113 (2014), p. 266403.

[273] A. A. Mostofi, J. R. Yates, Y.-S. Lee, I. Souza, D. Vanderbilt, and N. Marzari. "wannier90: A tool for obtaining maximally-localised Wannier functions". Computer Physics Communications 178 (2008), pp. 685–699.

[274] V. I. Anisimov, J. Zaanen, and O. K. Andersen. "Band theory and Mott insulators: Hubbard U instead of Stoner I". Phys. Rev. B 44 (1991), pp. 943–954.

[275] T. Miyake, C. Martins, R. Sakuma, and F. Aryasetiawan. "Effects of momentum-dependent self-energy in the electronic structure of correlated materials". Phys. Rev. B 87 (2013), p. 115110.

[276] J. M. Tomczak, M. Casula, T. Miyake, and S. Biermann. "Asymmetry in band widening and quasiparticle lifetimes in $SrVO_3$: Competition between screened exchange and local correlations from combined GW and dynamical mean-field theory GW + DMFT". Phys. Rev. B 90 (2014), p. 165138.

[277] N. Parragh, A. Toschi, K. Held, and G. Sangiovanni. "Conserved quantities of $SU(2)$-invariant interactions for correlated fermions and the advantages for quantum Monte Carlo simulations". Phys. Rev. B 86 (2012), p. 155158.

[278] M. Wallerberger, A. Hausoel, et al. "w2dynamics: Local one- and two-particle quantities from dynamical mean field theory". Comp. Phys. Comm. 235 (2019), pp. 388–399.

[279] T. Maier, T. Berlijn, and D. J. Scalapino. "Two pairing domes as Cu2+ varies to Cu3+". Physical Review B 99 (2019).

[280] J. E. Gubernatis, M. Jarrell, R. N. Silver, and D. S. Sivia. "Quantum Monte Carlo simulations and maximum entropy: Dynamics from imaginary-time data". Phys. Rev. B 44 (1991), pp. 6011–6029.

[281] A. W. Sandvik. "Stochastic method for analytic continuation of quantum Monte Carlo data". Phys. Rev. B 57 (1998), pp. 10287–10290.

[282] Y. Ni, Y.-M. Quan, J. Liu, Y. Song, and L.-J. Zou. "Electronic correlation-driven orbital polarization transitions in the orbital-selective Mott compound $Ba_2CuO_{4-\delta}$". Phys. Rev. B 103 (2021), p. 214510.

Die approbierte gedruckte Originalversion dieser Dissertation ist an der TU Wien Bibliothek verfügbar.
The approved original version of this doctoral thesis is available in print at TU Wien Bibliothek.
TU Bibliothek Your knowledge hub WIEN

[283] D. Rybicki, M. Jurkutat, S. Reichardt, C. Kapusta, and J. Haase. "Perspective on the phase diagram of cuprate high-temperature superconductors". Nat Commun 7 (2016), p. 11413.

[284] Z.-Q. Gao, K.-W. Sun, and F. Wang. "Nodeless s-Wave Superconducting Phases in Cuprates with Ba_2CuO_3-Type Structure". The European Physical Journal B 94 (2020), pp. 1434–6036.

[285] M. Klett, T. Schwemmer, et al. "From high T_c to low T_c: Multiorbital effects in transition metal oxides". Phys. Rev. B 104 (2021), p. L100502.

[286] M. Zegrodnik, P. Wójcik, and J. Spałek. "Superconducting dome with extended s-wave pairing symmetry in the heavily hole-overdoped copper-oxide planes". Phys. Rev. B 103 (2021), p. 144511.

[287] K. Shigeta, S. Onari, K. Yada, and Y. Tanaka. "Theory of odd-frequency pairings on a quasi-one-dimensional lattice in the Hubbard model". Phys. Rev. B 79 (2009), p. 174507.

[288] M. G. Smith, A. Manthiram, J. Zhou, J. B. Goodenough, and J. T. Markert. "Electron-doped superconductivity at 40 K in the infinite-layer compound Sr1–yNdyCu02". Nature 351 (1991), pp. 549–551.

[289] N. P. Armitage, P. Fournier, and R. L. Greene. "Progress and perspectives on electron-doped cuprates". Rev. Mod. Phys. 82 (2010), pp. 2421–2487.

[290] A. Kreisel, B. M. Andersen, A. T. Rømer, I. M. Eremin, and F. Lechermann. "Superconducting Instabilities in Strongly Correlated Infinite-Layer Nickelates". Phys. Rev. Lett. 129 (2022), p. 077002.

[291] V. Christiansson, F. Petocchi, and P. Werner. "GW + EDMFT investigation of $Pr_{1-x}Sr_xNiO_2$ under pressure". Phys. Rev. B 107 (2023), p. 045144.

[292] B. Kang, C. Melnick, et al. "Infinite-layer nickelates as Ni-eg Hund's metals". arXiv preprint arXiv:2007.14610 (2020).

[293] M. Osada, B. Y. Wang, K. Lee, D. Li, and H. Y. Hwang. "Phase diagram of infinite layer praseodymium nickelate $Pr_{1-x}Sr_xNiO_2$ thin films". Phys. Rev. Materials 4 (2020), p. 121801.

[294] Y.-T. Hsu, M. Osada, et al. "Correlated Insulating Behavior in Infinite-Layer Nickelates". Frontiers in Physics 10 (2022).

[295] L. Si, P. Worm, and K. Held. "Formation of hydrogen chains in ABO_2 nickelate superconductors". 2022.

[296] V. I. Anisimov, D. Bukhvalov, and T. M. Rice. "Electronic structure of possible nickelate analogs to the cuprates". Phys. Rev. B 59 (1999), pp. 7901–7906.

[297] J. Chaloupka and G. Khaliullin. "Orbital Order and Possible Superconductivity in $LaNiO_3/LaMO_3$ Superlattices". Physical Review Letters 100 (2008), p. 16404.

Die approbierte gedruckte Originalversion dieser Dissertation ist an der TU Wien Bibliothek verfügbar.
The approved original version of this doctoral thesis is available in print at TU Wien Bibliothek.
TU Bibliothek Your knowledge hub WIEN

[298] P. Hansmann, X. Yang, A. Toschi, G. Khaliullin, O. K. Andersen, and K. Held. "Turning a Nickelate Fermi Surface into a Cupratelike One through Heterostructuring". Phys. Rev. Lett. 103 (2009), p. 16401.

[299] P. Hansmann, A. Toschi, X. Yang, O. K. Andersen, and K. Held. "Electronic structure of nickelates: From two-dimensional heterostructures to three-dimensional bulk materials". Phys. Rev. B 82 (2010), p. 235123.

[300] T. Siegrist, S. M. Zahurak, D. W. Murphy, and R. S. Roth. "The parent structure of the layered high-temperature superconductors". Nature 334 (1988), pp. 231–232.

[301] G. Balestrino, P. G. Medaglia, et al. "Very Large Purely Intralayer Critical Current Density in Ultrathin Cuprate Artificial Structures". Phys. Rev. Lett. 89 (2002), p. 156402.

[302] P. Orgiani, C. Aruta, et al. "Direct Measurement of Sheet Resistance $R_{\square}$ in Cuprate Systems: Evidence of a Fermionic Scenario in a Metal-Insulator Transition". Phys. Rev. Lett. 98 (2007), p. 36401.

[303] D. Di Castro, C. Cantoni, et al. "High-T_c Superconductivity at the Interface between the $CaCuO_2$ and $SrTiO_3$ Insulating Oxides". Phys. Rev. Lett. 115 (2015), p. 147001.

[304] E. Pavarini, I. Dasgupta, T. Saha-Dasgupta, O. Jepsen, and O. K. Andersen. "Band-Structure Trend in Hole-Doped Cuprates and Correlation with $T_{c\max}$". Phys. Rev. Lett. 87 (2001), p. 47003.

[305] M. Jiang, M. Berciu, and G. A. Sawatzky. "Critical Nature of the Ni Spin State in Doped $NdNiO_2$". Phys. Rev. Lett. 124 (2020), p. 207004.

[306] P. Werner and S. Hoshino. "Nickelate superconductors: Multiorbital nature and spin freezing". Phys. Rev. B 101 (2020), p. 41104.

[307] H. Sakakibara, H. Usui, K. Suzuki, T. Kotani, H. Aoki, and K. Kuroki. "Model Construction and a Possibility of Cupratelike Pairing in a New d^9 Nickelate Superconductor $(Nd,Sr)NiO_2$". Phys. Rev. Lett. 125 (2020), p. 77003.

[308] M. Hirayama, T. Tadano, Y. Nomura, and R. Arita. "Materials design of dynamically stable d^9 layered nickelates". Phys. Rev. B 101 (2020), p. 75107.

[309] L.-H. Hu and C. Wu. "Two-band model for magnetism and superconductivity in nickelates". Phys. Rev. Research 1 (2019), p. 32046.

[310] X. Wu, D. Di Sante, et al. "Robust $d_{x^2-y^2}$-wave superconductivity of infinite-layer nickelates". Phys. Rev. B 101 (2020), p. 60504.

[311] Y. Nomura, M. Hirayama, T. Tadano, Y. Yoshimoto, K. Nakamura, and R. Arita. "Formation of a two-dimensional single-component correlated electron system and band engineering in the nickelate superconductor $NdNiO_2$". Phys. Rev. B 100 (2019), p. 205138.

Die approbierte gedruckte Originalversion dieser Dissertation ist an der TU Wien Bibliothek verfügbar.
The approved original version of this doctoral thesis is available in print at TU Wien Bibliothek.
TU Bibliothek Your knowledge hub WIEN

[312] G.-M. Zhang, Y.-F. Yang, and F.-C. Zhang. "Self-doped Mott insulator for parent compounds of nickelate superconductors". Phys. Rev. B 101 (2020), p. 20501.

[313] F. Lechermann. "Late transition metal oxides with infinite-layer structure: Nickelates versus cuprates". Phys. Rev. B 101 (2020), p. 81110.

[314] F. Lechermann. "Multiorbital Processes Rule the $Nd_{1-x}Sr_xNiO_2$ Normal State". Phys. Rev. X 10 (2020), p. 41002.

[315] P. Adhikary, S. Bandyopadhyay, T. Das, I. Dasgupta, and T. Saha-Dasgupta. "Orbital-selective superconductivity in a two-band model of infinite-layer nickelates". Phys. Rev. B 102 (2020), p. 100501.

[316] S. Bandyopadhyay, P. Adhikary, T. Das, I. Dasgupta, and T. Saha-Dasgupta. "Superconductivity in infinite-layer nickelates: Role of f orbitals". Phys. Rev. B 102 (2020), p. 220502.

[317] J. Zaanen, G. A. Sawatzky, and J. W. Allen. "Band gaps and electronic structure of transition-metal compounds". Phys. Rev. Lett. 55 (1985), pp. 418–421.

[318] V. J. Emery. "Theory of high–T_c superconductivity in oxides". Phys. Rev. Lett. 58 (1987), pp. 2794–2797.

[319] J. Hubbard. "Electron correlations in narrow energy bands". Proceedings of the Royal Society of London. Series A, Mathematical and Physical Sciences 276 (1963), pp. 238–257.

[320] M. C. Gutzwiller. "Effect of Correlation on the Ferromagnetism of Transition Metals". Phys. Rev. Lett. 10 (1963), pp. 159–162.

[321] M. Jarrell. "Hubbard model in infinite dimensions: A quantum Monte Carlo study". Phys. Rev. Lett. 69 (1992), pp. 168–171.

[322] A. Georges and W. Krauth. "Numerical solution of the $d = \infty$ Hubbard model: Evidence for a Mott transition". Phys. Rev. Lett. 69 (1992), pp. 1240–1243.

[323] S. Zeng, C. S. Tang, et al. "Phase Diagram and Superconducting Dome of Infinite-Layer $Nd_{1-x}Sr_xNiO_2$ Thin Films, arXiv:2004.11281". Phys. Rev. Lett. 125 (2020), p. 147003.

[324] G. Kresse and J. Hafner. "Ab initio molecular dynamics for open-shell transition metals". Phys. Rev. B 48 (1993), pp. 13115–13118.

[325] K. Koepernik and H. Eschrig. "Full-potential nonorthogonal local-orbital minimum-basis band-structure scheme". Phys. Rev. B 59 (1999), pp. 1743–1757.

[326] Y. Nomura and R. Arita. "Superconductivity in infinite-layer nickelates". Reports on Progress in Physics 85 (2022), p. 052501.

[327] P. Hansmann, N. Parragh, A. Toschi, G. Sangiovanni, and K. Held. "Importance of d–p Coulomb interaction for high T_c cuprates and other oxides". New J. Phys. 16 (2014), p. 33009.

Die approbierte gedruckte Originalversion dieser Dissertation ist an der TU Wien Bibliothek verfügbar.
The approved original version of this doctoral thesis is available in print at TU Wien Bibliothek.
TU Bibliothek Your knowledge hub WIEN

[328] K. Held, I. A. Nekrasov, et al. "Realistic investigations of correlated electron systems with LDA+DMFT". physica status solidi (b) 243 (2006), pp. 2599–2631.

[329] M. Hepting, D. Li, et al. "Electronic structure of the parent compound of superconducting infinite-layer nickelates". Nature Materials 19 (2020), pp. 381–385.

[330] K. Higashi, M. Winder, J. Kuneš, and A. Hariki. "Core-Level X-Ray Spectroscopy of Infinite-Layer Nickelate: LDA + DMFT Study". Phys. Rev. X 11 (2021), p. 41009.

[331] Y. Gu, S. Zhu, X. Wang, J. Hu, and H. Chen. "A substantial hybridization between correlated Ni-d orbital and itinerant electrons in infinite-layer nickelates". Commun. Phy. 3 (2020), p. 84.

[332] P. Jiang, L. Si, Z. Liao, and Z. Zhong. "Electronic structure of rare-earth infinite-layer $R\mathrm{NiO}_2$ ($R = \mathrm{La}, \mathrm{Nd}$)". Phys. Rev. B 100 (2019), p. 201106.

[333] M.-Y. Choi, K.-W. Lee, and W. E. Pickett. "Role of $4f$ states in infinite-layer NdNiO_2". Phys. Rev. B 101 (2020), p. 20503.

[334] S. Zeng, C. Li, et al. "Superconductivity in infinite-layer lanthanide nickelates". arXiv:2105.13492 (2021).

[335] A. E. Antipov, E. Gull, and S. Kirchner. "Critical Exponents of Strongly Correlated Fermion Systems from Diagrammatic Multiscale Methods". Phys. Rev. Lett. 112 (2014), p. 226401.

[336] T. Schäfer, A. A. Katanin, K. Held, and A. Toschi. "Interplay of Correlations and Kohn Anomalies in Three Dimensions: Quantum Criticality with a Twist". Phys. Rev. Lett. 119 (2017), p. 46402.

[337] T. Schäfer, A. A. Katanin, M. Kitatani, A. Toschi, and K. Held. "Quantum Criticality in the Two-Dimensional Periodic Anderson Model". Phys. Rev. Lett. 122 (2019), p. 227201.

[338] G. Li, N. Wentzell, P. Pudleiner, P. Thunström, and K. Held. "Efficient implementation of the parquet equations: Role of the reducible vertex function and its kernel approximation". Phys. Rev. B 93 (2016), p. 165103.

[339] Y. Cui, C. Li, et al. "NMR Evidence of Antiferromagnetic Spin Fluctuations in $\mathrm{Nd}_{0.85}\mathrm{Sr}_{0.15}\mathrm{NiO}_2$". Chin. Phys. Lett. 38 (2021), p. 67401.

[340] J. M. Tomczak, T. Miyake, R. Sakuma, and F. Aryasetiawan. "Effective Coulomb interactions in solids under pressure". Phys. Rev. B 79 (2009), p. 235133.

[341] N. Wang, M. Yang, et al. "Pressure-induced monotonic enhancement of T_c to over 30 K in the superconducting $\mathrm{Pr}_{0.82}\mathrm{Sr}_{0.18}\mathrm{NiO}_2$ thin films". arXiv:2109.12811 (2021).

[342] Z. Chen, M. Osada, et al. "Electronic structure of superconducting nickelates probed by resonant photoemission spectroscopy". arXiv:2106.03963 (2021).

[343] T. Katayama, A. Chikamatsu, et al. "Epitaxial growth and electronic structure of oxyhydride $\mathrm{SrVO}_2\mathrm{H}$ thin films". Journal of Applied Physics 120 (2016), p. 85305.

Die approbierte gedruckte Originalversion dieser Dissertation ist an der TU Wien Bibliothek verfügbar.
The approved original version of this doctoral thesis is available in print at TU Wien Bibliothek.
TU Bibliothek Your knowledge hub WIEN

[344] O. I. Malyi, J. Varignon, and A. Zunger. "Bulk $NdNiO_2$ is thermodynamically unstable with respect to decomposition while hydrogenation reduces the instability and transforms it from metal to insulator". Phys. Rev. B 105 (2022), p. 14106.

[345] G. A. Pan, D. F. Segedin, et al. "Superconductivity in a quintuple-layer square-planar nickelate". Nature Materials (2021).

[346] H. LaBollita and A. S. Botana. "Electronic structure and magnetic properties of higher-order layered nickelates: $La_{n+1}Ni_nO_{2n+2}(n = 4 - 6)$". Phys. Rev. B 104 (2021), p. 35148.

[347] Z. Liu, H. Sun, et al. "Evidence for charge and spin density waves in single crystals of La3Ni2O7 and La3Ni2O6". Science China Physics, Mechanics & Astronomy 66 (2022), p. 217411.

[348] G. Kresse and J. Furthmüller. "Efficiency of ab-initio total energy calculations for metals and semiconductors using a plane-wave basis set". Computational Materials Science 6 (1996), pp. 15–50.

[349] P. Haas, F. Tran, and P. Blaha. "Calculation of the lattice constant of solids with semilocal functionals". Phys. Rev. B 79 (2009), p. 85104.

[350] A. Kokalj. "XCrySDen—a new program for displaying crystalline structures and electron densities". Journal of Molecular Graphics and Modelling 17 (1999), pp. 176–179.

[351] I. A. Nekrasov, K. Held, et al. "Momentum-resolved spectral functions of $SrVO_3$ calculated by LDA + DMFT". Phys. Rev. B 73 (2006), p. 155112.

[352] G. Lantz, M. Hajlaoui, et al. "Surface Effects on the Mott-Hubbard Transition in Archetypal V_2O_3". Phys. Rev. Lett. 115 (2015), p. 236802.

[353] G. J. Kraberger, R. Triebl, M. Zingl, and M. Aichhorn. "Maximum entropy formalism for the analytic continuation of matrix-valued Green's functions". Phys. Rev. B 96 (2017), p. 155128.

[354] D. Bergeron and A.-M. S. Tremblay. "Algorithms for optimized maximum entropy and diagnostic tools for analytic continuation". Phys. Rev. E 94 (2016), p. 23303.

[355] M. Kitatani, R. Arita, T. Schäfer, and K. Held. "Strongly correlated superconductivity with long-range spatial fluctuations". Journal of Physics: Materials 5 (2022), p. 034005.

[356] Q. Han, B. Chakrabarti, and K. Haule. "Investigation into the inadequacy of cRPA in reproducing screening in strongly correlated systems". 2018.

[357] C. Honerkamp, H. Shinaoka, F. F. Assaad, and P. Werner. "Limitations of constrained random phase approximation downfolding". Phys. Rev. B 98 (2018), p. 235151.

[358] Q. Gu, Y. Li, et al. "Single particle tunneling spectrum of superconducting Nd1-xSrxNiO2 thin films". Nature Comm. 11 (2020), p. 6027.

Die approbierte gedruckte Originalversion dieser Dissertation ist an der TU Wien Bibliothek verfügbar.
The approved original version of this doctoral thesis is available in print at TU Wien Bibliothek.
TU Bibliothek Your knowledge hub WIEN

[359] S. P. Harvey, B. Y. Wang, et al. "Evidence for nodal superconductivity in infinite-layer nickelates". 2022.

[360] L. E. Chow, S. K. Sudheesh, et al. "Pairing symmetry in infinite-layer nickelate superconductor". 2022.

[361] F. Petocchi, V. Christiansson, F. Nilsson, F. Aryasetiawan, and P. Werner. "Normal State of $Nd_{1-x}Sr_xNiO_2$ from Self-Consistent $GW + EDMFT$". Phys. Rev. X 10 (2020), p. 41047.

[362] Y.-f. Yang and G.-M. Zhang. "Self-Doping and the Mott-Kondo Scenario for Infinite-Layer Nickelate Superconductors". Frontiers in Physics 9 (2022).

[363] Á. A. C. Álvarez, L. Iglesias, S. Petit, W. Prellier, M. Bibes, and J. Varignon. "Charge ordering as the driving mechanism for superconductivity in rare-earth nickel oxides". 2022.

[364] T. Schäfer and A. Toschi. "How to read between the lines of electronic spectra: the diagnostics of fluctuations in strongly correlated electron systems". Journal of Physics: Condensed Matter 33 (2021), p. 214001.

[365] P. A. Lee, N. Nagaosa, and X.-G. Wen. "No Title". Rev. Mod. Phys. 78 (2006), p. 17.

[366] E. Fradkin, S. A. Kivelson, and J. M. Tranquada. "Colloquium: Theory of intertwined orders in high temperature superconductors". Rev. Mod. Phys. 87 (2015), pp. 457–482.

[367] H. Lin, D. J. Gawryluk, et al. "Universal spin-glass behaviour in bulk LaNiO2, PrNiO2 and NdNiO2". New Journal of Physics 24 (2022), p. 013022.

[368] R. A. Ortiz, P. Puphal, et al. "Magnetic correlations in infinite-layer nickelates: An experimental and theoretical multimethod study". Phys. Rev. Res. 4 (2022), p. 023093.

[369] M. Oda, N. Momono, and M. Ido. "Electronic phase diagram of $La_{2-x}Sr_xCuO_4$". Journal of Physics and Chemistry of Solids 65 (2004), pp. 1381–1390.

[370] J. Fowlie, M. Hadjimichael, et al. "Intrinsic magnetism in superconducting infinite-layer nickelates". Nature Physics 18 (2022), pp. 1043–1047.

[371] L. J. P. Ament, M. van Veenendaal, T. P. Devereaux, J. P. Hill, and J. van den Brink. "Resonant inelastic x-ray scattering studies of elementary excitations". Rev. Mod. Phys. 83 (2011), pp. 705–767.

[372] J.-Y. P. Delannoy, M. J. P. Gingras, P. C. W. Holdsworth, and A.-M. S. Tremblay. "Low-energy theory of the $t-t'-t''-U$ Hubbard model at half-filling: Interaction strengths in cuprate superconductors and an effective spin-only description of La_2CuO_4". Phys. Rev. B 79 (2009), p. 235130.

[373] R. Coldea, S. M. Hayden, et al. "Spin Waves and Electronic Interactions in La_2CuO_4". Phys. Rev. Lett. 86 (2001), pp. 5377–5380.

Die approbierte gedruckte Originalversion dieser Dissertation ist an der TU Wien Bibliothek verfügbar.
The approved original version of this doctoral thesis is available in print at TU Wien Bibliothek.
TU Bibliothek Your knowledge hub WIEN

[374] Y. Fukuzumi, K. Mizuhashi, K. Takenaka, and S. Uchida. "Universal Superconductor-Insulator Transition and T_c Depression in Zn-Substituted High- T_c Cuprates in the Underdoped Regime". Phys. Rev. Lett. 76 (1996), pp. 684–687.

[375] H. Hobou, S. Ishida, et al. "Enhancement of the superconducting critical temperature in $Bi_2Sr_2CaCu_2O_{8+\delta}$ by controlling disorder outside CuO_2 planes". Phys. Rev. B 79 (2009), p. 064507.

[376] H. Eisaki, N. Kaneko, et al. "Effect of chemical inhomogeneity in bismuth-based copper oxide superconductors". Phys. Rev. B 69 (2004), p. 064512.

[377] K. Fujita, T. Noda, K. M. Kojima, H. Eisaki, and S. Uchida. "Effect of Disorder Outside the CuO_2 Planes on T_c of Copper Oxide Superconductors". Phys. Rev. Lett. 95 (2005), p. 097006.

[378] D. A. Bonn, S. Kamal, et al. "Comparison of the influence of Ni and Zn impurities on the electromagnetic properties of $YBa_2Cu_3O_{6.95}$". Phys. Rev. B 50 (1994), pp. 4051–4063.

[379] J. M. Tomczak. "Private communication". 2022.

[380] Q. Gao, S. Fan, et al. "Magnetic Excitations in Strained Infinite-layer Nickelate PrNiO2". 2022.

[381] M. Hücker, K. Chung, M. Chand, T. Vogt, J. M. Tranquada, and D. J. Buttrey. "Oxygen and strontium codoping of La_2NiO_4: Room-temperature phase diagrams". Phys. Rev. B 70 (2004), p. 064105.

[382] L. Si, P. Worm, and K. Held. "Fingerprints of Topotactic Hydrogen in Nickelate Superconductors". Crystals 12 (2022).

[383] B. Geisler and R. Pentcheva. "Correlated interface electron gas in infinite-layer nickelate versus cuprate films on $SrTiO_3(001)$". Phys. Rev. Research 3 (2021), p. 13261.

[384] H. LaBollita and A. S. Botana. "Correlated electronic structure of a quintuple-layer nickelate". Phys. Rev. B 105 (2022), p. 085118.

[385] Y. Kamihara, T. Watanabe, M. Hirano, and H. Hosono. "Iron-Based Layered Superconductor $La[O_{1-x}F_x]FeAs$ (x = 0.05-0.12) with $T_c = 26$ K". Journal of the American Chemical Society 130 (2008), pp. 3296–3297.

[386] L. Boeri, O. V. Dolgov, and A. A. Golubov. "Is $LaFeAsO_{1-x}F_x$ an Electron-Phonon Superconductor?" Phys. Rev. Lett. 101 (2008), p. 26403.

[387] K. Held, A. A. Katanin, and A. Toschi. "Dynamical Vertex Approximation: An Introduction". Progress of Theoretical Physics Supplement 176 (2008), pp. 117–133.

[388] F. Bernardini, A. Bosin, and A. Cano. "Geometric effects in the infinite-layer nickelates". Phys. Rev. Mater. 6 (2022), p. 044807.

Die approbierte gedruckte Originalversion dieser Dissertation ist an der TU Wien Bibliothek verfügbar.
The approved original version of this doctoral thesis is available in print at TU Wien Bibliothek.
TU Bibliothek Your knowledge hub WIEN

[389] P. Puphal, V. Pomjakushin, et al. "Investigation of Hydrogen Incorporations in Bulk Infinite-Layer Nickelates". Frontiers in Physics 10 (2022).

[390] L. Bellaiche and D. Vanderbilt. "Virtual crystal approximation revisited: Application to dielectric and piezoelectric properties of perovskites". Phys. Rev. B 61 (2000), pp. 7877–7882.

[391] C. Eckhardt, K. Hummer, and G. Kresse. "Indirect-to-direct gap transition in strained and unstrained Sn_xGe_{1-x} alloys". Phys. Rev. B 89 (2014), p. 165201.

[392] G. Kresse and J. Hafner. "Ab initio molecular dynamics for liquid metals". Phys. Rev. B 47 (1993), pp. 558–561.

[393] A. Togo and I. Tanaka. "First principles phonon calculations in materials science". Scripta Materialia 108 (2015), pp. 1–5.

[394] S. Baroni, S. de Gironcoli, A. Dal Corso, and P. Giannozzi. "Phonons and related crystal properties from density-functional perturbation theory". Rev. Mod. Phys. 73 (2001), pp. 515–562.

[395] M. Rossi, M. Osada, et al. "A broken translational symmetry state in an infinite-layer nickelate". Nature Physics 18 (2022), pp. 869–873.

[396] G. Krieger, L. Martinelli, et al. "Charge and Spin Order Dichotomy in $NdNiO_2$ Driven by the Capping Layer". Phys. Rev. Lett. 129 (2022), p. 027002.

[397] X. Ren, J. Li, et al. "Strain-induced enhancement of T_c in infinite-layer $Pr_{0.8}Sr_{0.2}NiO_2$ films". 2021.

[398] P. Puphal, B. Wehinger, et al. "Synthesis and physical properties of $LaNiO_2$ crystals". Phys. Rev. Mater. 7 (2023), p. 014804.

[399] C. C. Tam, J. Choi, et al. "Charge density waves in infinite-layer NdNiO2 nickelates". Nature Materials 21 (2022), pp. 1116–1120.

[400] M. Kitatani, L. Si, P. Worm, J. M. Tomczak, R. Arita, and K. Held. "Optimizing superconductivity: from cuprates via nickelates to palladates". 2022.

[401] Z. Wang, G.-M. Zhang, Y.-f. Yang, and F.-C. Zhang. "Distinct pairing symmetries of superconductivity in infinite-layer nickelates". Phys. Rev. B 102 (2020), p. 220501.

[402] F. Lechermann. "Emergent flat-band physics in $d^{9-\delta}$ multilayer nickelates". Phys. Rev. B 105 (2022), p. 155109.

[403] H. Chen, A. Hampel, J. Karp, F. Lechermann, and A. J. Millis. "Dynamical Mean Field Studies of Infinite Layer Nickelates: Physics Results and Methodological Implications". Frontiers in Physics 10 (2022).

[404] N. N. Wang, M. W. Yang, et al. "Pressure-induced monotonic enhancement of Tc to over 30 K in superconducting Pr0.82Sr0.18NiO2 thin films". Nature Communications 13 (2022), p. 4367.

Die approbierte gedruckte Originalversion dieser Dissertation ist an der TU Wien Bibliothek verfügbar.
The approved original version of this doctoral thesis is available in print at TU Wien Bibliothek.
TU Bibliothek Your knowledge hub WIEN

[405] J. T. Heath and K. S. Bedell. "Necessary and sufficient conditions for the validity of Luttinger's theorem". New Journal of Physics 22 (2020), p. 63011.

[406] J. M. Luttinger and J. C. Ward. "Ground-State Energy of a Many-Fermion System. II". Phys. Rev. 118 (1960), pp. 1417–1427.

[407] H.-S. Jin, W. E. Pickett, and K.-W. Lee. "Two-band conduction and nesting instabilities in superconducting $Ba_2CuO_{3+\delta}$: First-principles study". Phys. Rev. B 104 (2021), p. 054516.

[408] E. Gull, P. Staar, et al. "Submatrix updates for the continuous-time auxiliary-field algorithm". Phys. Rev. B 83 (2011), p. 75122.

[409] C. J. Halboth and W. Metzner. "Renormalization-group analysis of the two-dimensional Hubbard model". Phys. Rev. B 61 (2000), pp. 7364–7377.

[410] A. Läuchli, C. Honerkamp, and T. M. Rice. "*d*-Mott Phases in One and Two Dimensions". Phys. Rev. Lett. 92 (2004), p. 37006.

[411] C. Honerkamp, M. Salmhofer, and T. M. Rice. "Flow to strong coupling in the two-dimensional Hubbard model". The European Physical Journal B - Condensed Matter 27 (2002), pp. 127–134.

[412] N. J. Robinson, P. D. Johnson, T. M. Rice, and A. M. Tsvelik. "Anomalies in the pseudogap phase of the cuprates: competing ground states and the role of umklapp scattering". Reports on Progress in Physics 82 (2019), p. 126501.

[413] R. Comin, A. Frano, et al. "Charge Order Driven by Fermi-Arc Instability in $Bi_2Sr_{2-x}LaxCuO_{6+\delta}$". Science 343 (2014), pp. 390–392.

Die approbierte gedruckte Originalversion dieser Dissertation ist an der TU Wien Bibliothek verfügbar.
The approved original version of this doctoral thesis is available in print at TU Wien Bibliothek.
TU Bibliothek Your knowledge hub WIEN

Acknowledgments

My doctor says that I have a malformed public-duty gland and a natural deficiency in moral fibre and that I am therefore excused from saving universes.
— Douglas Adams

A doctoral thesis is a single document written by a single author, yet it would hardly be possible to complete it without the continuous support of others. During my time as a Ph.D. student, I had the great opportunity to meet and work with many great minds and I would like to say a few words of gratitude toward them.

First, let me thank my supervisor **Karsten Held**, without whom this journey would never have started in the first place. I am genuinely impressed by his deep understanding of physics, specifically about strongly correlated systems. But I am most grateful that he always supported me in attending scientific conferences and summer schools. Nothing increased my motivation like a conference where you can meet some of the brightest minds in the field. Special thanks also go to **Liang Si**, who co-supervised my thesis and continually spearheaded new projects and ideas. He never tired of explaining the necessary physics or introducing me to codes. I would not be where I am today without him.

The daily work would, however, not be the same without my office colleagues. My thanks go to **Michael Wais** for good laughs, great discussions, and generally staying a close friend to this day. Also, to **Josef Kaufmann** for onboarding me regarding scientific codes, to **Clemens Watzenböck** who worked with me on the first project and to **Mathias Winder** for always bringing a vivid atmosphere into the office. I would also like to thank **Patrick Kappl**, who has all the answers to grammar, layout, diagrammatics and what movie to watch on Friday. Further, let me thank **Matthias Reitner**, who was already a great office colleague during the time of my master's thesis and has now rejoined the Ph.D. office. Last but not least, my thanks go to the "new kids on the block", **Juray Krsnik** and **Simone Di Cataldo**.

But our group is more than just the office and I would like to thank **Anna Kauch**, **Jan M. Tomczak**, **Patrick Chalupa-Gantner**, **Sebastian Huber**, **Motoharu Kitatani** and **Andriy Smolyanyuk** for sharing their knowledge and always taking time for discussions. My thanks also go to **Matthias Pickem** for continually helping debug my code and install the necessary software and to **Severino Adler** with whom I got to spend two of my over-seas scientific trips, both of which we extended to do some sightseeing. The same goes for **Friedrich Krien**, with whom I got to attend the M2S conference in Vancouver and subsequently visited the Jasper national park in Canada. Special thanks also go to **Markus Wallerberger**, with whom it was always a special joy to discuss physics, education and everything else while going for a relaxing run after work. Though not from our research group **Benjamin Knebel-Knobloch** has continually challenged my view on cuprates and provided invaluable and fun discussions.

Nevertheless, the time during a Ph.D. is not only filled with science. Here I would like

Die approbierte gedruckte Originalversion dieser Dissertation ist an der TU Wien Bibliothek verfügbar.
The approved original version of this doctoral thesis is available in print at TU Wien Bibliothek.
TU Bibliothek Your knowledge hub WIEN

to thank **Michael Scherbela** for the many unforgettable hikes that balanced the time sitting in the office. Also, many thanks to **Markus Ruplitsch** with whom I had many (online) discussions during the Covid lockdown and who kept me focused on what's important. Special thanks also go to my girlfriend **Veronika**, who was always there for me during that time.

In the end, my utmost gratitude goes to my parents **Ulrike** and **Harald**, who have shown me unwavering support over the years. Without you, this all would truly not have been possible.

Die approbierte gedruckte Originalversion dieser Dissertation ist an der TU Wien Bibliothek verfügbar.
The approved original version of this doctoral thesis is available in print at TU Wien Bibliothek.
TU Bibliothek Your knowledge hub WIEN

List of Talks and Posters

Conference Talks

10/2022 **Electronic structure of and superconductivity in nickelates**
Meeting of the Austrian Physical Society Leoben (Austria)

09/2022 **Nickelate superconductors: from infinite to finite layers**
Meeting of the German Physical Society Regensburg (Germany)

07/2022 **Nickelate superconductors: from infinite to finite layers**
M2S Conference on Magnetism and Superconductivity Vancouver (Canada)

07/2022 **Nickelate superconductors**
TU Wien Solid-state Physics Institute Seminar Neukirchen (Austria)

05/2022 **Nickelate superconductors: from infinite to finite layered systems**
Online Workshop on Two-particle Correlations Online

09/2021 **Electronic correlations in novel superconductor Ba_2CuO_{3+y}**
Meeting of the Austrian Physical Society Innsbruck (Austria)

Poster presentations

10/2022 **Nickelate superconductors from a DMFT+DΓA perspective**
Autumn School on Correlated Electrons Jülich (Germany)

06/2022 **Nickelate superconductors from a DMFT+DΓA perspective**
Summer School on Computational Quantum Materials Sherbrook (Canada)

03/2020 **Diagrammatic analysis of optical excitations in strongly correlated systems: π-tons**
Aspen Conference on Quantum Matter Aspen (USA)

Die approbierte gedruckte Originalversion dieser Dissertation ist an der TU Wien Bibliothek verfügbar.
The approved original version of this doctoral thesis is available in print at TU Wien Bibliothek.

PAUL WORM

Computational Material Science & Physics

CONTACT

[redacted]

SKILLS

German	Native
English	Fluent
Teaching	3+ yrs
Python	3+ yrs
LaTeX	3+ yrs
Fortran	2+ yrs
MS Office	3+ yrs
Matlab	2+ yrs
Linux	3+ yrs
Machine Learning	1+ yrs
C,C++	1+ yrs

EDUCATION

Ph. D. candidate - Computational Material Science — 2020 - ongoing
Technical University of Vienna, Vienna (Austria)
Current Status: Writing thesis.

Dipl.-Ing. (MSc) - Technical Physics — 2018 - 2020
Technical University of Vienna, Vienna (Austria)
Graduated with distinction: **1.1 mean grade**

BSc - Technical Physics — 2016 - 2018
Technical University of Vienna, Vienna (Austria)
Graduated with distinction: **1.3 mean grade**

Bachelors Programme - Technical Physics — 2014 - 2016
Technical University of Graz, Graz (Austria)

Highschool — 2006 - 2014
Seebacher Gymnasium, Graz (Austria)
Graduated with distinction.

WORK EXPERIENCE

Project Intern — Jun 22 - Jun 22
Nagler & Company, Graz (Austria)
Task: create an easy to understand presentation about Machine learning applications.

Teaching Assistant - Machine learning in physics — Mar 21 - Jul 21
Technical University of Vienna, Vienna (Austria)
Weekly Q&A sessions covering the study material. (∼ 25 people)

Teaching Assistant - Numerical and theoretical physics — Oct 17 - Jul 19
Technical University of Vienna, Vienna (Austria)
Give weekly exercise classes in various study courses from the field of numerical and theoretical physics. (∼ 20 people)

Project Intern — Sep 2014
Montanuniversity Leoben, Leoben (Austria)
Work in the atomic force microscopy laboratory.

WORKSHOPS & CONFERENCES

Annual meeting of the German physical society — Sep 2022
Regensburg, Germany
Talk: New insights into nickelate superconductors

M2S: Magnetism and Superconductivity — Jul 2022
Vancouver, Canada
Talk: Importance of electronic correlations in nickelate superconductors

Summer-school on Computational Quantum Materials — Jun 2022
Jouvence, Quebec, Canada
Poster: Nickelate superconductors from a DMFT and DΓA perspective

Die approbierte gedruckte Originalversion dieser Dissertation ist an der TU Wien Bibliothek verfügbar.
The approved original version of this doctoral thesis is available in print at TU Wien Bibliothek.
TU Bibliothek Your knowledge hub WIEN

ACHIEVEMENTS

Research

Condensed Matter

12 publications in peer reviewed journals
(8 accepted, 4 in review).

Competitions

PLANCKS - International:
Team competition for master students in physics.

Participated: 2016/2019

PLANCKS - National:
1. Place: 2016/2019

AYPT - National:
Physics team competition for high-school students

1. Place: 2011/2013/2014
2. Place: 2012

Awards

Christiana Hörbiger award
2022

Scholarship grant TU Graz
2015

Dr. Hans Riegel-Fachpreis
2014 (2nd Price)

Trainings

Project management
One week in summer of 2022

Ballroom Dancing

Austrian national cadre
2017-2019

Austrian National Ballroom Championship
A-class: 4. place (2018)
B-class: 5. place (2017)

Conference on Novel Quantum Materials — Mar 2022
Amalfi, Italy

Annual meeting of the Austrian Physical Society — Okt 2021
Innsbruck, Austria
Talk: Electronic correlations in the novel superconductor Ba_2CuO_{3+y}

IYPT - International Young Physicists' Tournament — Summer 2020
Gold: Kutaisi, Georgia
Team leader (supervisor) of the Austrian national team of high-school students that present and discuss their own research results.

Conference on Strongly Correlated Materials — Mar 2020
Aspen, Colorado, USA
Poster: On the electron-light interaction in strongly correlated electron systems.

IYPT — Summer 2012-14
Bronze: Shrewsbury, England (2014)
Silver: Taipeh, Taiwan (2013)
Silver: Bad Saulgau, Germany (2012)
Participant as member of the Austrian national team.

SELECTED PUBLICATIONS

Correlations tune the electronic structure of penta-layer nickelates into the superconducting regime — Phys. Rev. M.
Phys. Rev. Materials 6, L091801 (2022)
P. Worm, L. Si, M. Kitatani *et al.*

Phase diagram of nickelate superconductors calculated by dynamical vertex approximation — Front. Phys.
Front. Phys. 9 (2021)
K. Held, L. Si, P. Worm *et al.*

Explaining the pseudogap through damping and antidamping on the Fermi surface by imaginary spin scattering — Commun. Phys.
Commun. Phys. 5, 336 (2022)
F. Krien, P. Worm, P. Chalupa-Ganter *et al.*

EXTRACURRICULAR

- Member of the Austrian Young Physicist's Tournament (AYPT)
- Member of the organising committee of the International Young Physicist's Tournament (IYPT)
- Member of Young Minds, a network to popularise and support physics in Austria.
- Hobbies: ballroom dancing (former competitive), hiking, running, mountaineering
- Licenses: driving license for cars

Die approbierte gedruckte Originalversion dieser Dissertation ist an der TU Wien Bibliothek verfügbar.
The approved original version of this doctoral thesis is available in print at TU Wien Bibliothek.
TU Bibliothek Your knowledge hub WIEN